TECHNISCHE
UNIVERSITÄT
WIEN
Vienna University of Technology

DISSERTATION

Ab initio modelling of Transition Metal Oxides - Studies on stoichiometric and substituted TiO_2 and $GaFeO_3$.

Ausgeführt zum Zwecke der Erlangung des akademischen Grades eines Doktors der technischen Wissenschaften unter der Leitung von

Univ. Prof. Dipl.-Ing. Dr. techn. Peter Mohn
E 134
Institut für Angewandte Physik

eingereicht an der Technischen Universität Wien
Fakultät für Physik

von

DI Jacqueline Atanelov
0625326
Praterstrasse 11/1/4, 1020 Wien

Wien, am 24. Februar 2016

Kurzfassung

Übergangsmetalloxide zeichnen sich durch eine Vielzahl unterschiedlicher magnetischer und elektrischer Eigenschaften aus. Diese sind von großem Interesse, da sie die Grundlage für Anwendungen in der Industrie, Medizin und Computertechnik liefern. Die vorliegende Arbeit untersucht zwei in dieser Hinsicht viel versprechende Materialien, TiO_2 und $GaFeO_3$. Beide zeichnen sich durch einen Grundzustand aus, der nicht magnetisch und halbleitend ist. Dotiert man beide Systeme, so verändern sich Ihre magnetischen und elektrischen Eigenschaften. TiO_2 ist vorwiegend für seine photokatalytischen Eigenschaften bekannt, während $GaFeO_3$ als magnetoelektrisches multiferroisches Material immer mehr an Bedeutung gewinnt.

Der erste Teil der Arbeit beschäftigt sich mit der elektronischen und magnetischen Struktur von Kohlenstoff und Stickstoff dotiertem Rutil TiO_2. Dabei werden substitutionelle als auch interstitielle Fehlstellen untersucht. Hierzu werden *ab initio* Berechnungen an einer 48 Atome großen Superzelle mit Hilfe des VASP Codes durchgeführt. Um eine realistische Beschreibung der physikalischen Eigenschaften zu erhalten, wird der Austausch-Korrelations Anteil mit dem HSE06 hybrid Funktional angenähert. Ersetzt man nun ein Sauerstoffatom mit einen Kohlenstoff- oder Stickstoffatom, so wird ein magnetisches Moment induziert. Während Kohlenstoff ein Gesamtmoment von $2\mu_B$ pro Superzelle erzeugt, liefert Stickstoff ein magnetisches Moment von $1\mu_B$. Besetzt man mehrer Sauerstoffplätze, so zeigen beide Atome die Tendenz einer langreichweitigen antiferromagnetischen Kopplung. Im Fall von interstitiellen Fehlstellen, verliert Kohlenstoff sein magnetisches Moment, während Stickstoff weiterhin ein Moment von 1 μ_B pro Superzelle erzeugt. Für die interstitiellen Fehlstellen finden sich zwei Lösungen. Eine beschreibt einen Sattelpunkt, auf dem das Fremdatom zwischen den benachbarten Titan- und Sauerstoffatomen liegen bleibt. Die stabile Lösung hingegen ist jene, bei der der Kohlen- und Stickstoff eine Bindung mit einem der benachbarten Sauerstoffatome eingeht. Dadurch formen sich C-O und N-O Dimere, deren Bindungslängen sehr ähnlich jenen von doppellt gebundenen CO und NO Molekülen sind. Dieses Ergebnis bestätigt die schon in XPS-Experimenten nachgewiesenen N-O Komplexe. Dadurch motiviert, wurden die dazugehörigen symmetrischen Streckschwingungsfrequenzen ausgerechnet, um eine zukünftig mögliche experimentelle Verifikation zu erleichtern. Für alle untersuchten Dotierungskonfigurationen wurden Kohlenstoff- und Stickstoff Zustände in der TiO_2 Bandlücke gefunden. Diese neu induzierten Zustände werden im Zusammenhang mit den photokatalytischen Eigenschaften von TiO_2 diskutiert.

Der zweite Teil der Arbeit untersucht die magnetischen und elektrischen Eigenschaften von $GaFeO_3$. Wir beginnen mit *ab initio* DFT Berechnungen, durchgeführt an stoichiometrischen $GaFeO_3$. Im Detail wird dabei der Ursprung des antiferromagnetischen (AFM) Grundzustandes untersucht. Mit Hilfe der erhaltenen Ergebnisse lässt sich der dafür verantwortliche Superaustausch in einem Molekülorbital-Bild darstellen. Dieser wird über die Fe-O-Fe Bindungen im Kristall transferiert und gehorcht den sogenannten Goodenough-Kanamori Regeln. Der AFM Grundzustand wird durch zwei dominante Fe-O-Fe Verbindungen erzeugt, die sich in c-Richtung durch den Kristall ausbreiten und eine Kette bilden. Des Weiteren werden die magnetokristallinen Anisotropien berechnet und dabei auch intrinsische Kationenfehlstellen beachtet. Diese werden immer wieder in Experimenten nachgewiesen und führen zu einem ferrimagnetischen Grundzustand. Zusätzlich wird eine vom Untergitter abhängige Anisotropie betrachtet. Neben der stoichiometrischen Einheitszelle werden auch verschiedene Dopingkonfigurationen untersucht. Dabei wird der Eisengehalt in der Zelle variiert und ein Bereich von $0.0 \leq x \leq 2.0$ in $Ga_{2-x}Fe_xO_3$ simuliert. Bei den Grenzwerten von x=0.0 und x=2.0 transformiert $GaFeO_3$ in die isomorphen ε-Ga_2O_3 und ε-Fe_2O_3 Strukturen. Weiters wird eine Stauchung und Streckung der reinen und dotierten Zelle simuliert. Die dadurch veränderte Zellgeometrie steht unter Verdacht, die magnetischen Kopplungen zu beeinflussen.

Neben unterschiedlichen Eisenkonzentrationen wird auch die Substitution von Sauerstoff untersucht. Dabei wird ein Sauerstoffatom durch ein Kohlenstoff-, Stickstoff- oder Schwefelatom ersetzt. Da das Sauerstoffatom den Superaustausch zwischen benachbarten Eisenatomen überträgt, kann sich ein Austausch besonders auf die magnetischen Eigenschaften auswirken. Die daraus resultierenden Zustände können für neue technische Anwendungen attraktiv sein. Es werden vier verschiedene Sauerstoffsubstitutionen pro Dotierungsatom untersucht, wobei sich herausstellt, dass die resultierenden magnetischen Eigenschaften vom Gitterplatz abhängen. Kohlenstoff kann dabei anstatt einer AFM Kopplung - wie im Falle des Fe1-O-Fe2 Komplexes - eine ferrimagnetische Wechselwirkung in der Fe1-C-Fe2 Verbindung induzieren. Ab-hänging von der Dotierungsstelle führt Kohlenstoff zu einer AFM oder ferrimagnetischen Kopplung zwischen den benachbarten Eisenatomen. Auch Stickstoff beeinflusst die magnetische Kopplung der Eisenatome, während Schwefel große strukturelle Deformationen in der Zelle mit sich bringt. All dies hat Auswirkungen auf die Bandlücke und die magnetischen Kopplungen in $GaFeO_3$. Die jeweiligen Austauschmechanismen werden dabei im Detail beschrieben und eine mögliche Verwendung als Photokatalystator diskutiert. Zusätzlich wird wieder eine Stauchung und Streckung der dotierten Zelle simuliert und die magnetischen Anisotropien berechnet.

Die an beiden Systemen durchgeführten Simulationen und Berechnungen stimmen mit den Ergebnissen zahlreicher experimenteller Studien überein. Neben unterstützenden Rechnungen, die oft Klarheit über Experimente bringen, werden *ab initio* DFT Berechnungen in dieser Arbeit auch als Innovationswerkzeug verwendet. Dadurch sollen bisher im Experiment nicht untersuchte Konfigurationen simuliert werden und Anstoß für zukünftige Verwendungen und weitere Untersuchungen liefern.

Abstract

Transition metal oxides show a big varitey of physical properties that are interesting for a multitude of applications, including industries, medicine and electronic devices. This thesis investigates the properties of two promising compounds, TiO_2 and $GaFeO_3$. Both are nonmagnetic semiconductors in their ground state, but show different magnetic and electronic properties incorporating impurity atoms. TiO_2 is mostly known as a photocatalyst and $GaFeO_3$ as a magnetoelectric multiferroic.

The first part of the thesis studies the electronic and magnetic structure of carbon and nitrogen doped rutile TiO_2. We investigate the effects of substitutional and interstitial anion doping. To this end we perform *ab initio* calculations of a 48-atom supercell employing the VASP code. In order to obtain a realistic description of the electronic and magnetic structure, exchange and correlation are treated with the HSE06 hybrid functional. Substitutional carbon and nitrogen are found to have a magnetic moment of 2 and $1\mu_B$, respectively, with a tendency for antiferromagnetic long range order. For C/N on interstitial sites we find that carbon is non-magnetic while nitrogen always possesses a magnetic moment of $1\mu_B$. We find that these interstitial positions are on a saddle point of the total energy. The stable configuration is reached when both carbon and nitrogen form a C-O and N-O dimer with a bond length close to the double bond for CO and NO. This result is in agreement with earlier experimental investigations detecting such N-O entities from XPS measurements. The frequencies of the symmetric stretching mode are calculated for these dimers, which could provide a means for experimental verification. For all configurations investigated both C and N states are found inside the TiO_2 gap. These new electronic states are discussed with respect to tuning doped TiO_2 for the application in photocatalysis.

The second part of the thesis studies studies $GaFeO_3$. We start with *ab initio* DFT calculations on stoichiometric $GaFeO_3$. A detailed discussion of the origin of the antiferromagnetic (AFM) superexchange in stoichiometric $GaFeO_3$ is given, including a molecular orbital description of the exchange mechanism derived from our calculations. In addition, we study the properties of the Fe-O-Fe bonds for different geometries to underline the angle and distance dependence of the AFM coupling as formulated in the Goodenough-Kanamori rules. We describe the AFM ground state of $GaFeO_3$ as a result of two intrinsic Fe-O-Fe chains that meander through the crystal along the c direction. The magnetocrystalline anisotropy energies are calculated for the stoichiometric phase with and without inner cationic site disorder. Furthermore, we show the presence of a sub-lattice dependent anisotropy. Moreover, we perform studies on cation doped $Ga_{2-x}Fe_xO_3$ for varying Fe concentrations x ($0.0 \leq x \leq 2.0$). At a value of x=0.0 and x=2.0 $GaFeO_3$ transforms into the isomorphic ε-Ga_2O_3 and ε-Fe_2O_3 phase, respectively. The effect of strain

was also studied. Incorporating dopants and applying strain to the simulation cell changes the intrinsic geometry and thus the magnetic properties of gallium ferrite.

Subsequently we examine the effect of anion doping substituting O by a C, N and S atom, respectively. Replacing the superexchange mediating O atom with p-elements of a different valence electron configuration changes the underlying magnetic exchange mechanism and influence the ground state properties. This may be used for tuning properties interesting for technical applications. Four different doping configurations were examined revealing a cell site dependent influence on the magnetic properties. Carbon, for example, changes the AFM coupling present in the Fe1-O-Fe2 configuration into a ferrimagnetic exchange for the Fe1-C-Fe2 bond. Depending on the respective cell site C substitution introduces a ferrimagnetic or AFM ground state. Nitrogen alters the ground state magnetic moment as well and Sulfur introduces large structural distortions affecting the band gap and the overall AFM coupling inside the doped $GaFeO_3$ simulation cell. We give a detailed discussion on the respective magnetic exchange mechanisms and electronic properties with regard to applications as photocatalysts. Further, we again investigate the effect of strain and determine a possible change of the magnetocrystalline anisotropy energies.

The performed calculations and results obtained for both investigated systems agree with previous experimental studies. In addition to that, we use the predictive power of *ab initio* DFT simulations, examine doping configurations that have not been investigated yet. That, however, may trigger future experiments in the very promising field of tunable multifunctional devices and photocatalysts.

Contents

Chapter 1

Transition Metal Oxides

A brief overview

Transition metal oxides (TMO) appear in many different crystal structures and exhibit a wide range of technically important electronic, magnetic and optical properties. They exist as dielectrics, semiconductors, metals, ferroelectrics, catalysts, thermoelectrics and high temperature superconductors. Multiferroics are TMO that combine more than one electronic phenomena in a single phase [1, 2]. These are of great interest, since materials providing multifunctionalities can give rise to new applications and innovations for sensors, spintronics and data storage devices, to name but a few. TMO are used in various applications including photo induced water splitting, giant magnetoresistance devices and batteries [2]. Many of these phenomena like the high temperature superconductivity, however, still have not been entirely understood yet. High efforts and intensive research has been made to extent the to the date not fully exhausted potential of these fascinating materials.

TMO have been studied for about nearly fifty years, starting with the discovery of ferroelectricity in $BaTiO_3$ [3–5]. The dielectric properties of perovskites have been intensively investigated since then. Followed by that superconductivity was first discovered in doped $BaBiO_3$ [6]. The technically even more valuable high temperature superconductivity was found in cuprates, like $YBa_2Cu_3O_{7-X}$ and aroused high scientific interest in the late 1980s and 1990s [7, 8]. The manifold magnetic properties and exchange mechanisms present in TMO have attracted great attention regarding both new technological applications and fundamental research. Studying the various antiferromagnetic (AFM) structures of $(La_{1-x}Ca_x)MnO_3$ gave rise to the Goodenough-Kanamori (GK) rules of superexchange [9–11]. The more recently discovered phenomena of multiferroicity [12–14] and the colossal magnetoresistance [15–17] currently excites the scientific community and triggered off intensive investigations [18].

Leaving all the technically valuable and promising perspectives aside, TMO gives historical objects like statues and buildings their unique appearance and furthermore characterizes some of the most impressive nature landscapes.

> *[...] oxidized transition metals can lend themselves to aesthetic values, from the captivating green hue of the Statue of Liberty to the reddish landscape of the Grand Canyon.*
>
> Sang-Wook Cheong, "Transition metal oxides - The exciting world of orbitals",
> Nature Materials, volume 6, 2007, p. 927-928, at p. 928

1.1 Transition Metals

Transition metals are characterized by an open *d* shell and exhibit many different oxidation states leading to a big variety of physical properties in TMO. The transition metal elements are listed in the groups 3 to 12 of the periodic table of elements (PTE) and form the so called *d* block. According to the official definition a transition metal is defined as an atom with a partially filled *d* subshell, or which can give rise to cations with an incomplete *d* subshell [19].

Considering the electronic configuration of the *d* block elements, following the Madelung rules the $4s$ shell is lower in energy compared to the $3p$ shell and therefore filled first. Spectroscopic investigations, however, show that the Madelung rules do not apply to all *d* block elements [20–22]. Focussing on the first $3d$ series (Sc-Zn) following these rules Cr and Cu should exhibit a fully occupied $4s$ shell. Experiments, however, report to a half filled $4s$ orbital with only one *s* electron. The second $4s$ electron becomes added to the $3d$ shell. Regarding the Cr atom the number of $3d$ electrons increases from 4 to 5, giving Cr a half filled $3d$ shell. The total energy is reduced by the respective electronic configuration compared to the one predicted by the Madelung rules. Adding one of the $4s$ electrons to the $3d$ orbital, in the case of Cu, yields a fully occupied $3d$ shell. A closed $3d$ shell is lower in energy and brings Cu into a more stable state.

However, one has to differentiate between a free space atom and an atom inside a crystal forming chemical bonds and being influenced by a crystal field. Latter can enter different electronic ground state configurations that depend on the respective oxidation state and is influenced by the chemical surrounding. The vast majority of the *d* block elements exhibit more than one oxidation state. Regarding the first row *d* block elements (Sc-Zn), Mn exhibits the biggest number of oxidation configurations. The number of oxidation states decreases moving to the left and right inside the PTE starting from

Mn ending at Sc and Zn, respectively. Sc and Zn can enter only a single oxidation state, namely the Sc^{3+} and the Zn^{2+} configuration. In these states both atoms have no electrons left in their $4s$ shells. Sc^{3+} exhibits an empty $3d$ shell as well, whereas Zn^{2+} has a fully occupied closed $3d$ shell. According to the aforementioned definition of a transition metal, both elements do not fulfill the criteria of a partially filled d subshell and are therefore not considered as a transition metal element in the context of a TMO. Same is true for the d block elements Y, Zn, Cd, La and Hg.

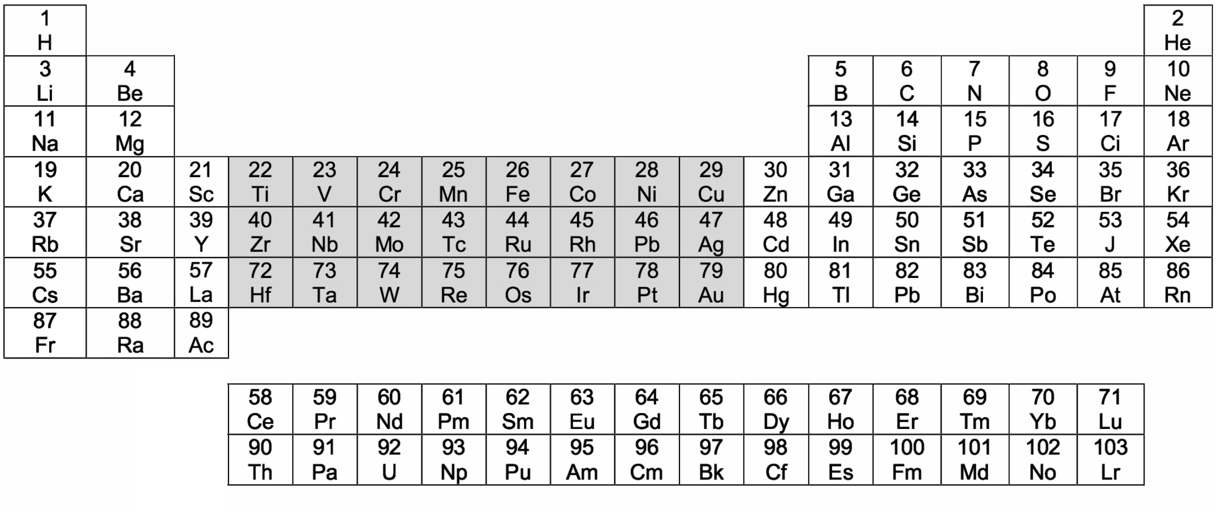

1 H																	2 He
3 Li	4 Be											5 B	6 C	7 N	8 O	9 F	10 Ne
11 Na	12 Mg											13 Al	14 Si	15 P	16 S	17 Ci	18 Ar
19 K	20 Ca	21 Sc	22 Ti	23 V	24 Cr	25 Mn	26 Fe	27 Co	28 Ni	29 Cu	30 Zn	31 Ga	32 Ge	33 As	34 Se	35 Br	36 Kr
37 Rb	38 Sr	39 Y	40 Zr	41 Nb	42 Mo	43 Tc	44 Ru	45 Rh	46 Pb	47 Ag	48 Cd	49 In	50 Sn	51 Sb	52 Te	53 J	54 Xe
55 Cs	56 Ba	57 La	72 Hf	73 Ta	74 W	75 Re	76 Os	77 Ir	78 Pt	79 Au	80 Hg	81 Tl	82 Pb	83 Bi	84 Po	85 At	86 Rn
87 Fr	88 Ra	89 Ac															
			58 Ce	59 Pr	60 Nd	61 Pm	62 Sm	63 Eu	64 Gd	65 Tb	66 Dy	67 Ho	68 Er	69 Tm	70 Yb	71 Lu	
			90 Th	91 Pa	92 U	93 Np	94 Pu	95 Am	96 Cm	97 Bk	98 Cf	99 Es	100 Fm	101 Md	102 No	103 Lr	

Figure 1.1: Periodic table of the elements. Transition metal elements are highlighted in grey.

1.1.1 Transition Metal Elements and Oxygen

The wide range of electronic properties present in TMO can be attributed to the numerous oxidation states transition metal elements can enter. Elements in lower oxidation states are mostly found as simple ions, whereas transition metals in higher oxidation states tend to form covalent bonds with elements like O and F as anions.

Oxygen is a highly reactive non metallic element. Due to its high electronegativity it readily forms compounds with other elements and has a strong tendency to fill up its p shell exhibiting a noble gas configuration. Entering an ionic bond with a transition metal element oxygen takes two of its electrons and ends up in a O^{2-} state. Forming a covalent bond O shares two electrons with the respective element. Both atomic orbitals overlap.

The electronegativity X can be used as a quite meaningful quantity to estimate the bonding character of a transition metal and oxygen atom. Knowing the electronegativity of both atoms Hannay and Smyth formulated an empirical relation to calculate the percentage of the ionic character of a bond by [23]

$$P(\%) = 16(\chi_B - \chi_A) + 3.5(\chi_B - \chi_A)^2 \quad , \tag{1.1}$$

where $\chi_B > \chi_A$ with $\chi_B = \chi_O$ and $\chi_A = \chi_{TM}$. Figure 1.2 plots P(%) as a function of the electronegativity difference χ_O-χ_{TM} for O and the 3*d*-5*d* transition metal elements using the revised pauling scale of electronegativities [24].

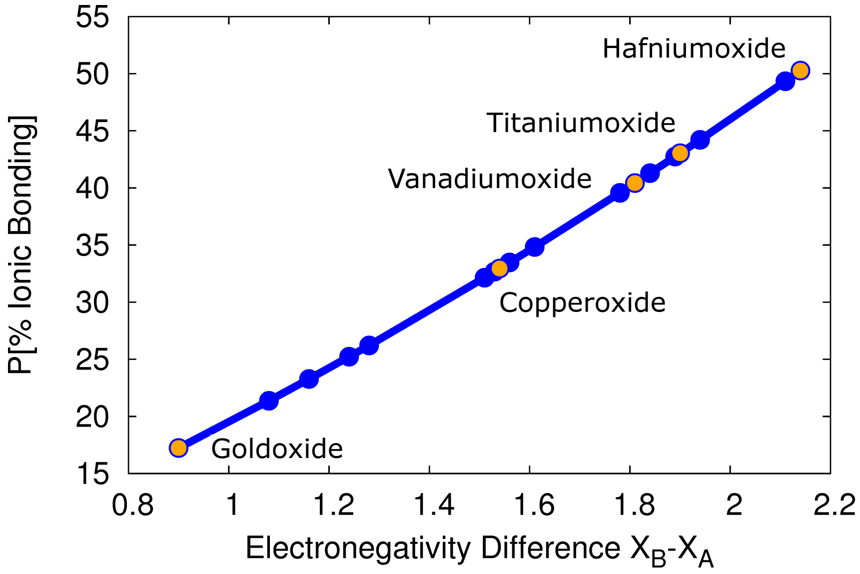

Figure 1.2: P(%) as a function of the electronegativity difference χ_O-χ_{TM} for O and 3*d*-5*d* transition metal elements.

Transition metals on the right side of the *d* block exhibit an increased covalent bonding character compared to the transition metal elements on the left side of the PTE. Goldoxide shows minimal ionic bonding character with only 17.23% and Hafniumoxide maximum with 50.26%.

The various possible oxidation states of transition metals gives rise to many different bonding types in TMO and crystal structures. TMO appear in the perovskite, spinel, rutile, cesium chloride, fluorite, zinc blende, rocksalt and corundum structure among others. An example on how oxidation states and the surrounding chemical environment influences the type of bonding and the crystal structure is given by Cu_2O (cuprite) and CuO (tenorite). Cuprite has a cubic crystal structure with linear bonds between the Cu and O atoms exhibiting a sp-hybridization [25, 26]. Cu_2O crystallizes in a monoclinic structure with a quadratic planar coordination of the Cu and O atoms and a covalent spd^2-hybridization [27, 28]. Both structures have different cation-anion distances and radius ratios r_{cation}/r_{anion} (r_{Cu^+}=87 pm, $r_{Cu^{2+}}$=93 pm) which, after the rules published by L Pauling in 1929 [29], affects the coordination number, the crystal structure and consequently the electronic properties.

1.1.2 Crystal Field Splitting

The *d* orbitals of a transition metal element are degenerate in free space, assuming the absence of any other atom or potential. Consequently all of the five *d* orbitals are equal in energy. Considering a transition metal element inside a crystal the chemical surrounding and the crystallographic environment can lift the degeneracy of the states leading to an energetic splitting of the orbitals. Supposing the transition metal atom to be surrounded by an oxygen octahedra there are two main contributions that yield in an energetic splitting of the *d* orbitals d_{xy}, d_{yz}, d_{zx}, d_{z^2} and $d_{x^2-y^2}$. First the electrostatic interactions between the charged transition metal ion and oxygen atoms has to be considered. The respective contribution is small and can be described within the *crystal field theory*, using a point charge approximation. Secondly, hybridizations can be formed with the surrounding ligands, the O atoms, shifting the *d* orbitals in energy as well. This, however, has more effect on the transition metal *d* orbital energies and is described in the *ligand field theory*. The ligand field theory is based on the crystal field theory but includes the molecular orbital theory. The crystal field theory, however, describes the vanishing degeneracy and splitting of the *d* orbitals as a consequence of the electric field produced by adjacent static charges. It was developed by Hans Bethe and John Hansbrouck van Vleck in the 1930s [30]. The crystal field theory was successful describing the experimentally observed photoemission and spectroscopy of TMO with a rather ionic bonding character. It not surprisingly failed for structures that consist of mainly covalent bonds, since it does not consider the atomic orbital structure. To overcome this shortcoming Griffith and Orgel [31] included the molecular field theory to the existing crystal field theory and derived the ligand field theory.

Figure 1.3 shows the degenerate *d* states of a free transition metal atom and compares them to the energetically split *d* orbitals of different O surroundings. Presented are the *d* orbital energy levels inside a cubic, a tetragonal and an orthorhombic oxygen octahedra, as well as for a square planar geometry. The latter corresponds to an octahedra with and infinitely long *z* axis.

Starting with the cubic structure (x=y=z) the *d* states segregate into the so called e_g and t_{2g} orbitals. The first one includes the degenerate d_{z^2} and $d_{x^2-y^2}$ states and the second the d_{xy}, d_{yz} and d_{zx} orbitals. The angular functions given in figure 1.3 show the spatial probability of the electrons (shown in figure 1.3) in the respective *d* orbital. In the cubic geometry the t_{2g} states are lower in energy than the e_g states. Electrons occupying the d_{z^2}

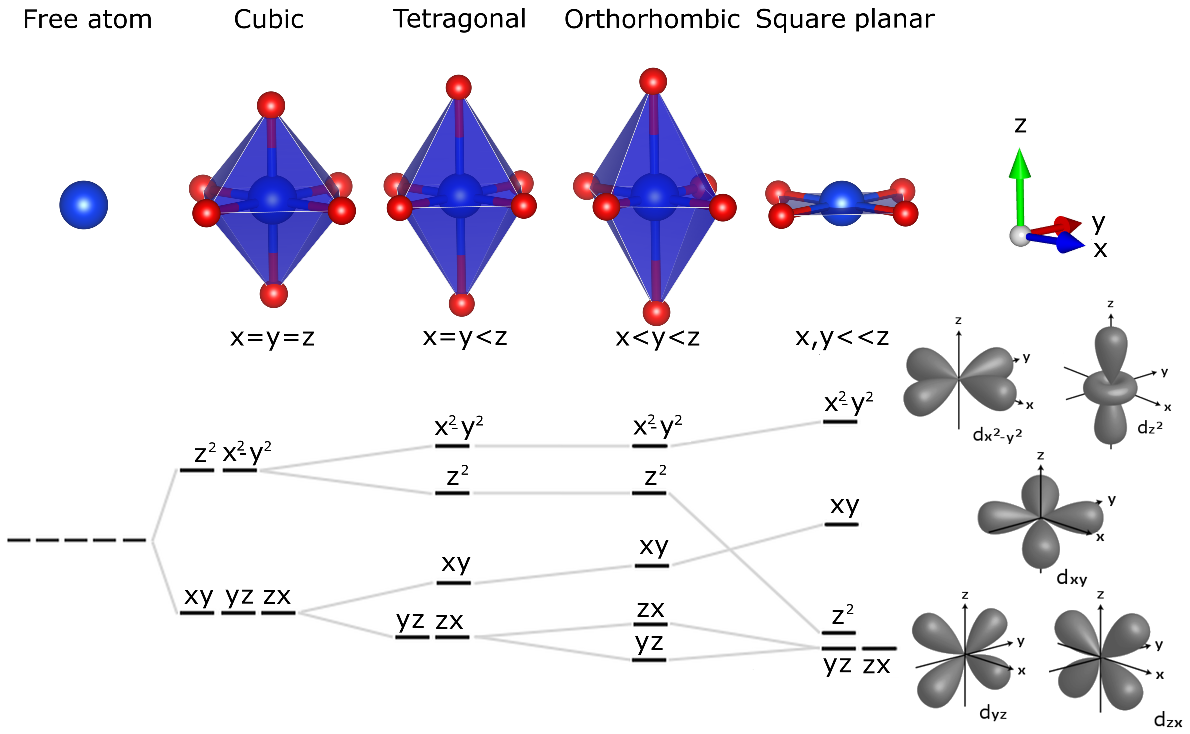

Figure 1.3: *d* orbital splitting of a tranistion metal atom (highlighted in blue) evoked by the surrounding O octahedra (atoms highlighted in red). Atomic obitals using real angular functions are presented as well. *d* orbital splitting is shown for different octahedra geometries.

and $d_{x^2-y^2}$ orbitals, point towards the oxygen atoms and hence experience an enhanced coulomb repulsion. The t_{2g} orbitals point towards planes and edges of the octahedra and consequently experience a minimized repulsive potential of the O ions.

In a square planar geometry the d_{z^2} states become shifted to lower energies. The repulsive potential of the O atoms vanishes in z direction with $x,y<<z$. Noteworthy, the energy levels shown in figure 1.3 represent the transition metal *d* anti-bonding states.

The electronegativity and the spatial overlap of the transition metal ion *d* and the O *p* states make the structure either to become magnetic, insulating or metallic. Magnetic insulating states occur for weak covalent bonds between the transition metal ion and the oxygen atom, yielding localized valence electrons. Enhancing the interaction strength by increasing the electronegativity or the orbital overlap leads to a partial delocalization of the valence electrons resulting in a metallic conductor. Structural changes induced by point defects (see section 1.3.1) or strain (see section 1.3.2) can distort the ground state crystal structure. This again alters properties like the orbital overlap and the surrounding symmetries which may lead to changes in the electronic properties of the corresponding material.

It is noteworthy to consider that the sequence of the molecular orbitals as shown in figure 1.3 is a consequence of the underlying ionic bond. In systems with covalent bonds the next neighbour bonds are formed by the d_{z^2} and $d_{x^2-y^2}$ orbitals. These are therefore lower in energy than the d_{xy}, d_{yz} and d_{zx} orbitals, so that the e_g and t_{2g} splitting becomes reversed.

Before discussing the various ways of altering the electronic and magnetic properties of a TMO it is important to understand and define the underlying exchange mechanisms in the corresponding material. Hence a short introduction of the main exchange mechanisms present in TMO is given.

1.2 Exchange Interactions

Simplified and broken down to its core there are two types of magnetism. Type one has individual magnetic moments located at different crystal sites that do not interact or influence each other. At finite temperature the magnetic moments point into random directions and corresponding to dia- or paramagnetic materials. Type two exhibits a spontaneous ordering of the magnetic moments. Depending on the exchange interaction this ordering can be either short or long ranged. The respective phenomena is called collective magnetism.

Exchange interactions can not be described classically. They are based on quantum mechanics while at the same time being purely electrostatic in nature. Combining the Coulomb interaction with the Pauli principle, demanding an antisymmetric electron wavefunction, gives the basis of all exchange interactions. 1923 Dirac and Heisenberg independently discovered that exchange phenomena are crucial for the appearance of collective magnetism [32, 33]. When nearest or long ranged permanent magnetic moments become aligned either parallel or antiparallel we speak of a ferro-, antiferro- or ferrimagnet, respectively. The underlying exchange mechanisms can be divided into a direct and indirect exchange interaction. All in all, as mentioned before, these interactions origin out of an interplay between the Pauli principle and the electron-electron Coulomb repulsion.

There are different exchange mechanisms present in magnetic metals or insulator. Magnetic insulating states are produced by the superexchange mechanism wheres in metals exchange is governed by the double exchange and the RKKY (Ruderman, Kittel, Kasuya and Yoshida) interaction. All of them are variations of the indirect exchange.

1.2.1 Direct Exchange

Electrons are fermions and treated as indistinguishable particles. In the non relativistic case the electronic wavefunction is defined as the antisymmetric product of a spatial part and a spin part. Providing an antisymmetric wavefunction either the spatial or the spin part has to be antisymmetric. The respective other part then must be symmetric yielding the provided antisymmetric product wave function.

Assuming two electrons with equal spins the electron wavefunction is the product of a symmetric spin and an antisymmetric spatial function. The probability of finding two electrons with equal spin close to each other is reduced by the antisymmetric spatial function creating a so called Fermi hole. Considering the other case of two electrons with opposite spin the spatial function is symmetric leading to a higher probability of the two electrons to be found close to each other. In that case we speak of a so called Fermi heap. Due to the Coulomb repulsion of two particles of like charge, Fermi holes and heaps drastically affect the energy of a many electron systems.

In the case of parallel spins the potential energy, corresponding to the Coulomb interaction, is reduced due to the enhanced spatial distance between the electrons. The kinetic energy increases, since the Fermi energy rises with two electrons occupying the same spin channel. This instance is also considered by the Hund's rule of multiplicity stating that higher multiplicities form states of lower energies. The direct exchange mechanisms consequently appears as an intra-atomic interaction. It becomes dominant in the case of two neighbouring atoms with reduced distance and a pronounced orbital overlap. Effectively the respective interaction is short ranged and decreases with increasing distance. Assuming the trivial case of two atoms possessing an electron each, as in the case of a H_2-molecule, the intra-atomic exchange interaction can be described with the Heitler-London Method [34] which is derived from the Heisenberg model [32]. The two electrons can either form a singlet or triplet state. In the first case the spatial function is symmetric and the electrons show antiparallel spins and are most probably found between the nuclei. In the case of a H_2-molecule this would correspond to a bonding state. The triplet state on the other hand has an asymmetric spatial function and the electrons have equal spins. Calculating the energy difference between the singlet and the triplet state gives the so called exchange interaction J. A positive value of J favours the singlet state and describes an "antiferromagnetic coupling". Negative values of J favour a triplet state and a "ferromagnetic coupling".

The exchange interaction corresponds to an interplay between the electron-electron Coulomb interactions and the constraints of the Pauli exclusion principle. The Bethe-Slater curve, shown in figure 1.4, represents the exchange interaction J of transition metals alloys as a function of the ratio of the interatomic distance a to the diameter d of the $3d$ orbital [35]. According to the Heisenberg Model the exchange energy is given by

$$E_{ex} = -2J\vec{S_i}\vec{S_j} \quad , \tag{1.2}$$

with $\vec{S_i}$ and $\vec{S_j}$ representing the electron spins of the atoms i and j. J is the exchange integral including both electron wavefunctions. For positive values of J $\vec{S_i}$ and $\vec{S_j}$ are parallel and therefore ferromagnetic. A negative value of J corresponds to an antiparallel orientation and hence represents an antiferromagnetic state. Elements above and below the ordinate couple FM and AFM, respectively.

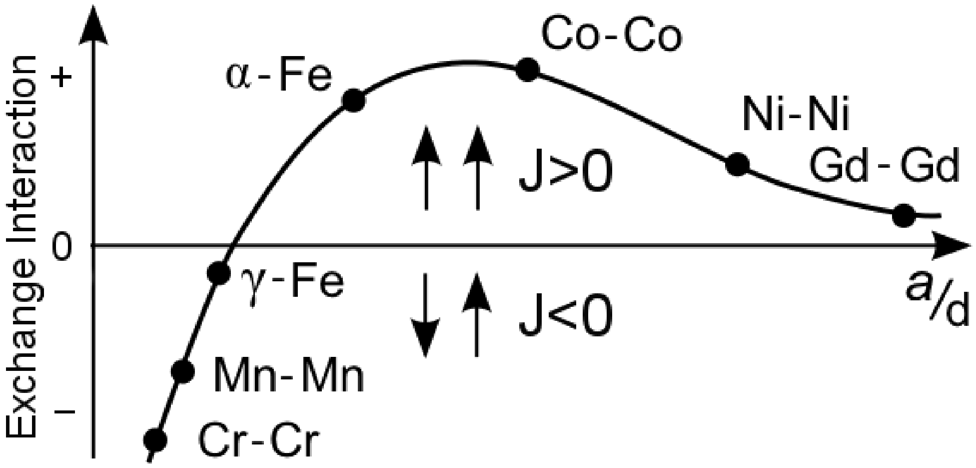

Figure 1.4: The Bethe-Slater curve represents the exchange interaction as a function of the a/d ratio. a corresponds to the interatomic distance and d is the diameter of the respective $3d$ transition metal electronic shell [35, 36]. It should be noted that this famous historical curve is only half true, since the inclusion of the RKKY interaction would lead to additional oscillations between positive and negative vaules of J which are not included here.

1.2.2 Indirect Exchange

The indirect exchange mechanism describes magnetic phenomena mediated by an intermediary. The concept of indirect exchange is not uniquely defined including a wide range of different phenomena. The indirect exchange mechanism is a long ranged interaction in contrast to the spatially restricted direct exchange. A number of indirect exchange mechanisms can be described in the framework of second order perturbation theory leading to an effective Hamiltonian of the Heisenberg type. This is in contrast to the direct exchange which results from a perturbation theory of first order [37]. Different types of indirect exchange mechanisms are the RKKY interaction, the double exchange and the superexchange. The RKKY and the double exchange mechanism are present in metallic systems, whereas the superexchange occurs in insulators and semiconductors.

RKKY

The magnetic ordering introduced by the RKKY interaction is transferred by the conduction electrons [38–40]. Assuming a magnetic ion polarizing the surrounding conduction electrons their polarization interacts and influences the magnetic moment of other ions inside the crystal. Supposing the itinerant electrons not to be localized but traveling throughout the system the RKKY interaction introduces a short ranged magnetic coupling falling off like $1/r^3$. Similar to the exchange interaction J of the direct exchange the RKKY exchange mechanism can be described by the coefficient j. The RKKY exchange coefficient oscillates from positive to negative changing with the separation of the ions and shows a damped oscillatory. Hence, depending on the ionic distance the magnetic coupling turns out to be either AFM or FM. The RKKY exchange interaction happens in rare-earth metals, whose strongly localized $4f$ electrons are shielded by the valence $5s$ and $5p$ electrons. There is no orbital overlap between the d orbitals of neighboring atoms so that the direct exchange becomes suppressed. The magnetic ordering is mediated by the conduction electrons.

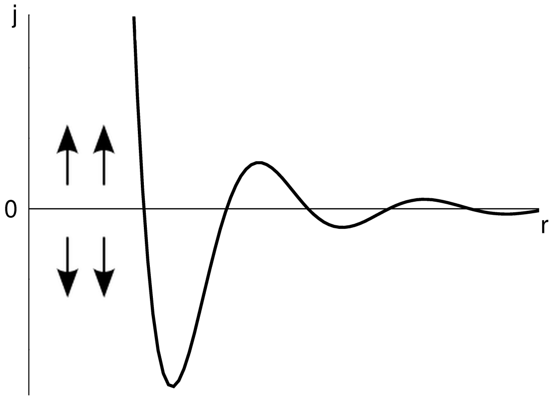

Figure 1.5: Oscillatory behaviour of the RKKY-coupling constant j as a function of the ionic distances. Positive and negative values of j describe a ferromagnetic and antiferromagnetic coupling, respectively [37].

Superexchange

The superexchange mechanism is mediated by an intermediary atom. Cation-anion-cation configurations couple either antiferromagnetically or introduce a weak ferromagnetic ground state. Regarding a TMO this depends on the geometry of the respective cation-anion orbital overlap and the filling of the cation d orbitals. $GaFeO_3$ is a semiconducting antiferromagnet whose ground state originates from the superexchange mediated via the Fe-O-Fe bonds. A detailed discussion on the superexchange mechanism, the Goodenough-Kanamori rules and the magnetic coupling in $GaFeO_3$ is given in section 2.

Double Exchange

Double exchange typical takes place in structures where the magnetic ions occur in two different valence states. $La_{1-x}M_xMnO_3$, doped with M=Ba, Ca,Sr was found to be such a system. Jonker and van Sautern [15, 37, 41] discovered and studied these compounds showing unusual electric and magnetic behavior. Replacing one of the trivalent La^{3+} by a divalent Ca^{2+}, for example, decreases the number of electrons contributing to the formation of bonds from three to two. The missing third electron, however, is taken from a Mn^{3+} ion. Mn then exists in a valence mixture of Mn^{3+} and Mn^{4+}. Depending on the doping concentration x the ratio of the valence mixture of Mn^{3+} and Mn^{4+} anions vary. Exceeding a critical doping concentration x the conductivity rises and the initial insulating and paramagnetic state becomes conductive and ferromagnetic. This can be attributed to the electron hopping that takes place between the Mn^{3+} and Mn^{4+} atoms which was first described by Zener [42]. Even though the electron hopping is mediated via an oxygen atom double exchange still is more similar to the RKKY interaction than to the superexchange. The superexchange mechanism originates from a covalent bond between the cations and anions whereas in the RKKY mechanism there is a quasi free electron interacting with a localized spin. This, however, is more consistent with the double exchange [37].

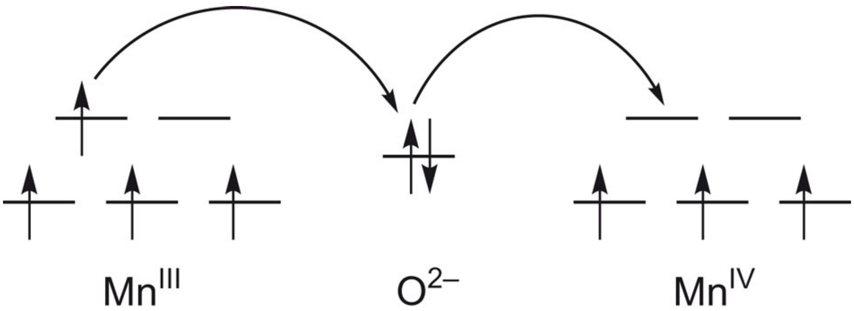

Figure 1.6: Double exchange mechanism mediated via an oxygen atom between two mixed-valence manganites Mn^{3+} and Mn^{4+}. Picture taken from Bechlars et al. 2010 [43].

1.3 Engineering TMO

Beside the various and technical promising characteristics of TMO, some of the ground state properties need to be tailored in order to enhance the performance required for certain applications. Hence, one sometimes wishes to change specific properties for a particular application. This concerns the magnetic and electronic ground state structure. Like in the case of $La_{(1-x)}M_xMnO_3$ mentioned before critical doping concentrations of M_x can change the initially insulating nonmagnetic structure into a conductive ferromagnetic state. The aim of this thesis was to investigate and compare the electronic and magnetic properties of rutile TiO_2 and $GaFeO_3$ (GFO) to existing computational and experimental studies but also to improve certain characteristics like the photocatalytic property and the magnetic ground state structure for future applications. There are several ways of altering these properties which are going to be briefly discussed in the following.

1.3.1 Point Defects

Point defects are local distortions of the crystal structure and can be divided into intrinsic and extrinsic point defects. **Intrinsic point defects** include *vacancies* and *interstitialcies*. First describes an empty lattice site which in the materials stoichiometric ground state should be occupied by an atom. Second corresponds to a crystal site occupation that is originally free. In infinite crystals point defects can only be created in pairs, meaning that if an atom leaves a certain crystal site it creates a vacancy and occupies an interstitial site creating a so called *Frenkel defect* (see figure 1.7). Assuming a crystal surface vacancies and interstitialcies can be generated independently. Vacancies, however, are more common in crystals than interstitialcies. Vacant cell sites enable atoms to move throughout the crystal. The higher the number of vacancies the higher becomes the diffusion rate. Intrinsic defects, however, can destroy the local charge balance. Vacancies in ionic solids create excess charges which are balanced by the surrounding atoms. In less strongly ionized structures or systems with equally ionized atomic species atoms can change crystal sites. An atom A can therefore appear on the sublattice site of atom B and vice versa as e.g. reported for stoichiometric GFO (see section 2). This kind of defects are called *anti-site* defects. Examining the effect of anti-site defects in GFO we speak of an inner cationic site disorder (see section 2). The term intrinsic point defects only includes defects produced by atomic species that are found in the ground state structure.

Extrinsic point defects are defined as local distortions created by foreign atoms. Incorporated intentionally to a system they are called *solutes* and *impurities* otherwise. The actual work examines the effect of foreign atoms incorporated to the stoichiometric

TiO_2 and GFO crystal structure and uses the term *impurity*. Impurity atoms occupy substitutional or interstitial sites (see figure 1.7). Atoms with a small radius tend to be found on interstitial sites, whereas larger atoms mostly occupy substitutional lattice sites [44]. Extrinsic point defects affect various properties and can be used to tailor and improve the performance of a material regarding a specific application. Beside changes of the electrical properties, foreign atoms can alter the magnetic ground state and create donor and acceptor states which are crucial for photocatalysts (see section 3.2), among others. Point defects can cause lattice distortions evoked by different atomic radii or bond length variations due to newly formed bonding types. As discussed in section 1.1.2 changes in the geometry can alter the atomic orbital energies similar to transition metal ions surrounded by a distorted oxygen octahedra.

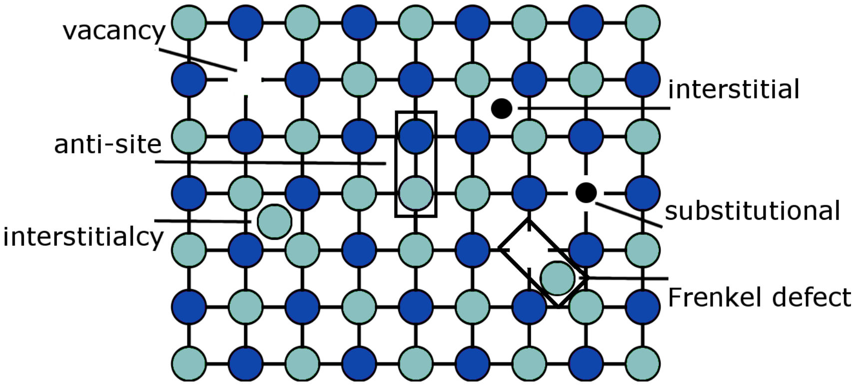

Figure 1.7: Intrinsic and extrinsic point defects inside a periodic crystal structure that consists of two different atomic species (dark blue and light blue sphere). First includes vacancies, Frenkel defects and interstitialcies. Extrinsic defects formed by forgein atoms are substiutional and interstitial impurities (black spheres).

The current thesis investigates the effect of anion and cation doped TiO_2 and GFO, referring to actual performed experimental and theoretical studies. Furthermore it describes the effect of doping on the photocatalytic properties of the respective system. Thereby motivated a detailed discussion on the properties important for photocatalysis and the role of impurity states inside the band gap is given in section 3.2.2.

1.3.2 Strain

Most of the remarkable properties of TMO arise from the interplay between, spin, lattice, charge and orbital degrees of freedom. These, however, can not solely be tuned by point defects. The application of strain is another effective way of altering the electronic and magnetic properties. Stretching and compressing a material along a certain direction affects the crystal lattice. Angles, distances and orbital overlaps are either reduced or enhanced influencing the thereof dependent physical properties. Similar to the crystal field splitting that changes with the octahedra's symmetry (see figure 1.3), varying the intrinsic angles and distances applying strain can lift the degeneracy of states. Straining a material one can easily run into plastic deformations and fractures. Intrinsic exchange mechanisms can thereby be destroyed instead of moderately altered and changed. TMO thin films and nanowires are capable to stand a larger amount of stress compared to their bulk counterpart. They show a smaller number of structural defects due to their reduced dimensionality and are therefore less prone to plastic deformations [45].

Thin films are commonly stretched using substrates. Depending on the respective lattice mismatch between the substrate and the epilayer several percent of biaxial strain can be achieved. Misfit dislocations can induce partial relaxation of the epilayer causing structural and physical inhomogeneities in the film. These are basically missing or dangling bonds in the lattice between the substrate and the epilayer due to mismatching lattice constants. This method, however, is limited by the respective lattice mismatch and different thermal expansion coefficients between both layers. [45]

Figure 1.8 shows a schematic picture of the tensile-strain relaxation for typical growth conditions (a) and for a film with oxygen vacancies (b) based on scans performed on $HoMnO_3$ films [46, 47]. In both (a) and (b) a strain gradient is present inside the film. Regarding (a), we see that above a critical thickness the upper most atomic layers are fully relaxed and free of strain. Dislocations and defects like oxygen vacancies evoke larger gradients. Oxygen vacancies present in (b) even lead to an enhanced film volume. (c) shows the lattice tensile strain as a function of the oxygen pressure during film growth. The lower the oxygen pressure the more oxygen vacancies are created.

Investigating free-standing nanoscale single crystals one can circumvent lattice mismatch correlated problems. Free of dislocations nanoscale single crystals can sustain high uniaxial strains without fracturing. Moreover the applied strain is continuously tunable, not depending on a given lattice mismatch of the substrate [48, 49]. Concluding a wide range of crystal properties can be altered applying strain. This can be done either by choosing the appropriate substrate with the desired lattice mismatch and orientation or by producing single free standing crystals. A large number of experimental and computational studies examine the effect of strain on properties like the magnetic ground state, transition temperatures, ferroelectricity and the intrinsic polarization.

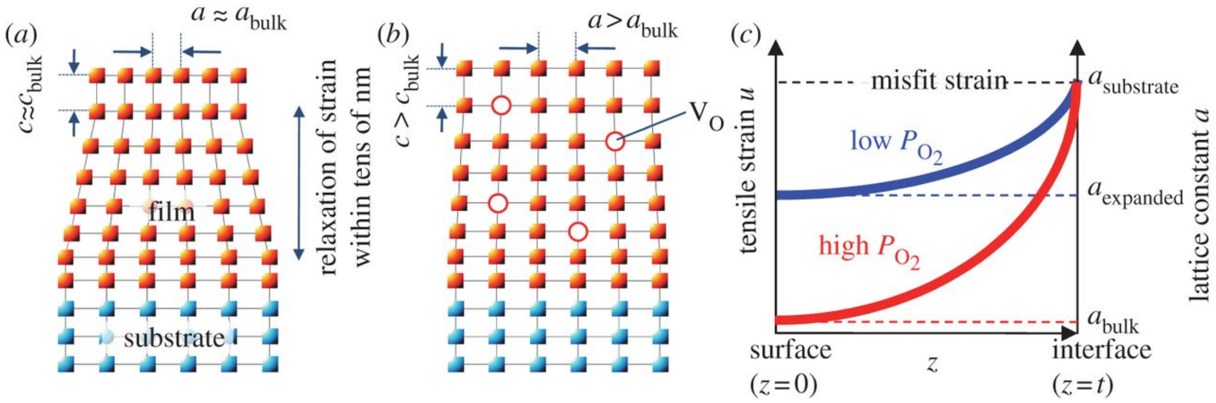

Figure 1.8: Tensile-strain relaxation between a substrate and a film. (a) describes a typical growth condition. (b) sketches a film with oxygen vacancies, denoted by red open circles. (c) shows the tensile strain gradient for oxygen poor and rich film grow conditions. Picture taken from Lee and Noh [46].

Chapter 2

Theoretical Background and Computational Methods

Physicists are atoms' way of thinking about atoms.

Bill Bryson

2.1 Solid States Physics in a Nutshell

Materials consist of nuclei and electrons and assuming an ideal solid they are arranged on a regular lattice. Trying to describe a solid one deals with a many-body system. This can be described with a quantum mechanical Hamiltonian that is subdivided into three parts

$$\hat{H} = \hat{H}_N + \hat{H}_e + \hat{V}_{N-e} \quad . \tag{2.1}$$

It contains a description of the nuclei $\hat{H}_N$, the electrons $\hat{H}_e$ and the potential between the nuclei and the electrons $\hat{V}_{N-e}$. $\hat{H}_N$ and $\hat{H}_e$ are comprised of a kinetic and potential part including the nuclei-nuclei and electron-electron interaction, respectively. Dealing with solids solely the Coulomb interaction is considered to be dominant in the energy range of interest, whereas forces like gravity, the strong and the weak interaction are neglected. Relativistic effects are not included in a first approximation. For heavy elements like gold, however, relativistic effects can not be neglected and have to be involved for a better description. To quantummechanically describe the respective system given in equation (2.5) the time dependent Schrödinger equation

$$\hat{H}\Psi = i\hbar \frac{\partial}{\partial t}\Psi \quad , \tag{2.2}$$

has to be solved in a next step. Assuming the system to be time independent the Schrödinger equation simplifies to

$$\hat{H}\Psi = \hat{E}\Psi \quad . \tag{2.3}$$

Ψ is the many body wave function and given by

$$\Psi = \Psi(\vec{r}_1, s_1, ..., \vec{r}_n, s_n, \vec{R}_1, I_1, ..., \vec{R}_m, I_m) \quad . \tag{2.4}$$

It depends on the electron and nuclear coordinates ($\vec{r}_i$, $\vec{R}_j$) and spins (s_i, I_j). Although one may easily define equation (2.3) for a certain solid, the Schrödinger equation can not be solved analytically for a many-body problem. Even for a single particle system it can be solved under certain constraints. Analytical solutions for the single particle Schrödinger equation exist for e.g. the finite and infinite deep potential well, the three dimensional Coulomb potential (describing the hydrogen atom), the potential barrier simulating the tunneling effect and the harmonic and Morse potential. For all other cases approximations have to be made. The first approximation usually made is the Born-Oppenheimer approximation. It separates the motion of the electrons and the nuclei. This is done assuming that the electrons move much faster than the in mass much larger nuclei and hence follow the ionic motion almost instantaneously. The resulting wave function can be written as a product of an ionic and electronic contribution resulting in two Schrödinger equations. The respective electronic Hamiltonian formulates to

$$\hat{H}_e = \hat{T}_e + \hat{V}_{e-e} + \hat{V}_{N-N} + \hat{V}_{N-e} \quad , \tag{2.5}$$

with the kinetic energy and the potential terms including the electron-electron, the nuclear-nuclear and the nuclear-electron interactions. Further approximations and models are necessary to deal with the vast number of particles in a solid, making the Schrödinger equation manageable.

One of the first models were the *free electron*, the *nearly free-electron* and the *tight binding model*. The *free electron model* also known as the *Drude-Sommerfeld model* was derived by Arnold Sommerfeld in 1927 and combines the classical Drude model with quantum mechanical Fermi-Dirac statistics. The electrons are assumed to be detached from the nuclei moving as free particles forming an ideal electron gas. The electron-electron interaction is neglected and the crystal lattice is described by a constant potential background. Adding the Fermi-Dirac statistics the electrons' energies are discrete like for a particle in a box of constant energy. The Pauli principle is applied as well and the electrons are treated as indistinguishable particles. Even though the Drude-Sommerfeld model is a great oversimplification of reality it quite successfully describes properties as the electrical and thermal conductivity and the heat capacity but fails to explain the existence of insulators.

The *nearly free-electron model* approximates the interaction between the electrons and the ions which form the crystal lattice by a weak potential. This weak perturbing potential is assumed to be periodic as it follows the arrangement of the nuclei of the respective crystal structure. The solution of the Schrödinger equation and the electron wave function is then described by the product of plane waves and a periodic function representing the crystal lattice, so called Bloch waves. Introducing this weak interaction creates band gaps at the Brillouin zone boundaries solving the Schrödinger equation. The nearly free-electron model therefore successfully describes insulators.

The *tight binding model* does not as the models above treat electrons as almost free particles. It describes the opposite limit assuming the crystal potential to be strong. Supposing this model the electronic motion is approximated as follows: an electron is trapped by a nucleus while moving through the crystal and remains there for a long time before tunneling to the next ion. Trapped by an ion the electronic state function is essentially that of an atomic orbital uninfluenced by the neighbouring atoms. The atomic orbitals and potentials of neighbouring atoms show very small overlap so that the particular atomic solutions can be approximated by the wave functions of isolated atoms. The solution of the Schrödinger equation is given by a linear combination of single-electron atomic orbitals and allows for a good description of materials like diamond and silicon. For a more detailed discussion on the models mentioned above see [50, 51].

More sophisticated approximations are the so called *Hartree* [52] and *Hartree-Fock method* [53]. The Hartree method solves the time-independent electronic Schrödinger equation using the Rayleigh-Ritz variational principle. The thereby obtained Hartree equations are effective one-particle Schrödinger equations with single particle solutions. These solutions then enter the effective one-particle Hamiltonian and the Hartree equations are solved iteratively. Electron-electron and nuclei-electron interactions are included to some extent. The underlying method describes a non-interacting N-particle problem of N-electrons. Even though the electrons do not directly interact with each other every electron feels the presence of the other electrons indirectly through an effective potential that is described by the single-particle Hamiltonians. The Hartree wave function, however, has a very important shortcoming, it does not treat the electrons as fermions and shows no antisymmetry under odd permutations of the electronic variables. Including the Pauli principle the Hartree wave function has to be antisymmetrized. This was achieved for the *Hartree-Fock method* using Slater determinants for the electronic wave functions. The *Hartree-Fock equations* describe the Coulomb part of the electron-electron interaction (Hartree term) and the *exchange energy* (Fock term). Latter is a quantum mechanical effect and follows from the exchange symmetry of indistinguishable particles. The Fock term describes the interaction of electrons with same spin. These, however, are repelled by an additional Coulomb like interaction and form a so called *exchange hole* that decreases the total energy. The approximation of the many body wave function by a product of single particle wave functions supresses the individual electron-electron correlation which is both missing in straight forward Hartree and Hartree-Fock (HF). This contribution called *electron correlation*, keeps the electrons apart and would further reduce the total energy by the *correlation energy*. Missing out this interaction, the HF method fails to describe metals correctly because of problems with a vanishing density of states at the Fermi level. In addition, relativistic effects are usually neglected in the HF method.

Post-Hartree-Fock methods try to overcome these shortcomings by mainly approximating the electron correlation. There are methods as the *configuration interaction* (CI) [54, 55] and the *coupled cluster* method (CC) [55–57], which add electronic excitations to the HF wave functions. The CCSD(T) method includes triple excitations that are accounted for perturbatively and used for high valuable quantum chemistry reference calculations for small to medium-sized molecules. Another ansatz is the *Møller-Plesset perturbation theory* (MP) [58] that treats the difference between the many-body and the HF Hamiltonian perturbatively. Even though *Post-Hartree-Fock* methods yield reliable results they are comupationally cumbersome and only feasible for rather small systems. Hence, other methods are needed to efficiently describe larger systems but still reveal the required accuracy. That is where *denstiy functional theory* comes into play. It fulfills the requirements of accuracy and computational cost making it a powerful tool for many fields in physics, chemistry and industries as well.

2.2 Densitiy Functional Theory

Denstiy functional theory (DFT) is currently the most common method for electronic structure calculations in chemistry and solid state physics. According to a paper by Sidney Redner in 2005 [59], five of the 11 papers with more than 1000 citations published in Physical Review (PR) are discussing ideas relevant to DFT. Redners study includes publications in PR, a group of journals published by the American Physical Society (APS), considering only internal citations meaning citations of PR articles in a PR journal. The top two papers are by Hohenberg & Kohn and Kohn & Sham [60, 61] who lay the foundation of density functional theory. Places 3 and 4 are studies by J. P. Perdew & A. Zunger and D. M. Ceperley & B. J. Alder. First discusses the self energy correction problem and second the correlation energy in the local density approximation. Place 11, a paper by H. J. Monkhorst and J. D. Pack [62], deals with efficient Brillouin zone integration which is of great importance for the implementation of DFT codes. Including non-PR journals the number of citations vastly increases for all publications mentioned above. Regarding the citations of papers published by people developing DFT codes one as well find tremendous numbers. Considering some papers dealing with the Vienna ab initio simulation package VASP, Gaussian, Wien2k and the Abinit code the number of citations range from about 16700 to 1650 (in the prescribed order).

This vast number of citations illustrates the great importance of DFT in science nowadays. It covers a very broad field of applications, including the simulation of AFM images, supporting and elucidating experimental findings. One can examine the adsorption of molecules on surfaces and calculate reaction energies important for catalytic processes. Band structure calculations and the prediction of magnetic order are performed as well. These are just some of the many fields DFT can be very useful. It has become indispensable in interpreting experimental results and as a tool to predict phenomena. Using this very poweful method one can design and alter specific properties of a material for application in industries and medicine.

2.2.1 Formalism

The following describes the theoretical fundamentals of DFT. For a more detailed discussion and further derivations see books on density functional theory such as [63]. Dealing with many body systems and many body wave functions is rather complicated. Latter is a function of 3N variables and assuming a system of N electrons the computational effort of solving the many electron wave function scales with the power of 3N. Hence, it would be convenient to find another quantity that is easier to handle but still contains information of the full system. The electron density $\rho(\vec{r})$ is such a quantity that fulfills these criteria. The idea of using the electron density was first proposed by L. Thomas [64] and E. Fermi [65] in 1927. Their method treats electrons of the atomic shell as gaseous particles. The Thomas-Fermi model, however, is not based on solid theory and therefore does not relate the electronic density to the many body wave function. Furthermore, its crude assumptions yield poor results for real systems. Almost 30 years later Hohenberg and Kohn derived a formalism which represents the many-electron wave function by the electron density $\rho(\vec{r})$. This formalism is expressed by the so called *Hohenberg-Kohn theorems* [60] that build the cornerstones of DFT. They state that the ground state energy is a unique functional of the electronic density E$[\rho]$ which is minimized at the equilibrium density $\rho(\vec{r})$=$\rho_0(\vec{r})$. The electron density $\rho(\vec{r})$ of a system of N interacting electrons uniquely determines the external potential $V_{ion}(\vec{r})$ apart from an additive constant (proof given in [66]). The total number of electrons N is also determined by the electron density,

$N = \int \rho(\vec{r}) d\vec{r}$. Expressing now the total energy as a functional of $\rho(\vec{r})$ gives

$$E[\rho] = T[\rho] + V_{ion}[\rho] + E_H[\rho] + E_{xc}[\rho] \quad . \tag{2.6}$$

The external potential $V_{ion}[\rho]$ and the classical electron Coulomb interaction, corresponding to the Hartree energy $E_H[\rho]$, can be easily described using the electron density

$$V_{ion}[\rho] = \int d\vec{r}\, V_{ion}(\vec{r})\rho(\vec{r}) \quad , \tag{2.7}$$

$$E_H[\rho] = \frac{1}{2} \int d^3r' \int d^3r\, \frac{\rho(\vec{r'})\rho(\vec{r})}{\vec{r} - \vec{r'}} \quad . \tag{2.8}$$

Reforming equation (2.6) to $E[\rho]$-$V_{ion}[\rho]$ gives a universal functional. It only depends on the number of electrons in the system, but not on the ionic potential. Hence, if the exact expression of the $T[\rho]$, $E_H[\rho]$ and $E_{xc}[\rho]$ term would be known all materials could be described by simply adding the adequate potential. This, however, can not be achieved for $E_{xc}[\rho]$, the *exchange-correlation term*, which handles all quantum mechanical many-body effects. Since there is no exact representation approximations are necessary which will be discussed below in section 2.3.

Expressing the kinetic energy through ρ, Kohn and Sham [61] introduced auxiliary single-electron orbitals $\varphi_i(\vec{r})$, which form the same charge density

$$\rho(\vec{r}) = \sum_{i=1}^{N} \varphi_i(\vec{r})^2 \quad . \tag{2.9}$$

The kinetic energy term $T[\rho]$ can be divided into two parts,

$$T = T_0[\rho] + T_{corr}[\rho] \quad , \tag{2.10}$$

first describes the single-electron and second the correlation contribution. $T_0[\rho]$ is determined by the single electron orbitals and can be written as

$$T = \sum_{i=1}^{N} \int d^3r \frac{\hbar}{2m} (\nabla \varphi_i(\vec{r}))^2 \quad . \tag{2.11}$$

$T_{corr}[\rho]$ is added to the exchange-correlation energy. The Kohn Sham theorem [61] states that for every interacting electron system exposed to an external potential $V_{ion}(\vec{r}))$ there is a unique local potential $V_{ion,l}(\vec{r}))$ that gives the same ground state energy for a system of non-interacting electrons. The uniqueness of the local potential $V_{ion,l}(\vec{r}))$ follows from the Hohenberg-Kohn theorem and its existence is given by the V-representability theorem [67]. Any on a discrete lattice normalizable positive electron density function $\rho(\vec{r})$, compatible with the Pauli principle, is ensemble-V-reprentable. Calculating the energy ground state the energy functional $E[\rho]$ has to be minimized with respect to ρ

$$\frac{\delta\{E[\rho]-\mu(\int d^3r\rho(\vec{r})-N)\}}{\delta\rho(\vec{r})} \quad . \tag{2.12}$$

The Lagrange operator μ fixes the number of electrons N. Applying the variational principle above to (2.6) gives the Kohn-Sham equations [61]

$$\{-\frac{\hbar^2}{2m_e}\nabla+\upsilon_{ion}(\vec{r})+\upsilon_H(\vec{r})+\upsilon_{xc}(\vec{r})\}\varphi(\vec{r})=\epsilon_i\varphi(\vec{r}) \quad . \tag{2.13}$$

Equation (2.13) was minimized with respect to $\varphi(\vec{r})$ instead of $\rho(\vec{r})$ and ϵ_i ensures the normalization of $\varphi(\vec{r})$. Equation (2.14) describes Schrödinger equations of single-electrons moving in the effective (single-particle) potential

$$\upsilon_{eff}(\vec{r})=\upsilon_{ion}(\vec{r})+\upsilon_H(\vec{r})+\upsilon_{xc}(\vec{r}) \quad . \tag{2.14}$$

The exchange correlation functional $\upsilon_{xc}(\vec{r})$ can be expressed by the functional derivative of the exchange correlation energy $E_{xc}(\vec{r})$ yielding

$$\upsilon_{xc}(\vec{r})=\frac{\delta E_{xc}[\rho(\vec{r})]}{\delta\rho(\vec{r})} \quad . \tag{2.15}$$

If all contributions were known, the Kohn-Sham potential and the charge density could be solved self-consistently and the ground state energy is determined exactly. Since $E_{xc}(\vec{r})$ can not be expressed directly, however, approximations have to be made. Dealing with phenomena like magnetism the electron spin has to be included using the electron densities for spin up and spin down instead of the total density. This can be achieved by using the Kohn-Sham spin density functional theory [61]. Treating heavy elements like gold the Hohenberg-Kohn theorem has to be extended by a relativistic description of the electrons [68].

2.3 Exchange-correlation functionals

2.3.1 The LDA and GGA functional

The exchange-correlation functional $E_{xc}[\rho]$ can be expressed as

$$E_{xc}[\rho]=\int d^3r\rho(\vec{r})\epsilon_{xc}[\rho] \quad , \tag{2.16}$$

and is only known in general. ϵ_{xc} is the exchange-correlation energy density and depends on the electron density. Since the exact form of υ_{xc} is not known approximations have to be made. Two very successful approximations are the *Local Density Approximation* (LDA) and the *Generalized Gradient Approximation* (GGA). Both describe the electrons as a homogeneous gas, often referred as jellium. LDAs in general evaluate the exchange-correlation energy in non-homogeneous systems by assuming a homogeneous electron gas at each point (local densities)

$$\epsilon_{xc}^{LDA}[\rho(\vec{r})] := \epsilon_{xc}^{hom}(\rho_0)|_{\rho_0 \to \rho(\vec{r})} \quad . \tag{2.17}$$

This works well for systems with slowly varying charge densities, like s and p states but should fail for d and f electrons. Including the electronic spin one usually speaks of the Local Spin Density Approximation (LSDA). $\rho(\vec{r})$ is then defined as $\rho_+(\vec{r}) + \rho_-(\vec{r})$. The exchange-density ϵ_x^{LDA} can be obtained applying the Hartree-Fock approximation to jellium (homogeneous electron gas in a uniform positive background) using plane waves. ϵ_x^{LDA} of the therewith calculated ground state of a homogeneous electron gas then reads as

$$\epsilon_x^{LDA}[\rho(\vec{r})] = -\frac{N}{V}\frac{3}{4}\frac{e^2 k_F}{\pi} = -\frac{3}{4}\left(\frac{3}{\pi}\right)^{\frac{1}{3}} e^2 \rho_0^{\frac{4}{3}} = -C_x \rho_0^{\frac{4}{3}} \quad , \tag{2.18}$$

where N is the number of electrons, V the volume and k_F the Fermi wave vector [69]. The correlation term ϵ_c^{LDA} of the jellium density ρ_0 can be calculated with advanced many-body techniques like Monte Carlo simulations [70]. $E_{xc}[\rho]$ is then obtained by integrating $\epsilon_{xc}^{LDA} = \epsilon_x^{LDA} + \epsilon_c^{LDA}$

$$E_{xc}[\rho] \approx^{LDA} \int d^3r \epsilon_{xc}^{LDA}(\rho_0 = \rho\vec{r}) \quad . \tag{2.19}$$

Inserting equation (2.19) into equation (2.13) the Kohn-Sham equations can be solved self consistently. The LDA approximation, however, does not only work well for systems with slowly varying charge densities but still yields acceptable results for many other systems. One reason of this rather surprisingly good performance is that the exchange correlation hole does not need to be modeled exactly. The LDA does not have to describe an exact replica of the true hole to obtain good results [71]. It is already sufficient to provide a reasonable approximation of the spherical average of the exact exchange-correlation hole and to fulfill the sum rules. Nevertheless, the LDA exhibits several shortcomings. Beside the poor treatment of systems with rapidly changing electron densities, it often gives larger binding and cohesive energies than found in experiment [72].

Another approximation of the exchange-correlation term that tries to overcome these limitations is the so called Generalized Gradient Approximation (GGA). It does not only consider the local electronic density but also includes its gradients. The resulting functional, however, still does not take non-local contributions into account but obtains a semilocal exchange-correlation term by adding the electronic density gradients

$$\epsilon_x^{GGA}[\rho, \nabla\rho] = \int d^3r \epsilon_{xc}^{GGA}(\rho\vec{r}, |\nabla\rho\vec{r}|) \quad . \tag{2.20}$$

The GGA tends to improve the total energies and the atomizations energies compared to the LDA [73]. It favours density inhomogeneities more than the LDA does and considering different parameterizations softens bonds to correct [74] or overcorrect the LDA [75]. Latter often results in an under-binding compared to experiment. There is no standard functional for the LDA and the GGA. The PW91 [73] by Perdew et al. and PBE [76] by Perdew, Burke and Ernzerhof functional was used in the present work, a very common method. For the LDA the variations in the parameters are much smaller compared to the GGA. A commonly used parameterization for the LDA can be found in [77].

2.3.2 On site Coulomb interaction: L(S)DA / GGA + U

Another way to overcome the difficulties of the L(S)DA in describing high localized states is the L(S)DA+U method. Same is true for the GGA, since is does not provide a satisfactory self interaction correction either. As a result both approximations tend to predict itinerant d states and a metallic ground state for many systems which are observed to have a broad band gap in experiment. Rare-earth and transition metal compounds are mostly affected by that. A way to compensate for this shortcoming is the decomposition of the complete Hilbert space into two subsystems, following the Anderson model [78]. Subsystem one includes the localized d or f states for which an orbital-dependent treatment of all Coulomb effects is necessary. Subsystem two contains the s and p states which are already well described with the LDA and the GGA [63]. The technical implementation in DFT calculations is provided by the L(S)DA/GGA+U method [77–79], introducing the on site Coulomb interaction as a parameter. Since this work focusses on the theoretical description and calculation of the properties of TMO this is a very important concept. There are two prominent approaches, namely the Liechtenstein et al. [80] and the Dudarev et al. [81] method. Latter was used for the calculations presented in this thesis. The Dudarev method uses the parameters U and J. U is the effective on site Coulomb interaction parameter and J the effective on site exchange interaction parameter. Applying Dudarev's approach the effective on site coulomb- and exchange parameters not enter separately, but in the form of $U_{eff} = U - J$. The simplified (rotationally invariant) approximation according to Dudarev et al. [81] has the following form

$$E_{LSDA+U} = E_{LSDA} + \frac{U-J}{2} \sum_{\sigma} \left[\left(\sum_{m_1} \hat{n}^{\sigma}_{m_1,m_1} \right) - \left(\sum_{m_1 m_2} \hat{n}^{\sigma}_{m_1,m_2} \hat{n}^{\sigma}_{m_2,m_1} \right) \right] \quad . \tag{2.21}$$

$\hat{n}$ is the operator for the number of electrons with a given projection of spin σ and m defines the orbital momentum. The second term in equation (2.21) can be understood as adding a penalty functional to the LSDA total energy. Applying the GGA the E_{LSDA} term becomes replaced by the corresponding E_{GGA} functional.

2.3.3 Hybrid Functionals

DFT on the level of the LDA and the GGA works well for many system but still shows several drawbacks. Beside the before mentioned over- and underbinding of the LDA and GGA, respectively, both approximations insufficiently describe strongly correlated systems. They underestimate band gaps and do not include non-local interactions like van der Waals forces. Various approaches and approximations have been made to overcome these weaknesses. One is the so called *meta*-GGA functional [82] which includes higher order powers of the density gradient or the local kinetic energy. Then there are *hybrid functionals* like the HSE [83] and B3LYP [84, 85] where a portion of exact exchange obtained with the Hartree-Fock method is combined with DFT exchange correlation contributions. Hybrid functionals are known to give more accurate results to a wide range of systems, however, they are computationally cumbersome.

In the present work we use the Heyd-Scuseria-Ernzerhof (HSE) hybrid functional for calculating properties like the band gap and for highly accurate cell relaxations. Latter are of great importance for the calculation of magnetic anisotropy energies. The HSE exchange correlation functional uses an error function screened Coulomb potential for the exchange portion and is decomposed into a short-range (sr) and a long-range (lr) part. This decomposition is based on the error function,

$$\frac{1}{r} = \underbrace{\frac{\text{erfc}(\omega r)}{r}}_{short-range} + \underbrace{\frac{\text{erf}(\omega r)}{r}}_{long-range}$$

$$\text{erf}(x) = \frac{2}{\sqrt{\pi}} \int_0^x dt e^{-t^2}, \quad \text{erfc}(\omega r) = 1 - \text{erf}(\omega r) \tag{2.22}$$

where the empirical parameter ω remains to be determined. The reason of using the error function erf is that integrals with Gaussian basis functions can be solved analytically. The critical term which complicates the description of metallic systems is the long-range Hartree Fock exchange part, $E_x^{exact,lr}$. For suitable values of ω this term is rather small and $E_x^{exact,lr}$ is often close to $E_x^{PBE,lr}$. $E_x^{exact,lr}$ can therefore be replaced, e.g. taken together to $E_x^{PBE,lr}$ yielding the following HSE exchange correlation functional

$$E_{xc}^{HSE} = aE_x^{exact,sr}(\omega) + (1-a)E_x^{PBE,sr}(\omega) + E_x^{PBE,lr}(\omega) + E_c^{PBE} \quad . \tag{2.23}$$

a is the mixing parameter and can be derived e.g. from perturbation theory [86]. ω controls the short-rangeness of the interaction and corresponds to the PBE0 hybrid functional if ω=0. Values that have shown to yield good results for many systems are a=0.25 and ω=0.2. They define the so called HSE06 hybrid functional.

Chapter 3

Rutile TiO_2

3.1 Titanium Dioxide in Science and Industries

Titanium dioxide has been used for nearly 100 years and has become very important to many different branches of industry. Its first industrial use and commercial manufacture was as a pigment almost simultaneously between 1908 and 1916 in Norway and the USA, respectively. The annual production of titanium dioxide is about 5.1 million tons. Most of it is produced in China, Europe and the US. More than 90 percent of the produced titanium dioxide is used as a white pigment providing whiteness and opacity for paints and coatings, plastics and paper. Titanium dioxide is an inert material and not classified as hazardous, which is why it is used as a food colorant and for cosmetics and pharmaceuticals. It is also processed in sunscreens, since it scatters visible light but absorbs in the UV region. Only a very small part of the produced amount per year is used and fabricated to semiconductors and to catalyse the photodecomposition of water into hydrogen and oxygen [87].

Using titanium dioxide as a semiconductor or as a catalyst its performance can be enhanced by altering its ground state structure. This can be achieved by different experimental set ups that produce various modifications of the TiO_2 structure. Its ground state properties can thereby be tailored to better fit a certain application.

3.1.1 Motivation

In recent scientific research TiO_2 plays an important role in the fields of dilute magnetic semiconductors (DMS) and photocatalysis. For both applications TiO_2 requires tailor made electronic properties. These, however, can be manipulated by selectively diluting the system incorporating dopants to the host matrix.

DMS have been investigated in the past in order to gain new insights in the functional principles and the manipulation of the magnetic and semiconducting properties. The search for magnetic semiconductors or for half-metals used for spin-injection led to the discovery of the new material class of p electron magnets. The prospect of controlling the charge and the electron spin as information carriers would make it possible to combine information processing and storage at the same time [88–90]. The second major application is in the field of photocatalysis, where the favourable electronic gap range of $1.65 - 3.1$ eV can be also achieved by doping [91–93].

Regarding rutile TiO_2 from a photocatalytic point of view we are especially interested in the manipulation of the band gap by incorporation of impurities. Rutile TiO_2 has a band gap of 3.0 eV, which corresponds to an absorption spectrum near the ultraviolet region. The absorption of photons leads to the creation of electron hole pairs, which are of special relevance for photocatalytic and photoelectrochemical applications like the photo-induced decomposition of water on TiO_2 electrodes demonstrated by Fujishima and Honda [94]. Another line of research regards the photocatalytic properties; due do the creation of electron hole pairs the valence band (VB) becomes oxidative and the conduction band (CB) reductive. Surrounding molecules can therefore be oxidized or reduced and as a consequence, form radicals which are harmful to organic compounds like bacteria and fungi. Hence, TiO_2 can be used as a purifier, removing gaseous or aqueous contaminants [95, 96]. Beside water- and air-purification there is a wide range of other photocatalytic applications, like antifogging and self-cleaning surfaces [97]. Since UV light only makes up 5% of the sunlight spectrum one aims to shift the absorption spectrum of TiO_2 into the visible region to improve the absorption rate and therefore the photocatalytic efficiency. Several studies have shown that impurities like nitrogen and carbon verifiable modify the band gap. Beside computational studies done by DiValentin et al. [98, 99] and Yang et al. [100] there are experimental studies confirming the earlier theoretical results. Diwald et al. [101] reported a blueshift in the band gap after doping with nitrogen. In a second study [102] they observed a redshift by inducing nitrogen into the TiO_2 rutile host matrix. For the first case they assumed oxygen atoms being substituted by nitrogen impurities and for the latter nitrogen atoms being placed on interstitial sites. Batzill et al. [103] on the other hand reported to see a redshift when substituting O by N. Motivated by these partly contradictory reports we perform our theoretical investigation in order to interpret the experimental results.

The present work investigates properties of rutile TiO_2 doped with carbon and nitrogen atoms, respectively. C and N are assumed either to replace oxygen or to occupy interstitial positions. Although magnetic order is most common in metallic materials with narrow bands of d or f electrons, the carriers of the magnetic moments in doped semiconductors or insulators like TiO_2 are the carbon or nitrogen atoms. The magnetic moment is produced by the *p* electrons which become polarized because of the flat *p* bands formed by these impurity atoms [104]. This is called *p* electron magnetism and has been investigated intensively during the last years.

In the course of this thesis we discuss the photocatalytic and magnetic properties of doped rutile TiO_2. We thereby focus on the band gap structure regarding the width and the existence of impurity states. Furthermore we determine the relative position of the redox potentials with respect to the valence and conduction band for all investigated TiO_2 doping configurations.

3.2 Photocatalytic Water Splitting

The abundance of traditional fossil fuels runs out at an extreme rate whereby its demand and consumption rises every year. Alternative energy sources have become an urgent topic in current research trying to find sustainable ways of energy production. A very promising source of a potentially clean and renewable source of energy is visible-light-driven photocatalytic water splitting. In this process H_2 molecules are produced under the influence of solar light absorbed by semiconducting photoelectrodes immersed by an aqueous electrolyte. Photocatalytic water splitting is a very attractive research topic in the field of renewable energy. The scientific community focusses on finding new photocatalytic materials and to enhance the properties of already known and widely used compounds. TiO_2 has the advantage of being a cheap, non-toxic, inert and thermodynamically stable material. Its ground state properties, however, have to be tailored in order to enhance its photocatalytic behaviour.

3.2.1 Main Mechanisms of Photocatalytic Hydrogen Generation

The photocatalytic process of hydrogen generation includes several steps. Step one involves the photon absorption. Depending on the respective material photons are absorbed under UV and/or visible light irradiation. An electron of the VB gets thereby shifted into the CB and creates a negative electron (e^-) - positive hole (h^+) pair. This electron-hole pair then migrates to the surface of the photocatalyst and reacts with its surrounding. Regarding the water-splitting reaction both the e^- and h^+ act as a reducing and oxidizing agent producing H_2 and O_2, respectively. Water splitting is an uphill reaction and requires a standard Gibbs free energy of 237 kJ/mol equivalent to 1.32 eV per water molecule [105].

$$H_2O(aq) \rightarrow \frac{1}{2}O_2(g) + H_2(g), \quad \Delta G = +237 kJ/mol \quad . \tag{3.1}$$

The reaction above consists of two substeps, involving the H_2O/O_2 oxidation reaction

$$H_2O(aq) + 2h^+ \rightleftharpoons \frac{1}{2}O_2(g) + 2H^+(aq) \tag{3.2}$$

and the $H^+/H2$ reduction reaction

$$2H^+(g) + 2e^- \rightleftharpoons H_2(g) \quad . \tag{3.3}$$

The respective semiconductor has to have a minimum band gap (E_g) of 1.32 eV so that the water splitting reaction can take place. To harvest visible light E_g should be lower than 3.0 eV, otherwise the absorption region enters the UV region which makes up only 5% of the sunlight spectrum. The relative position of the semiconductor band edges with respect to the H_2O/O_2 and H^+/H_2 redox levels is crucial for the thermodynamics of the water splitting process. The semiconductor VB has to be below the oxidation level so that the oxidation process becomes thermodynamically favourable while the semiconductor CB should be above the reduction level (see figure 3.5). Concluding these conditions

$$E_{HOMO} < E_{H_2O/O_2} < E_{H^+/H_2} < E_{LUMO} \quad , \tag{3.4}$$

has to be fulfilled to enable photocatalytic water splitting. HUMO and LUMO stands for *highest unoccupied molecular orbital* and *lowest unoccupied molecular orbital*, respectively.

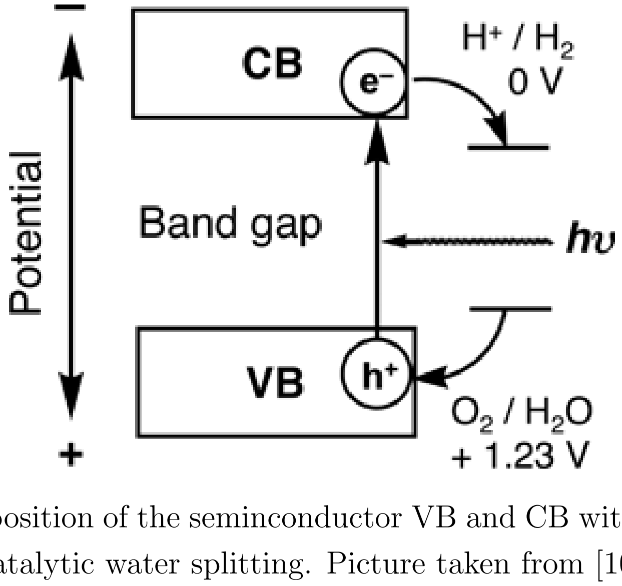

Figure 3.1: Relative position of the seminconductor VB and CB with respect to the redox potentials for photocatalytic water splitting. Picture taken from [106].

Even though most materials do not fulfill these conditions there a several ways to overcome this problem. One includes the application of an external bias voltage shifting the VB and CB of the corresponding semiconductor with respect to the oxidation levels. Furthermore, tandem devices can be constructed which use more than one material. Assuming two compounds, material one has to have an appropriate band gap and a suitable potential alignment for the oxidation process with its VB below the oxidation potential (n-type photoanode). Compound number two demands an appropriate band gap as well and requires a CB lying above the reduction potential (p-type photocathode). The oxidation and redox potentials can be shifted by altering the pH value of the aqueous solution the semiconductor is immersed in [107]. Even though this can compensate for an initially bad potential alignment, changing the pH environment may affect the semiconductor's phase stability.

Beside the issue of redox potential alignment factors as charge separation, charge mobility and charge lifetime have to be considerend, since these highly affect the compound's ability of water splitting (see figure 3.2). These involve processes like the recombination, the separation and the migration of electron-hole pairs. Only if an electron-hole pair mirgrates to the semiconductors surface before it recombines it can react with water and other molecules. Recombination reduces the number of the electron-hole pairs and takes place in both the surface and bulk area. It is accompanied by the emission of light or the generation of phonons. Efficient charge separation and fast charge transport are fundamentally important to avoid and reduce bulk and surface recombinations. Regarding the efficient charge seperation of excited electron-hole pairs (excitons), however, one has to overcome an energy barrier.

Concluding a good photocatalyst (in the sense of sunlight water splitting) should exhibit a direct band gap in the energy range of $1.23 \text{ eV} < \mathrm{E}_g < 3.0 \text{ eV}$ to both efficiently harvest visible light and provide the minimum energy for water decomposition. Further, recombination rate should be reduced and migration and separation should be sufficiently high. A detailed description of the main mechanisms of photocatalytic water generation and different approaches on tuning the materials properties for enhanced photocatalytic performance is given by Kudo and Misek, Chen et al. and Linsebigler et al. [106, 108, 109].

Figure 3.3 shows the band edges of commonly used semiconductors with respect to the water splitting potentials. Regarding TiO_2 the CB is very close to the H^+/H_2 reduction potential. Hence, doping rutile TiO_2 we desire a band gap reduction and an simultaneous upward shift of the VB. This prevents the CB potential to fall below the reduction potential as e.g in WO_3.

3.2.2 Shockley-Read-Hall recombination

In principle one can distinguish three different recombination mechanisms. These are the *radiative (band to band) recombination*, the *Auger recombination* and the recombination through defect levels called *Shockley-Read-Hall recombination*.

Regarding the band to band recombination we distinguish between a direct and an

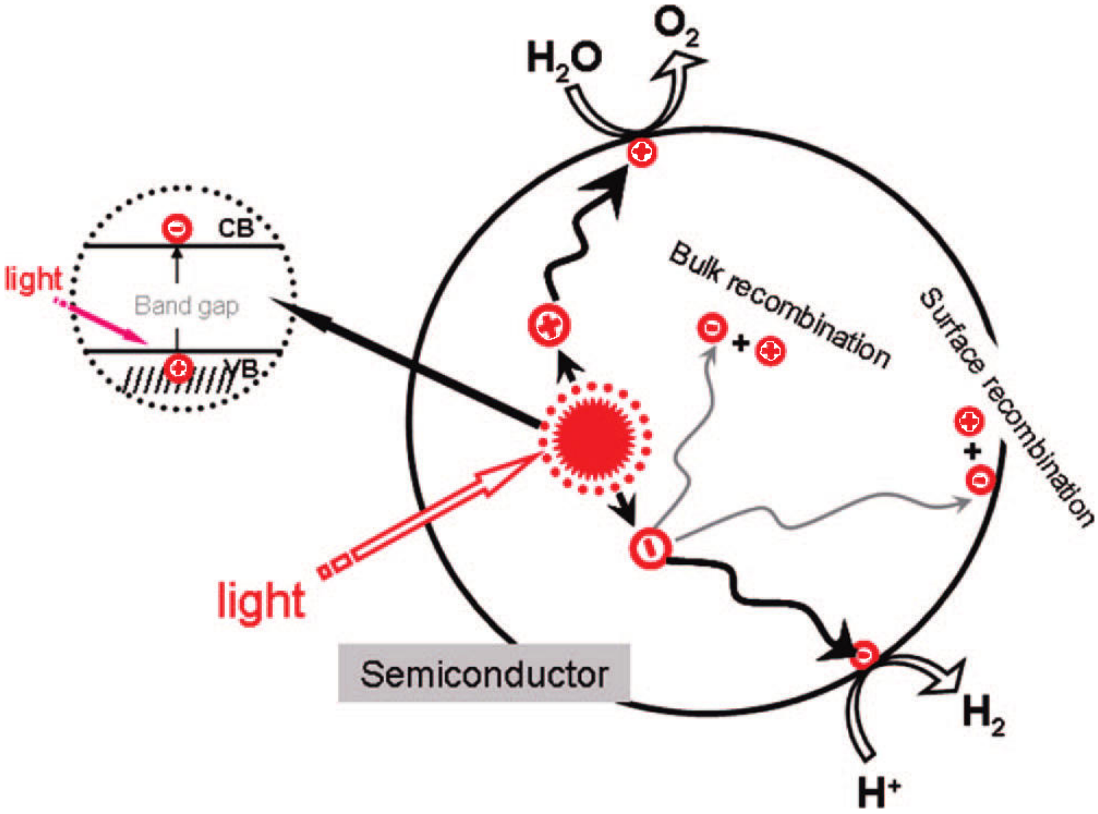

Figure 3.2: Processes involved in photocatalytic water splitting. Picture initally adapted from [108] and taken from [109].

indirect band gap. In an direct band gap semiconductor the electron-hole pair recombines radiatively and emits a photon. Assuming an indirect band gap, recombination is non radiative and phonon induced. The Auger recombination process involves three carriers. Here, the recombination released energy is not photon emitted nor transformed into heat. It is given to a third electron in the CB which after some time thermalizes back down to the CB edge. Auger recombination becomes important at high level injections under concentrated irradiation and heavy doping leading to high carrier concentrations. An increased rate of recombination and short lifetime reduces the photocatalytic efficiency (see figure 3.4 (a)(c)).

The Shockley-Read-Hall (SRH) recombination describes the electron-hole pair recombination as a process driven by defect levels inside the band gap. Incorporating impurity atoms into the rutile TiO_2 host matrix, indeed introduces such impurity states and affects the photocatalytic performance. Hence, interpreting our results in terms of the photocatalytic property of p element doped rutile TiO_2 we consider the SRH recombination.

The SRH recombination considers four different recombination scenarios, described from the viewpoint of a trap state. Scenario (a) assumes the generation of an electron-

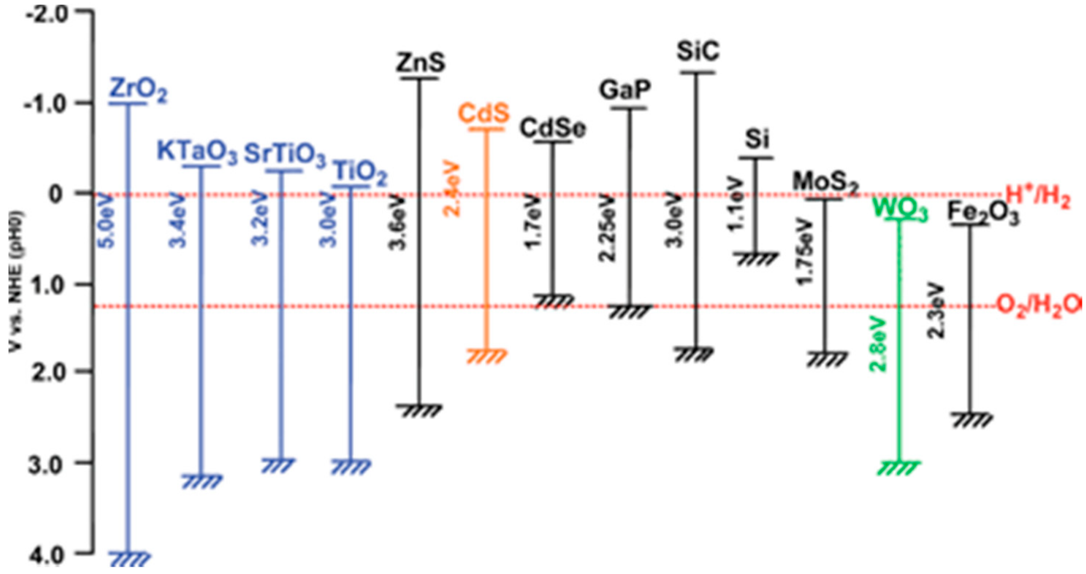

Figure 3.3: Band gaps and band edge positions of prominent semiconductors with respect to the redox potentials for hydrogen generation (red dotted lines) at pH=0. Picture taken from [106].

hole pair in a first step, while the respective excited electron, sitting inside the CB, can then be trapped by an empty impurity state (electron capture). Regarding a filled impurity state it can (b) emit an electron to the CB (electron emission) or (c) let it relax to the VB (hole capture). Supposing an empty trap state (d) a hole can be emitted to the VB with an electron that becomes attracted (hole emission) (see figure 3.5).

Considering these four processes Shockley, Read and Hall derived a formula that describes the recombination rate in such a system [110, 111]. They use Fermi-Dirac statistics and include the probabilities of states being occupied and unoccupied. Further, they consider average probabilities per unit time describing the electron capture rates for the different processes shown in figure 3.5. Including all that the following formula was derived

$$R_{SRH} = \frac{np - n_i^2}{\tau_{p0}(n + n_1) + \tau_{n0}(p + p_1)} \quad . \tag{3.5}$$

τ_{p0} and τ_{n0} are the lifetime parameters for the holes and electrons respectively and defined by the inverse value of C_p and C_n. C_n is the probability per unit time that an electron of the CB will be captured by an impurity state assuming that all traps are empty and therefore in the position to capture electrons. It is defined as $C_n = \sigma_n v_{t,n} N_t$, which is the product of the electron capture cross-section, the average thermal velocity of the electrons and the density of the recombination levels. The inverse of C_n corresponds to the lifetime of the electrons, τ_{n0}. The electron (and hole) lifetime therefore depends on the number of

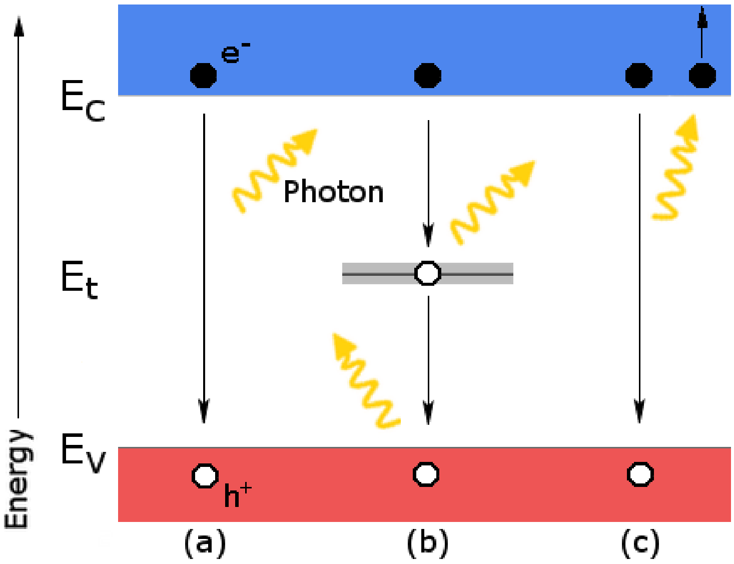

Figure 3.4: (a) shows a schematic picture of the band to band radiative recombination process. (b) corresponds to the SHR recombination with a trap state at E$_t$ (c) gives the Auger recombination involving a second electron that absorbs the emitted photon from the electron-hole recombination in the first step.

recombination levels N$_t$ and the capture coefficient $c_n = \sigma_n v_{t,n}$. C_p is the probability per unit time that a hole will be captured assuming that all traps are filled with electrons. It is defined as $C_p = \sigma_p v_{t,p} N_t$ and its inverse correponds to τ_{p0} describing the lifetime of injected holes. n gives the density of electrons in the CB and p corresponds to the density of holes in the VB (number of electron and hole carrier concentrations in non-equilibrium). n_i is the intrinsic electron or hole concentration of a system in thermodynamic equilibrium in which p and n are equal and where the generation and recombination of electron-hole pairs is assumed to be commensurate. n_1 and p_1 introduce the dependence of the recombination rate on the trapping energy level E_t and are defined as

$$\begin{aligned} n_1 &= N_c exp\left(\frac{E_t - E_c}{k_B T}\right) \quad , \\ p_1 &= N_v exp\left(\frac{E_v - E_t}{k_B T}\right) \quad , \\ n_1 p_1 &= n_i^2 \quad . \end{aligned} \tag{3.6}$$

n_1 (p_1) expresses the equilibrium number of electrons (holes) in the CB (VB) for the case the Fermi level falls at E_t (number of electron and hole carrier concentrations in equilibrium). N_c and N_v are the effective density of states for the conduction and valence band. k$_B$ is the Boltzmann constant and T the temperature. The equations given in 3.6 are of the same form as the charge carrier concentrations in terms of the Fermi energy

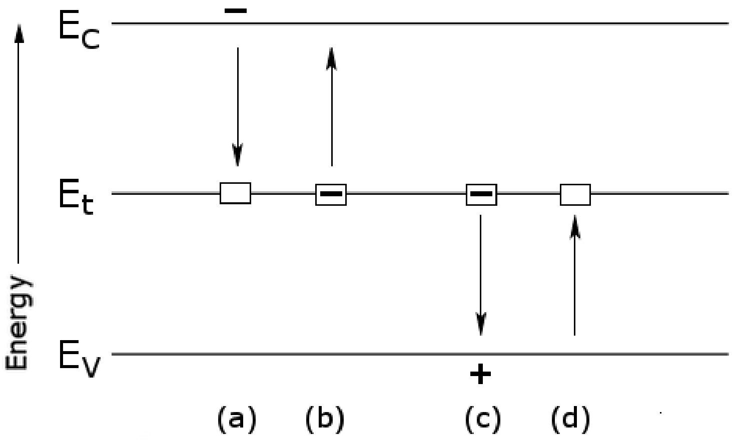

Figure 3.5: Processes involved in recombination by an impurity state. (a) shows electron capture, (b) electron emission, (c) hole capture and (d) hole emission.

level.

The recombination rate depends on the product of $n * p$. At fixed temperature $n * p$ is constant and equal to the intrinsic carrier concentration n_i. Subsequently, the product of n_1 and p_1 equals n_i^2, since they are equilibrium charge carrier concentrations. In equilibrium ($n_1 p_1 = n_i^2$) the denominator vanishes and the net electron hole recombination is zero. For $np \gg n_i^2$ there is an excess concentration of carriers. The respective systems tries to restore equilibrium through recombination and equation 3.6 becomes positive (positive net recombination rate). If $np \ll n_i^2$ there is a net depletion of carriers and the system will try to restore its equilibrium through the generation of electron-hole pairs (negative net recombination rate) [110–112].

R_{SRH} maximizes for defect levels that are near the middle of the band gap and $n_1 = p_1 = n_i$. Impurity states (traps) introduced in the mid band gap energy range are very efficient recombination centers and decrease the photocatalytic performance. Recombination due to defect levels also plays an important role at surfaces. They have a larger abundance of defect states and traps.

3.3 Calculations on p-element (C,N) doped rutile-TiO_2

TiO_2 is oft great importance for industries and as a phtotocatalyst for hydrogen generation. Introducing the main mechanisms of photocatalysis and referring to experiments performed by various groups, the effect of C and N doping on pure TiO_2 will be discussed. Doped TiO_2 is also of interest in the field of DMS. Hence, the magnetic structures and a possible magnetic coupling between the impurities is examined as well.

3.3.1 Crystal Structure and Doping Configurations

There are three common polymorphs of Titanium dioxide: rutile, brookite and anatase. Rutile is the thermodynamically most stable modification of TiO_2 and is an indirect wide band gap semiconductor with an experimental band gap of 3.0 eV [113]. The rutile structure belongs to the $P4_2/mnm$ (No. 136) tetragonal space group with unit cell parameters of $a = b = 4.587$ Å and $c = 2.954$ Å. In rutile TiO_2 every titanium atom is octahedrally coordinated to six oxygen atoms. The so formed octahedrons show an orthorhombic distortion, with the apical Ti-O bond length being slightly longer than the equatorial Ti-O bond length. Each TiO_6 octahedron is in contact with 10 neighbour octahedrons. The TiO_2 rutile crystal structure therefore can be seen as a chain of edge and corner-sharing TiO_6 units [113, 114].

Beside the investigation of the electronic properties of pristine TiO_2, we examined the effect of C and N atoms incorporated in various concentrations and positions into the host matrix. In total seven different doping configurations (per doping atom) were examined using *ab initio* calculations. Figure 3.6 depicts the different positions of the C and N dopants in the TiO_2 $2 \times 2 \times 2$ (48 atoms) supercell. In one of the performed calculations we assumed a single oxygen atom of the host matrix to be replaced by C or N (position (1)). This corresponds to a doping concentration of 2.1%. Further, two substitutional oxygen sites were occupied with two C or two N atoms, respectively, leading to a doping rate of 4.2%. This was done for two different configurations investigating the effect of increasing distance between the two impurity atoms. In the first configuration the distance between the two dopants was chosen to be minimal (position (1) and (2)). In the second the two dopants were placed on arbitrary oxygen sites (positions (1) and (3)) increasing the distance. Moreover, two different interstitial positions of C and N (positions (4) and (5)) in the TiO_2 host lattice were examined. Finally, we performed a set of calculations exchanging these interstitial dopants by their next nearest oxygen neighbour, so that O and C or N respectively switch position, with a doping concentration of again 2.1%.

3.3.2 Calculational Details and Methods

All calculations were performed employing the *Vienna Ab-initio Simulation Package* (VASP) [116–121] which uses projector augmented wave (PAW) pseudopotentials [122] to describe the potential between the ions. The semi-core s and p states for Ti and the $2s$ states for O, C and N respectively were incorporated in the calculations. To save

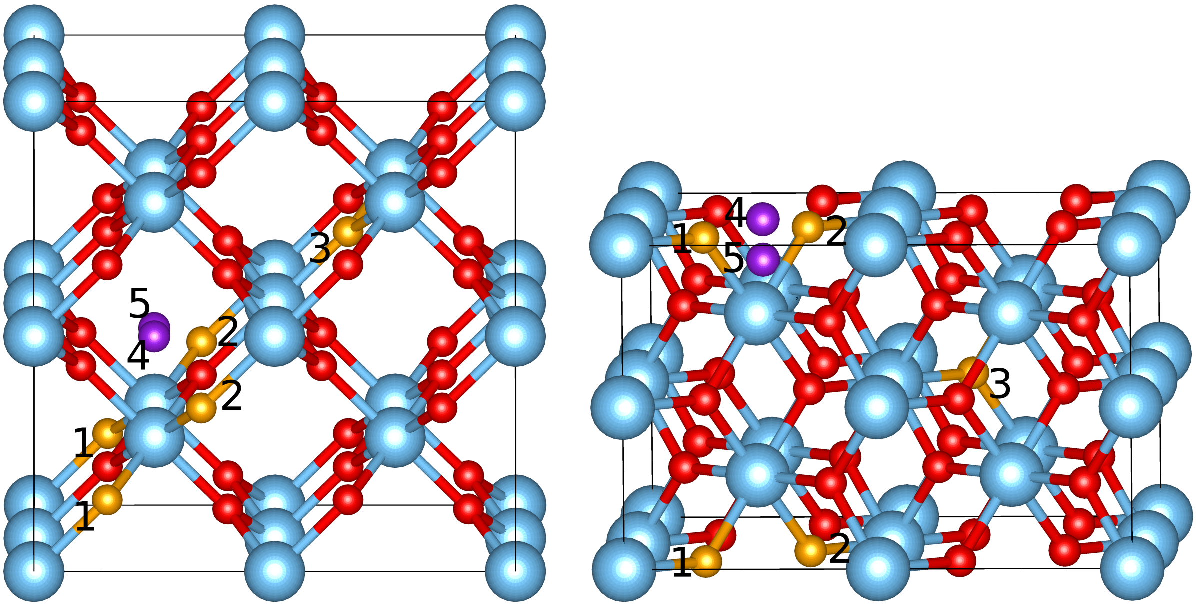

Figure 3.6: (a) and (b) shows the 48-atom supercell of TiO_2. The large blue and the small red spheres represent the Ti and the O atoms. The orange numbered spheres (1-3) denote the positions of O substituted by the C and N dopants and the violet numbered spheres (4-5) notify the interstitial doping positions.This figure were created using the VESTA program [115].

computation time, the effects of exchange and correlation were initially treated using the GGA-PBE approximation [123, 124], until all force components were smaller than 0.01 eV/Å. During the relaxation we allowed for a change of the atomic positions, shape and volume of the cell. The final convergence was done with the post-DFT HSE06 functional [125] which is known to yield reliable results for the gap size and the position of the impurity bands inside the gap.

Plane waves with an energy up to 530 eV were included in the basis set, in order to avoid Pulay stress and other related problems. The Brillouin-Zone integration was performed using a $4 \times 4 \times 4$ Γ centered k-mesh with Gaussian smearing set to 0.05 eV. The total energy was converged better than 1×10^{-6} eV for all cases investigated. The limitations of LDA and GGA+U in predicting the equilibrium lattice constant and the proper band gap [126] poses problems in the description of the structural and electronic properties of the pristine and doped system. Thus, predicting the position of the impurity states, crucial for photocatalytic reasons, becomes only possible after extracting the appropriate U from experimental data.

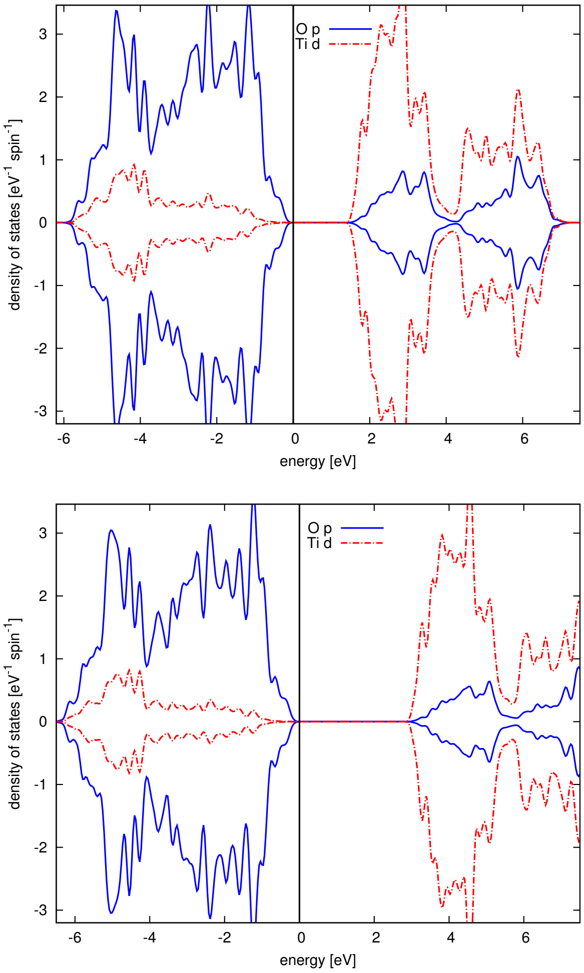

Figure 3.7: (a) and (b) show the GGA+U and HSE calculated projected DOS of stoichiometric TiO_2. Given in blue are the O *p* states and highlighted in red are the Ti *d* states. The "bulk" oxygen and titanium state are plotted for 2 titaniums and 5 neighbouring O atoms.

Figure 3.7 shows the GGA+U and HSE calculated projected DOS of O *p* (highlighted in blue) and Ti *d* states (highlighted in red) of stoichiometric TiO_2. Comparing (a) and (b) shows that applying the HSE functional leads to an enhanced more realistic band gap. Regarding the electronic structures, both approximations yield similar results. Assuming that the HSE functional describes the systems in a more realistic way, similar electronic structures confirms the chosen U value for the GGA+U approximation.

3.3.3 C/N-substitutions

To compare and evaluate the structural changes induced by the impurities calculations on pure TiO_2 were done initially to obtain structural and electronic data that can be used as a reference. The calculated lattice parameters of pure TiO_2 rutile (a=4.65 Å; c=2.97 Å) are in good agreement with the experimental values (a=4.59 Å; c=2.95 Å). The direct band gaps calculated using the HSE06 functional (3.24 eV) show a considerably improvement over the GGA results (1.77 eV) [127] and are again in in good agreement with experimental values (3.1 eV) [113].

Single carbon and nitrogen substitution

In total three substitutional cases were investigated. i) one single oxygen becomes substituted by a C or N impurity. Further, two oxygen sites are substituted by either two carbon or nitrogen atoms, considering two different cases ii) minimizing the distance of the impurities occupying two adjacent oxygen sites, and iii) the impurities occupy two distant oxygen positions. The latter two cases allow to study the dependence of the magnetic coupling on the distance of the magnetic ions.

Substituting just one oxygen atom by a carbon impurity leads to a magnetic moment of $2\mu_B$ per supercell and arises mainly from the C atom with $0.72\mu_B$ per carbon atom (measured within the muffin tin radius 1.63 Å). Substituting oxygen by carbon introduces two holes into the system. As a consequence, one complete band on the average becomes unoccupied leading to a semiconducting ground state with a magnetic moment. The total magnetic moment of $2\mu_B$ per unit cell is composed of the magnetic moment at the carbon site plus the polarizations of the surrounding oxygen. Figure 3.8 depicts the density of states (DOS) for the single substitutional case. The upper panel shows the nonmagnetic case of carbon substitution. The lower one depicts the DOS of the equilibrium magnetic state with $2\mu_B$.

The substitution of N introduces one hole and consequently leads to a magnetic moment of $1\mu_B$ per supercell where $0.57\mu_B$ are located at the N site (measured within the muffin tin radius 1.40 Å). This result agrees with the experimental finding of room temperature ferromagnetism in N-doped rutile TiO_2 films by Bao et al. [128] who report a nitrogen moment of about $0.9\mu_B$. The DOS for the magnetic and the nonmagnetic state is shown in Figure 3.9. Introducing dopants into the TiO_2 rutile crystal leads to a change in the atomic distances. Changes of the bond lengths between the oxygen (of the undoped system), the substituted carbon and the substituted nitrogen atom to its next neighbours (NN), respectively, were compared. The atomic distances of the pristine crystal lattice were normalized to those of the doped systems using its relaxed volume. By doing so we

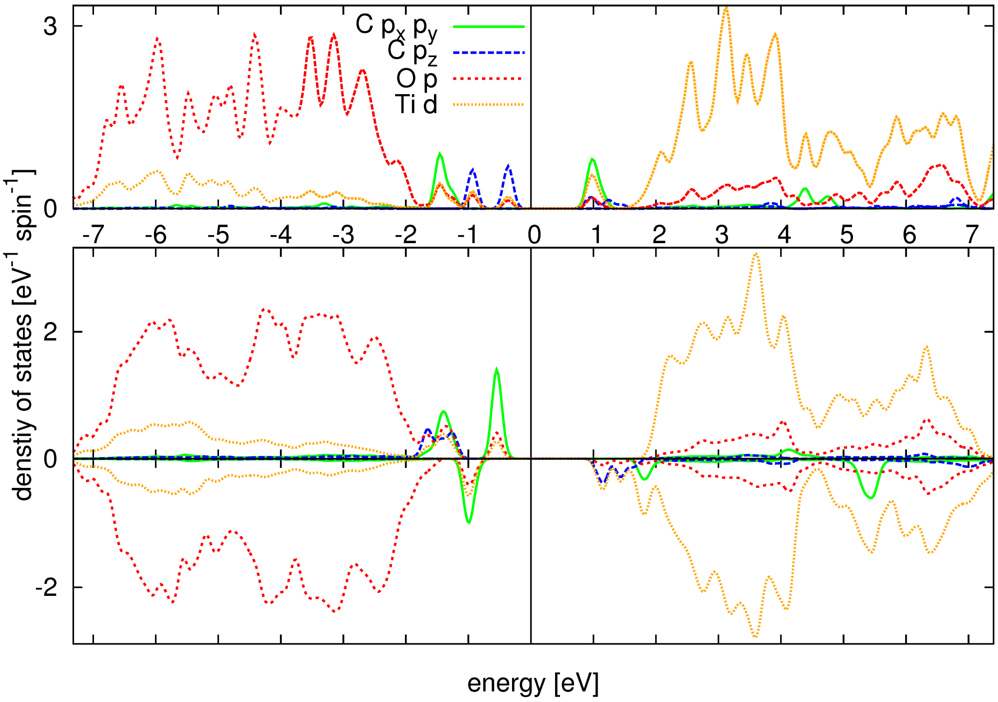

Figure 3.8: Density of states of the nonmagnetic (upper panel) and magnetic (lower panel) state of C substituted TiO_2. The DOS shown includes only the NN around the C impurity, thus 2 Ti and 5 O atoms.

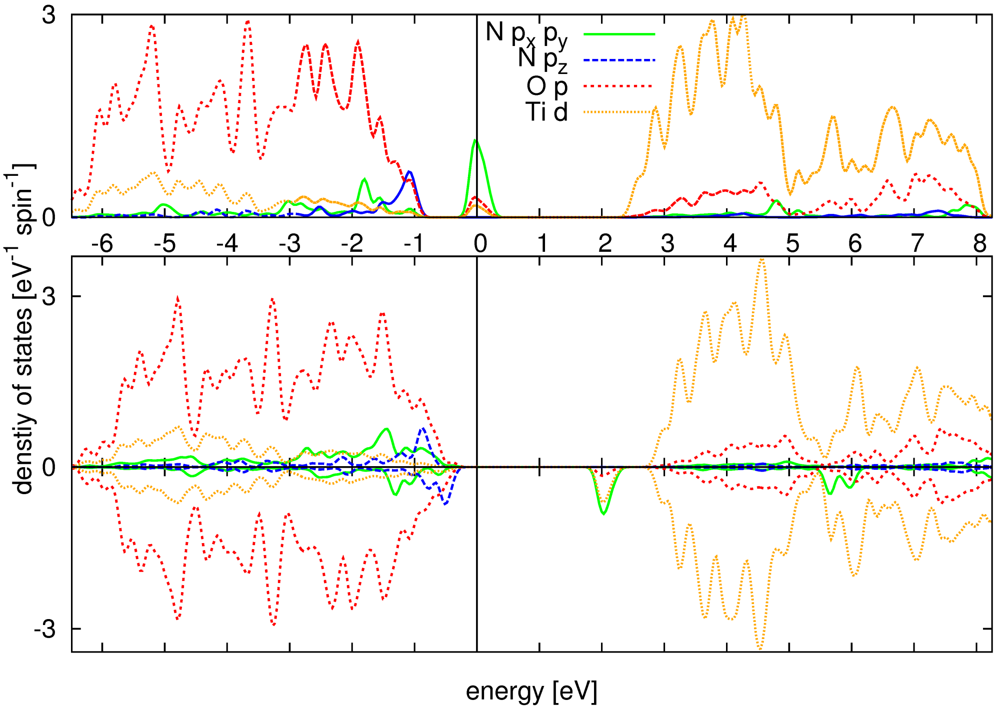

Figure 3.9: Density of states of the nonmagnetic (upper panel) and magnetic (lower panel) state of N substituted TiO_2. The DOS shown includes only the next neighbours around the N impurity, thus 2 Ti and 5 O atoms.

considered increased distances caused by the larger ionic volume of the C and N dopant. Table 3.1 gives an overview on the bond lengths in the respective system. The N and the C atom causes an enlargement of the atomic distances in the crystal. Due to the higher electronegativity of N(3.04)>C(2.55) [24], nitrogen tends to interact more with the host semiconductor in particular with the neighbouring oxygens. This leads to shorter bond lengths for N to its next neighbours than for C. These results are again in line with the DOS shown in figure 3 and 4. The larger bond lengths and the consequently weaker bonding to the host semiconductor makes the $2p$ states of the C atom more localized in the gap and the C states which occur in the VB and CB due to the weaker interaction with O are smaller than in the N case. The $2p$ states of nitrogen are mostly located in the VB and CB, induced by the stronger bonding. As a consequence, carbon doped TiO_2 rutile has a smaller band gap than the nitrogen doped system (table 3.1).

To investigate the stability of the doped system we calculated the defect formation energies according to the following formula [129]:

$$E^{form}[X] = E_{tot}[X] - E_{tot}[bulk] + n(\mu_O - \mu_X) \tag{3.7}$$

where E_{tot} is the total energy of the doped supercell with one oxygen atom replaced by the impurity X(X=C,N), $E_{tot}[bulk]$ the total energy for the pristine system. n indicates the number of oxygen atoms that have been replaced in the supercell by dopant atoms, μ_O and μ_X are the corresponding chemical potentials. The stability of the various configurations differ with the oxygen chemical potential. μ_O describes the oxygen environment during synthesis and therefore effects the defect formation energies. We define the oxygen chemical potential being μ_O=$\frac{1}{2}\mu_{O_2}$+$\mu_{O'}$ with $\mu_{O'}$ ranging from 0 eV to -4 eV, whereas $\mu_{O'}$=0 eV defines the oxygen rich and $\mu_{O'}$=-4 eV the oxygen poor case. The oxygen poor case is approximately half the HSE calculated formation enthalpy of rutile TiO_2 with $\Delta H_f(TiO_2) = -9.95eV$ which is in good agreement with the experimental value of 9.80 eV [130]. To give a more conceptual measure of the oxygen concentration we convert $\mu_{O'}$ to oxygen pressure at a temperature of 1000K (top x axis), typical for annealing of rutile TiO_2 [131]. In the tables below we list the defect formation energy for the different doping configurations considering the oxygen rich case. The chemical potentials were calculated with respect to C in Diamond, N in N_2 and O in O_2. In addition, phase diagrams and $E^{form}[X]/\mu_{O'}$ plots are presented in figure 3.15.

Multiple carbon and nitrogen substitution

As a second step we study the substitution of 2 oxygens by 2 carbons or 2 nitrogens at different but crystallographically equivalent sites. The results are given in table 3.2 and the positions of the substituted atoms correspond with the site numbering given in figure

Table 3.1: Single carbon and nitrogen substitution: Cell volume, bond lengths of X-Ti$_{equatorial/axial}$ and X-O$_{[2]}$, total magnetic Moment M_{tot} of the supercell, defect formation energy $E^{form}[X]$, energy difference of the non spin polarized and spin polarized state $\Delta E[NSP - SP]$ and the direct band gap for spin up and spin down.

X=	C	N	O
Cell Volume (Å^3)	519.95 (+1.9%)	516.18 (+1.1%)	510.06
X-Ti$_{equatorial}$ (Å)	2.07 (+2.8%)	2.02 (+0.4%)	2.00
X-Ti$_{axial}$ (Å)	2.13 (+7.9%)	2.02 (+2.6%)	1.96
X-O$_{[2]}$ (Å)	2.74 (+6.0%)	2.62 (+1.9%)	2.57
M_{tot} (μ_B)	2	1	0
$E^{form}[X]$ (eV)	9.42	5.43	–
$\Delta E[NSP - SP]$ (eV)	0.24	0.80	–
Spin up gap (eV)	2.20	3.20	3.24
Spin down gap (eV)	2.06	2.60	3.24

3.6. For all 4 cases investigated we find a magnetically ordered ground state with $4\mu_B$ per supercell for 2 carbons and $2\mu_B$ per supercell for 2 nitrogens. The additional substitution leads to a further increase of the cell volume, but considerably smaller than for the single impurity (compare to table 3.1). The formation energy per atom remains almost constant and in general shows a slight increase with respect to the single impurity, only in the case of 2 distant nitrogens a very small reduction is found. Studying 2 impurities gives us the opportunity to discriminate between a ferromagnetic (FM) and an antiferromagnetic (AFM) coupling. In general we find the AFM state to be lower in energy, only for the case of 2 distant nitrogens an extremely small FM stabilization energy has been calculated, however, this small energy change is at the verge of the numerical accuracy. As expected, we find that for neighbouring impurities (C(1,2) and N(1,2)) the coupling energy is at least one order of magnitude larger than for the distant ones (C(1,3) and N(1,3)) which appear to be essentially decoupled. The largest energy gain is found for the case C(1,2) where our calculation shows, that in the FM case the spin down gap almost vanishes, so that the opening up of the gap in the AFM state leads to the observed energy gain. The band gaps are reduced compared to the case of a single impurity, the strongest effect is found for C(1,2) where the interaction of the neighbouring C atoms reduces the gap to 1.4 eV. For the N substitution we find that the "distant" N(1,3) case is lower in energy, while for the C substitution the "close" C(1,2) configuration is more stable, which is again a consequence of the stronger interaction and points to a tendency of the C atoms to form clusters. The multiple nitrogen substitution configuration N(1,3) has a lower E^{form} per impurity atom than the single substitutional case N(1). N(1,3) is about 140 meV more stable in energy than the N(1,2) configuration. Same is true for the C(1,3) and C(1,2) configuration, first is about 240 meV energetically more favourable. Regarding the defect formation energies reflects this behaviour.

Table 3.2: Multiple carbon and nitrogen substitution: Cell volume, total magnetic Moment M_{tot} of the supercell, defect formation energy per impurity atom $E^{form}[X]$, energy difference of the FM and AFM state $\Delta E[FM - AFM]$ and direct band gap for spin up and spin down.

X=	C (1,2)	N (1,2)	C (1,3)	N (1,3)
Cell Volume (Å^3)	522.85(+2.5%)	519.51(+1.8%)	522.85(+2.5%)	517.87(+1.5%)
M_{tot} (μ_B)	4	2	4	2
$E^{form}[X]$ (eV)	9.62	5.47	9.65	5.41
$\Delta E[FM - AFM]$ (eV)	0.160	0.018	1.14×10^{-3}	-0.019×10^{-3}
Spin up gap (eV)	1.40	2.45	1.90	3.16
Spin down gap (eV)	1.40	2.45	1.90	2.33

3.3.4 C/N-interstitial

The final investigation deals with carbon and nitrogen placed on interstitial sites (sites (4),(5) in figure 3.6) and their interaction with the respective neighbouring oxygen. Putting carbon on either one of the two interstitial sites we find that the electronic structure is very similar and no magnetic moment appears.

Relaxing the TiO_2 host matrix with N and C sitting either on the interstitial site (4) or (5) gives similar geometric ground state structures. The initial position (before relaxation) of the C(5) and N(5) impurities are in line and respectively on an axis with their two next nearest Ti atoms. Relaxing these systems the C(5) and N(5) atoms more or less stay in this position. The Ti-C(5)/N(5)-Ti distance, however, minimizes by about 11 percent compared to the unrelaxed structure, for both cases. Placing the C and N atom at cell site (4) the starting point is shifted out of line and C(4) and N(4) are not on an axis with their two next nearest Ti atoms. Allowing the system to relax C(4) and N(4) move towards position (5), since its energetically more favourable to be in line with

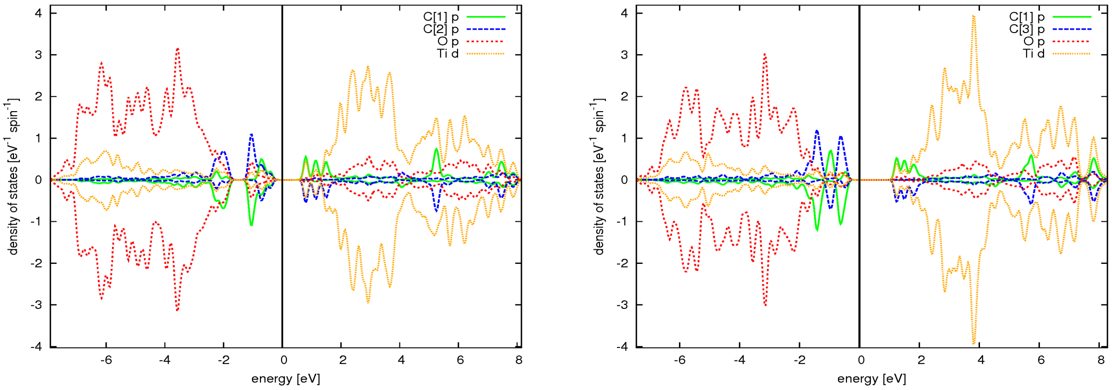

(a) C(1,2)

(b) C(1,3)

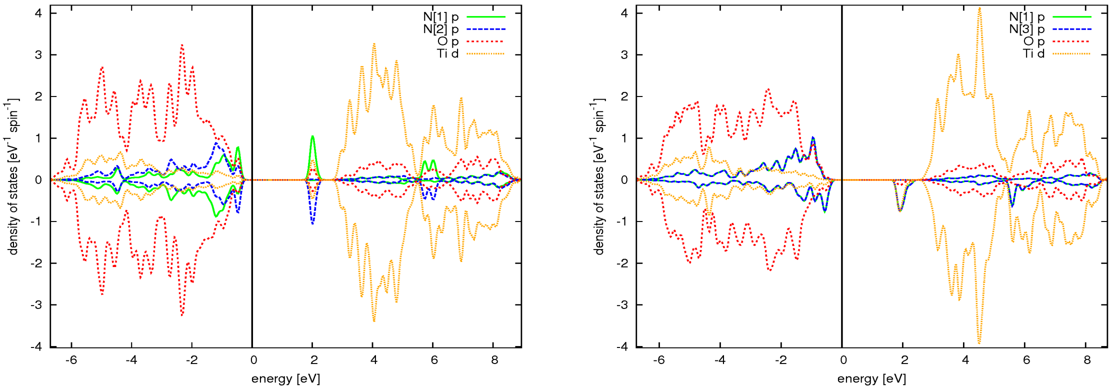

(c) N(1,2)

(d) N(1,3)

Figure 3.10: Densities of states for the substitution of 2 oxygens by 2 carbons or 2 nitrogens. The densities of states are given for the calculated ground state which is AFM for C(1,2), C(1,3), N(1,2), and FM for N(1,3). The “bulk” oxygen and titanium states are plotted for 5 neighbouring oxygens and 2 titaniums.

two Ti atoms. Hence, is not surprising that both sites (4) and (5) give similar electronic and magnetic structures for C and N, respectively. We thus restrict ourselves to present only the density of states for interstitial site (4) (see figure 3.11). The respective electron density is given in figure 3.12(a). Figure 3.12(a), however, gives the electron density of the C(5) structure. Since both the C(4) and C(5) doping configurations relax into similar ground state structures (with alomst equal ground state properties), as mentioned before, it is valid to make conclusions by comparing the DOS given in figure 3.11 and the electron-density in figure 3.12(a). The interaction of the interstitial carbon with the host lattice is almost negligible and C forms atomic like flat bands at the bottom of the TiO_2 gap, which is also reflected in the electron density. The nonmagnetic state is easily explained from the even number of electrons. In contrast to the metastable carbon postition, which has a total spin of 1, the small but present crystal field from the host lattice leads to a double occupation of a single p orbital and hence a total spin of zero. The same mechanism can be applied to nitrogen with the only difference that N has 3 p electrons and consequently always one singly occupied orbital with a resulting total spin of $\frac{1}{2}$. Energetically we find that C/N sits on a saddle point of the total energy surface. Upon shifting C/N slightly to either side, the interstitial atoms approach their oxygen neighbours and form CO and NO molecule type entities which is accompanied by a dramatic change in the electronic structure. The highly reactive oxygen tries to reach its 2^- state, by forming a CO or NO molecule which ends up almost at the original oxygen position. The electron density once the C(5)-O dimer formed is shown in figure 3.12(b). We also performed a second set of calculations, where C/N are placed on an oxygen position and this oxygen is put at an interstitial site. Starting from this configuration and after relaxation again led to the formation of CO and NO dimers with the same total energy as before. The only difference is that the C/N interstitial sits at an energy saddle point, while the oxygen interstitial immediately starts to move towards the C/N. Figure 3.13(a) and (c) shows the charge densities for the CO and NO case. One clearly sees the molecular structure with a bond length of 1.22 Å for CO and 1.31 Å for NO. For carbon the bond length agrees with the CO double-bond length of 1.20 Å, for nitrogen the agreement is less good and lies between the NO single-bond length of 1.45 Å and the double-bond length of 1.17 Å [132] which may be caused by the fact that the NO "molecule" exhibits a magnetic moment of $1\mu_B$.

Table 3.3 summarizes the results of our calculations. The first 2 lines contain the data for the C/N interstitials at their saddle point positions. Also for this non-equilibrium state a semiconductor is found. Again nitrogen becomes magnetic with $1\mu_B$, while carbon remains nonmagnetic. The stable configuration is found, when both carbon and nitrogen become inserted on site (5). For both cases a CO or NO dimer is found, which considerably lowers the total energy. In an experimental study done by Chen et al. [133] nitrogen

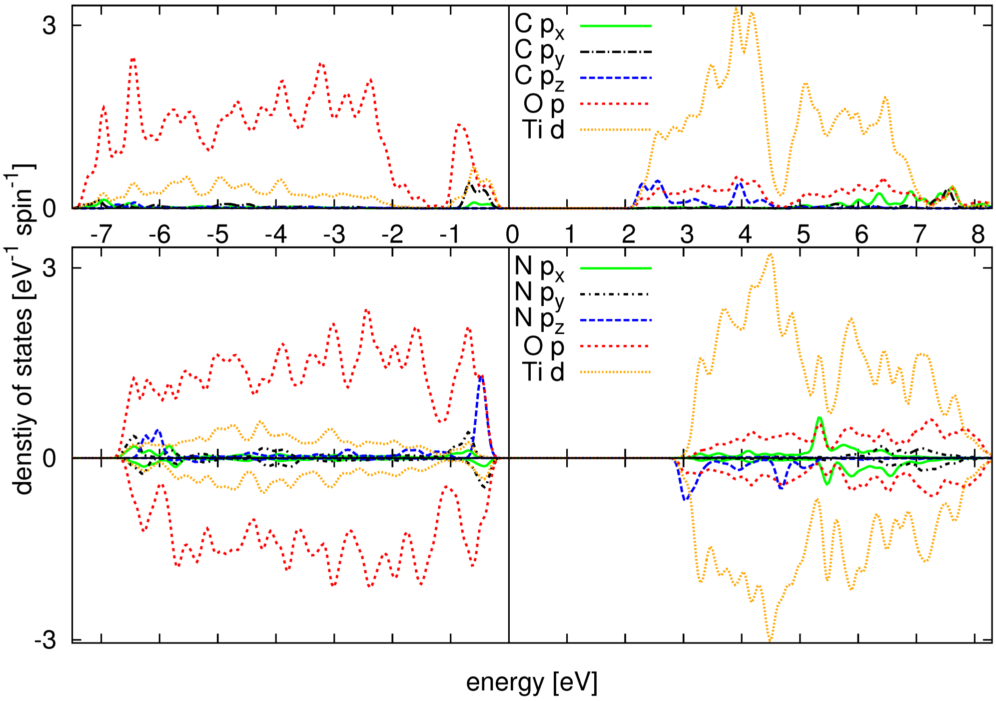

Figure 3.11: Densities of states for interstitial carbons or nitrogen placed on site (4). The densities of states are given for the calculated ground state which is nonmagnetic for carbon, and magnetic for nitrogen. The "bulk" oxygen and titanium states are plotted for 5 neighbouring oxygens and 2 titaniums.

doped TiO_2 nanocolloids have been prepared and their photocatalytic properties were investigated. XPS measurements done by this group suggest the formation of NO binding regions in these samples, which again underlines our findings of the NO dimers. Asahi et al. [134] report about experiments supported by *ab initio* calculations where they study various kinds of N complex species incorporated into a TiO_2 anatase host matrix and as well encountered the formation of NO bonds. DiValentin et al. [99] again found single bonded CO dimers from ab initio calculations.

The C(4)-O and the C(5)-O dimers are rotated differently in space. Here, the initial position effects the ground state structure in contrast to the C(4) and C(5) doped cases. Same is true for the N(4)-O and the N(5)-O dimers. The C(4)-O and N(4)-O dimers axes are oriented in the x-y direction and in plane with the next nearest Ti atoms. In that particular case the impurity atom's position (C and N) equals more the initial O cell site position of the undoped TiO_2 host matrix. In the C(5)-O and N(5)-O doped case both dimers and their binding axes are rotated in the z axis and their barycenters are in plane with the Ti atoms. Here the O atom is closer to its ground state position of the undoped cell. Hence, this may explain why the C(5)-O and the N(5)-O dimers form the energetically more stable doping configuration.

The defect formation energies are lower for the interstitial configuration compared to the oxygen substitutional case. For N(5) E^{form} decreases by 1.5 eV compared to the single substitutional case N(1) and E^{form} for interstitial C(5) and substitutional C(1) even differ by 4.35 eV.

The N(5)-O configuration is 1.41 eV energetically more favourable than the N(5) configuration. When comparing N(4) and N(4)-O the latter is by 1.24 eV more stable. Regarding the C doped cases, C(5)-O is 1.87 eV more favourable in energy than the C(5) doping case. The metastable magnetic C(4)-O structure, however, is still about 1.90 eV energetically more stable than the C(4) configuration. These conclusions are also reflected by the formation energies given in 3.3.

The densities of states, given in figure 3.14, show the basically different behaviour as compared to the C/N impurity on the saddle point state (see figure 3.11). The oxygen states are below the bulk oxygens and the C/N p states are inside the gap. The charge transfer of 2 electrons leads to a strong splitting of the occupied oxygen and the unoccupied carbon/nitrogen states. It is noteworthy that there exists also an interaction of the high lying carbon p states and the Ti d states. The NO interaction is weaker, which is established by the larger bond length. The oxygen states are again below the oxygen bulk, but the nitrogen p states are just at the bottom of the TiO_2 gap. The unpaired electron leads to a magnetic moment of $1\mu_B$ and the interaction with the Ti d states is much smaller than for the carbon case. The respective charge and spin density is

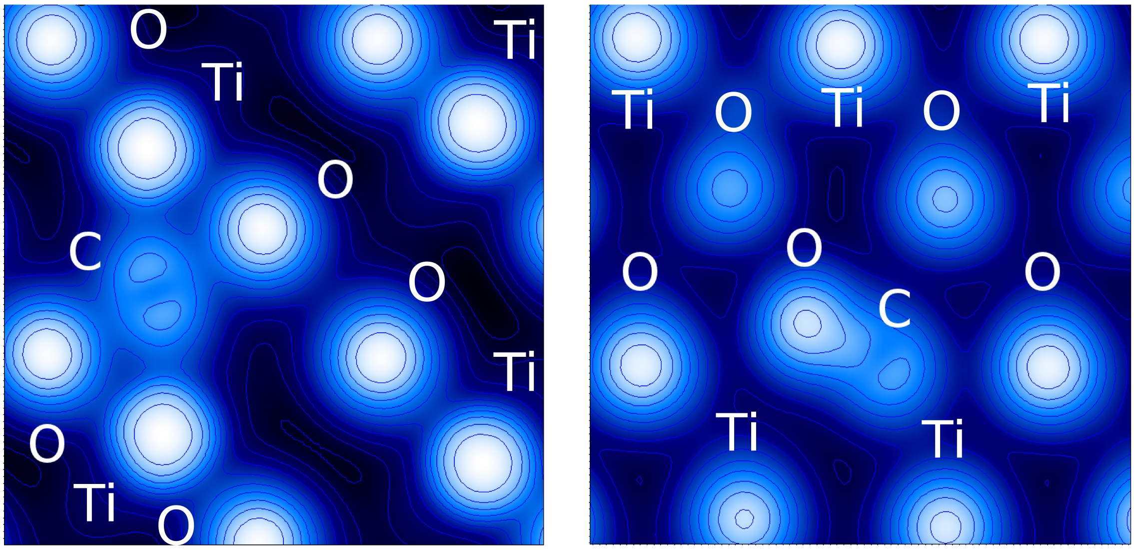

(a) C(5)

(b) C(5)-O

Figure 3.12: Electron-density on a logarithmic scale for substitutional C and the CO dimer in the TiO_2 lattice, lighter colors denote larger electron densities. (a) Electron-density of the nonmagnetic saddle point configuration of C; (b) Electron density of the stable configuration of CO. (b) and (a) are different planes of the crystal lattice, since the bond-axes of the CO dimer turns during formation out of plane (a). This figure was created using the VisIt program [135].

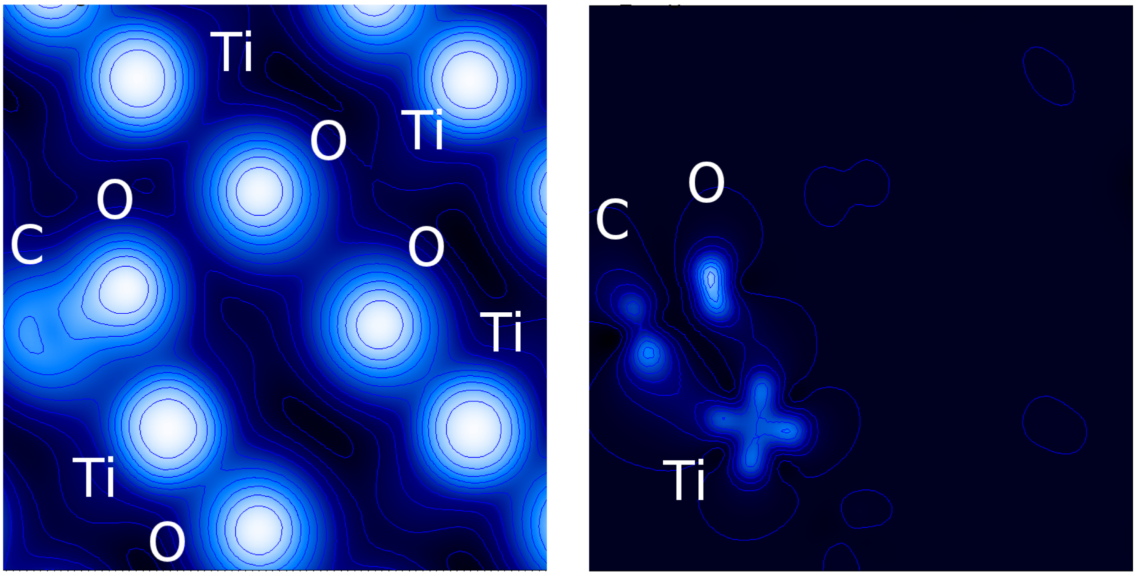

(a) C(4)-O (b) C(4)-O

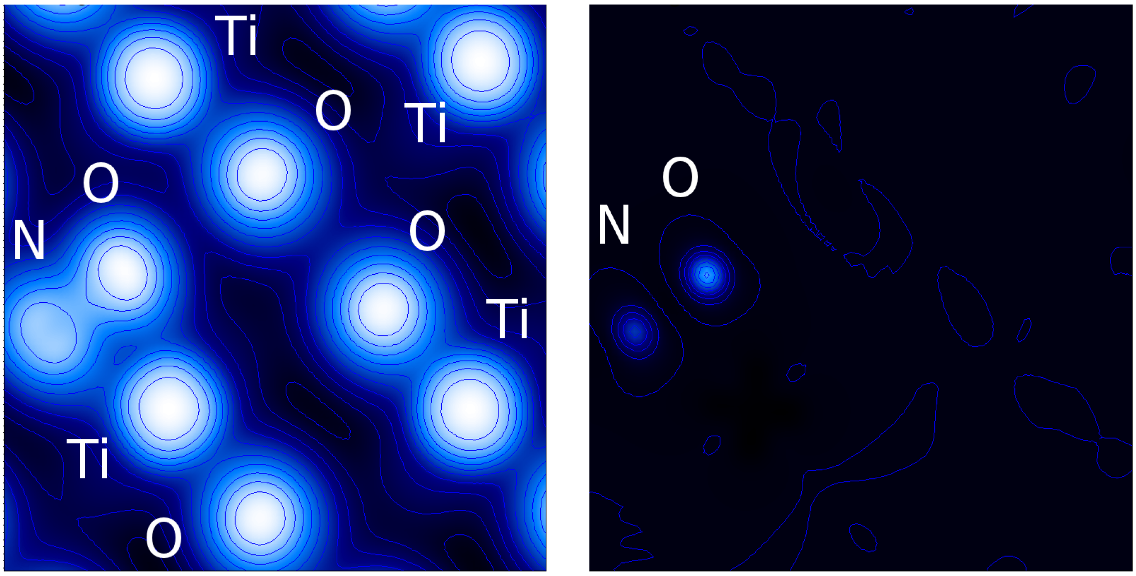

(c) N(4)-O (d) N(4)-O

Figure 3.13: Electron (logarithmic scale) and spin-density (linear scale) for substitutional CO and NO dimers in the TiO_2 lattice, lighter colors denote larger electron densities. Electron (a) and spin density (b) of the metastable magnetic ($2\mu_B$) configuration of CO; Electron (c) and spin density (d) of the stable magnetic ($1\mu_B$) configuration of NO. This figure was created using the VisIt program [135].

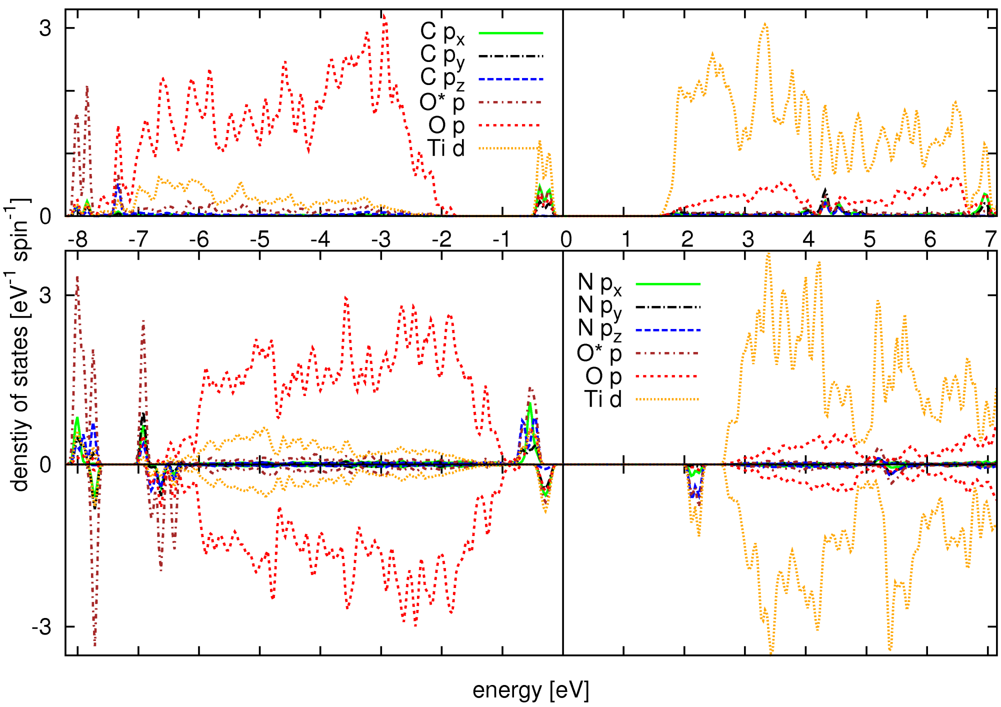

Figure 3.14: Densities of states for the interstitial C(5)-O and N(5)-O doping configuration. The densities of states are given for the nonmagnetic state for carbon, and the magnetic state for nitrogen. The “bulk” oxygen and titanium states are plotted for 5 neighbouring oxygens and 2 titaniums. O* is the oxygen of the CO or NO dimer.

Table 3.3: C/N-interstitial: Atomic distance of C/N and its nearest neighbouring oxygen, total magnetic moment M_{tot} of the supercell, defect formation energy per impurity atom $E^{form}[X]$, and direct band gap for spin up and spin down.

	C(4)	N(4)	C(4)-O	C(5)-O	N(4)-O	N(5)-O
Atomic Distance C/N-O (Å)	1.80(+6.4%)	1.81(+6.9%)	1.22	1.24	1.32	1.32
M_{tot} (μ_B)	0	1	2	0	1	1
$E^{form}[X]$ (eV)	6.92	5.33	6.04	5.05	4.08	3.91
Spin up gap (eV)	2.59	3.51	0.77	1.92	2.89	3.16
Spin down gap (eV)	2.59	3.40	3.39	1.92	2.32	2.35

shown in figure 3.13(c), (d). We restricted ourselves to present only the N(4)-O and N(4) configuration, since the N(5)-O and N(5) cases represent similiar results, respectively.

For the case of carbon with oxygen on position (4) we find a metastable magnetic solution with a magnetic moment of $2\mu_B$ per supercell. Unlike the cases discussed earlier in this paper, the magnetic moment is no longer located at carbon only, but is distributed between carbon, oxygen and 3 neighbouring Ti atoms. Figure 3.13(a), (b) shows the electron density and the spin density, respectively, where the polarization of the Ti d states is easy to recognize. However, due to the unfavourable total energy of this magnetic state we expect that this case will not be present in real samples.

Calcuating the stretching mode frequency

From our calculations we suggest the formation of NO and CO dimers in TiO_2 and a possible experimental proof could be the detection of the (symmetric) stretching mode frequency. For calculating the (symmetric) stretching mode frequency we started with Hooke's law $F = -k\Delta r$ and used its second derivation

$$E_{pot} = \frac{1}{2}k\Delta r^2 \quad , \tag{3.8}$$

with k being characteristic for the respective system and Δr the replacement out of the equilibrium position. Calculating the stretching mode frequency for the C(5)-O and the N(5)-O dimers (we neglected the C(4)/(5)-O configurations, since they are less stable in energy) we stretched and compressed their equilibrium bond length r_0 in a symmetric way so that Δr is given by $\Delta r = r - r_0 = x_1 + x_2$ with $x_1 = x_2$. x_1 and x_2 are the deflections of the C(5)/N(5) and the O atom out of the equilibrium position, respectively.

To gain E_{pot} as a function of the displacement Δr we stretched and compressed the C(5)-O and the N(5)-O dimer and performed a static on top calculation using the GGA+U approximation. Applying the HSE hybrid functional would not have brought any benefits expect of higher computational costs in that particular case.

The C(5)-O dimer with its equilibrium bond length of 1.24 Å was stretched and compressed from 1.40 Å to 1.19 Å in steps of 0.01 Å. Same was done for the N(5)-O dimer with an equilibrium bond length of 1.32 Å which again was stretched and compressed from 1.19 Å to 1.40 Å. The therefore gained energy curves for both dimers have a parabolic shape. In a next step we fitted a polynomial second degree of the form $f(r) = a + cx^2$ to the calculated curves. Regarding equation 3.8 its second derivation equals the characteristic constant k. Taking the fitted polynomial and its second derivative $f(x)'' = 2c$ it follows that $E''_{pot} = f(r)''$ and $k = 2c$. The frequency can be expressed by rewriting Hooke's law to

$$M\frac{\mathrm{d}^2x}{\mathrm{d}t^2} = -kx \quad , \tag{3.9}$$

and using the ansatz $x = x_0 \sin \omega_0 t$. With $\omega_0 = 2\pi\nu$, k can then be written as

$$\nu = \frac{1}{2\pi}\sqrt{\frac{k}{\mu}} \quad with \quad \mu = \frac{1}{m_1} + \frac{1}{m_2} \tag{3.10}$$

where m_1 and m_2 are the C/N and O masses respectively. Inserting $k = 2c$ into equation 3.10 the stretching frequencies can be calculated. Vibrational frequencies are usually written as $\bar{\nu} = \nu c^{-1} = cm^{-1}$. We calculate the symmetric stretching frequency to be 1605 cm^{-1} for the C(5)-O and 1234 cm^{-1} for the N(5)-O dimer inside the TiO_2 lattice.

3.3.5 Valence and conduction band edges

As discussed in subsection 3.2.1 a proper band gap of about at least 1.32 eV is necessary for the water splitting reaction in the process of hydrogen generation. Doping TiO_2 does not only affect the band gap but can also shift the valence band potential. The CB of stoichiometric TiO_2 is already very close to the H^+/H_2 reduction potential [106], hence we desire a band gap reduction and simultaneously an upward shift of the VB so that the CB potential does not fall below the reduction potential (see figure 3.5). The VB of the doped system must be below the oxidation level (5.67eV below the vacuum level) in order to make the oxygen oxidation reaction O_2/H_2O thermodynamically favourable. The CB must be above the standard hydrogen electrode level (4.44 eV below the vacuum level) so that the H^+/H_2 reaction becomes energetically favourable [136].

Referring the band edges of the undoped TiO_2 simulations cell to the vacuum level we used the in experiment determined work function of the rutile TiO_2 (100) surface of 4.13 eV [137]. Defining zero as the vacuum level on the energy scale the CB band edge of pure TiO_2 is located at -4.13 eV and the VB edge at -7.37 eV (subtracting the HSE calculated band gap of the work function). Assuming that the anion doping concentrations are too small to affect and alter the experimental work function in a significant way we consider it as constant for all investigated cases. Since all calculations were performed on bulk systems with different atomic potentials we need to define a reference energy for all systems. For slab calculations, including vacuum that would be the vacuum level. In our case we choose the $1s$ core level energy of an O atom as reference. The respective O atom was selected to have sufficiently large distance to the impurity atom thus its $1s$ state stays unaffected. The calculation of the core level states using HSE hybrid functionals is not implemented in the VASP code so far. We therefore used the GGA+U approximation calculating the core level shifts and added the more realistic HSE calculated band gaps.

Table 3.4 and 3.5 list the calculated core level shifts, the position of the VB and CB edge and the spin up and down gap with respect to the energy scale described above. As long as the VB and CB edges are below and above -5.67 eV and -4.44 eV, respectively photocatalytic hydrogen generation is possible.

Table 3.4: VB and CB edges of interstitial and substitutional C doped TiO_2. Further given are the band gap and the respective calculated core level shifts. Red coloured numbers denote band edges and band gaps unfavourable for hydrogen generation. Band gaps highlighted in orange meet the requirements for hydrogen generation but belong to configurations with mid band gap states reducing the photocatalytic performance.

	core level shift	VB edge ↑	VB edge ↓	CB edge ↑	CB edge ↓	Band gap ↑	Band gap ↓
C(1)	-0.726	-6.65	-7.20	-4.45	-5.14	2.20	2.06
C (1,2)	-0.687	-6.69	-6.69	-5.29	-5.29	1.40	1.40
C (1,3)	-0.978	-6.70	-6.70	-4.79	-4.79	1.90	1.90
C(4)	-0.722	-6.65	-6.65	-4.06	-4.06	2.59	2.59
C(5)	-0.739	-6.63	-6.63	-4.04	-4.04	2.59	2.59
C(4)-O	0.083	-7.29	-10.09	-6.52	-6.70	0.77	3.39
C(5)-O	-1.263	-6.11	-6.11	-4.19	-4.19	1.92	1.92

Regarding table 3.4 substitutional C doping tends to shift the CB edges below the H^+/H_2 reaction potential making hydrogen generation unfavourable. Same is true for the metastable magnetic C(4)-O doping configuration. In that case the spin down gap enhances and shifts into the UV region. The band gap of the C(1,2) doping configuration is 1.40 eV for both the spin up and spin down gap and hence, absorbs in the infrared region. Since a minimum band gap of 1.32 eV is necessary for the water splitting reaction regarding only its band gap width the photocatalytic properties should be enhanced compared to stoichiometric TiO_2. Figure 3.10(a) however shows that the C(1,2) substitution case possesses mid band gap states that, as derived by SRH, lead to an enhanced electron-hole recombination rate and thus to a reduced photocatalytic performance. Due to that its band gap values given in table 3.4 are highlighted in orange even though its absolute band gap values would fulfill the requirements for hydrogen generation. Regarding the C(5)-O configuration the band edges and band gaps meet the requirements for water splitting. Taking a look at the respective DOS given in figure 3.14, however, exhibits the presence of mid band gap states. Considering all that only the metastable interstitial doping configurations C(4) and C(5) meet all criteria and show enhanced photocatalytic performance compared to stoichiometric TiO_2.

The VB edges of all the examined C doped configurations are below the O_2/H_2O reaction potential. Regarding this C doped TiO_2 may be used as a n-type photoanode splitting H_2O into $\frac{1}{2}O_2$ and $2H^+$ in a first step (see section 3.2). Considering the band gap widths and the location of the introduced impurity states the C(1), C(1,3), C(4) and C(5) doping configurations may be taken into account as a n-type photoanode.

Table 3.5: VB and CB edges of interstitial and substitutional N doped TiO_2. Further given are the band gap and the respective calculated core level shifts. Red coloured numbers denote band edges and band gaps unfavourable for hydrogen generation.

	core level shift	VB edge ↑	VB edge ↓	CB edge ↑	CB edge ↓	Band gap ↑	Band gap ↓
N(1)	-0.097	-7.28	-7.28	-4.07	-4.68	3.20	2.60
N (1,2)	-0.057	-7.32	-7.32	-4.87	-4.87	2.45	2.45
N (1,3)	-0.079	-7.59	-7.29	-4.44	-4.49	3.16	2.33
N(4)	-0.369	-7.00	-7.00	-3.49	-3.61	3.51	3.40
N(5)	-0.369	-7.00	-7.00	-3.49	-3.60	3.51	3.40
N(4)-O	-0.646	-7.13	-6.73	-4.24	-4.04	2.89	2.32
N(5)-O	-1.013	-6.36	-6.96	-3.12	-3.61	3.16	2.35

Table 3.5 lists the core level shifts, the VB and CB edges as well as the band gap widths of the investigated N doped TiO_2 configurations. The VB edges of all examined N doping configurations are below the O_2/H_2O reaction potential similar to the C doped cases. In contrast to C, N tends to introduce shallow acceptor states near the CB and does not exhibit mid band gap states. Due to that none of the band gap values given in table 3.5 are highlighted in orange. Substitutional doping shifts the CB edges below the H^+/H_2 reaction potential making the corresponding reaction thermodynamically unfavourable. These systems may therefore be used as n-type photoanodes. Regarding the interstitial doping configurations the metastable N(4) and N(5) configuration have proper VB and

CB edges but absorb in the UV region. The N(4)-O and N(5)-O configuration fulfill all requirements for photo-induced hydrogen generation and show the best photocatalytic properties of all investigated doping configurations.

3.3.6 Discussion

Phase Diagrams

Figure 3.15 and 3.16 show the calculated $\mu_C/\mu_{O'}$ and $\mu_N/\mu_{O'}$ phase diagrams as well as the corresponding defect formation energy $E^{form}[X]$ versus the oxygen chemical potential $\mu_{O'}$. In figure 3.15(a) μ_C vs. $\mu_{O'}$ is plotted giving the thermodynamically stable phases of carbon doped TiO_2 dependent on the chemical potentials of C and O. On the top x axis the oxygen chemical potential is converted into equivalent oxygen pressure at a fixed temperature (T=1000 K). A detailed discussion on the used formula and values converting the oxygen chemical potential into equivalent oxygen pressure at a fixed temperature is given by Reuter and Sheffler [131].

Highlighted in color are the thermodynamically different phases for the single carbon substitutional case C(1). The phase boundaries for the multiple substitutional cases C(1,2) and C(1,3) are indicated by grey and black lines, respectively. Comparing these three phase boundaries shows that they are almost identical over a large range of $\mu_{O'}$ and only differ for very small chemical potentials of oxygen. For a large range of $\mu_{O'}$ and μ_C the pure undoped TiO_2 is the thermodynamically preferred phase (Figure 3.15(a)). Only for very small oxygen chemical potentials, i.e. an oxygen poor phase, the substitution of oxygen by carbon becomes favourable. Interstitial doping of rutile is energetically practicable only for higher carbon chemical potentials together with an oxygen rich environment. Different values of μ_C correspond to different reservoirs of carbon atoms. $\mu_C = \frac{1}{2}\mu_{C_{Diamond}}$=-10.55 eV corresponds to a reservoir of C in Diamond and $\mu_C = \mu_{CO_2} - \mu_{O2}$=-15.17 eV to C in CO_2. That indicates that for interstitial carbon doping using CO_2 as a C reservoir only the substitutional and the pristine crystal phases are stable configurations. Figure 3.15(b) shows the intersection points of the defect formation energy for the different doping configurations C(1), C(1,2), C(1,3). As a reference for the carbon chemical potential Diamond was chosen as a reservoir. The grey line is the interstitial carbon doped case C(5) which has a constant defect energy and does not vary with the oxygen chemical potential. Only for $\mu_{O'}$ about ≤ -4.5 eV the substitutional phases become thermodynamically more stable. Since all intersection points for the different doping configurations are located close to each other at extremely low oxygen pressure, sole thermodynamical reasoning would only allow for interstitial doping.

Figure 3.16(a) shows the μ_N over $\mu_{O'}$ phase diagram. In contrast to figure 3.15(a) the thermodynamically stable area of pure TiO_2 is smaller than in the carbon case. Thus, looking at the corresponding oxygen pressure and at the nitrogen chemical potential, all three doping configurations become feasible. Nitrogen atoms taken out of a NO_2 reservoir correspond to a chemical potential of $\mu_N = \mu_{NO_2} - \mu_{O2}$=-11.36 eV and a N_2 reservoir leads to a nitrogen chemical potential of $\mu_N = \frac{1}{2}\mu_{N_2}$=-10.249 eV. Again, as in the CO_2 case, NO_2 would only allow for a stable substitutional and pure phase at varying oxygen chemical potential. Figure 3.16(b) shows the intersection of the interstitial and substitutional doped defect formation energy lines, where N_2 is assumed as the nitrogen reservoir. In contrast to the carbon case, for nitrogen doping the intersection point is in a region of realistic oxygen pressures, which may allow for both substitutional and interstitial doping.

Band gap structure of C and N doped TiO_2

Nitrogen doped TiO_2

Doping the TiO_2 rutile bulk structure with nitrogen atoms does not lead to the creation of impurity states at the mid-band energy level (E_{MB} - defined as half of the energy difference of the top energy level of the VB and the bottom energy level of the CB). In the cases studied here, the dopant levels created inside the band gap are mostly located in the lower or top third of the band gap. Hence, the lifetime of the charged carriers is reduced but does not reach its minimum like for the case of impurity states at E_{MB}. Comparing the different nitrogen doped systems, one sees that the spin up gap remains almost unchanged, showing a maximum reduction of 0.08 eV. The spin down gap on the other hand shows a minimal reduction of up to 0.91 eV. For the case of single nitrogen doping there is a negligible small narrowing of the spin up gap by 0.04 eV. The spin down gap is reduced by a dopant state in the upper third of the gap by 0.64 eV. For the case of two nitrogen impurities the spin down gap again is reduced by 0.79 eV for the impurity atoms located at (1) and (2) and by 0.91 eV at (1) and (3). For the first case the spin up gap again is reduced by 0.79 eV and for the latter one narrowed by 0.08 eV. In both systems there is, like in the case of single nitrogen doping, an impurity level introduced in the upper third of the band gap near the CB. Regarding the unstable interstitial state we see a blueshift ,since both gaps are widened. The spin up gap by 0.27 eV and the spin down gap by 0.16 eV. For the case of the NO bond like formation the band gap narrowing for the spin up state again is inconsiderably with a reduction of 0.08 eV. The spin down gap is reduced by 0.89 eV. Impurity states are introduced in the upper and lower third of the band gap. In total nitrogen doped TiO_2 causes a redshift in the absorption and introduces band gap states that do not cause the recombination

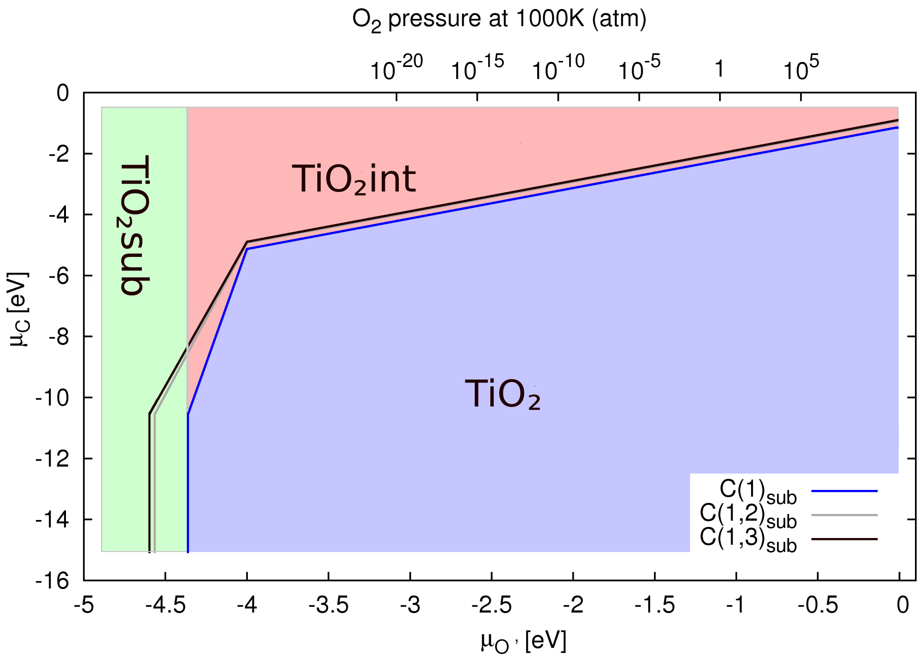

(a) Phase diagram $\mu_C/\mu_{O'}$

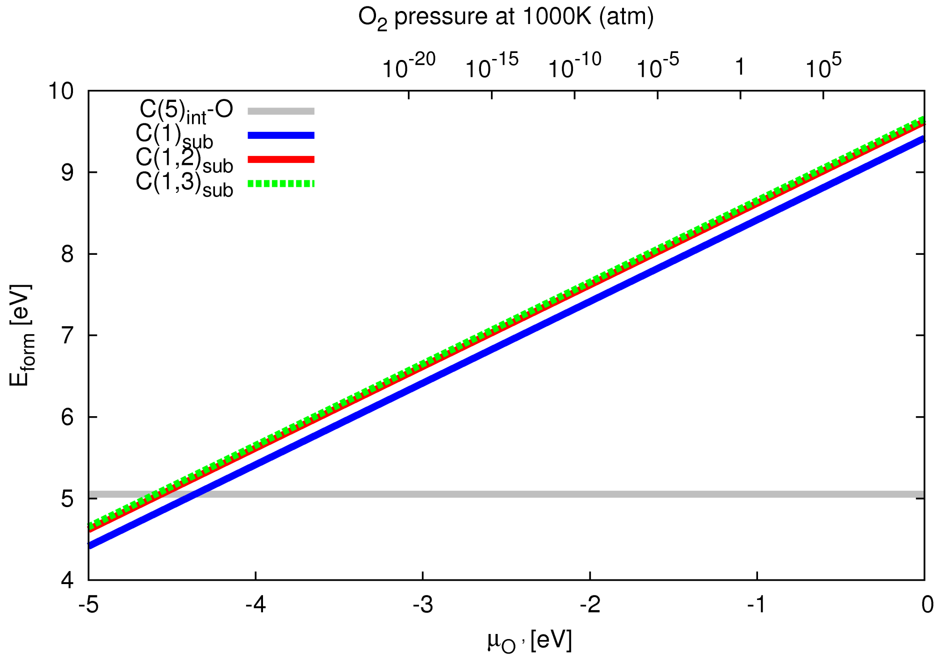

(b) C-doped $E^f/\mu_{O'}$

Figure 3.15: (a): phase diagram as a function of the chemical potentials $\mu_{O'}$ and μ_C; (b): formation energie $E^{form}[X]$ as a function of the oxygen chemical potential $\mu_{O'}$.

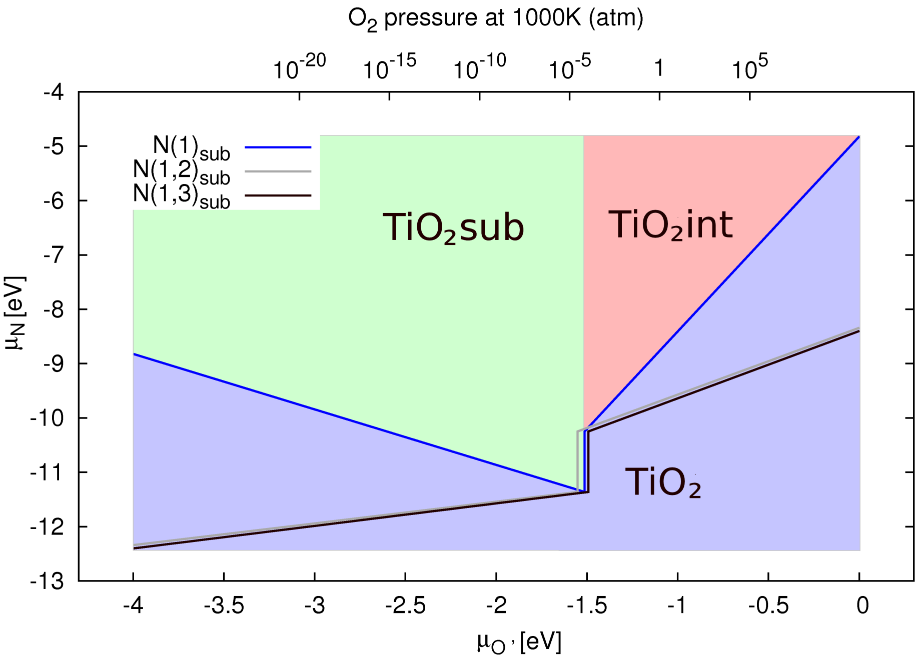

(a) Phase diagram $\mu_N/\mu_{O'}$

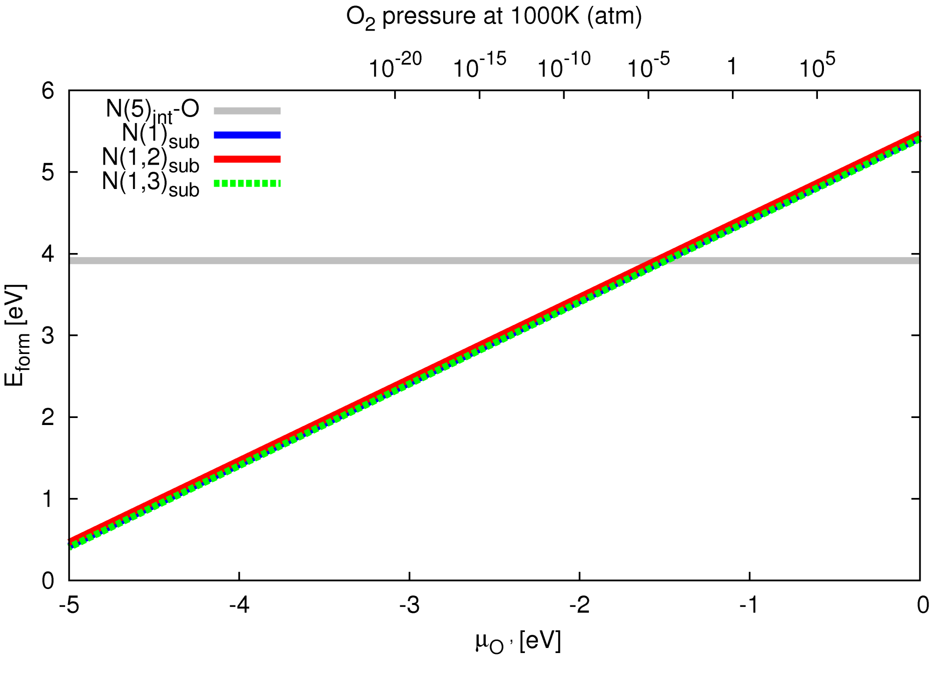

(b) N-doped $E^f/\mu_{O'}$

Figure 3.16: (a): phase diagrams as a function of the chemical potentials $\mu_{O'}$ and μ_N; (b): formation energie $E^{form}[X]$ as a function of the oxygen chemical potential $\mu_{O'}$.

rate to maximize and therefore conserve a reasonable photocatalytic efficiency. The only case where a blueshift could be detected was in the unstable case of interstitial doping for nitrogen at the positions (4) and (5) without the formation of NO dimers. Hence, there have to be other reasons leading to the blueshift observations in N-doped rutile crystals.

Carbon doped TiO_2

Doping with carbon always leads to a significant redshift but introduces mid-band gap levels at E_{MB}, thus maximizing the recombination rate of the electron-hole pairs causing minimal photocatalytic efficiency. For the case of single carbon doping the spin up band reduces by 1.04 eV and the spin down gap by 1.18 eV. New states are created inside the band gap but not in the region of E_{MB}. For the case of two carbon dopants at the positions (1) and (2) mid-band gaps are created and the gaps for both spin directions are reduced to 1.40 eV which is beyond the visible spectrum and rather unfavourably for photocatalysis. Carbon at the substitutional positions (1) and (3) in contrast shows a desirable behaviour with no impurity states in the region of E_{MB} and a band gap of 1.90 for both spin states. Carbon on the interstitial position (4) and (5) is similar to the latter case, there are no states in the mid-band gap and a gap reduction to 2.59 eV. In the case of the CO dimer there are again states at the energy level E_{MB}, making the system unattractive for photocatalytic application even with a putative band gap of 1.92 eV. In summary there are only two favourable configurations of carbon in the rutile TiO_2 lattice, the single carbon impurity and the one with the carbon impurities at positions (1) and (3).

When we replace oxygen by C/N both impurities become magnetic. For two impurities on oxygen sites we find an antiparallel orientation of the magnetic moments to be favoured, however, the low energy gain due to the formation of magnetic order suggests that the ordering temperatures will be rather low. When C/N is placed on an interstitial site, C remains nonmagnetic while N always shows a magnetic moment of $1\mu_B$. Once the CO and NO dimers are formed, nitrogen remains with $1\mu_B$ while carbon is nonmagnetic [138–142].

3.3.7 Conclusion

The magnetic structure of carbon and nitrogen doped rutile TiO_2 was investigated for different doping configurations and concentrations. Carbon shows to induce a magnetic moment of $2\mu_B$ per unit cell for the substitutional doping case and a nonmagnetic solution for the interstitial doping configuration where a CO dimer is formed. For both configurations the band gap is reduced, whereas for the CO dimer case mid-band states are created which could lead to a reduction in the photocatalytic performance. Two substitutional

C impurities close to each other show AFM coupling and for the case of maximum distance paramagnetic behaviour. Relating to the phase diagram carbon is most stable as an interstitial impurity for low chemical potentials.

The VB edges of all the examined C doped configurations are below the O_2/H_2O reaction potential. Hence, C doped TiO_2 may be used as a n-type photoanode. Considering the band gap widths and the location of the introduced impurity states the C(1), C(1,3), C(4) and C(5) doping configurations may be used as n-type photoanodes. Only the metastable C(4/5) interstitial doping configurations have enhanced photocatalytic properties as a single phase material compared to stoichiometric TiO_2.

Nitrogen induces a magnetic moment of $1\mu_B$ for both the substitutional and the interstitial doping configuration. For the latter a NO dimer is formed like in the interstitial carbon doping case. Nitrogen doping reduces the band gap of rutile TiO_2 as well, whereas no mid-band gap state is induced as for the carbon interstitial doping case.

The VB edges of all investigated N doping configurations are below the O_2/H_2O reaction potential as well. Substitutional doping gives CB edges that are below the H^+/H_2 reaction potential. These systems may therefore be used as n-type photoanodes. For the interstitial doping configurations the metastable N(4) and N(5) configuration have proper VB and CB edges but absorb in the UV region. The N(4)-O and N(5)-O configuration fulfill all requirements for photo-induced hydrogen generation and show the best photocatalytic properties of all investigated doping configurations. N doping should therefore lead to an increase in photocatalytic efficiency. This, however, has been shown by several experiments [138, 141, 142].

Looking at the calculated phase diagram, there is also a wide range of partial oxygen pressures where substitutional N doping shows to be energetically preferable, in contrast to carbon. Nitrogen therefore may allow for both substitutional and interstitial doping, whereas C only allows for interstitial doping assuming realistic oxygen pressures. The magnetic coupling of two adjacent N atoms shows to be AFM and like in the carbon case and for two N atoms with greater distance to be paramagnetic. Paramagnetic behaviour for the N doping case, however, has already been observed in experiment [138] and can be reproduced by our calculations. Recently experimental groups [138–140] which investigated N-doped rutile single crystals, indeed measured ferromagnetic behaviour but cannot exclude the role of vacancies, created by the N ion implantation technique as a possible sources of ferromagnetism.

3.3.8 Outlook

The big number of studies that have been performed on rutile TiO_2 use various different approaches and calculation schemes. They try to predict, understand and tailor the electronic properties of TiO_2 to better fit and improve its performance for specific applications. Oxygen vacancies, e.g. have attracted great attention and are known to influence the electronic and magnetic properties of a system. Introducing vacancies creates unbound electrons that are either free or spatially trapped at the vacancy site depending on the surrounding potential landscape. One differentiates between neutral and charged vacancies [127]. Replacing O with another *p* element of a different valence electron configuration also introduces electrons or holes, which may lead e.g. to magnetism as described and discussed in the former sections. A lot of effort is made trying to calculate and engineer the band gap edges of two or more compounds that either can be mixed or physically attached to each other. Assuming matching band gap edges this can lead to an enhanced photocatalytic performance [143, 144]. Another interesting topic are nano structures and their shape dependent properties. In that sense, calculations have been performed on pure and doped TiO_2 nano-rods [145] and nano particles [146]. Further, there are calculations dealing with TiO_2 particles in an aqueous solution. They try to simulate the effect of saturated dangling bonds on the band edge potentials [147, 148]. The above mentioned investigations show how versatile and complex simulations on TiO_2 can be.

Assuming a "realistic" simulation on an atomic scale a surface and the presence of Ti and O vacancies have to be considered. Further impurity atoms located at the surface and/or in the bulk as well as geometric distortions have to be included. In the sense of photocatalytic water splitting most importantly the compound's interaction with its surrounding (air, vacuum, aqueous solution,...) has to be reconstructed. Trying to computationally simulate such a realistic system that comprises all these aspects would at least include some hundreds if not thousands of atoms. A considerable size that requires a lot of computational time and power to gain reliable results. Hence, one passes over to decompose the realistic system into sub-configurations, investigating e.g oxygen vacancies or Ti vacancies at a surface.

We focussed on substitutional and interstitial doping and ignored surfaces as well as all kinds of vacancies. Even though this is an idealization of a realistic system the performed calculations agree with experimental studies. That proofs that carefully designed simple models are still capable of describing more complex realistic systems.

Chapter 4

$GaFeO_3$

4.1 Magnetoelectric Multiferroic Gallium Iron Oxide

Gallium Iron Oxide (GFO) is a multiferroic material and combines two ferroic states in a single-phase. It is antiferromagnetic and ferroelectric in its ground state and exhibits a coupling of both phases. Hence, applying a magnetic or electric field changes the polarization or the magnetization of the material, respectively. This behaviour is described by the so called magnetoelectric effect.

Multiferroic and magnetoelectric structures like $GaFeO_3$ (GFO) are promising materials for a broad field of applications and have attracted great attention during the last years [149–151]. Multifunctionalities combined in a single phase are very attractive and of high interest for various applications and further development of sensors (e.g. for the sensitive detection of magnetic fields), spintronics, tunable microwave filters and data storage/switching devices including the concept of the magneto-electric random access memory device [152]. Additionally recent studies report photocatalytic properties for stoichiometric and anion doped GFO. However, regarding all these promising applications there is only a small number of materials exhibiting both multiferroic and magnetoelectric properties at the same time.

Motivated by that we investigated stoichiometric GFO, including the effect of cation/anion doping and strain. We thereby focussed on the magnetic and photocatalytic properties.

4.2 The Magnetoelectric Effect

The magnetoelectric (ME) effect describes the coupling between magnetic and electric fields in matter. A simple phenomenological approach to the ME effect is given by the Landau-Theory [153]. It involves the expansion of the free energy of the electric $\vec{E}$ and the magnetic $\vec{H}$ field yielding

$$\begin{aligned} F(\vec{E},\vec{H}) = F_0 - P_i^S E_i - M_i^S H_i - \frac{1}{2}\varepsilon_0\varepsilon_{ij}E_iE_j - \frac{1}{2}\mu_0\mu_{ij}H_iH_j \\ - \alpha_{ij}E_iH_j - \frac{1}{2}\beta_{ijk}E_iH_jH_k - \frac{1}{2}\gamma_{ijk}H_iE_jE_k - ... \quad , \end{aligned} \tag{4.1}$$

where i,j and k denote spatial indices. $\vec{P}^S$ and $\vec{M}^S$ describe the spontaneous polarization, whereas the tensors $\hat{\varepsilon}$ and $\hat{\mu}$ correspond to the electric and magnetic susceptibilities. The tensor $\hat{\alpha}$ accounts for the ME effect and describes the induction of polarization by a magnetic field or of magnetization by an electric field. The first term in equation 4.1 is part of the free energy not associated with electromagnetism. Terms two to four describe the spontaneous polarization and magnetization as well as the usual polarization and magnetization by electric and magnetic fields, respectively. It includes the relative permittivity ε_{ij} and permeability μ_{ij}. The sixth term describes the lowest order of magnetoelectric coupling introducing the α_{ij} tensor. The following terms represent higher order magnetoelectric coupling coefficients parametrized by the $\hat{\beta}$ and $\hat{\gamma}$ tensors. The vast majority of research is performed on the linear ME effect. Hence, it is generally acceptable to omit the prefix linear and simply refer to the non quadratic linear "ME effect".

For given electric or magnetic fields, the polarization and the magnetization are obtained by minimizing the free energy given in equation 4.1. Derivation leads to the polarization

$$P_i(\vec{E},\vec{H}) = -\frac{\partial F}{\partial E_i} = P_i^S + \varepsilon_0\varepsilon_{ij}E_j + \alpha_{ij}H_j + \frac{1}{2}\beta_{ijk}H_jH_k + \gamma_{ijk}H_iE_j - ... \quad , \tag{4.2}$$

and to the magnetization

$$M_i(\vec{E},\vec{H}) = -\frac{\partial F}{\partial H_i} = M_i^S + \mu_0\mu_{ij}H_j + \alpha_{ij}E_j + \beta_{ijk}E_iH_j + \frac{1}{2}\gamma_{ijk}E_jE_k - ... \quad . \tag{4.3}$$

The ME response, however, is limited by the relation [154]

$$\alpha_{ii}^2 \leq \varepsilon_0\varepsilon_{ii}\mu_0\mu_{ii} \quad . \tag{4.4}$$

Equation 4.4 is obtained from equation 4.1 forcing the sum of terms three to five to be greater than zero ignoring higher-order coupling terms. Since ferroelectric and ferromagnetic materials have particularly large ε and μ strong magnetoelectric coupling is expected in ferroelectric ferromagnetic multiferroics [18, 155, 156]. No such restriction applies to higher-order couplings including the $\hat{\beta}$ and $\hat{\gamma}$ tensor. In some materials $\beta_{ijk}H_jH_k$ dominates the linear term $\hat{\alpha}H_j$.This was first shown for piezoelectric paramagnet $NiSO_4{\cdot}6H_2O$ at low temperatures [157]. In the case of $BiFeO_3$ we have a commensurate ferroelectric [158] and an incommensurate antiferromagnet at room temperature [159]. The spins are not collinear but arranged in a long-wavelength spiral of about 62 nm [159]. The linear magnetoelectric coefficient averages to zero whereas only the quadratic term is observed [160]. The spin spiral can be unwound applying either a large magnetic field of about 20 Tesla [161], incorporating chemical substitutions [162] or by epitaxial strain on thin films [163]. The linear coefficient may be recovered in that particular cases [14].

There are a lot of ferroelectric and ferromagnetic materials, respectively. Materials exhibiting both properties at the same time, however, are rare. One reason for the scarcity of multiferroics can be ascribed to symmetry. In a ferroelectric ferromagnetic material both spatial and time reversal symmetry have to be broken. Out of the 122 magnetic point groups (Shubnikov magnetic point groups) there are only 13 that allow for both a spontaneous magnetization and polarization. Still, many of the materials that belong to one of these 13 groups are not multiferroic. A simple reason of the rarity of both ferroelectric ferromagnetic materials is that ferromagnets tend to be metals and electric polarization requires an insulating state. The magnetoelectric coefficients $\hat{\alpha}$, $\hat{\beta}$ and $\hat{\gamma}$ possess the symmetry of the material so that $\hat{\alpha}$ can only be nonzero for materials that do not have a center of symmetry and are time-asymmetric [14]. Both are requirements for the presence of polarization and magnetism. The other way round information on the magnetic point group symmetry of a material can be extracted from experiments determining the magnetoelectric coefficients. This can be done by electrical and optical experiments, recording the magnetic response to an applied electric field or the electric response to an applied magnetic field.

Dzyaloshinskii was the first to show violation of time-reversal symmetry explicitly for a particular system, namely antiferromagnetic Cr_2O_3 [164]. Shortly afterwards there was the first experimental confirmation of an electric field induced magnetization by Astrov [165, 166] and the first proof of a magnetic field induced polarization [167, 168]. The experiments on Cr_2O_3 constituted a breakthrough in the research of ME materials. The ME effect in solids was first theoretically predicted by Laudau and Lifshitz (1980) [153].

Referring to Cr_2O_3 technical applications were not feasible due to its small magnitude of induced polarization and magnetization. The ME effect in Cr_2O_3 was found to be α_{zz} =4.13 psm^{-1} [169]. Assuming an electric field of about 10^6 Vcm^{-1} this would correspond to a magnetization obtained after reversing only five of every 10^6 spins in an AFM lattice [155].

Hence, the research community was very keen on finding materials with higher ME coefficients. Prominent single-phase ME perovskite oxides are $BiMnO_3$, $BiFeO_3$ and $Pb(Fe_{0.5}Nb_{0.5})O_3$ among others. For a detailed list on single phase ME materials see [170]. The largest ME coefficients have been observed for $LiCoPO_4$ (α_{yx} =30.6 psm^{-1} [171]), YIG (yttrium iron garnet) films ($\sim$ 30 psm^{-1} [172]) and $TbPO_4$ (α_{aa} =36.7 psm^{-1} [173])

[155]. The ME voltage coefficient $dE/dH{=}\varepsilon_0\varepsilon\alpha$ is typically specified in units of $\mathrm{mVcm^{-1}Oe^{-1}}$ which corresponds to $\alpha{=}\mathrm{psm^{-1}}$.

To overcome the above-mentioned issue of the incompatibility of ferroelectricity and magnetism in a single phase material the conceptual simplest approach is the fabrication of multi-phase materials or thin film heterostructures. An example for such a multi-phase material is the combination of $BaTiO_3$ and $CoFe_2O_4$. First is ferroelectric and second magnetostrictive [174]. In that particular case the ME coupling is mediated directly via strain.

4.2.1 Microscopic Models

Beside group theory considerations of the symmetry-related criteria for the presence of the magnetoelectric effect, it is important to understand its microscopic origin. Gehring [175] gives a detailed discussion on the different microscopic origins of the ME effect and its behaviour with temperature trying to understand the temperature dependence of the magnetoelectric tensor. The relevant interactions are listed below. i and j denote the lattice sites and $\vec{r}_{ij}$ their distance. α, $\beta \in \{x, y, z\}$ are the ME tensors. $\vec{m}$ and $\vec{B}$ are the magnetic dipole moment and the applied magnetic field, respectively.

Single-ion Anisotropy $\propto (S_i^\alpha)^2$: Spin-orbit coupling is responsible for single-ion magnetocrystalline anisotropies. There is a preferential axis for the orientation of the spin, the so called easy axis. Applying an external field moves the ions with respect to their ligands and change the local symmetry. This can effect the strength of the anisotropy and the direction of the easy axis. In the case of single-ion anisotropy spins of a magnetically ordered compound are coupled to an external field.

Symmetric superexchange $\propto r_{ij}(S_i^\alpha S_j^\beta + S_i^\beta S_j^\alpha)$: The interactions of spins of transition metals is mainly provided by the superexchange and mediated by an intermediary atom (mostly oxygen). This interaction depends on the distance and the enclosed angle between the magnetic and ligand atoms. Applying an electric field shifts the inversely charged transition metal cations and ligand anions against each other and changes both electron wave functions. This again modifies the orbital overlap and thus the exchange integrals and energies altering the superexchange. Magnetic properties may therefore be controlled through an external magnetic field.

Asymmetryic superexchange $\propto r_{ij}(S_i^\alpha S_j^\beta - S_i^\beta S_j^\alpha)$: The Dzyaloshinskii-Moriya exchange interaction [176, 177] successfully describes a spin canted state. The spins are arranged in a wave like geometry propagating along a certain crystal direction with a specific wave length. Although the asymmetric superexchange is smaller than that of the symmetric exchange, both interactions are modified by the same absolute values by the aforementioned mechanisms.

Dipolar interactions $\propto \vec{m}_i\vec{m}_j/r_{ij}^3 - 3(\vec{m}_i r_{ij})(\vec{m}_j r_{ij})$: A nonuniform movement caused e.g. by a piezoelectric distortion of the magnetic ions inside a compound may change the dipolar fields and hence affect the magnetic anisotropy.

Zeeman energy $\propto \vec{B}^{\alpha} g_i^{\alpha\beta} S_i^{\beta}$: An electric field can affect and change the $\hat{g}$ value in two different ways. Either by inducing local distortions changing the crystal field or by modifying the wave function. Assuming the electrons to be shifted out of their equilibrium position around the core by an electric field an electronic polarization can be induced and modifies the wave function. This shift may change the orbital contribution to the magnetic moment and therefore affect the $\hat{g}$ factor [155, 175].

Figure 4.1 shows the emgergence of a ME net magnetization in an (in its ground state) intrinsically compensated antiferromagnet. It becomes subjected to an electric field which is parallel to its magnetization axis. The exaggerated movement of the Cr_{3+} ions in an electric field breaks the equivalence of the ferromagnetic Cr^{3+} sublattices and consequently introduces a ME magnetization. This appears due to a combination of the micoscopic models described above which are discussed in [178].

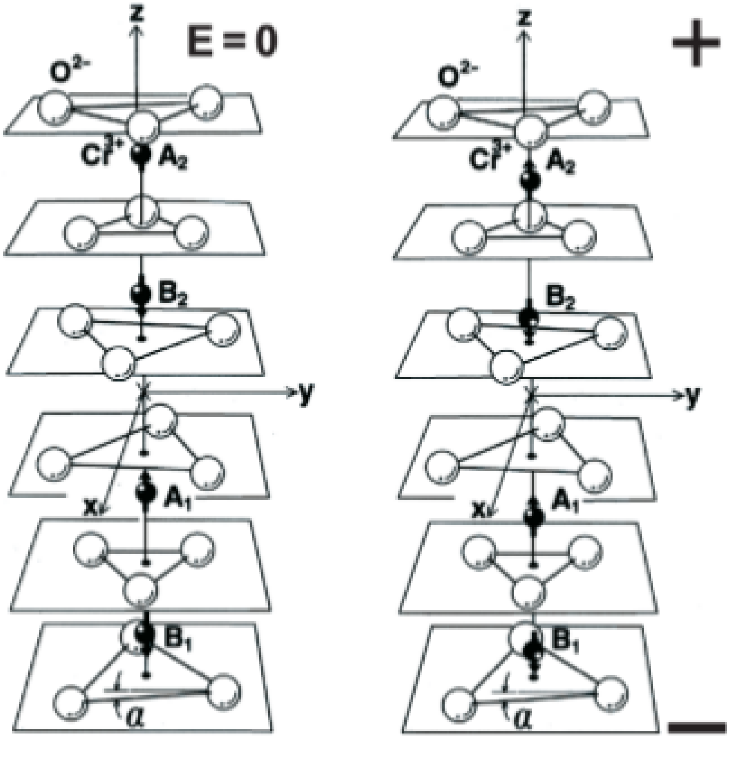

Figure 4.1: An applied electric field shifts the magnetic Cr^{3+} $A_{1,2}$ and $B_{1,2}$ ions away from its equilibrium state and introduces a ME magnetization. This breaks the equivalence of the ferromagnetic sublattices. Picture taken from [155].

4.3 Multiferroicity

Regarding equation 4.4 the only way of achieving a noticeable ME response in a single phase material is the presence of a strong internal electromagnetic field with a large dielectric or magnetic susceptibility. The largest dielectric coefficients and magnetic permeabilities are found in ferroelectrics and ferromagnets. Hence, we would assume ferromagnetic ferroelectric materials as prime candidates for displaying giant ME effects. Such a material would be called a multiferroic. According to the definition of Schmid [179] crystals are multiferroic if they exhibit at least two kinds of ferroic orders in a single phase. A ferroic order induces a spontaneous order that forms switchable domains. These domains can be described by an order parameter that couple to a suitable external field. In ferromagnets, e.g. the magnetization (order parameter) forms domains that can be switched by an applied magnetic field. Plotting the varying magnetic field strength as a function of the order parameter (magnetization) results in a hystersis loop that is characteristic for the respective compound. Domains can be formed in the case of ferroelectric, ferromagnetic, ferrotoroidic or ferroelastic ordering. A straightforward switching of antiferroic domains is in general not possible because of macroscopic compensation, so that antiferroics are not considered at this stage. One possible approach to include and define antiferroics is on looking at them as being made of two equivalent ferroic sublattices whose arrangement leads to a macroscopic compensation [155]. Ferroic orders can be classified according to their transformation properties of their order parameter referred to time reversal and spatial inversion. The magnetic moment e.g. changes its sign under timer inversion yielding M(-t)=-M. Polarization on the other hand remains invariant under time reversal, P(-t)=P(t). Considering space inversion the magnetic moment is unchanged with M(-x)=M, whereas polarization changes its sign according to P(-x)=-P. Ferroelastic order, e.g. is invariant under both operations, whereas the order parameter of ferrotorodicity changes sign under both operations. Latter describes the alignment of toroidal moments arising from a ring like arrangement of spins [180]. Similar to ferrotorodicity a multiferroic material with both a ferromagnetic and ferroelectric order breaks both symmetries. Table 4.1 lists the spatial and time symmetry properties of the respective ferroic order.

A multiferroic material that is ferroelectric and ferromagnetic has by definition a spontaneous magnetization and a spontaneous electric polarization. Both are switchable by a magnetic and electric field, respectively. Assuming a sufficient electromagnetic coupling it becomes possible to switch the spontaneous magnetization by an external electric field and to alter the spontaneous polarization by a magnetic field. However, most important to notice is that multiferroicity does not imply ME coupling and conversely ME effects can

Table 4.1: Spatial inversion and time reversal symmetry in ferroics. The considered multiferroic phase is ferromagnetic and ferroelectric.

Characteristic symmetry	Spatial inversion	Time reversal
Ferroelastic	Yes	Yes
Ferroelectric	No	Yes
Ferromagnetic	Yes	No
Ferrotoroidic	No	No
Multiferroic	No	No

occur in a much wider class of materials. ME materials are simultaneously magnetically and electrically polarizable without exhibiting both a spontaneous magnetic and electric ordering.

Figure 4.2 shows the relationship between multiferroic and magnetoelectric materials. As indicated by the overlapping spheres multiferroicity (red hatching) and magnetoelectricity (blue hatching) are not mutually dependent on each other. Ferromagnets form a subset of magnetically polarizable materials including paramagnets and antiferromagnets. Ferroelectrics include electrically polarizable materials as paraelectrics and antiferroelectrics. The ME coupling (blue hatching) is an independent phenomenon that can but needs not to arise in materials that are both magnetically and electrically polarizable [14].

The lower part of figure 4.2 shows the time reversal and spatial inversion symmetry in different ferroics. Figure 4.2 (a) shows the time reversal and spatial inversion symmetry of the magnetic oder parameter in a ferromagnetic material. The magnetic order parameter is, as mentioned before, variant for time reversal but invariant under spatial inversion. (b) gives the time and spatial symmetry of a ferroelectric. The ferroelectric parameter is invariant under time but variant under spatial inversion. (c) finally shows the time reversal and spatial inversion symmetry of a multiferroic material combining both order parameters in a single phase. As listed in table 4.1, both symmetries are broken in that particular case [14].

The first multiferroic material was grown in 1958. Magnetically active $3d$ ions were incorporated and substituted ions with a noble gas shell in ferroelectrically distorted perovskite lattices [179, 181] and led to ferroelectric antiferromagnetic compositions like $PbFe_{1/2}Nb_{1/2}O_3$ and $PbFe_{1/2}Ta_{1/2}O_3$ [182]. Currently four major crystallographic types of multiferroics are known. These comprise pervoskite structures of the form ABO_3 including

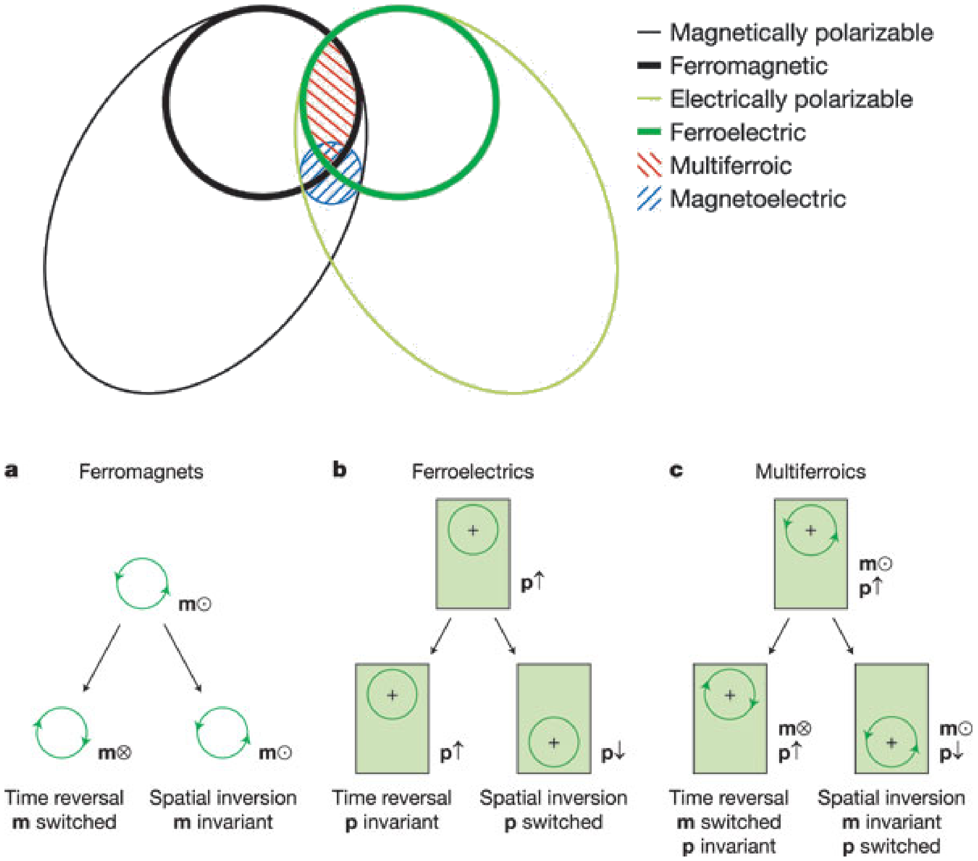

Figure 4.2: Upper part: Coupling between multiferroic and ME materials dividing the materials into magnetically and electrically polarizable materials. Lower part: Time reversal and spatial inversion symmetry in (a) a ferromagnetic material, (b) a ferroelectric material and (c) in a mulitferroic being both ferroelectric and ferromagnetic. Pictures taken from [14].

$BiFeO_3$ which is ferroelectric, ferroelastic and weakly ferromagnetic [183, 184] and shows a rhombohedrally distorted crystallographic structure. The largest and best known group of hexagonal mutiferroics is formed by the ferroelectric antiferromagnetic manganites $RMnO_3$ (R=Sc, Y, In, Ho, Er, Tm, Yb, Lu). Then there are Boracites compounds with the general formula of $M_3B_7O_{13}X$ which are ferroelastic ferroelectric antiferromagnets, accompanied by a weak ferromagnetic moment. Also $BaMF_4$ compounds are ferroelectric ferroelastic structures showing a purely antiferromagnetic or weak ferromagnetic ordering. For a more detailed discussion see [155, 185, 186]. Beside these major types a large number of multiferroics with different crystallographic structures are known.

4.4 The Superexchange Mechanism

Indirect exchange mechanisms are of great importance realizing long ranged magnetic order. These processes involve the “hopping” of electrons, virtual or real, so that they change their lattice sites with a certain probability trying to minimize the system’s total energy. The superexchange mechanism is such a process and can be described with second order perturbation theory. Since this task is not all too trivial in its extensive form we restrict ourselves on giving a short overview on the mathematical model and the Goodenough-Kanamori rules. Latter form a considerably satisfactory system of semi-empirical rules that account for the various occupation of the d levels, as indicated by ligand field theory, and the cation-ligand-cation bond geometry (angle and bond lengths). Since we try to explain the antiferromagnetic ground state of stoichiometric GFO, which originates from the superexchange mediated via the Fe-O-Fe bonds, these are of great interest.

Starting with a simple mathematical approach assuming a two dimensional lattice with a possible occupation of two electrons per site the respective model has to describe the “hopping” of electrons changing their lattice sites, their spins and the corresponding Coulomb interaction. The Hubbard model is an appropriate ansatz for such a system. Its hamiltonian has the form

$$\hat{H} = \hat{H}_t + \hat{H}_U \quad . \tag{4.5}$$

The first term describes the kinetic energy

$$\hat{H}_t = -t \sum_{\langle ij \rangle \sigma} \left(c^\dagger_{i\sigma} c_{j\sigma} + c^\dagger_{j\sigma} c_{i\sigma} \right) \quad , \tag{4.6}$$

and includes the $c_{i\sigma}$ and $c^\dagger_{i\sigma}$ operator that creates and annihilates an electron with spin σ at the lattice site i (and j), respectively. Equation 4.6 sums over the nearest neighbours i<j (represented by the angular brackets) and considers the Pauli principle by allowing only for double occupation with opposite spin. t is the so called hopping parameter and gives the kinetic energy gained by delocalization. $\hat{H}_t$ describes the virtual hopping of an electron from site i to j and back preserving the total spin. The second term

$$\hat{H}_U = U \sum_i n_{i\uparrow} n_{i\downarrow} \quad , \tag{4.7}$$

accounts for the Coulomb energy U that two electrons have to overcome to occupy the same lattice site. Operator $n_{i\sigma}$ counts the number of electrons with spin σ at site i. Figure 4.3 shows a spin resolved hopping of electrons on a two dimensional lattice. Assuming the Hubbard model an electron hopping to a vacant cell site enhances its kinetic energy by -t. Supposing that the electrons hops to a cell site not vacant but already occupied by another electron with opposite spin the Coulomb repulsion U has to be added. According to the ration of t and U the material's properties change. Figure 4.3 (a) and (b) show the limiting cases of U≪t and U≫t, respectively. Assuming U≪t the majority of the cell sites are double occupied, describing a metallic state. If U≫t it is not energetically favourable for the electrons to switch cell sites. Hence, we end up with a localized atomic like description of the spins that corresponds to a Mott-Hubbard-Insulator.

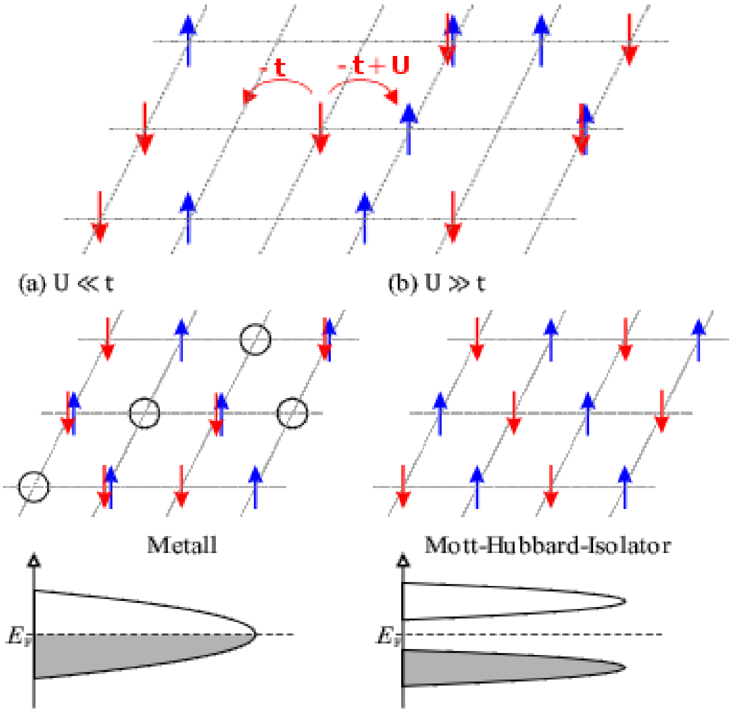

Figure 4.3: Spin resolved electrons on a two dimensional lattice grid. Upper part : Schematic sketch of the hopping paramter t and the Coulomb repulsion U. (a) and (b) show the limiting cases of U≪t and U≫t, respectively. First describes a metallic phase whereas second ends up with an insulating material. Pictures taken from [187].

The above given model describes the hopping between two neighbouring lattice sites. Dealing with transition metal oxides and the superexchange mechanism we have to consider a three body interaction. The exchange interaction is mediated via an intermediary, that referring to transition metal oxide, is an oxygen atom. Describing the superexchange mechanism we have to model the interaction between two transition metal $3d$ and a single oxygen $2p$ orbital. Accounting for such a system, considering the d and p electrons of the transition metal and oxygen atom, respectively equation 4.5 transforms to

$$\hat{H}_t = \sum_{i,j} \left\{ \epsilon_d d^\dagger_{i\sigma} d_{i\sigma} + \epsilon_p p^\dagger_{j\sigma} p_{j\sigma} - t_{pd} \left(d^\dagger_{i\sigma} p_{j\sigma} + p^\dagger_{j\sigma} d_{i\sigma} \right) \right\} + U \sum_i n_{d_i\uparrow} n_{d_i\downarrow} \quad . \tag{4.8}$$

U describes the Coulomb interaction inside the respective transition metal $3d$ orbitals. $d^\dagger_{i\sigma}$ ($d_{i\sigma}$) and $p^\dagger_{j\sigma}$ ($p_{j\sigma}$) are the electron annihilation (creation) operators of the transition metal $3d$ (d) and oxygen $2p$ (p) orbital. ϵ_d and ϵ_p are the energies of the $3d$- and $2p$ states, respectively. t_{pd} corresponds to the hopping amplitude between the transition metal $3d$ and oxygen $2p$ states. Crucial for the hopping process is the corresponding energy difference, the so called charge transfer gap $\Delta_{CT} = \epsilon_d - \epsilon_p$. We distinguish two limiting cases, namely $\Delta_{CT} \gg U$ and $\Delta_{CT} \ll U$. For the first case there is an enhanced energy gap between the oxygen p and the transition metal d states. The oxygen p states are lower in energy. The size of the band gap is in the range of U and exhibits d-d character. This corresponds to a Mott-Hubbard insulator like Cr_2O_3 and Ti_2O_3. The charge transfer happens via the oxygen atom. A transition metal d electron is transferred to the other transition metal passing the oxygen p states (see figure 4.4(a)).

For $\Delta_{CT} \ll U$ there is only a small energy difference between the oxygen p and the transition metal d states. The oxygen atoms transfers one electron to each transition metal ion. In that case a single electron is transferred to each transition metal ion, creating an isolating AFM ground state (see figure 4.4(b)) [187]. Both limiting cases lead to an AFM isolating ground state. However, they differ in their excitation spectrum and transport properties due to their varying U and Δ_{CT} values.

Regarding our calculations, GFO represents the case of $\Delta_{CT} < U$. As discussed in the following sections we report a charge transfer from the O p states to the neighbouring Fe atoms $3d$ states. The valence and conduction band edges exhibit no d-d character and the energy gap between the barycentre of the O $2p$ and Fe $3d$ states is small, supporting the before made assumption.

4.4.1 The Goodenough-Kanamori rules

The superexchange interaction in transition metal oxides is highly dependent on the overlap of the O p and transition metal d orbitals. This overlap is influenced by the relative spatial orientation of the orbitals, e.g. by the atomic distances and the enclosed angle, whereas the exchange itself is also affected by possible orbital degeneracies. Discussing the magnetic interactions can therefore become very complex.

The Goodenough-Kanamori (GK) rules were first formulated by Goodenough in 1955 [9, 188] and became mathematically underpinned by Kanamori in 1959 [10]. Before that Kramers proposed the superexchange in 1934. Investigating crystals like MnO he noticed that the Mn atoms interact with one another despite having nonmagnetic oxygen atoms between them [189]. Anderson then refind Kramers' model in 1950 [190].

The GK rules are semi-empirical rules that are quite successfully in predicting the

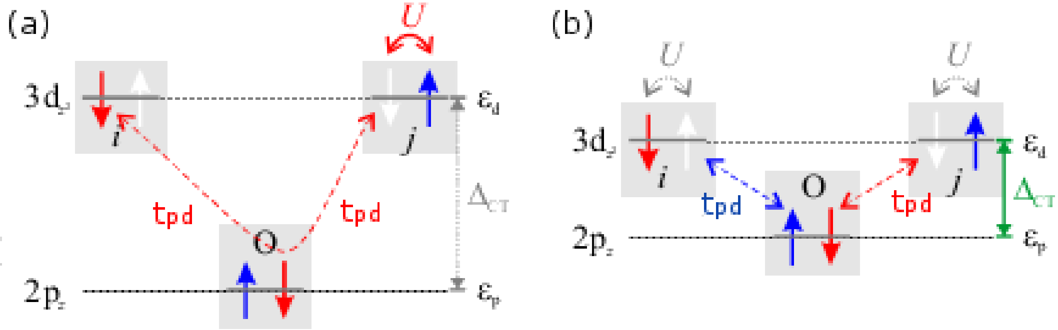

Figure 4.4: (a) shows a schematic picture of the virtual hopping process for the limiting case of $\Delta_{CT} \gg U$. The hopping parameter t_{pd} describes the hopping process of the $3d$ transition metal electron to the oxygen atom forward to the second transition metal ion. (b) shows the case of $\Delta_{CT} \ll U$. The oxygen atom transfers an electron to each transition metal atom, like in the case of GFO. White arrows indicate unoccupied electronic states. Pictures taken from [187].

magnetic interactions for a large number of systems. They take into account the occupation of the various *d* levels as described by the ligand field theory. According to these rules a 180° superxchange of two magnetic ions with partially filled *d* shells is strongly AFM. Assuming a bond angle of 90° the superexchange interaction becomes FM and much weaker, as a first guideline. A FM coupling only appears if both transition metal cations overlap with different anion (oxygen) orbitals. Figure 4.5 represents the GK rules, adapted from the formulation of Anderson [190] stating: **i) There is a strong AFM exhange if the half-filled orbitals of two cations overlap with the same empty or filled anion orbital. ii) There is a weaker FM exchange interaction if the half-filled orbitals of two cations overlap with orthogonal orbitals of the same anion [191].**

Statement i) concludes the cases shown in figure 4.5 (a)-(c). (a) represents a σ-bond formed between the oxygen *p* and the transition metal *d* orbitals (assuming a transition metal oxide), leading to a strong AFM superexchange interaction. (b) shows the formation of a much weaker π-bond yielding a reduced AFM superexchange. Case (c) sketches a cation-anion-cation bond with an enclosed angle of 90°. Since both cations overlap with the same anion orbital the superexchange is AFM but very weak though. (d) represents statement ii) and shows the orbital orientation of both cations and the anion atom leading to a FM superexchange. The two cations overlap with different orthogonal orbitals of the anion introducing a weak FM coupling.

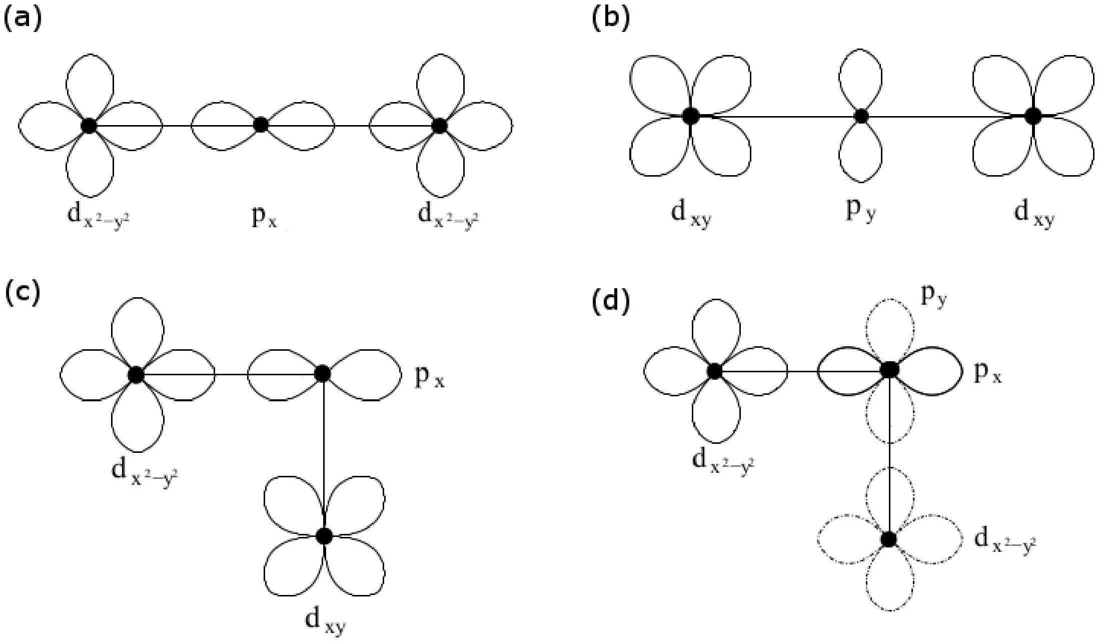

Figure 4.5: Various orbital configurations of a cation *d* - anion *p* - cation *d* bond underlining the GK rules. Configuration (a),(b) and (c) give a AFM coupling, whereas (d) yields a weak FM superexchange interaction. Picture taken from [191].

Figure 4.6 illustrates the GK rules by the example of a Mn^{3+}-O^{2-}-Mn^{3+} bond in $LaMnO_3$, sticking to the lecture notes of [187]. Sketched are the Mn d_{z^2} and $d_{x^2-y^2}$ (shaded) orbitals as well as the superexchange mediating O p_z orbital. The group of three spins beneath every Mn atom correspond to the core electrons occupying the three t_{2g} orbitals.

We distinguish three different magnetic interactions considering different occupation states of the transition metal *d* orbitals and their spatial orientation to the oxygen *p* orbital. Figure 4.6(a) and (b) represent a cation-anion-cation bond with an enclosed angle of 180°. The orbitals of the cations point into the direction of the orbitals of the anion. In case (a) the cation orbitals are half filled and empty in (b). Both configurations, however, lead to a AFM superexchange interaction concluding that a *the 180° exchange between empty or filled orbitals is strong and antiferromagnetic.*

Figure 4.6(c) shows the case of a weak FM coupling mediated along a cation-anion-cation bond with an enclosed angle of 180°. The FM coupling occurs due to not equally saturated charges. The situation on the left hand side of the Mn-O-Mn bond corresponds to case (a). Regarding the right hand side Mn-O bond the d_{z^2} orbital is empty, whereas a single electron occupies the orthogonal $d_{x^2-y^2}$ orbital. The in energy most favourable electronic configuration fulfills Hund's rule requiring the total spin to be maximum for the right hand side Mn-O bond, whereas the left O *p* electron prefers an AFM orientation to its next nearest Mn atom. Hence, one can say that the *the 180° exchange between one empty and one filled orbital is weak and ferromagnetic.*

The situation illustrated in figure 4.6(d) represents the case described in statement ii). Regarding the left Mn ion the virtual hopping process takes place between its d$_{z^2}$ orbital and the O p$_z$ orbital. The situation is different for the right Mn ion. Here the virtual hopping process occurs between the d$_{z^2}$ and the O p$_y$ orbital. The resulting interaction is weak and ferromagnetic. From an energetic point of view it is more favourable for the oxygen atom to face the Mn orbitals with electrons of equal spin. Assuming them to hop to the neighbouring Mn atoms the O atom remains with two electrons, one in the p$_y$ and the other in the p$_z$ orbital. Occupying the energetically most favourable electronic configuration the electrons need to fulfill Hund's rules and show equal spins. Concluding on can say that the *the 90° exchange between filled cation orbitals and the orthogonal orbitals of an anion is weak and ferromagnetic.*

Regarding our calculations performed on stoichiometric GFO interpreting the thereby obtained results and density of states we find a situation similar to figure 4.6(a).

4.5 Crystal structure and magnetoelectric properties of GFO

$GaFeO_3$ (GFO) has a noncentrosymmetric crystal structure and belongs to the $Pc2_1n$ (No. 33) space group. The unit cell is orthorhombic with experimentally determined lattice parameters of a= 8.735 Å, b= 9.383 Å, and c= 5.077 Å [192]. Formally, Iron and Gallium are both in a 3^+ state, whereas oxygen is in a 2^- state. The magnetic moment is located on the Fe atoms, showing a magnetic moment of about $4\mu_B$ per atom [192–194] making GFO an AFM semiconductor in its ground state structure. GFO has four cationic sublattices indexed by 1 and 2 for Ga and Fe, respectively (see figure 4.7). Fe atoms on the Fe1 and Fe2 sites couple antiferromagnetically and as well as Ga2 sites are surrounded by an oxygen octahedron. Ga1 is located inside an oxygen tetrahedron.

GFO is also known to exhibit inner cationic site disorder [192, 194–196] causing the total magnetic moment to be non zero without changing the Fe concentration. Physical properties, especially magnetism, strongly depend on the method of preparation [194, 197–199] and are correlated to the cation distribution among the four (Fe1/2 and Ga1/2) crystallographic anion sites. It further effects the transition temperature. Single crystals prepared at lower temperatures with the flux method [199] show transition temperatures of about 300 K, whereas single crystals grown by the float zone method [194] or solid state reaction [197] show a magnetic transition temperature of about 200 K. For slowly

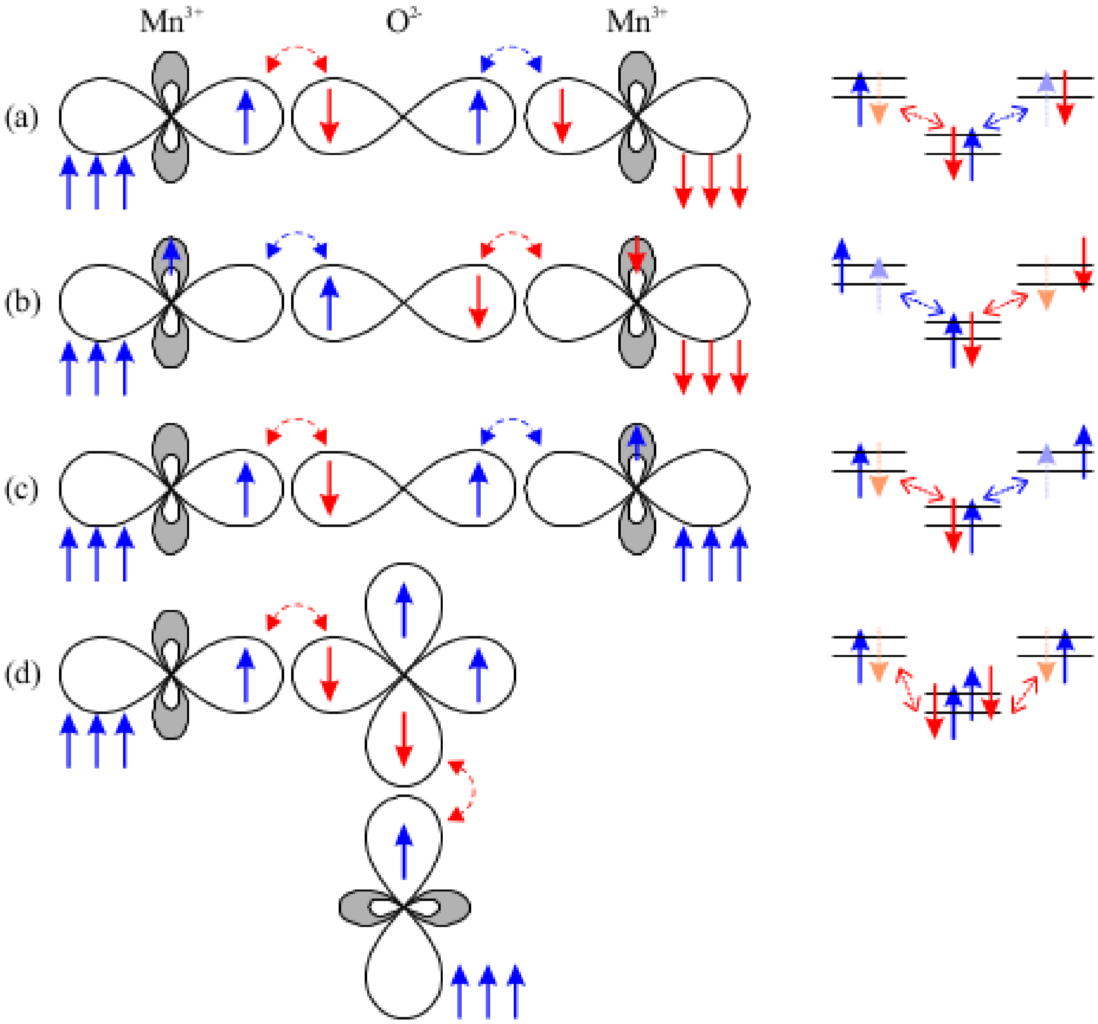

Figure 4.6: GKA rules illustrated by a Mn-O-Mn chain inside the LaMnO$_3$ structure. Sketched are the Mn d$_{x^2-y^2}$ (shaded), d$_{z^2}$ as well as the O p$_z$ orbitals. The group of three spin beneath every Mn atom corresponds to the core electrons occupying the three t$_{2g}$ orbitals (not sketched). According to occupation number and geometry the coupling becomes AFM (a,b) or FM (c,d). Picture taken from [187].

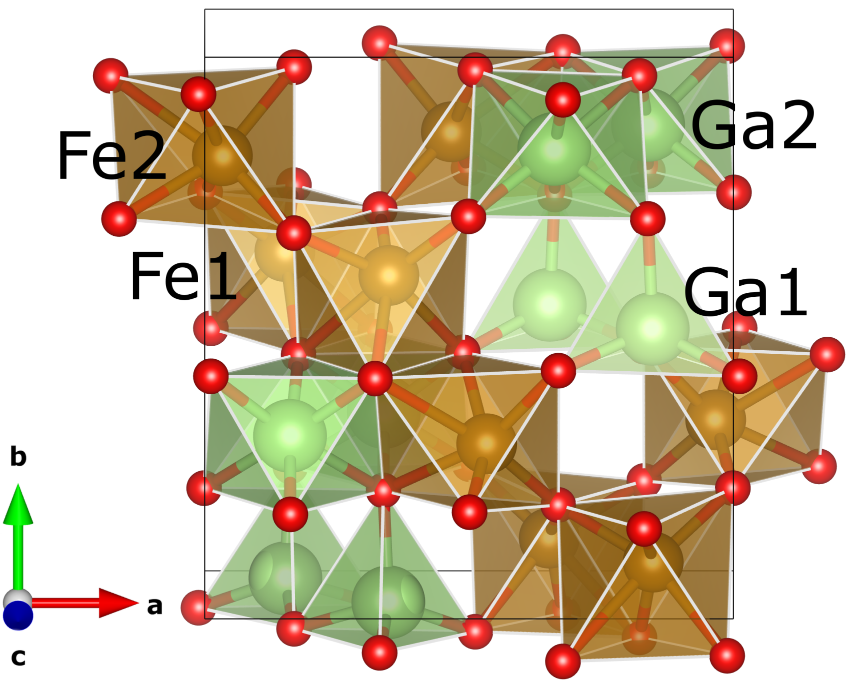

Figure 4.7: Cell structure of pure GFO. The Ga1, Ga2, Fe1 and Fe2 sublattices are indicated. This figure was created using the VESTA program [115].

cooled down samples the magnetic transition temperature was reported to be 260 K and 210 K for quenched samples prepared by the solid state reaction method [198].

Most of the multiferroic materials have magnetic ordering temperatures below room temperature as well as an AFM ground state. A common method to increase the magnetic ordering temperature and to overcome the AFM ground state is the incorporation and exchange of atoms. A great number of recent experimental and computational studies examined the effect of excess Fe mainly focussing on a doping concentration of $0.9 \leq x \leq 1.4$ in $Ga_{2-x}Fe_xO_3$. They report an increase of the ordering temperature and the total magnetic moment with increasing amount of Fe [194, 195, 197, 200, 201]. Mukherjee et al. prepared pure and x=1.4 doped $Ga_{2-x}Fe_xO_3$ bulk samples by a solid state reaction method and measured an increase of the Néel temperature from 210 K to 360 K increasing the iron content of the cell [202].

Another interesting property of GFO is its magnetocrystalline anisotropy energy (MAE). Experimental and computational studies [193, 194, 203] reveal the c axis as the magnetic easy axis and the b axis as the magnetic hard axis of the system. In addition, Reddy et al. [201] have shown a sublattice dependent MAE in GFO.

GFO shows both a spontaneous magnetization and polarization. Latter has been recently investigated in experimental and theoretical studies discussing the origin and the possible alteration of the polarization in GFO [200, 202, 204, 205]. Stoeffler compares the polar nonsymmetric ground state structure of GFO to a corresponding centrosymmetric structure and changes the Fe/Ga ratio trying to calculate and predict the spontaneous polarization yielding a value of 25 μC/cm^2 [204, 205]. The first estimations on the electric polarization in GFO was given by Arima et al. [194] giving a value of 2.5 μC/cm^2. Spontaneous polarization was also investigated by Roy et al. [206] who determined the Born effective charges from first principles calculations and obtained a value of 59 μC/cm^2.

Mukherjee et al. [202] report that increasing the iron content in GFO does not vary the distortion parameter enough to have any significant influence on the polarization. It remains almost unchanged. The polarization values calculated from experimentally determined crystallographic positions are -25.8 μC/cm^2 and -24.5 μC/cm^2 at room temperature for GFO and GFO x=1.4, respectively [202]. Similar was observed from Mishra et al. [207]. These results indicate that while the magnetic properties are enhanced increasing the iron content the ferroelectric properties are only slightly modified by doping.

The polarization in GFO points into the *b* direction. There are two main assumptions on the origin of the spontaneous polarization. Abrahams et al. [208] proposed that the piezoelectric effect primarily originates from the Ga1 tetrahedra and the Ga1-O4 bonds which are almost parallel to the *b* axis. Applying pressure along this direction may compress these particular bonds and induce a dipole which could explain the piezoelectricity observed by Remeika et al. [197]. Abrahams et al. [208] also report a decrease in the piezoelectric effect increasing the iron content in $Ga_{2-x}Fe_xO_3$. As the iron content increases Ga2 sites are occupied distorting the Ga2 octahedra which again alters the Ga1-O4 angles. Applying pressure along the polar direction would thus tend to rotate the Ga1-O4 angle rather than compressing it, producing a smaller polarization and piezoelectric effect.

Arima et al. [194] assume that the origin of the spontaneous polarization lies within the slight displacement of the Fe1 and Fe2 atom out of the center of the respective O octahedra (see figure 4.7 and figure 4.9 (a)). This shift is about +0.26 Å for the Fe1 ions and -0.11 Å for the Fe2 sites along the *b* axis and induces a spontaneous polarization in *b* direction. Similar values were obtained in experiment by Mukherjee et al. [202] who measured a shift of about +0.25 Å and -0.13 Å for the Fe1 and Fe2 atoms, respectively at a temperature of 10 K for stoichiometric GFO and a displacement of +0.27 Å and -0.14 Å for the Fe1 and Fe2 ions in GFO x=1.4.

Arima et al. [194] and Popov et al. [209] have pointed out in previous publications that the large magnetoelectric effect in GFO should be ascribed to both the opposite displacement of the Fe1 and Fe2 ions and the antiparallel direction of their magnetic moments.

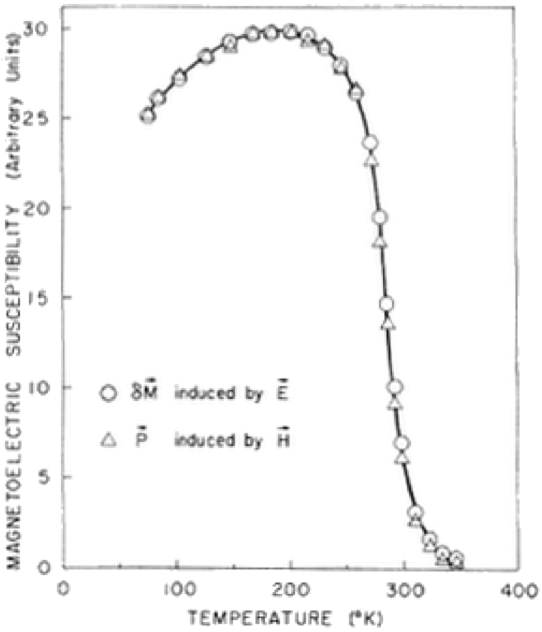

Figure 4.8: Temperature dependence of the ME susceptibility α measured under the application of an electric field $(\mathrm{ME})_E$ (circles) and a magnetic field $(\mathrm{ME})_H$ (triangles). α vanishes at high temperatures when the magnetic order disappears. Picture taken from [210].

Considering the $Pc2_1n$ magnetic space group of GFO, two components of the linear ME effect tensor α, namely α_{bc} and α_{ac}, are expected to be nonzero. Rado et al. [210] investigated the ME coupling in GFO inducing a polarization in b direction by the application of a magnetic field along the c axis and by inducing a magnetization in c direction applying an electric field along the b axis. Figure 4.8 shows the respective ME susceptibilities α measured under the application of an electric field $(\mathrm{ME})_E$ (circles) and a magnetic field $(\mathrm{ME})_H$ (triangles) as a function of the temperature (see figure 4.8). Both sets tend towards zero as the magnetic order disappears exceeding the magnetic ordering temperature. This method allows the qualitative approach of the linear ME tensor α measuring both ME effects applying a magnetic and an electric field. Rado et al. [210] explained the magnetoelectric effect as a combination of piezoelectricity and magnetostriction effects.

Popov et al. [209] demonstrated in their work no direct link between the magnetostriction and the ME coupling in GFO. Arima et al. [194] also observed an induced polarization along the b axis by a magnetic field applied along the c axis, similar to Rado. Their study estimated α_{bc} to be $2.1*10^{-11}$ s/m. In contrast to that little polarization was induced along the c axis applying a magnetic field along the b axis. The corresponding value α_{cb} was calculated to be less than 10^{-12} s/m. The measured contrast between α_{bc} and α_{cb} can be understood as follows. In the case where a magnetic field is parallel to the Fe1 and Fe2 spin moments (in c direction) the Fe1 magnetic moments decrease whereas the Fe2 magnetic moments increase. Both ions experience a magnetic field induced displacement along the b axis. The displacement of the Fe2 atom is enlarged by the modulation of its magnetic moment, whereas that of the Fe1 ion becomes reduced, conversely. Since both ions experience displacements in opposite direction, the magnetic field induced modulation of the displacement cooperatively affects the bulk polarization (see figure 4.9(b)). Applying the magnetic field in b direction, makes the Fe2 ion cant towards the $+b$ direction and the Fe1 moment rotates towards the -b direction. In that case both magnetic moments experience no modulation. Regarding figure 4.9(c) the displacement of the Fe1 and Fe2 ion are directed in the opposite c direction and consequently partially cancel out in terms of the bulk polarization according to Arima et al. [194].

4.6 Calculations on stoichiometric and cation doped GFO

Motivated by recent research and the very promising properties of GFO we focussed on a better understanding of the magnetic ground state. Gaining deeper insight in the magnetic coupling mechanism may allow to tailor the magnetic properties for a specific application.

The first part of this section presents *ab initio* DFT calculations performed on stoichiometric, cation doped and strained $GaFeO_3$. We start with a detailed discussion of the origin of the AFM superexchange in stoichiometric $GaFeO_3$ and give a molecular orbital description of the exchange mechanism derived from our calculations. In addition, we study the properties of the Fe-O-Fe bonds for different geometries to underline the angle and distance dependence of the AFM coupling as formulated in the Goodenough-Kanamori rules. We describe the AFM ground state of $GaFeO_3$ as a result of two intrinsic Fe-O-Fe chains that meander through the crystal along the c direction. The magnetocrystalline anisotropy energies are calculated for the stoichiometric phase with and without inner cationic site disorder. The presence of a sublattice dependent anisotropy is examined, as well. Furthermore we perform studies of $Ga_{2-x}Fe_xO_3$ for varying Fe concentrations x ($0.0 \leq x \leq 2.0$) where at a value of x=0.0 and x=2.0 the GFO simulation cell transforms into the isomorphic ε-Ga_2O_3 and ε-Fe_2O_3 structure. Moreover the effect of strain was studied. Incorporating dopants and applying strain to the simulation cell changes the intrinsic geometry and thus may alter the magnetic properties of GFO.

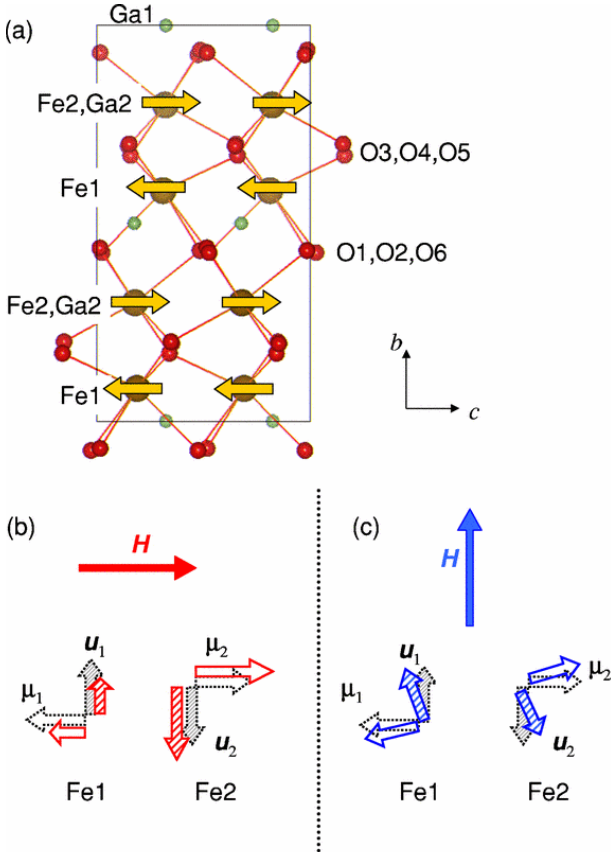

p]

Figure 4.9: Antiferromagnetic structure in GFO indicated by the as arrows highlighted magnetic moments of the Fe ions. The Fe1 and Fe2 atoms are shifted to $+b$ and -b, respectively. (b) and (c) gives a quantitive explanation of the difference of α_{bc} and α_{cb}. u_i gives the local displacement from the center of the octahedron and μ_i denotes the magnetic moment of the corresponding Fe i site (i=1,2). Highlighted in black and thin dotted lines are the ground state values and given in red and blue thick lines are the magnetic field modulated values. u_1 and u_2 are cooperative when H is parallel to the c direction (b) whereas they tend to cancel out in the case of H being parallel to the b axis (c). Picture taken from [194].

4.6.1 Computational Details and Methods

All calculations were carried out with the *Vienna Ab initio Simulation Package* (VASP) [116–121] which uses projector augmented wave (PAW) pseudopotentials [122] to describe the potential between the ions.

The simulations were conducted on an 8 formula unit cell, containing 40 atoms. To provide a reliable description of the effects of electronic correlation the calculations were performed using the GGA+U formalism [211] and HSE hybrid functionals [83, 125, 212, 213] . The GGA+U implementation uses the Dudarev formalism. The effective on site Coulomb- and exchange parameters were set to U=5 eV and J=1 eV, yielding reliable results for the magnetic moments and the cell parameters as compared to experiment.

In the case of doped and strained GFO the simulation cell was relaxed within the GGA+U approximation until all force components were smaller than 0.01 eV/Å. The atomic positions, the shape and the volume of the simulation cell was allowed to change during relaxation. Plane waves with an energy up to 550 eV were included in the basis set in order to avoid Pulay forces. The Brillouin-Zone integration was performed on a $6 \times 6 \times 6$ Γ centred k-mesh with a Gaussian smearing of 0.05 eV. Total energies were converged better than 1×10^{-6} eV.

We performed on top HSE calculations on the GGA+U relaxed cell geometries. HSE functionals are known to yield reliable results for the gap size and even more relevant the position of the impurity bands inside the gap which are of great importance regarding the photocatalytic properties [214–216] which are discussed in section 3.2. For the HSE functional the short range / long range splitting parameter was set to ω=0.7 yielding an optimal description of the experimental band gap and the crystal parameters. Accounting for the vastly increased computation time the k-space integration was performed on a smaller $4 \times 4 \times 4$ Γ centred k-mesh.

Calculating the MAE the spin orbit coupling was included to the calculations. Since spin orbit related properties are influenced by geometry we compared the MAE for simulation cells relaxed within the GGA+U or with the more realistic but computationally more elaborate HSE functional. Using the GGA+U approximation the simulation cell was relaxed until all force components were smaller than 0.001 eV/Å. Relaxing the simulation cell applying the HSE functional we again used a short range / long range splitting parameter of ω=0.7. Accounting for the vastly increased computation time the GFO simulation cell was relaxed until all force components were smaller than 0.01 eV/Å.

To quantify the AFM superexchange of the systems studied in this work we introduce the AFM coupling strength as a main parameter. In pristine GFO the AFM coupling strength is defined as the energy difference between the AFM ground state and a hypothetical ferromagnetic (FM) state. Forcing the system into a FM state breaks the ground state AFM couplings. The corresponding energy difference is taken as a reference to measure the AFM coupling strength of the respective investigated system. Doping GFO can induce a ground state with a total magnetic moment unequal to zero. The AFM coupling strength is then defined by the energy difference between the actual magnetic ground state of the doped systems and again a hypothetical ferromagnetic state.

To gain better insight in the magnetic exchange mechanism, we partly integrated the density of states of the investigated systems (see section 4.7). To some extent the thereby computed occupation numbers depend on the chosen muffin tin radii (O=1.55 Å, C=1.63 Å, N=1.40 Å, S=2.2 Å). Hence, the integrated O p and Fe d states have to be taken with caution and can not immediately be compared to oxidation numbers. Table 4.2 lists the cell parameters, band gaps and AFM coupling strengths of ε-GO, GFO and ε-FO in the GGA+U and HSE calculation scheme, respectively.

Table 4.2: Experimental and calculated cell parameters of $GaFeO_3$ (GFO), ε-Fe_2O_3 (ε-FO) and ε-Ga_2O_3 (ε-GO) in the AFM ground state. Given are the direct band gaps for each spin channel. The magnetic stabilization energy ΔE is given per 40 atom simulation cell. Indices denote ^{1} HSE, ^{2} GGA+U and ^{3} experimental values.

	GFO	ε-FO	ε-GO
Cell para. a|b|c (Å)^1	8.77 | 9.44 | 5.09	8.82 | 9.55 | 5.07	8.72 | 9.33 | 5.08
Cell para. a|b|c (Å)^2	8.82 | 9.50 | 5.14	8.85 | 9.56 | 5.12	8.81 | 9.42 | 5.13
Cell para. a|b|c (Å)^3	8.74 | 9.38 | 5.08 [192]	8.79 | 9.44 | 5.10 [217]	8.71 | 9.3 | 5.03 [218]
Band gap ↑ | ↓ (eV)^1	2.68	2.19 | 2.29	3.11
Band gap ↑ | ↓ (eV)^2	2.43	1.91 | 2.16	2.05
Band gap ↑ | ↓ (eV)^3	2.7-3.0 [219, 220]	—	—
ΔE[AFM-FM](eV)^1	-1.47	-4.94	—

4.6.2 Magnetic properties of GFO

AFM superexchange in $GaFeO_3$

The AFM ground state in GFO originates from the magnetic superexchange mediated via the Fe-O-Fe bonds. This AFM superexchange leads to a layer like magnetic ordering. The direction of the magnetic moments of the Fe atoms occupying Fe1 sites are opposite to those located at the Fe2 sites. If we apply a fully ionic picture Fe is in a 3^+ state and is left with 5 valence electrons in its $3d$ shell which would result in a magnetic moment of

$5\mu_B$. However, measurements and calculations show a local magnetic moment of about $4\mu_B$.

The calculated total density of states (DOS) in figure 4.10(a) (black line) shows the maximum of the O p states (blue line) located in the upper part of the valence band near the Fermi level (all DOS are calculated within the HSE approximation). The barycentre of the Fe $3d$ states (red line) is shifted downwards to lower energies. Both O p and Fe d states make up the majority of the total DOS near the Fermi level. Figure 4.10(b) shows the projected DOS of an Fe1-O-Fe2 complex inside the GFO simulation cell. There is a negative magnetic moment for iron on the Fe1 (red area) site and a positive magnetic moment for the iron on the Fe2 (yellow area) site. The Fe1 and Fe2 atom are antiferromagnetically coupled via an intermediate O atom (blue). The overlap of the oxygen and the iron states result in the DOS between -5 eV and the Fermi energy. The superexchange mechanism takes place in this particular energy range. Since, the superexchange is the same for Fe1 and Fe2 we now concentrate on the Fe1 states (figure 4.10(b)). Integrating the spin down part of the Fe DOS up to the Fermi energy (red area) yields 5 spin down electrons. However, the integration over the corresponding spin up states gives one electron, bringing the total magnetic moment on Fe down to the observed $4\mu_B$.

The corresponding schematic molecular orbital (MO) diagram shown in figure 4.11 describes the AFM superexchange as it appears in an electronic band picture and in the corresponding schematic DOS. Oxygen forms a bond with each Fe atom mediating the observed AFM superexchange. We start with an Fe 2^+ state with 6 Fe $3d$ electrons. The spin up electron of Fe1 forms a MO state with an O p electron. This covalent interaction not only leads to an increase of the Fe oxidation number towards 3^+ but also moves an Fe spin up state below the Fermi energy and thus reduces the magnetic moment to the observed $4\mu_B$. The same mechanism occures on the Fe2 atom. This mechanism is named “virtual electron transfer” and has been formulated in the Goodenough-Kanamori (GK) rules [9, 10, 188, 190] where they state “The net spin of the cation orbital is not changed by addition of a covalent component but the covalent component extends the cation wavefunction out over the anions to give an orbital overlap for the superexchange electron transfer.” [221] .

Distance and angle dependence of the AFM superexchange

To investigate the angle and distance dependence of the AFM superexchange a single Fe1-O-Fe2 complex was left inside the simulation cell (see figure 4.12). Six of the eight Fe atoms are therefore exchanged by addtional Ga atoms. Interactions with neighbouring Fe-O-Fe complexes can thereby be neglected, revealing the unaffected angle and distance dependence of the superexchange.

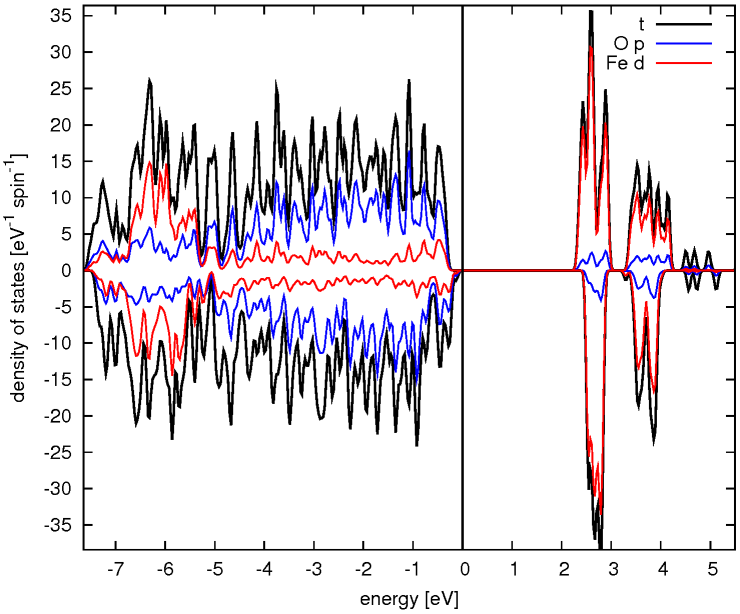

(a)

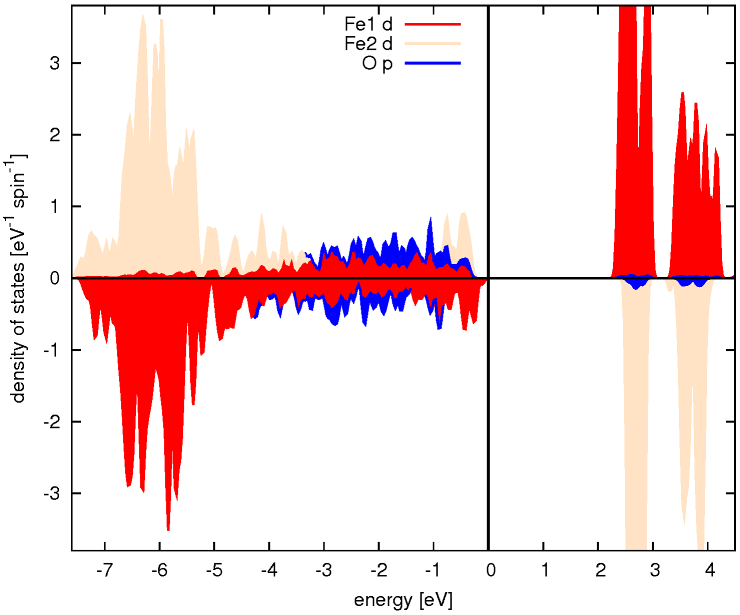

(b)

Figure 4.10: (a) shows the total DOS (black), the overall Fe *d* states (red) and the O *p* states (blue) of pure GFO. (b) shows the projected DOS of an Fe1-O-Fe2 complex. Plotted are the corresponding Fe1 (red area) and Fe2 (yellow area) *d* states and the O *p* state (blue area). All DOS are calculated within the HSE approximation.

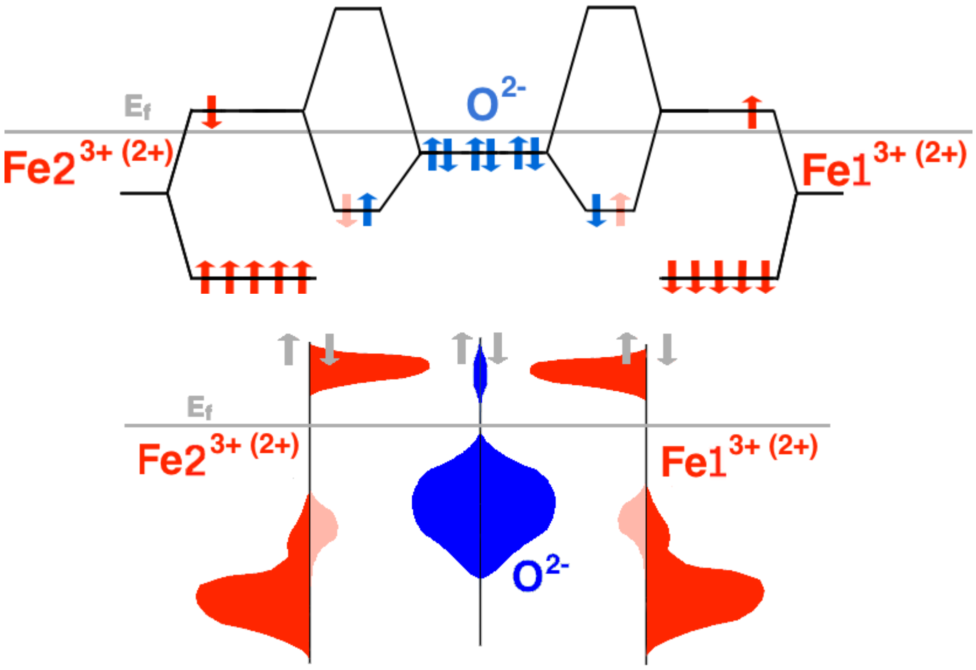

Figure 4.11: The upper part shows the MO diagram of an Fe1-O-Fe2 complex inside GFO. The lower part of the figure sketches the corresponding DOS. Marked in red and blue are the Fe d and the O p states, respectively. Pale red denotes the additional Fe electron which becomes shifted below the Fermi energy by the Fe-O interaction.

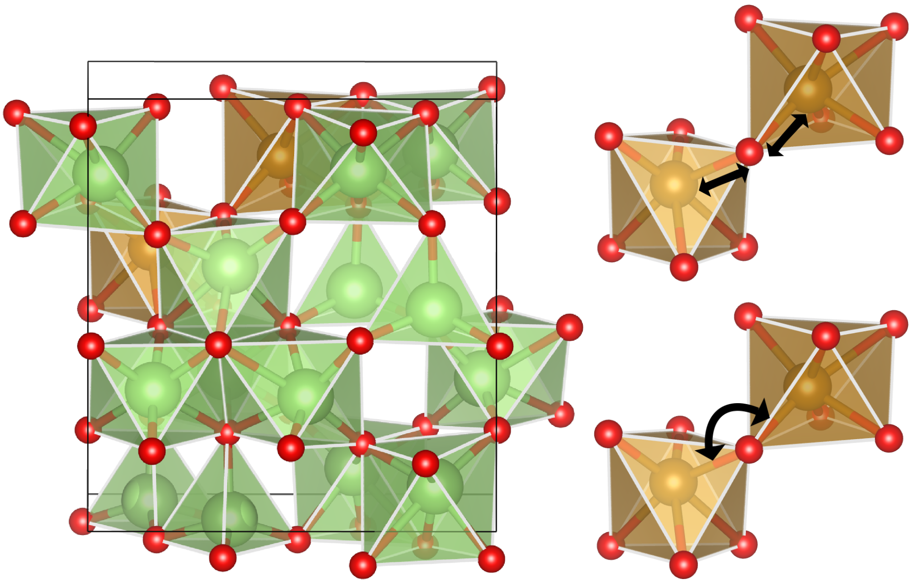

Figure 4.12: Unit cell with a single Fe1-O-Fe2 (125.84°) complex. Bond length and bond angle are varied to consider the alteration on the AFM superexchange.

In a first step the simulation cell in figure 4.12 was relaxed and allowed to change in shape and volume. The thereby obtained structure was used for further calculations. Determining the distance dependence of the AFM coupling strength the bond length of the Fe1-O-Fe2 complex was altered stepwise and kept fix during a second relaxation. The respective enclosed angle was kept constant at its equilibirum value obtained during the first relaxation. Investigating the angle dependence, the enclosed angle was varied but kept fixed during a second relaxation. The corresponding Fe1-O-Fe2 distance was taken from the first relaxation and kept fix as well. These calculations were performed using the GGA+U functional as described in the previous section. The equilibirum bond length of the Fe1-O-Fe2 structure is 3.85 Å. The respective Fe1-O (1.94 Å) and Fe2-O (1.91 Å) distances differ only slightly. The corresponding equilibrium angle is 125.84°.

Varying the bond length the Fe1-O and Fe2-O distances were stretched and compressed stepwise up to 20%. This leads to a maximum and minimum bond length of about 2.3 Å and 1.5 Å for the particular Fe-O bond. The equilibrium angle and the respective altered Fe1-O-Fe2 distance were kept fix during a second relaxation of the cell. Figure 4.13(a) shows the AFM coupling strength designated as E_{diff}[AFM-FM][eV/cell] as a function of the varied Fe1-O bond. The upper x axis gives the total energy difference between the equilibrium ground state and the strained state.

According to the calculations performed the AFM coupling strength increases with decreasing bond length. A decrease in bond length leads to an enhancement of the Fe1-O-Fe2 orbital overlap and therefore to an augmented exchange between the atoms resulting in stronger AFM coupling. Correspondingly, an increase of the Fe-O distance causes the AFM superexchange to decrease.

The equilibrium bond angle of 125.84° for the Fe1-O-Fe2 bond was altered stepwise between 128.11° and 122.23° corresponding to +1.8% und -2.9%, respectively. To calculate the energy as a function of the bond angle, the bond angle was kept fix during a second relaxation while the other atoms postition, the shape and the volume of the simulation cell were allowed to relax. Figure 4.13(b) shows that with increasing angle the AFM coupling strength increases. Structural alterations bigger than the presented ones caused by angle and distance changes are not meaningful in terms of the phase stability.

However, figure 4.13(a) and (b) show that altering the enclosed angle does not affect the AFM coupling strength as much as changing the Fe1-O-Fe2 bond length. Changing the enclosed angle causes a larger distortion of the oxygen octahedra than just varying the bond length. Increasing the bond angle rather than reducing it much earlier drives the system into a phase instability again because a larger bond angle leads to comparably higher distortions of the oxygen octahedra. The obtained results are in good agreement with the GK rules which would predict that the AFM superexchange reduces with increasing bond length and decreasing angle due to a decrease of the orbital overlap between the interacting atoms.

AFM superexchange in GFO - an additive quantity

The total AFM coupling strength of pure GFO turns out to be closely equal to the sum of the AFM coupling strengths of the individual Fe1-O-Fe2 complexes inside the simulation cell. These complexes differ in enclosed angle and bond length. A representative example is given in figure 4.14. Table 4.11 shows the corresponding AFM coupling strengths according to the respective angles shown in figure 4.14. The AFM coupling is the strongest for the (a) and (b) case and almost by one half smaller for the (c) and (d) configuration. Even though we found out that increasing the enclosed angle and reducing the Fe1-O-Fe2 bond length increases in the AFM coupling strength the (c) and (d) complexes show to have a reduced AFM superexchange.

Given the small differences both in angle and bond length, this feature can not be entirely related to the dependencies discussed in figure 4.14. The Fe atoms are surrounded by distorted oxygen octahedra that are tilted, stretched and compressed in different directions. This of course effects the Fe-O-Fe orbital overlap and leads to the calculated behaviour. In the (c) and (d) complexes the orbital overlap is reduced as compared to the (a) and (b) configurations where the coupling is stronger. Case (e) includes all Fe1-O-Fe2 complexes shown in (a)-(d). Their AFM coupling strength is almost the sum of the single configurations, indicating that the AFM superexchange appears to be an

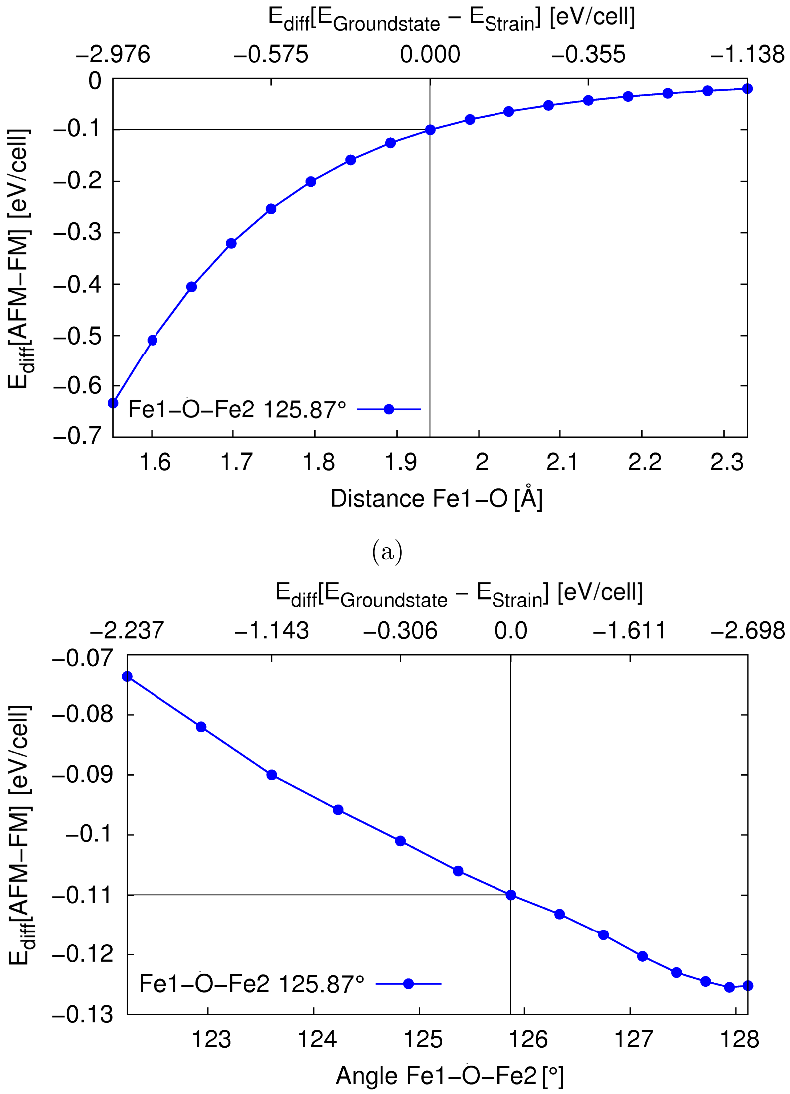

(a)

(b)

Figure 4.13: Plot (a) and (b) show the distance and the angle dependency of the AFM coupling strength, respectively. Increasing the distance and decreasing the angle leads to a decrease in AFM coupling strength. All energies are given per 40 atom simulation cell.

additive quantity. GFO in total has four Fe1-O-Fe2 complexes that differ in angle and

Table 4.3: AFM coupling strengths of the Fe1-O-Fe2 complexes drawn in figure 4.14. Interestingly, (e) equals the sum of the values in (a) to (d). The respective geometries are GGA+U relaxed.

	enclosed angle(°)	bond length(Å)	E_{diff}[AFM-FM](eV)
Fe1-O-Fe2 (a)	122.17	3.86	-0.210
Fe1-O-Fe2 (b)	122.17	3.86	-0.210
Fe1-O-Fe2 (c)	125.84	3.85	-0.113
Fe1-O-Fe2 (d)	125.84	3.85	-0.113
Fe1-O-Fe2 (e)	(a)-(d)	(a)-(d)	-0.648

distance and contribute to the AFM superexchange. The two Fe1-O-Fe2 complexes with the two strongest AFM coupling strengths are given in table 4.11. In addition, there is an Fe1-O-Fe2 complex with an enclosed angle of 166.16° and a bond length of 4.68 Å having an AFM coupling strength of -0.035 eV and a fourth weakly coupled complex with an angle of 102.52°, a bond length of 4.19 Å and an AFM coupling strength of only -0.008 eV. Both contributions to the AFM superexchange are small and almost negligible.

The instrinsic AFM chain in GFO

Concluding the obtained results so far there are two Fe1-O-Fe2 complexes dominating the AFM superexchange inside GFO. These are the Fe1-O-Fe2 complexes with an enclosed angle of 122.17° and 125.84° (see table 4.11). Geometrically, these two complexes are connected to each other forming an Fe-O-Fe twisted chain as shown in figure 4.15. Stoichiometric GFO contains two of these Fe-O-Fe chains as can be seen in figure 4.7 formed by the upper left and lower right Fe structures. The connection between these chains is mediated by the before mentioned very weak Fe1-O-Fe2 complexes. Figure 4.15 shows a particular Fe-O-Fe chain as it meanders through the crystal.

4.6.3 Magnetization density in GFO

Figure 4.16(a) shows the magnetization density (spin up minus spin down) of an Fe1-O-Fe2 complex with the highest AFM coupling strength and an enclosed angle of 122.17°. Red tones represent positive and blue tones indicate negative vaules of the magnetization. Accordingly, figure 4.16(a) shows a negative magnetization density around Fe1 and a

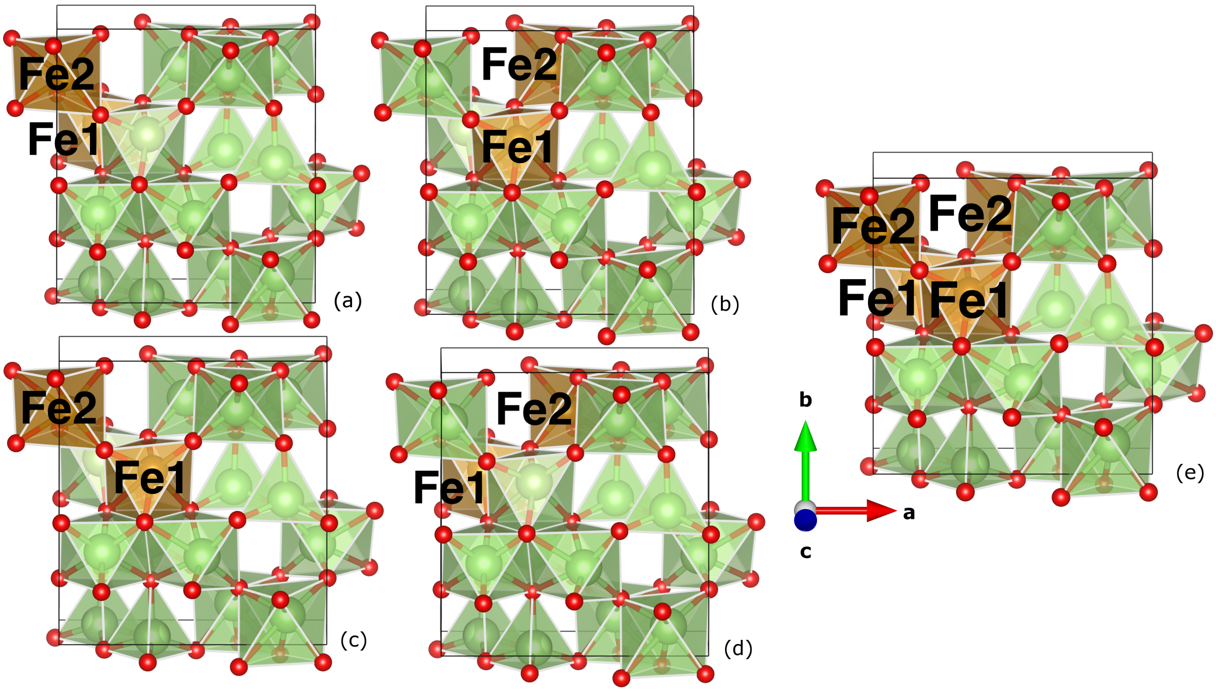

Figure 4.14: (a-d) Simulation cells with different single Fe1-O-Fe2 complexes. These complexes differ in their enclosed angle and bond length. The respective enclosed Fe1-O-Fe2 angles are 122.17° for (a) and (b) and 125.84° for (c) and (d). Case (e) is a modification which contains all complexes (a)-(d) in a single simulation cell. The total AFM coupling strength for the configuration (e) turns out to the be close to the sum of the individual coupling strengths. This figure was created using the VESTA program [115].

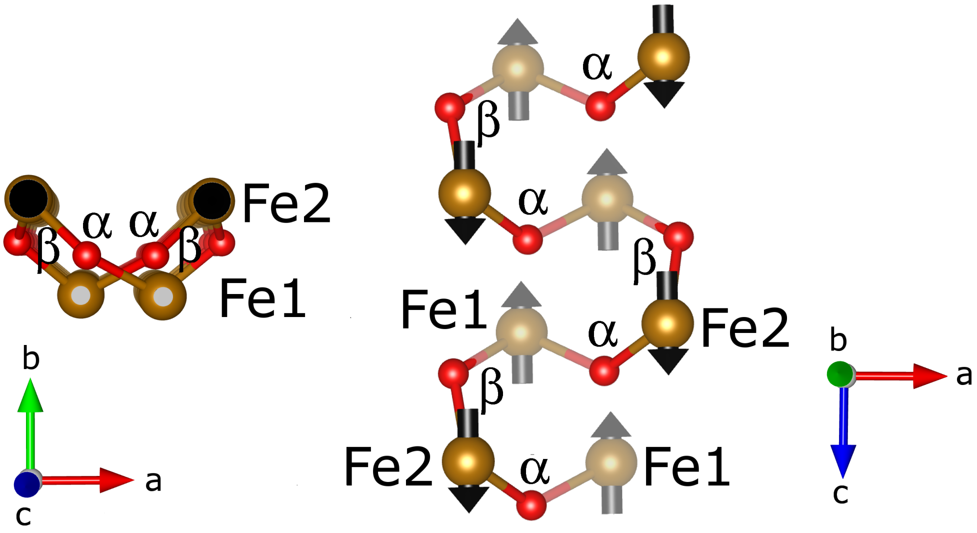

Figure 4.15: Dominant Fe1-O-Fe2 chain along the c axis in GFO. This figure was created using the VESTA program [115].

positive density around the Fe2 atom. The O atom in between has a spin polarized p orbital that is characterized by its dumbbell shape.

This dumbbell shape is induced by the covalent bond between the O atom and its two neighbouring Fe atoms. The negative magnetization density between the Fe2 atom and the positive polarized O p orbital corresponds to the additional Fe d electron that is shifted below the Fermi energy by the superexchange interaction. This particular Fe d electron is shown in figure 4.11 highlighted in pale red. It forms a molecular orbital with an O p electron. This p electron shows reversed spin according to Hund's rules and is represented by the positive magnetization density (red) next to it. The AFM superexchange is mediated by this molecular orbital. Due to the spin compensation between the Fe electron and the O electron the spin density is rather small, however an alaysis of the energy dependent electron density shows that this feature represents the Fe-O states between -5 eV and the Fermi energy (see figure 4.10). Same is true for the positive magnetization density left-hand side of the Fe1 atom. It belongs to the additional Fe d electron that reduces the initial magnetic moment of -5μ_B to about -4μ_B per Fe atom. The negative magnetization density next to it again belongs to the O p electron with which the molecular orbital is formed with (figure 4.16(a)).

The plotted magnetization density in figure 4.16(b) shows two O p orbitals which differ in shape. The left-hand side O is part of the Fe1-O-Fe2 (122.17°) complex with the strongest AFM superexchange and the right-hand side O is part of the weakest Fe1-O-Fe2 configuration with an enclosed angle of 102.52°. Since the O atoms mediate the superexchange the shape of the O p orbitals immediately indicates the strength of the AFM coupling. The shape of the left-hand side O p orbital forms a straight σ-bond between its neighbouring Fe1 and Fe2 atom. The shape of the right hand side O p orbital mediating almost no AFM coupling resembles a 90° bonding. According to the GK rules a bond along a 90° angle can couple ferromagnetically. Since in GFO we observe superexchange along an Fe1-O-Fe2 chain the AFM order is retained, however the AFM coupling strength along the 102.52° angle becomes only reduced.

4.6.4 Magnetocrystalline anisotropy energy in GFO

Magnetocrystalline anisotropy energy (MAE) is another interesting property of GFO. According to experiment the c axis of pure GFO is the easy axis and corresponds to the ground state direction of the magnetic moments while the hard axis is in b direction [194, 203]. F. Ibrahim and M. Alounani [193] already discussed the impact of excess Fe and the effect of varying U values in the GGA+U approximation on the calculated MAE. Independent of the U value the MAE decreases with increasing amount of excess Fe atoms.

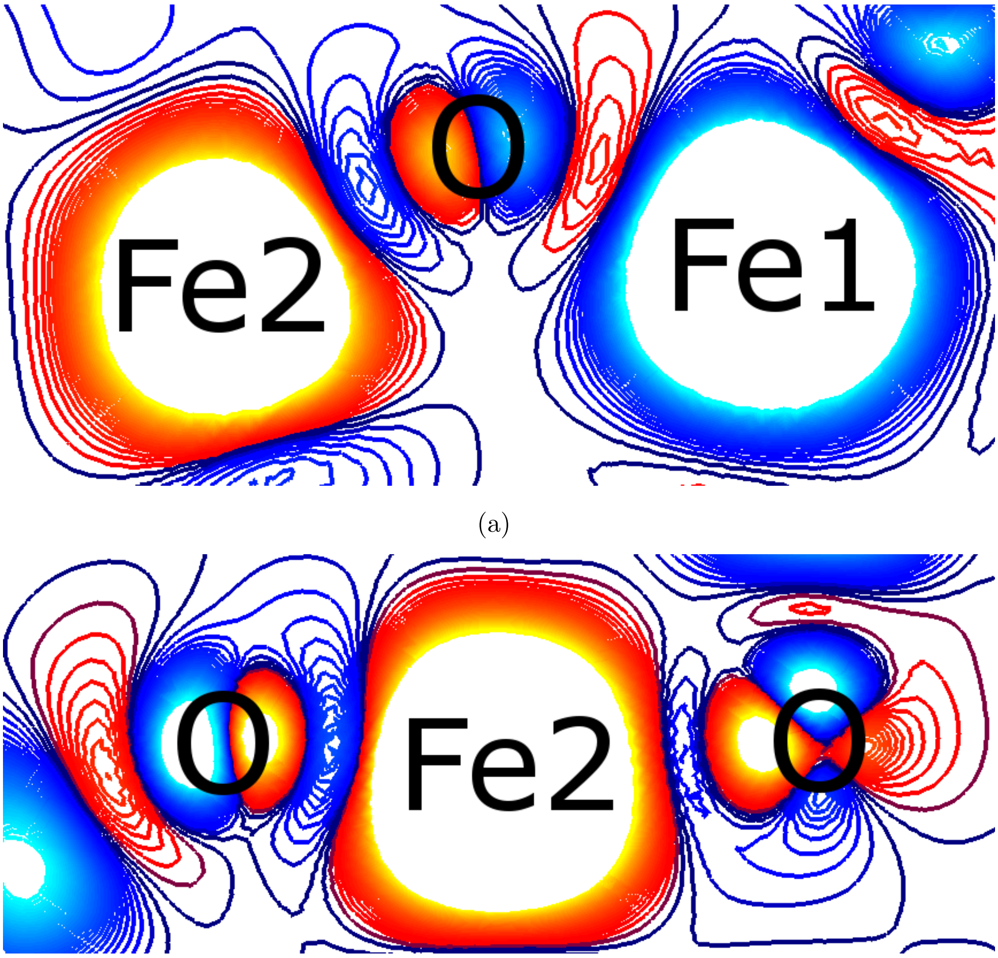

(a)

(b)

Figure 4.16: (a) shows the magnetization density (spin up minus spin down) of an Fe1-O-Fe2 couple inside the GFO simulation cell. Denoted in red and blue tones are the positive and negative magnetization values, respectively. (b) shows the magnetization density of an Fe2 atom being part of two Fe1-O-Fe2 complexes. The left O atom is part of a strong AFM coupling strength Fe1-O-Fe2 (122.17°) complex and the right O atom of a weak Fe1-O-Fe2 (102.52°) configruation. This figure was created using the VisIt program [135].

We focus on the partly predicted and experimentally measured [201, 203] but, to the best of our knowledge, not yet theoretically studied sublattice dependent MAE. Calculating the MAE of the *a*, *b* and *c* axis in pure GFO the simulation cells were both relaxed using the HSE functional and the GGA+U approximation. Hence, we could investigate the effect of the used exchange and correlation functional on the resulting crystal structure and the MAE.

The first entry in table 4.4 shows the energy difference of the [001] and [100] configuration. In the [001] configuration the magnetic moments of both the Fe1 and the Fe2 sublattice are oriented along the ground state *c* direction. This energy is then subtracted from the energy of the [100] configuration where the magnetic moments of both sublattices are rotated in *a* direction. The second row in table 4.4 gives the energy difference of the [001] and the [010] configuration. Here the magnetic moments are rotated first in *c* and then in *b* direction. The calculated MAE of pure GFO is in good agreement with experiment and previous calculations [193, 203]. Both the HSE and GGA+U relaxed crystal structures define the *c* axis as the easy axis and the *b* axis as the hard axis. The HSE relaxed geometry shows a larger MAE for the *b* axis making it less favourable. In the "Ga2-Fe1" simulation cell a Ga2 atoms exchanges its site with an Fe1 atom. The corresponding simulation cell has a net magnetic moment unequal zero, leading to a ferrimagnetic ground state of 5μB per simulation cell. A more detailed discussion of the different inner cationic site disorder configurations and their respective energies are given in the following section 4.6.5. Interestingly, this configuration leads to a change of the easy axis of the system, which is now the *a* axis. This is true for both the HSE and the GGA+U relaxed geometries, while HSE again yields larger anisotropies. Focussing on a further clarification of a sublattice dependent anisotropy, the magnetic moments of the Fe1 and Fe2 sublattice atoms were rotated against each other and the respective configuration energy calculated. First, a calculation was performed where the magnetic moments of the Fe1 sublattice atoms are rotated in *a* direction while the moments of the Fe2 atoms are fixed in *c* direction, followed by another calculation where the magnetic moments of the Fe2 sublattice atoms rotated in *a* direction and the magnetic moments of the Fe1 atoms held in *c* direction. Computing the energy difference of these two configurations makes it possible to determine a potential sublattice dependent magnetic anisotropy. The same was done rotating the magnetic moments of the sublattices vice versa in the *b* direction keeping the respective other one fixed in the ground state *c* direction. In both pure GFO and in the case of inner cationic site disorder the Fe1 sublattice is less anisotropic than the Fe2 sublattice. This was also predicted by experiment by Reddy et al. [201]. The anisotropy between the Fe1 and Fe2 sublattice is more pronounced in *a* direction. However, the overall sublattice dependent anisotropy is by one order of magnitude smaller in pure GFO. It was also investigated whether the magnetic moments of the Fe1 and Fe2 sublattice prefer being rotated in a or in b direction. Starting with the Fe1 sublattice the magnetic moments were once turned in a and then in b direction keeping the magnetic moments of the Fe2 sublattice fixed in the ground state c direction. It shows that the Fe1 sublattice moments prefer being rotated in a direction over the b direction. The same was done with the Fe2 sublattice magnetic moments. In that case the magnetic moments prefer being rotated in b direction rather than the a direction.

Table 4.4: MAE of pristine and inner cationic site disorder affected GFO. Indices denote HSE^1 and GGA+U^2 calculations.

MAE [meV]	GFO^1	GFO^2	Ga2-Fe1^1	Ga2-Fe1^2
[001]-[100]	-0.230	-0.182	-0.434	-0.423
[001]-[010]	-0.291	-0.212	-0.357	-0.309
Fe1[100]Fe2[001]-Fe1[001]Fe2[100]	-0.153	-0.163	-1.765	-1.655
Fe1[010]Fe2[001]-Fe1[001]Fe2[010]	-0.012	-0.028	-1.668	-1.522
Fe1[100]Fe2[001]-Fe1[010]Fe2[001]	-0.088	-0.060	-0.046	-0.044
Fe1[001]Fe2[100]-Fe1[001]Fe2[010]	0.053	0.076	0.051	0.090

4.6.5 Cation doping - ranging from ε-GO to GFO and ε-FO

From ε-GO to GFO - $0.0 \leq x \leq 1.0$

The magnetic properties of $Ga_{2-x}Fe_xO_3$ were investigated for a doping concentration of $0.0 \leq x \leq 2.0$ [1]. At a concentration of x=0.0 GFO turns into nonmagnetic isomorphic ε-GO. Raising the doping concentration stepwise up to x=1.0 by adding Fe atoms to the ε-GO cell gives stoichiometric GFO. Reaching the value of x=2.0, where all Ga atoms are exchanged by Fe atoms, turns the GFO simulation cell into the AFM isomorphic ε-FO structure (figure 4.17). The respective calculated lattice parameters and band gaps are given in table 4.2. In addition, we also studied the effect of inner cationic site disorder on the magnetic properties and the phase stability of stoichiometric GFO.

At a cation doping concentration of x=0.1 one Fe is added to the ε-GO simulation cell. There exist four different lattice sites the Fe atom can be placed on. To denote the respective doping site of the introduced Fe atom we use the Fe1/2 and Ga1/2 site notation of stoichiometric GFO (figure 4.7). The additional Fe atom prefers an Fe1 site

---

[1] In contrast to experimental values with an average doping concentration over the whole sample our substitutions are not strictly random but show long range order due to the periodicity of the supercell

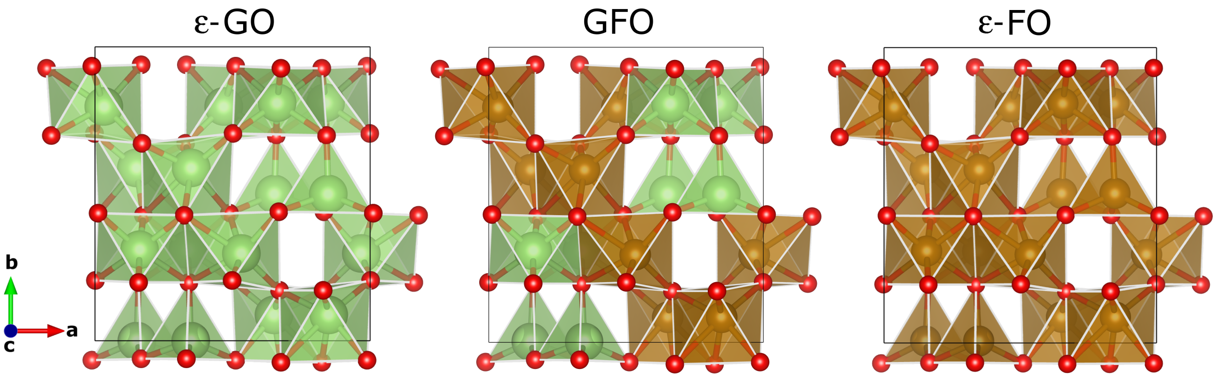

Figure 4.17: Shown are the respective simulation cells of $Ga_{2-x}Fe_xO_3$ for a doping concentration of x=0.0, x=1.0, and x=2.0. These are equivalent to the crystal structures of ε-GO, GFO and ε-FO. This figure was created using the VESTA program [115]

by about 31 meV over an Fe2 site. Placing the Fe atom on a Ga1 or Ga2 site is by 359 meV and 112 meV less favourable as compared to the occupation of an Fe1 site.

Adding a second Fe atom (x=0.2) to the ε-GO cell offers a multitude of doping configurations. In addition, to the already discussed Fe1-O-Fe2 configurations, we investigated the magnetic properties of possible Fe1-O-Fe1, Fe2-O-Fe2 and Fe-O-Fe(Ga1/2) configurations, where the latter means that an Fe sits either on a Ga1 or a Ga2 position. The calculated AFM coupling strengths of the Fe1-O-Fe1 and Fe2-O-Fe2 complexes are very small with 0.062 and 0.004 meV, respectively. Comparing their phase stabilities to the most stable Fe1-O-Fe2 (122.17°) configuration (see table 4.11) shows that the formation of an Fe1-O-Fe1 complex is only by 17 meV less favourable. The Fe2-O-Fe2 configuration has a higher energy difference of about 139 meV. The most stable Fe-O-Fe(Ga1/2) configurations are the Fe1-O-Fe(Ga2) and the Fe2-O-Fe(Ga1) configuration with an enclosed angle of 163.56° and 122.53°, respectively. The first configuration is 250 meV more stable than the latter one, whereas the latter has a by 55 meV larger AFM coupling strength. The most stable Fe1-O-Fe2 configuration is still by 153 meV more favourable than the Fe1-O-Fe(Ga2) configuration. Regarding the calculated phase stabilities of the investigated doping configurations two Fe atoms would first form an Fe1-O-Fe2 configuration. This is followed by an Fe1-O-Fe1 configuration, an Fe2-O-Fe2 configuration and an Fe1-O-Fe(Ga2) configuration. Occupying two Ga sites forming an Fe(Ga1/2)-O-Fe(Ga1/2) complex is at least 250 meV less probable than the energetically best Fe1-O-Fe2 configuration. No ferromagnetic ground state can be produced with any doping configurations at x=0.2.

At x=0.4 it is most favourable in energy when two Fe atoms occupy two adjacent Fe1 sites and the third Fe atom occupies a next nearest Fe2 site. The Fe1 atoms have a negative magnetic moment of about -4μ_B each and the Fe2 atom a positive magnetic moment of about +4μ_B, as expected from the arrangement of the magnetic moments in stoichiometric GFO. This leads to a total magnetic moment of -5μ_B per simulation cell and a ferrimagnetic ground state. It should be noted that this total magnetic moment also contains the contributions from the oxygens.

4 substitutional Fe atoms are added to the ε-GO structure at a doping concentration of x=0.5. In terms of phase stability they are best arranged in an Fe1 and Fe2 cluster (figure 4.14(e)), forming the earlier discussed Fe1-O-Fe2 chain (figure 4.15).

Adding stepwise another four Fe atoms until a doping concentration of x=1.0 a second Fe1-O-Fe2 chain is formed following the same mechanism as before. For a doping concentration of x=0.0 to x=1.0 the total magnetic moment per simulation cell thus turns out to be either 0μ_B or -5μ_B (figure4.18).

Inner cationic site disorder in stoichiometric GFO

Experimental studies also report to find a ferrimagnetic state in GFO beside the expected AFM ground state of stoichiometric GFO. These findings can be attributed to the of an inner cationic site disorder where Ga and Fe atoms exchange cell sites. Recently performed calculations also report to be in better agreement with experiment if they include an inner cationic site disorder in their systems [195, 222]. We investigate the possible inner cationic site disorder configurations in stoichiometric GFO and calculate their phase stabilities and total magnetic moment.

The energetically most favourable site disorder is the Fe2-Ga2 exchange where an Fe2 atom exchanges site with a Ga2 atom. Compared to stoichiometric GFO showing no inner cationic site disorder the loss of phase stability is about 157 meV. The AFM coupling strength reduces from 1.44 eV to 1.30 eV per simulation cell and has a total magnetic moment of 0μ_B. In that particular case no ferrimagnetic ground state is introduced. The case of an Fe1-Ga2 exchange leads to a loss in energy compared to pristine GFO of 183 meV and indeed yields a ferrimagnetic ground state with 5μ_B per simulation cell. Followed by that are the Fe2-Ga1 and Fe1-Ga1 exchange configurations. Both differ only by 10 meV in phase stability but are about 400 meV less favourable than pristine GFO. The increased loss in phase stability is due to the different O environment of Ga1 since Fe prefers being surrounded by an O octahedron rather than by an O tetrahedron. However, the Fe2-Ga1 exchange again leads to a ferrimagnetic ground state of -5μ_B per simulation cell. The magnetic moment of an Fe atom occupying a Ga1 or Ga2 site equals the one at an Fe1 or Fe2 site, respectively. The Fe1-Ga2 exchange is the energetically most favourable inner cationic site disorder configuration leading to a ferrimagnetic ground state.

From GFO to ε-FO - $1.0 \leq x \leq 2.0$

As discussed previously the Fe atoms prefer the occupation of Ga2 over Ga1 sites. Hence, ranging from a doping concentration of x=1.0 to x=1.5 all Ga2 sites are occupied first.

Substituting a Ga2 site forms an additional Fe1-O-Fe(Ga2) bond inside GFO which is about 232 meV energetically more stable than the formation of an Fe2-O-Fe(Ga1) complex where a Ga1 site is occupied by an excess Fe atom. However, the latter is about 57 meV stronger in AFM coupling strength. Increasing the doping concentration further up to a value of x=2.0 all Ga1 are occupied until no Ga atom is left inside the simulation cell. GFO turns into the ε-FO structure.

Figure 4.18 shows the AFM coupling strength as a function of the doping concentration x and the corresponding total magnetic moment of the respective simulation cell. For each concentration x (figure 4.18) the values of the lowest energy for the possible doping configurations are plotted. The additive character of the AFM coupling strength can be nicely seen in figure 4.18. Taking a closer look at the slope for a doping concentration of $0.1 \leq x \leq 1.0$ we see the same behaviour of the curve in the range of $0.1 \leq x \leq 0.5$ and $0.6 \leq x \leq 1.0$. Here, the two Fe1-O-Fe2 chains are formed inside the simulation cell. The first one in a range of $0.1 \leq x \leq 0.5$ and the second one for $0.6 \leq x \leq 1.0$.

The magnetic moment per simulation cell alternates between $0\mu_B$ or $-5\mu_B$. For a doping concentration of $1.1 \leq x \leq 1.5$ all Ga2 sites become substituted and additional Fe1-O-Fe(Ga2) configurations are formed. The slope of the curve shows an almost linear increase of the AFM coupling strength and again indicates the additive character of this property. The same is true for the range of $1.6 \leq x \leq 2.0$ where all Ga1 sites are substituted and Fe1-O-Fe(Ga1) complexes are formed.

The total magnetic moment is maximal at x=1.5 and yields $20\mu_B$ per simulation cell. At x=2.0 when transforming into the ε-FO structure we end up in an AFM ground state. The defect formation energy provides information on the phase stability of the doped system. According to the following formula [129]

$$E^{form}[x] = E_{tot}[x] - E_{tot}[bulk] + n(\mu_{Ga} - \mu_{Fe}) \quad , \tag{4.9}$$

where E_{tot} is the total free energy of the cation doped simulation cell. x is the doping concentration and $E_{tot}[bulk]$ stands for the total free energy of the pristine GFO simulation cell. n indicates the number of Ga atoms that are replaced by Fe atoms. μ_{Ga} and μ_{Fe} are the corresponding chemical potentials. The reference energies of the chemical potentials are calculated from the α-Fe and α-Ga phase.

Figure 4.19 shows the defect formation energy of the cation doping referenced to the energy of the pristine GFO simulation cell. The defect formation energy shows almost linear behaviour. A detailed account of the deviations of the linearity is shown by the red

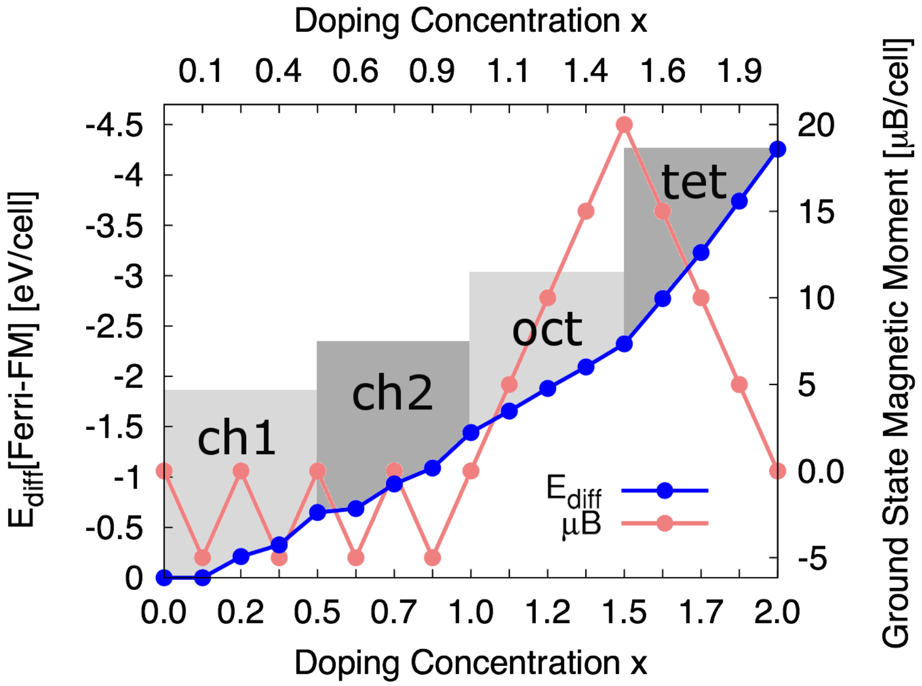

Figure 4.18: We show the AFM coupling strength E_{diff} (blue) and the corresponding ground state magnetic moment (red) as a function of the doping concentration x. In the range of x=0.0 to x=0.5 the first Fe1-O-Fe2 chain in formed in GFO denoted by "ch1" (chain 1). In the "ch2" highlighted area the second Fe1-O-Fe2 chain is formed, where E_{diff} for "ch1" and the "ch2" shows the same behaviour. In the area "oct" (octahedral) all Ga2 sites are substituted by Fe atoms. Here the slope is constant indicating the additive character of the AFM coupling strength of the formed Fe1-O-Fe(Ga2) configurations. In the area "tet" (tetrahedral) all Ga1 sites become stepwise occupied by Fe atoms. As before we find an almost linear increase in the coupling strength.

curve in figure 4.19 (note the much smaller energy scale). It shows the energy difference of two consecutive configurations which differ by one Fe atom, ΔE_{form}=$E_{form}[x+1]$-$E_{form}[x]$. The average value for the replacement of one Fe for one Ga is $\Delta E_{form} = 3.18$ eV.

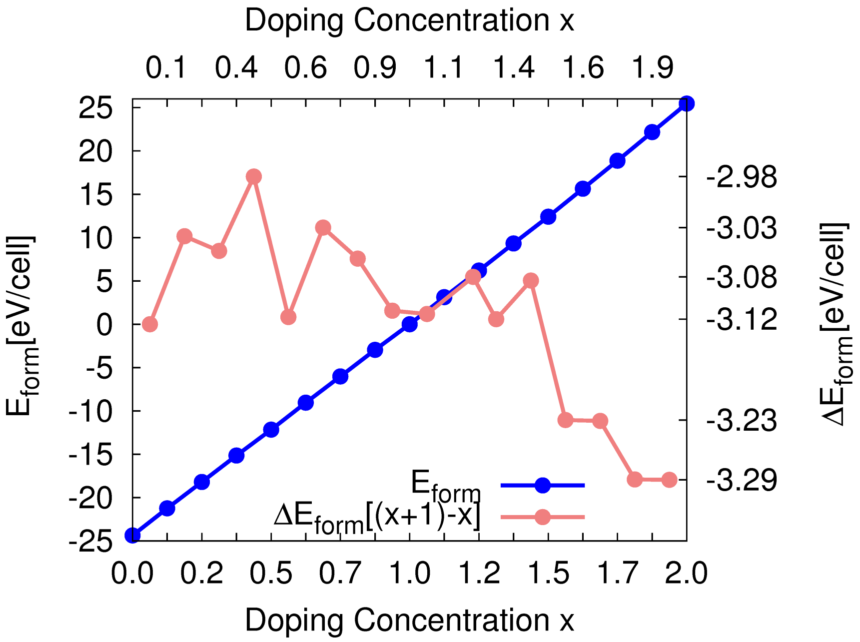

Figure 4.19: We show the defect formation energy E^{form} (blue) as a function of the doping concentration x and the difference ΔE_{form} (red) (see text).

4.6.6 The effect of strain in stoichiometric cation doped GFO

Straining the simulation cell induces a distortion of the ground state cell geometry. Intrinsic angles and atomic distances are altered and hence can lead to a change of the magnetic and optical properties partly discussed by Roy et al. [222]. However, in the present investigation we are interested in the effect of strain on the AFM coupling strength in pristine GFO and include inner cationic site disorder and cation doping concentrations of $0.9 \leq x \leq 1.4$.

Strain on stoichiometric GFO

Starting with pristine GFO, the simulation cell is stretched and compressed in a, b and c direction, respectively. Stretching or compressing the simulation cell along a certain cell direction the corresponding cell parameter is stretched/compressed by a factor x. The other two cell parameters change accordingly by $1/\sqrt{x}$ each, preserving the volume. In a following step the positions of the ions inside the simulation cell were allowed to relax with the volume and the shape of the cell being preserved and the crystal symmetry remains orthorombic.

Distorting the Fe1-O-Fe2 bonds by straining the simulation cell affects the AFM coupling strength. The two main parameters quantifying the geometric distortion of an Fe1-O-Fe2 bond are the enclosed angle and bond length. Further we focus on the two Fe1-O-Fe2 bonds that build the intrinsic AFM chain and therefore have the biggest effect on the AFM coupling. In stoichiometric unstrained GFO one finds two enclosed angles of 123.02° and 126.30° (relaxed within the GGA+U approximation).

Stretching the simulation cell by +3.5% in c direction increases the enclosed angle of the 123.02° Fe1-O-Fe2 bond up to 125.60°. Compressing the cell by 3.5% on the other hand reduces the enclosed angle to 120.39°. The 126.30° Fe1-O-Fe2 bond shows the opposite behaviour. The enclosed angle increases to 129.05° upon compression and reduces to 123.43° when stretching it by 3.5%. Compressing the simulation cell the Fe1-O-Fe2 bond length increases for the 126.30° case and reduces for the 123.02° bond and vice versa upon stretching. The total change of the bond length is 0.052 Å and 0.0044 Å for the first and latter Fe1-O-Fe2 bond, respectively.

Stretching the cell in b or a direction increases the enclosed angle and the bond length of the 126.30° Fe1-O-Fe2 bond. The 123.02° Fe1-O-Fe2 bond on the other hand reduces its enclosed angle when stretching the simulation cell in a direction and increases for positive strain in the b direction. The bond length of the 123.02° Fe1-O-Fe2 bond becomes reduced in both cases.

Calculations on the distance and angle dependence of the AFM superexchange have shown that variations of the bond length of an Fe1-O-Fe2 complex have more effect on the coupling strength than changes of the enclosed angle. This is also reflected in table 4.12. The AFM coupling strength of the 123.02° Fe1-O-Fe2 bond is almost twice as big as compared to the 126.30° Fe1-O-Fe2 configuration. We could show that the AFM coupling strength has an additive character. Geometric alteration of the stronger 123.02° Fe1-O-Fe2 bond should therefore have more effect on the AFM coupling strength. Straining the simulation cell in c direction leads to the biggest changes in bond length and enclosed angle of the particular 123.02° Fe1-O-Fe2 complex, also leading to maximal changes of the 126.30° Fe1-O-Fe2 bond. This explains the strong changes in the AFM coupling strength for straining the simulation cell in c direction (by 99 meV in the range of -3.5% - +3.5%), followed by straining the simulation cell in the b (60 meV) and a (50 meV) direction, respectively. The reversed slope of the AFM coupling strength for the a, b and c direction shown in figure 4.20 is mainly due to the fact that compressing the simulation cell in c direction reduces the enclosed angle and bond length of the dominant 123.02° Fe1-O-Fe2 bond enhancing the overall AFM coupling strength. Compressing the simulation cell in a

and b direction both increases the structural properties of the 123.02° Fe1-O-Fe2 complex and therefore reduces the AFM coupling strength.

Table 4.5: Enclosed angle and bond length of the 123.02° Fe1-O-Fe2 and 126.30° Fe1-O-Fe2 bond in strained and unstrained stoichiometric GFO. The respective geometries are GGA+U relaxed.

Strain	-3.5%	0.0%	+3.5%	Δ(-3.5% − +3.5%)
a direction				
Fe1-O-Fe2 126.30° enclosed angle(°)	123.791	126.295	128.404	-4.613
Fe1-O-Fe2 126.30° bond length(Å)	3.844	3.849	3.855	-0.011
Fe1-O-Fe2 123.02° enclosed angle(°)	125.519	123.023	120.313	5.206
Fe1-O-Fe2 123.02° bond length(Å)	3.877	3.863	3.856	0.021
b direction				
Fe1-O-Fe2 126.30° enclosed angle(°)	125.707	126.295	126.792	-1.085
Fe1-O-Fe2 126.30° bond length(Å)	3.857	3.849	3.850	0.007
Fe1-O-Fe2 123.02° enclosed angle(°)	122.976	123.023	123.202	-0.226
Fe1-O-Fe2 123.02° bond length(Å)	3.881	3.863	3.856	0.028
c direction				
Fe1-O-Fe2 126.30° enclosed angle(°)	129.054	126.295	123.433	5.621
Fe1-O-Fe2 126.30° bond length(Å)	3.851	3.849	3.846	0.006
Fe1-O-Fe2 123.02° enclosed angle(°)	120.388	123.023	125.596	-5.208
Fe1-O-Fe2 123.02° bond length(Å)	3.844	3.863	3.896	-0.052

Figure 4.20 shows the respective change of the AFM coupling strength. Compressing the simulation cell in a or b direction reduces the AFM coupling strength. Decreasing the length of the lattice c parameter on the other hand increases the coupling. The reversed increase and decrease of the AFM coupling strength in c direction can be explained by the geometric distortions induced in the simulation cell.

While some of the Fe1-O-Fe2 angles and distances become smaller or bigger stretching and compressing the simulation cell along the a or b direction they oppositely become bigger or smaller stretching the system in c direction.

Compressing the cell in a and b direction up to -3.5% leads to a decrease in the AFM coupling by 31 meV and 44 meV per simulation cell, respectively. Stretching the cell up to +3.5% enhances the coupling by 19 meV for the a and 16 meV for the b direction.

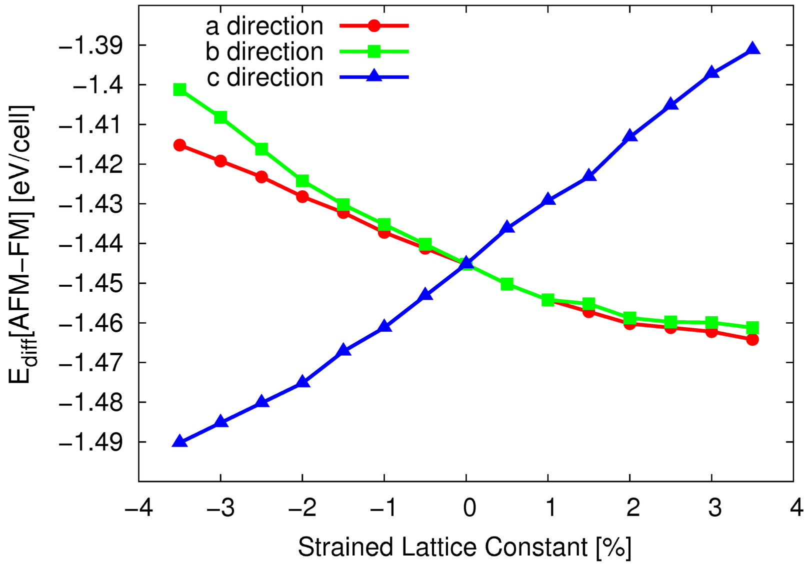

Figure 4.20: AFM coupling strength E_{diff} as a function of the strained lattice constant in a (red), b (green) and c (blue) direction.

The AFM coupling strength increases compressing the cell in c direction by 54 meV and decreases with extension by 45 meV per simulation cell. Straining the simulation in cell in c direction leads to the biggest change in the AFM coupling strength. The loss in total energy and phase stability of the strained simulation cell correlates with the absolute change of the AFM coupling strength. The higher the increase/decrease of the AFM coupling strength caused by the applied strain the bigger/smaller becomes the phase stability.

Compressing the cell in a direction reduces the total energy per simulation cell by 336 meV compared to the unstrained configuration. Stretching leads to an energy loss of 292 meV per simulation cell. In b direction the total energy of the strained simulation cell becomes decreased by 351 meV and 358 meV for compressing and stretching the system, respectively. The biggest loss in phase stability is caused by stretching and compressing the cell in c direction. Stretching and compressing the cell decreases the cell energy by 382 meV and 332 meV per simulation cell, respectively.

Strain on cation doped $Ga_{2-x}Fe_x$ O_3

The effect of strain in cation doped $Ga_{2-x}Fe_x$ O_3 was investigated for a doping concentration between x=0.9 and x=1.4. This corresponds to the cation doping range investigated in most experiments. Since strain along the c axis has the biggest impact on the AFM coupling strength strain was applied in c direction in the following calculations. For each doping concentration the previously determined energetically most stable doping configuration is used. In addition, we investigate two cases of inner cationic site disorder including the most stable Fe2-Ga2 site exchange leading to a total magnetic moment of zero and the Fe1-Ga2 site exchange causing the GFO ground state to become ferrimagnetic with $+5\mu_B$ per simulation cell.

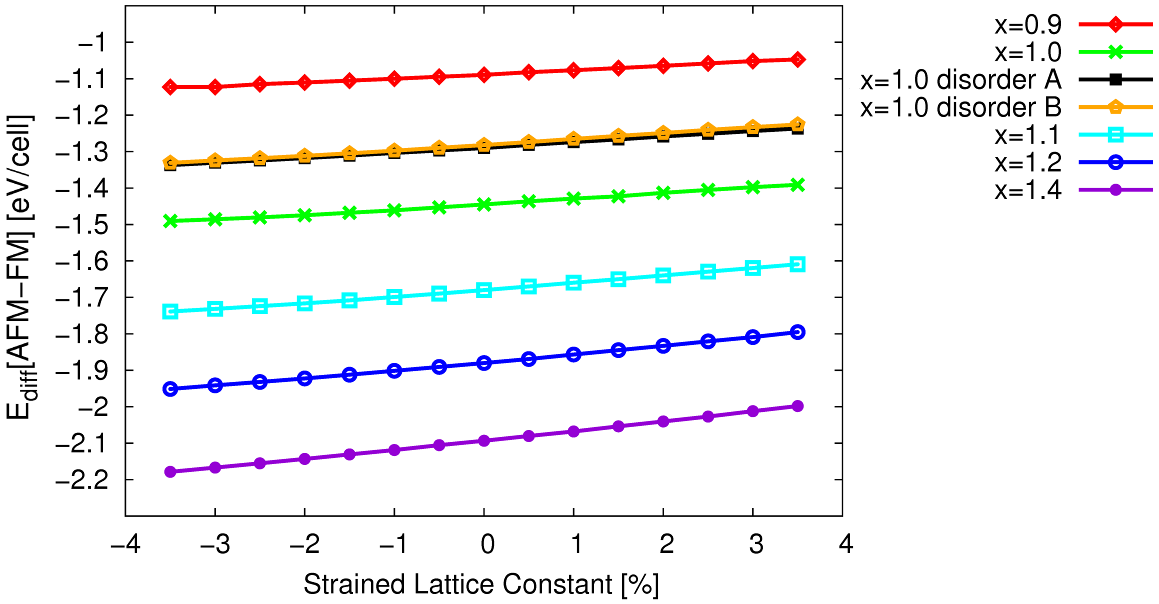

Figure 4.21: Straining the $Ga_{2-x}Fe_xO_3$ simulation cell in c direction for a doping concentration of x=0.9 to x=1.4 including the case of inner cationic site disorder. Plotted is the AFM coupling strength E_{diff} as a function of strain.

Figure 4.21 shows the calculated AFM coupling strength as a function of the applied strain. For all investigated configurations the AFM coupling strength increases upon compressing the corresponding simulation cell in c direction. The overall coupling strength increases with increasing Fe content. This can be seen by the downward shift to larger coupling strengths of the respective curves for higher cation doping concentrations x. The plotted curves have a steeper rise for higher Fe concentrations. The two investigated cases of inner cationic site disorder are almost equal in energy.

4.6.7 Conclusion

The performed calculations provide a detailed insight into the origin of the AFM superexchange mechanism in stoichiometric and cation doped GFO. The MO diagram given in figure 4.11 shows that molecular orbitals are formed between the O and Fe atoms. The Fe-O interaction reduces the formally $5\mu_B$ for an Fe 3^+ state to the observed about $4\mu_B$.

The AFM superexchange is mediated by these covalent bonds. Further we show that the AFM superexchange follows in principle the GK rules. The AFM exchange enhances with increasing bond angle and decreasing bond length due to an enhanced orbital overlap. The magnetization density given in figure 4.16(b) reflects this behaviour. According to the GK rules we find stronger AFM coupling for bond angles closer to 180° and a subsequent weakening when the bond angle approaches 90°. The AFM superexchange throughout the crystal is carried forward by an Fe1-O-Fe2 chain. This particular chain is build up by two Fe1-O-Fe2 complexes which differ in their enclosed angle and bond length (figure 4.15).

MAE is another interesting property of GFO. The calculated MAE and the obtained magnetic easy and hard axis are in agreement with experiment. The magnetic easy and hard axis are found to be along the c and b direction, respectively. Relaxing the GFO simulation cell within the HSE approximation yields larger anisotropies. The presence of an inner cationic site disorder can lead to a ferrimagnetic ground state. In that case the magnetic hard axis changes to the a direction.

Cation doping increases the AFM coupling strength. The magnetic moment per simulation cell is a maximum for a doping concentration of x=1.5. In this configuration all Ga2 sites are occupied by four excess Fe atoms leading to a magnetic moment of $20\mu_B$ per simulation cell. Figure 4.18 shows the additive character of the AFM coupling. Starting with the ε-GO structure the two Fe1-O-Fe2 chains are formed first. Increasing the cation doping concentration the Ga2 sites are occupied followed by the Ga1 sites until the ε-FO phase is formed.

Strain distorts the cell geometry and alters the intrinsic bond lengths and angles which can affect the AFM coupling strength. The biggest effect on the AFM coupling strength is obtained by stretching and compressing the pristine GFO simulation cell in c direction. Figure 4.21 shows the effect of cation doping on the strained simulation cell. The slopes of the curves are shifted to higher coupling strengths with increasing doping concentration x. The respective defect formation energy is almost constant with a mean value of 3.18 eV.

4.7 Calculations on anion doped (C, N, S) GFO

Replacing the superexchange mediating O atom with another p element of a different valence electron configuration changes the underlying magnetic exchange mechanism and as a consequence may influence the ground state properties. This again may be used for tuning properties which are useful and interesting for technical applications.

A great number of experimental und computational studies discuss the effect of varying iron concentration on the magnetic properties. Increasing the amount of Fe atoms increases the net magnetic moment [194, 195, 197, 200, 201]. Adding additional Fe atoms creates unsaturated Fe-O-Fe bonds and leads to the observed ferrimagnetic ground state.

A multitude of studies investigate the effect of cation doping in multiferroics like $BiFeO_3$, ZnO and GFO, to name but a few [223, 224]. They report changes in the ground state properties which may be important for tailoring materials regarding new technical applications. Theoretical and experimental studies on Cr, Mn and Co doped GFO report changes of the structural parameters, the magnetic ground state and the Curie temperature depending on the respective substitution site (Fe or Ga sites). [225–227]

A much smaller number of studies examine the effect of anion substitution, exchanging the O atom by another main group element. Nitrogen and fluorine doped $BiFeO_3$ and ZnO show changes in their ground state properties and report enhanced ferromagnetism, polarization and absorption shifts into the visible region [228, 229].

There is an experimental study performed by Dhanasekaran and Gupta [230], investigating the effect of N and S doping on the photocatalytic properties of GFO substituting O. Transition metal oxides and their occurrence as mulitferroics have proven to be good photocatalysts [231]. Dhanasekaran and Gupta [230] report a significant increase of the photocatalytic hydrogen generation rate of GFO substituting O with N and S atoms, respectively. Water splitting, using solar-radiation, is a most promising way for producing sustainable fuel.

This part of the thesis presents *ab initio* calculations performed on a single anion doped strained and unstrained GFO simulation cell. Based on the results discussed in the previous section four O substitutional sites (see figure 4.22) were chosen, exchanging O by a C, N and S atom, respectively.

A detailed discussion on the magnetic exchange mechanism present in the respective anion doped Fe-X-Fe (X=C,N,S) complexes will be given and its effect on ground state properties like the band gap and the total magnetic moment of the GFOX simulation cell will be discussed. Beside trying to explain the enhanced photocatalytic property reported by Dhanasekaran and Gupta [230] we use *ab initio* calculations as a predictive tool, revealing properties that are useful for new applications and may help to interpret future experimental results. The computational details and methods used in the following are given in section 4.6.1 Computational Details and Methods.

4.7.1 Choosing the anion doping sites in GFO

Figure 4.23 shows the projected density of states (PDOS) of an undoped $Fe1_a$-O(1)-Fe2 configuration inside the stoichiometric GFO simulation cell. Visible are the equal magnetic moments of the $Fe1_a$ and Fe2 d states given in red and yellow, respectively.

The O p states, highlighted in blue, are mainly populated in the energy range of -5 eV up to -1 eV. Taking a closer look at the Fe1$_a$ d states, one recognizes populated states in the spin up channel. In addition to the 5 electrons, occupying the spin down channel, we find an extra electron in the spin up channel. This additional electron originates from the "virtual electron transfer" and leads to the observed about $4\mu_B$ per Fe atom. Same is true for the Fe2 atom.

In stoichiometric GFO the AFM superexchange is dominated by two Fe1-O-Fe2 complexes. These are the Fe1$_a$-O(1)-Fe2 and Fe1$_b$-O(2)-Fe2 configuration with an enclosed angle of 126.34° and 123.01°, respectively (see figure 4.22). For visualizing the latter, the simulation cell has to be replicated in c direction. Geometrically these two complexes are connected to each other forming an Fe1-O-Fe2 twisted chain. The stoichiometric GFO unit cell contains two Fe1-O-Fe2 chains formed by the four upper left and four lower right Fe atoms (figure 4.22). The Fe1$_b$-O(3)-Fe2 complex, connecting these two chains, shows a reduced AFM coupling (see section 4.6.2).

Oxygen plays a crucial role in the AFM superexchange mechanism. Exchanging the O atom by another nonmetal X=C,N,S could affect and alter the magnetic exchange inside the respective doped Fe1-X-Fe2 complex and as a consequence change the electronic and magnetic properties of the GFO host matrix. Since there are two Fe1-O-Fe2 complexes dominating the AFM superexchange, the respective cell site occupation may be substantial for the resulting magnetic coupling and ground state magnetic moment.

Figure 4.22 shows the four substitutional O sites, highlighted in black. Site (1) and (2) form the AFM coupling strength dominating Fe1-O-Fe2 configurations. Lattice site (3) connects the Fe1$_b$ atom of the upper chain to an Fe2 atom of the lower magnetic chain, forming the Fe1$_b$-X(3)-Fe2 configuration that is characterized by a weak bonding in stoichiometric GFO. The next nearest neighbours of cell site (4) are a Ga and an Fe2 atom. In undoped GFO the corresponding Fe2-O(4)-Ga configuration shows no magnetic coupling, since the Ga atom is nonmagnetic.

Anion doping can affect the GFO simulation cell in several ways. Beside local alterations of the magnetic exchange mechanism changes in the cell geometry are introduced as well which again influence the magnetic coupling. To account for that various properties of the stoichiometric and doped simulation cells are compared to each other. These include the band gap, the total magnetic moment per simulation cell and the magnetic moment of the impurity atoms and the surrounding Fe atoms as well as the cell structure parameters. Structural parameters of interest are the Fe1-X-Fe2 (X= C,N,O,S) bond length and enclosed angle of the respective substitution site.

The corresponding parameters of the stoichiometric GFO simulation cell are given in table 4.6. The Fe1-O and Fe2-O distances are almost equal showing only small variations.

The respective O atoms are essentially nonmagnetic and the Fe atoms carry an absolute magnetic moment of about 4.1μ_B (see table 4.6). The band gap calculated within the HSE approximation is 2.68 eV for the spin up and 2.65 eV for the spin down gap. The calculated AFM coupling strength is -1.47 eV (E_{diff}[AFM-FM]). All energy differences given in this work are calculated per unit cell.

Figure 4.24(a) and (b) show the magnetization density (spin up minus spin down) of the Fe1_a-O(1)-Fe2 complex inside the stoichiometric GFO simulation cell. Given in red and blue are the positive and negative magnetization densities, respectively. (a) plots the spin density of all occupied states. Visible are the negative and positive spin densities of the Fe1_b and Fe2 atom, respectively. The O(1) p states are polarized, showing an inner and outer polarization. The inner polarization is more pronounced and has reversed orientation compared to the outer one which is decreased.

The outer polarization of the O(1) p states can be more clearly seen in figure 4.24(b). They form an orbital overlap between the Fe atom an the O atom. This overlap corresponds to the virtual electron transfer and induces the AFM superexchange. Figure 4.24(b) shows the partial spin density for the energy range of -5 eV up to the Fermi level and allows a better presentation of the superexchange mechanism. The O p states are almost evenly distributed over an energy range of -4 eV up to -1 eV (see figure 4.23).

Regarding the PDOS of the anion doped systems (see the following sections), there is an increased number of electronic states near the Fermi level. This most likely can be attributed to an enhanced interaction with the neigbouring Fe atoms and to the reduced electronegativity of the anion dopants. The magnetic exchange mechanism in these systems is located in the upper part of the PDOS between -1 eV up to the Fermi level. The following anion doped partial magnetization densities are therefore plotted in the respective energy range. Plotting the partial magnetization density for stoichiometric GFO in the range of -1 eV up to the Fermi level would yield equal spatial spin density distributions as shown in figure 4.24(b) but with vastly decreased intensities. The superexchange mechanism and its overlapping Fe-O orbitals are therefore much less visible anymore. Hence, comparing the partial magnetization densities of pure and anion doped GFO is still reasonable for the chosen energy ranges. Noteworthy we do not include inner cationic site disorder to our calculations, keeping the system simple in a first approach. Inner cationic site disorder describes site changes of Ga and Fe atoms which are well known for GFO and often seen in experiment [192, 194–196].

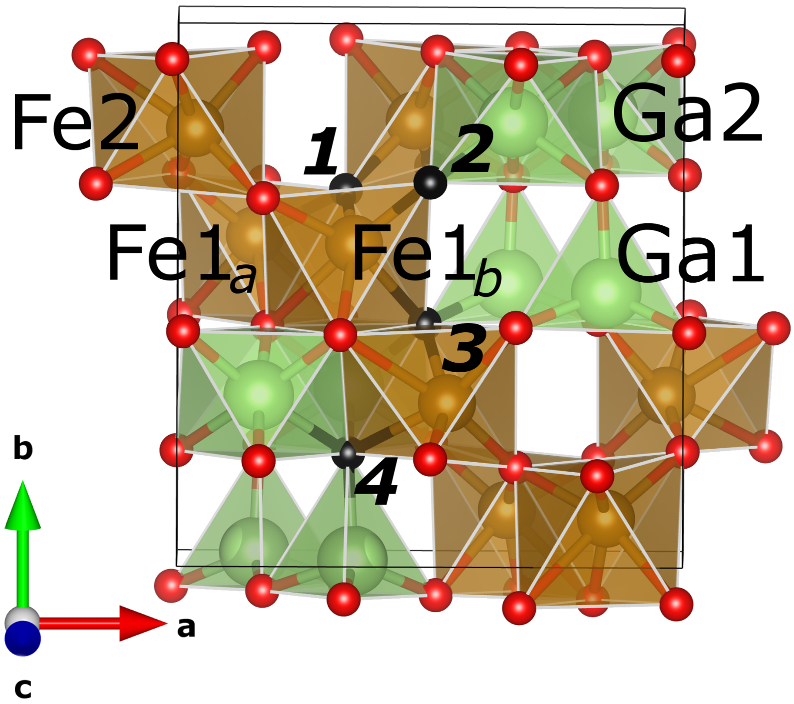

Figure 4.22: Cell structure of stoichiometric GFO. The Ga1, Ga2, Fe1 and Fe2 sublattices are indicated as well as the four investigated doping sites (1)-(4). This figure was created using the VESTA program [115].

4.7.2 Carbon doping

Substituting a single O atom with a C atom has various effects on the GFO host matrix. It increases the cell volume and can introduce a net magnetic moment to the GFO host matrix (see 4.7). The C(1) substitution is the energetically most stable doping configuration. Substituting cell site (2) is only 4 meV less probable compared to the C(1) substitution and placing the C atom on site (3) is by 235 meV less favourable in energy. The cell site (4) substitution is the most unfavourable doping configuration with 507 meV energy difference compared to the C(1) case.

C(1) substitution

In the following, we focus on the geometric, electronic and magnetic properties of C(1) doped GFO (GFOC(1)). Starting with the structural properties of the $Fe1_a$-C(1)-Fe2 complex, the $Fe1_a$-C(1) and Fe2-C(1) bonds show increased bond lengths variations compared to the $Fe1_a$-O(1)-Fe2 configuration in stoichiometric GFO (see table 4.6 and table 4.7). The $Fe1_a$-C(1) bond is increased to 2.15 Å the Fe2-C(1) distance is reduced to

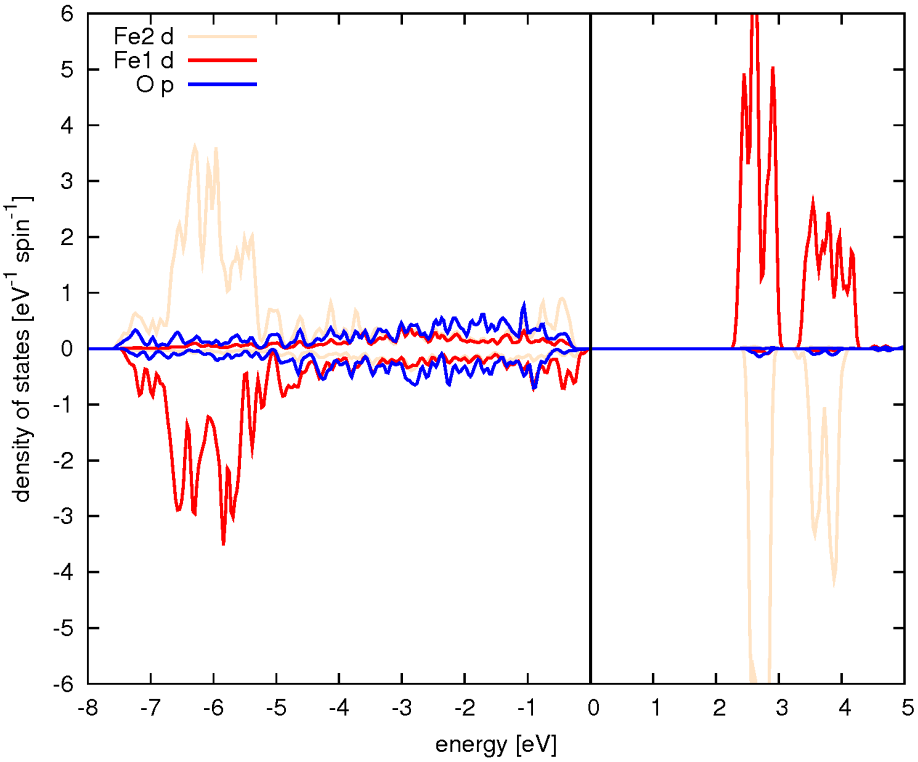

Figure 4.23: PDOS of the Fe1$_a$-O(1)-Fe2 configuration in stoichiometric GFO. Given in red and beige are the Fe1$_a$ and Fe2 d states. Highlighted in blue are the O p states.

1.70 Å compared to undoped GFO. The overall Fe1$_a$-X(1)-Fe2 bond length, however, almost remains the same. Exchanging O with C increases the Fe1$_a$-X(1)-Fe2 enclosed angle from 126.34° to 131.99° and reduces the Fe1$_b$-X(1)-Fe2 enclosed angle from 123.01° to 121.14°.

In stoichiometric GFO each Fe atom carries a magnetic moment of about $4\mu_B$. In the C(1) substitution case, however, the Fe2 atom next to the C(1) atom has a reduced magnetic moment of about $+3\mu_B$, changing the actual AFM coupling into a ferrimagnetic exchange.

Figure 4.25 shows the PDOS of the Fe1$_a$-C(1)-Fe2 complex inside GFOC(1) calculated within the HSE approximation. To gain better insight in the exchange mechanism the number of electrons are integrated, dividing the PDOS into two parts. First includes the energy range of -8 eV up to -1 eV and second from -1 eV up to the Fermi level.

The PDOS of the Fe1$_a$ d electrons in GFOC(1) and stoichiometric GFO are very similar (see figure 4.23 and figure 4.25). The magnetic exchange mechanism present between the Fe1$_a$-C(1) and the Fe1$_a$-O(1) atoms are therefore alike. Integrating the Fe1$_a$ d states between -8 eV up to -1 eV yields 4.61 electrons in the spin down channel and

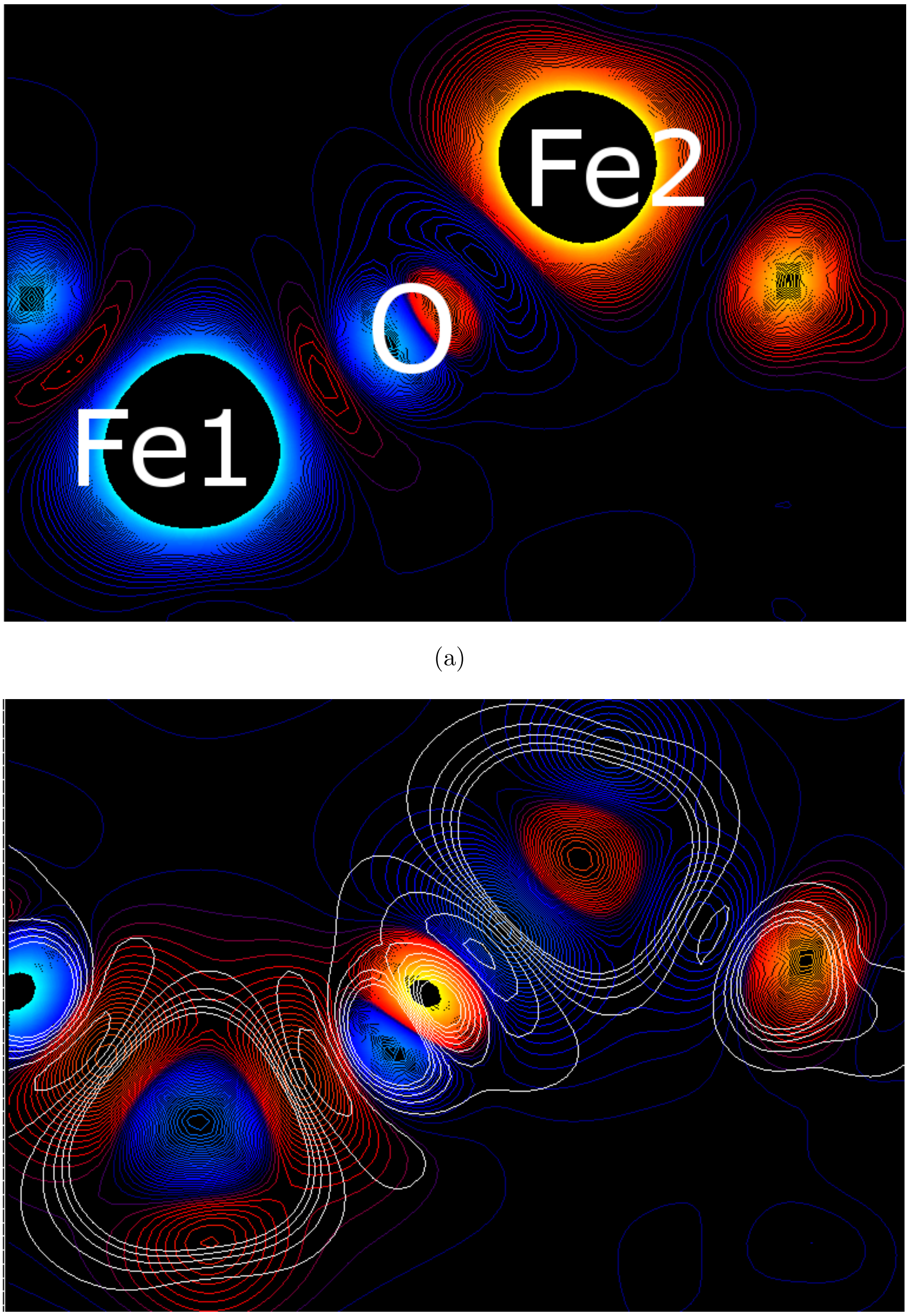

(a)

(b)

Figure 4.24: Magnetization density of the Fe1_a-O(1)-Fe2 complex inside stoichiometric GFO. Given in red and blue are positive and negative spin densities, respectively. (a) shows the spin density of all occupied states. (b) gives the partial spin density in the energy range of -5 eV up to the Fermi level. A coarse mesh of the total magnetization density shown in (a) is overlayed (highlighted in white) to illustrate the spatial extent of the covalent bond. This figure was created using the VisIt program [135].

Table 4.6: Geometric, magnetic and electronic properties of the respective cell sites (1)-(4) in stoichiometric GFO. The simulation cell was relaxed using the GGA+U approximation followed by an on top HSE calculation. Given are the direct band gap and the energy difference between the AFM and hypothetical FM structure.

X=	O(1)	O(2)	O(3)	O(4)
Cell volume (Å^3)	416.17	416.17	416.17	416.17
Fe1$_a$-X (Å)	1.96	—	—	—
Fe1$_b$-X (Å)	1.97	1.93	2.09	—
Fe2-X (Å)	1.89	1.94	2.09	2.13
Fe1$_a$-X-Fe2 (°)	126.34	—	—	—
Fe1$_b$-X-Fe2 (°)	123.01	123.01	102.62	—
M_{tot} (μ_B)	0	0	0	0
X(μ_B)	-0.07	-0.02	+0.003	+0.07
Fe1$_a$ (μ_B)	-4.10	-4.10	-4.10	-4.10
Fe1$_b$ (μ_B)	-4.10	-4.10	-4.10	-4.10
Fe2 (μ_B)	+4.09	+4.09	+4.09	+4.09
Band gap $\uparrow\|\downarrow$(eV)	2.68|2.65	2.68|2.65	2.68|2.65	2.68|2.65
E[AFM-FM](eV)	-1.47	-1.47	-1.47	-1.47

another 0.72 electrons in the spin up channel. Adding the occupied states from -1 eV up to the Fermi level gives another 0.22 electrons in the spin down and 0.15 in the spin up channel, respectively, yielding a total of 0.37 electrons. In sum there are about 5 electrons in the minority spin channel and another electron in the majority spin channel resulting in the observed -4μ_B.

The Fe2 *d* states on the other hand are shifted towards the Fermi energy compared to stoichiometric GFO. Integrating the Fe2 *d* states from -8 eV up to -1 eV gives 3.99 electrons in the spin up channel and another 0.92 electrons occupying the spin down channel, yielding a magnetic moment of about +3μ_B. Summing up the electronic states from -1 eV up to the Fermi level gives 0.413 electrons in the spin up and 0.632 electrons in the spin down channel, adding up to 1.05 electrons. Both the Fe1$_a$ and the Fe2 atom carry about 6 *d* electrons each. The Fe2 atom, however, shows an accumulation of *d* states near the Fermi level indicating an enhanced interaction with the C(1) atom.

Integrating the C *p* states in the energy range of -8 eV to -1 eV gives 0.45 electrons in the spin down channel and another 0.33 electrons in the spin up channel. Adding up the electronic states from -1 eV up to the Fermi level yields a total of 0.56 *p* electrons

Table 4.7: Geometric, magnetic and electronic properties of single carbon doped GFO, regarding the doping configurations (1) to (4). The simulation cell was relaxed using the GGA+U approximation followed by an on top HSE calculation. Given are the direct band gap and the energy difference between the AFM and hypothetical FM structure.

X=	C(1)	C(2)	C(3)	C(4)
Cell volume (Å^3)	432.37 (+3.9%)	433.64 (+4.2%)	431.94 (+3.8%)	433.56 (+4.2%)
Fe1$_a$-X (Å)	2.15 (+9.7%)	—	—	—
Fe1$_b$-X (Å)	2.17 (+10.2%)	2.14 (+10.9%)	2.01 (-4.0%)	—
Fe2-X (Å)	1.70 (-10.1%)	1.77 (-8.8%)	2.07 (-1.0%)	1.99 (-6.6%)
Fe1$_a$-X-Fe2 (°)	131.99 (+4.5%)	—	—	—
Fe1$_b$-X-Fe2 (°)	121.14 (-1.5%)	125.23 (+1.8%)	99.79 (-2.8%)	—
M_{tot} (μ_B)	-2	-2	0	-2
X(μ_B)	-0.42	-0.49	-0.03	-0.57
Fe1$_a$ (μ_B)	-4.10	-4.11	-4.10	-4.10
Fe1$_b$ (μ_B)	-4.10	-4.03	-3.72	-4.10
Fe2 (μ_B)	+2.88	+3.23	+3.78	+3.72
Band gap $\uparrow\|\downarrow$(eV)	1.52|2.23	1.76|2.13	1.40|1.36	1.42|2.38
E[AFM-FM](eV)	-1.19	-1.39	-1.15	-1.33

with 0.40 electrons occupying the minority spin channel and another 0.16 electrons in the majority spin channel. The C(1) anion has a magnetic moment of -0.42μ_B and carries 1.33 p electrons.

The enhanced interaction and hybridization of Fe2 d and C(1) p states near the Fermi level is favoured by the reduced Fe2-C(1) bond length. An Fe2 d electron therefore becomes shifted upwards the Fermi energy forming an additional covalent bond with the C(1) atom. The magnetic moment of the in energy shifted Fe2 d electron, however, becomes compensated in that respective bond, reducing the magnetic moment of the Fe2 atom to about +3μ_B introducing a ferrimagnetic coupling inside the Fe1$_a$-C(1)-Fe2 complex. Adding up all magnetic contributions of the C(1) and Fe atoms, considering that the O atom show a small polarization as well, yields in a net magnetic moment of -2μ_B per simulation cell.

Fig 4.26 (a) and (b) show spin density plots (spin up minus spin down) of the Fe1$_a$-C(1)-Fe2 complex with an enclosed angle of 131.99°. Given in red and blue are the positive and negative magnetization densities, respectively. Both (a) and (b) show an in-plane picture perpendicular to the z axis. (a) shows the spin density plot of the total DOS.

Clearly visible are the positive and negative magnetization densities located at the Fe1$_a$ and the Fe2 atom respectively. The C(1) atom is polarized. The negative polarization is turned towards the Fe2 atom and the smaller positive magnetization faces the Fe1$_a$ atom. (b) shows the partial magnetization density of the energy range of -1 eV up to the Fermi level. It reveals the spatial extent of the covalent bond formed within the Fe1$_a$-C(1)-Fe2 complex. A coarse mesh of the total magnetization density shown in (a) is overlaid (highlighted in white) to illustrate the spatial extent of the covalent bond. Clearly visible is the orbital overlap of the negative magnetization density given in blue between the C(1) and Fe2 atom. This overlap reduces the original $+4\mu_B$ of the Fe2 atom to the calculated $+3\mu_B$. The positive magnetization density overlap of the C(1) and the Fe1$_a$ atom on the other hand is less pronounced.

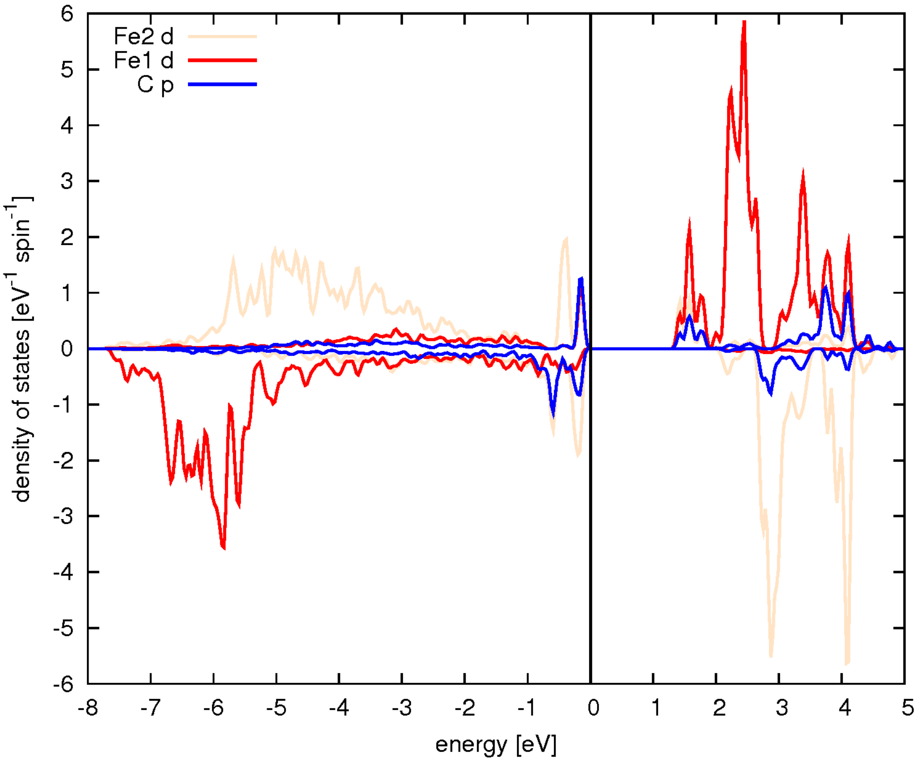

Figure 4.25: PDOS of the Fe1$_a$-C(1)-Fe2 configuration in GFOC(1). Given in red and beige are the Fe1$_a$ and Fe2 d states. Highlighted in blue are the C p states.

C(2) substitution

Introducing a C impurity at cell site (2) also yields a total magnetic moment of $-2\mu_B$ per simulation cell and evokes a ferrimagnetic coupling inside the Fe1$_b$-C(2)-Fe2 configuration. The Fe1$_b$-X(2)-Fe2 enclosed angle is increased by +1.8% to 125.23°. The C(2)-Fe1$_b$ and

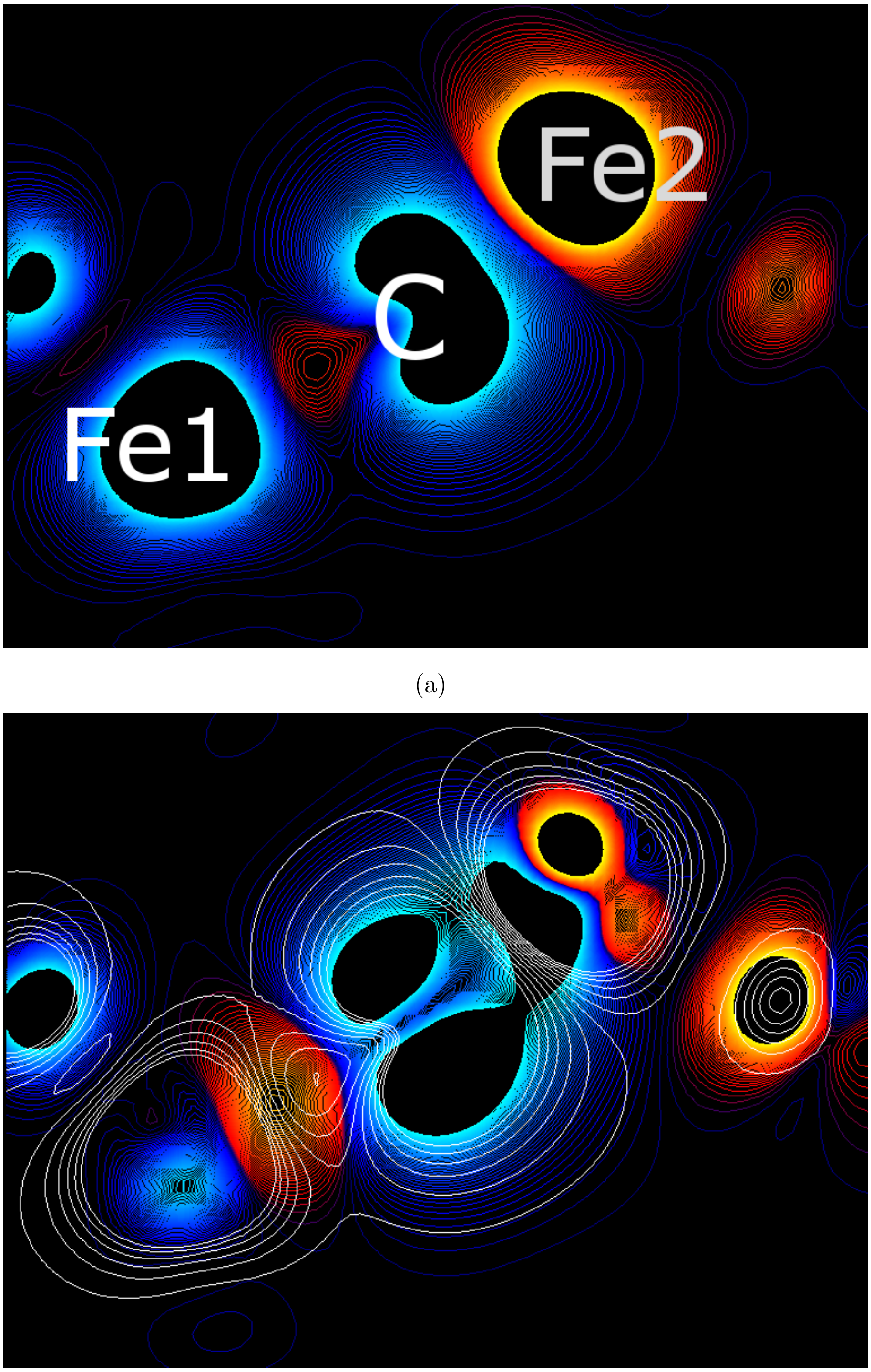

(a)

(b)

Figure 4.26: Magnetization density of the Fe1$_a$-C(1)-Fe2 complex in GFOC(1). Given in red and blue are positive and negative spin densities, respectively. (a) shows the spin density of all occupied states. (b) gives the partial spin density in the energy range of -1 eV up to the Fermi level. This figure was created using the VisIt program [135].

C(2)-Fe2 bond lengths again vary while the first one is elongated and the second one reduced due to the enhanced covalent exchange interaction between the C(2) and Fe2 atom. Both the C(1) and C(2) substitutions induce a ferrimagnetic ground state and reduce the band gap compared to stoichiometric GFO. The respective band gaps are not symmetric due to the magnetic ground state.

C(3) substitution

Whereas cell site (1) and (2) are part of the AFM coupling mediating Fe1-O-Fe2 chains, cell site (3) and (4) are not. In stoichiometric GFO the O(3) atom mediates a very weak AFM coupling between its next nearest Fe1_b and Fe2 atoms. The respective Fe1_b and Fe2 atoms are already "saturated" and do not enter further AFM superexchange interactions with additional O atoms outside these chains. Substituting cell site (3) with a C atom yields a nonmagnetic ground state. The C(3) impurity is nonmagnetic and the Fe1_b and the Fe2 atoms show an absolute magnetic moment of about $4\mu_B$, each. The Fe1_b-C(3) and C(3)-Fe2 bond lengths vary marginally and are similar to the corresponding bonds in stoichiometric GFO. However, there is a small reduction of the magnetic moment of the Fe1_b and Fe2 atom (see table 4.7), suggesting the presence of a small orbital overlap and a weak interaction with the C(3) atom. Substituting cell site (3) with a C impurity reduces the band gap the most.

C(4) substitution

The energetically most unfavourable doping configuration is the substitution of cell site (4). The next nearest cations are a Ga2 and Fe2 atoms. No Fe1-C(4)-Fe2 complex is formed in that particular case. However, the simulation cell shows a total magnetic moment of $-2\mu_B$. The Fe2-C(4) distance is reduced compared to the undoped Fe2-O(4) configuration. The cell volume is increased and the C(4) atom carries a magnetic moment of $-0.57\mu_B$. To rule out having found a meta stable solution a comparative calculation was performed, forcing the simulation cell into a nonmagnetic ground state. The magnetic solution however remains more favourable by about 200 meV. Regarding table 4.7 the next nearest Fe2 atom shows a reduced magnetic moment, indicating an orbital overlap with the C(4) atom.

Surprisingly, the C(3) and C(4) substitutions show different magnetic behaviour. The nonmagnetic state of the C(3) atom can be attributed to its neighbouring Fe1_b and Fe2 atom. The distances to both Fe cations, which are part of the Fe1_b-C(3)-Fe2 complex, are almost symmetric. No strong covalent bond is formed as in the C(1) and C(2) substitution. The magnetic polarization introduced by the Fe neighbours fully compensates at the C(3) site ending up in a nonmagnetic state. In the C(4) substitution case the anion interacts only with its next nearest Fe2 cation. The C(4)-Fe2 distance is reduced compared to stoichiometric GFO and the C anion polarizes asymmetric with a finite magnetic moment.

4.7.3 Nitrogen Doping

Substituting O with N leads to a ground state magnetic moment of -1μ_B per simulation cell for all investigated doping configurations. In any of the studied cases the N atom shows increased interaction with its next nearest Fe2 atom. The respective Fe2-N distances are reduced compared to the corresponding Fe2-O bonds in stoichiometric GFO. The decreased Fe2-N bond length introduces a larger orbital overlap between the N and the Fe2 atom. The magnetic moment of the Fe2 atom is slightly reduced by this overlap, especially notable for the N(3) and N(4) substitution sites (see table 4.8). Introducing a N impurity enhances the cell volume and reduces the band gap for all doping configurations. The N(1) substitution is the energetically most stable doping configuration similar to the C(1) substitution. Almost equal in energy is the N(3) lattice site substitution with only 6 meV energy difference. Followed by that is the N(4) doping configuration being 43 meV less favourable. The energetically least probable N doping case is the N(2) lattice site occupation, with 70 meV energy difference compared to the N(1) configuration. The overall energy differences, however, are very small compared to the C substitutions.

N(1) substitution

Regarding the structural properties of the Fe1$_a$-N(1)-Fe2 complex, the Fe1$_a$-N(1) bond length is decreased and the N(1)-Fe2 bond increased by -1.6% and +4.1% respectively compared to stoichiometric GFO. Both Fe-O bonds experience less geometric alterations compared to the C(1) doped case. The Fe1$_a$-N(1)-Fe2 enclosed angle is enhanced by +1.1% to 127.75°. The cell volume is increased and the ground state shows a magnetic moment of -1μ_B per simulation cell, which could be expected, since one hole is introduced, substituting O by N.

Figure 4.27 shows the PDOS of the Fe1$_a$-N(1)-Fe2 configuration (calculated within the HSE approximation). Given in beige and red are the Fe2 and Fe1$_a$ *d* states, respectively. Highlighted in blue are the N(1) *p* states. The DOS of the Fe1$_a$ and Fe2 *d* states is similar to the undoped Fe1$_a$-O(1)-Fe2 configuration in stoichiometric GFO shown in figure 4.23. The Fe2 *d* states are not shifted towards the Fermi level like in the C(1) doped case and the N(1) impurity introduces an acceptor state located near the center of the band gap.

There is an enhanced accumulation of N(1) *p* states near the Fermi energy similar to the C(1) doped case. The covalent bonding between the N(1) and Fe2 atom, however, is

Table 4.8: Geometric, magnetic and electronic properties of single nitrogen doped GFO, regarding the doping configurations (1) to (4). The simulation cell was relaxed using the GGA+U approximation followed by an on top HSE calculation.Given are the direct band gap and the energy difference between the AFM and hypothetical FM structure.

X=	N(1)	N(2)	N(3)	N(4)
Cell volume (Å^3)	432.80(+4.0%)	432.84(+4.0%)	429.90(+3.3%)	429.70(+3.3%)
Fe1$_a$-X (Å)	2.04(+4.1%)	—	—	—
Fe1$_b$-X (Å)	2.05(+4.1%)	2.03(+5.2%)	2.07(-1.0%)	—
Fe2-X (Å)	1.86(-1.6%)	1.91(-1.5%)	1.94(-7.2%)	1.96(-8.0%)
Fe1$_a$-X-Fe2 (°)	127.75(+1.1%)	—	—	—
Fe1$_b$-X-Fe2 (°)	119.75(-2.7%)	122.83(-0.1%)	102.47(-0.1%)	—
M_{tot} (μ_B)	-1	-1	-1	-1
X(μ_B)	-0.61	-0.57	-0.29	-0.24
Fe1$_a$ (μ_B)	-4.06	-4.11	-4.11	-4.11
Fe1$_b$ (μ_B)	-4.05	-4.06	-4.07	-4.10
Fe2 (μ_B)	+3.97	+4.00	+3.66	+3.68
Band gap ↑|↓(eV)	1.38|2.36	1.26|2.53	1.19|1.91	1.14|2.23
E[AFM-FM](eV)	-1.58	-1.45	-1.28	-1.39

not as strong as in the C(1) substitution case. No additional covalent bond is formed, reducing the magnetic moment of the corresponding Fe2 atom. Integrating the number of N(1) *p* states in the energy range of -1 eV up to the Fermi level gives a total of 0.51 electrons. The respective electrons are almost evenly distributed among both spin channels. 1.81 N *p* states are occupied in the energy range of -8 eV up to -1 eV yielding a magnetic moment of -0.55μ_B. The N atom has a total of 2.31 *p* electrons and a magnetic moment of about 0.61μ_B.

While 42% of the C(1) *p* states are located in the small energy range of -1 eV up to the Fermi level only 22% of the N(1) *p* electrons are found in the respective energy range. The N(1) *p* states are therefore mainly located in lower energy ranges compared to the C(1) *p* electrons. This can be attributed to the higher electronegativity of the N atom as well as to the weak N(1)-Fe2 covalent bond. The enhanced C(1)-Fe2 interaction shifts both the C(1) *p* states and Fe2 *d* states towards the Fermi level. The number Fe2 *d* states in the energy range of -1 eV up to the Fermi level therefore gives information on the interaction with the respective anion dopant. In the C(1) doped case 1.05 Fe2 *d* electrons are located in the corresponding energy range, whereas there are only 0.50 Fe2 *d* electrons in the N(1) substitution case. The over all number of Fe2 *d* electrons, though, differs negligible with 5.95 and 5.71 Fe2 *d* electrons in the N(1) and C(1) doped case, respectively. The number of the $\mathrm{Fe1}_a$ *d* electrons are similar as well with 5.69 and 5.72 in the N(1) and C(1) substitution case.

Figure 4.28(a) shows the total magnetization density and (b) the partial spin density for the energy range of -1 eV up to the Fermi level. All values are calculated within the HSE approximation. The negative magnetic density of the N(1) atom is peanut like shaped and has a small droplet formed positive magnetization density next to it. The positive magnetization density is more pronounced in the C(1) substitution, which can be attributed to the decreased magnetic moment of the C(1) impurity.

Figure 4.28 (b) shows the magnetic interaction present within the $\mathrm{Fe1}_a$-N(1)-Fe2 complex. The interaction mediated via the N(1) atom is similar to the undoped $\mathrm{Fe1}_a$-O(1)-Fe2 complex in stoichiometric GFO (see figure 4.24). Both show an inner and outer polarization of the anion *p* states. The orbital overlap between the O(1) and the Fe states, however, is more pronounced. The magnetization density of the energy range of -2 eV up to -1 eV (not shown here) is similar to the one shown in (a). The electrons, forming the covalent bond, are therefore solely located in the energy range of -1 eV up to the Fermi level.

N(2) substitution

The $\mathrm{Fe1}_b$-N(2)-Fe2 complex shows larger differences in the single bond lengths and a slightly reduced magnetic moment of the N(2) atom. Cell volume and band gap are similar to the N(1) doped case. The enclosed angle is reduced by only 0.1% compared to stoichiometric GFO.

N(3) substitution

In the N(3) substitution case the respective the Fe2-N(3) bond experiences larger structural distortions compared to the N(1) and N(2) doping cases. The Fe2-N(3) distance becomes reduced by -7.2% and the $\mathrm{Fe1}_b$-N(3) distance decreased by -1.0% compared to stoichiometric GFO. The enclosed angle however reduces by small -0.1%. The magnetic moments of the Fe2 and N(3) atom are decreased, compared to the N(1) and N(2) doping configurations. Spin up and spin down gap are reduced the most in this doping case.

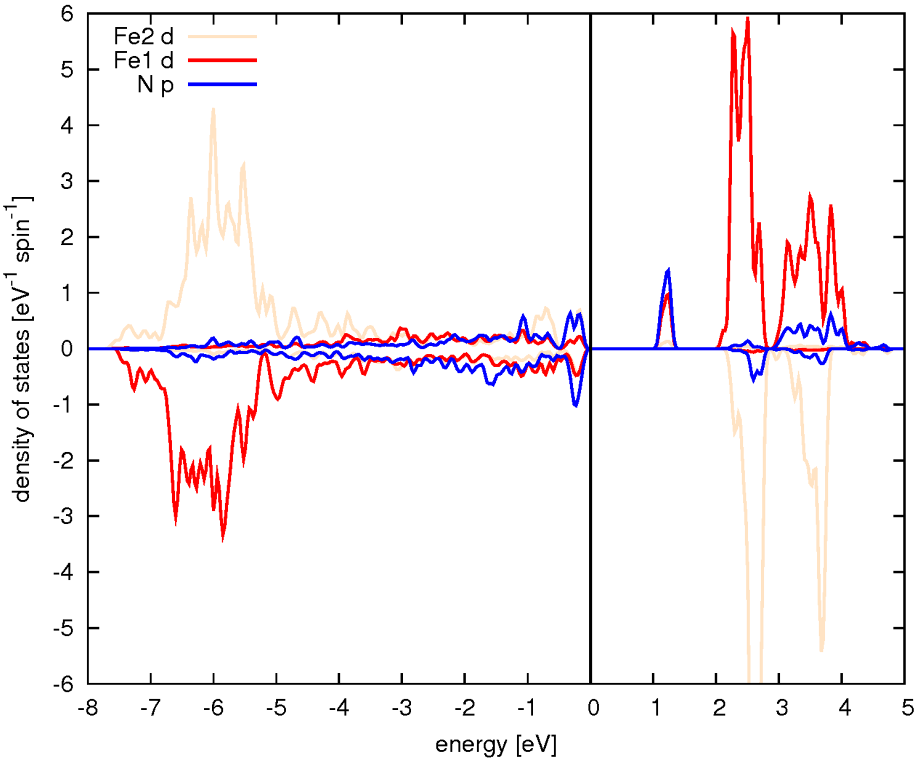

Figure 4.27: PDOS of the Fe1$_a$-N(1)-Fe2 configuration in GFON(1). Given in red and beige are the Fe1$_a$ and Fe2 *d* states. Highlighted in blue are the N *p* states.

N(4) substitution

In the N(4) substitution the next nearest cationic neighbours of the N(4) atom are a Ga2 and an Fe2 atom. The respective Fe2-N(4) distance is reduced by -8.0%. This is the largest Fe-N bond length reduction of all N doping cases. The magnetic moment of the Fe2 and N(4) atoms are reduced to +3.68μ_B and -0.24μ_B, respectively.

4.7.4 Sulfur Doping

Sulfur and oxygen have the same number of valence *p* electrons. The S atom shows no magnetic moment in any of the investigated doping configurations leaving the ground state AFM. Incorporating a S atom introduces considerable lattice distortions due to the larger atomic radius and as a consequence influences the AFM coupling inside the crystal.

The S(1) doping configuration is the energetically most favourable substitution site. Followed by that is the S(2) substitution which is about 140 meV less probable. S(3) is the most unfavourable doping configuration with more than half an eV energy difference compared to the S(1) substitution. Placing the S atom on cell site (4) is about 450 meV

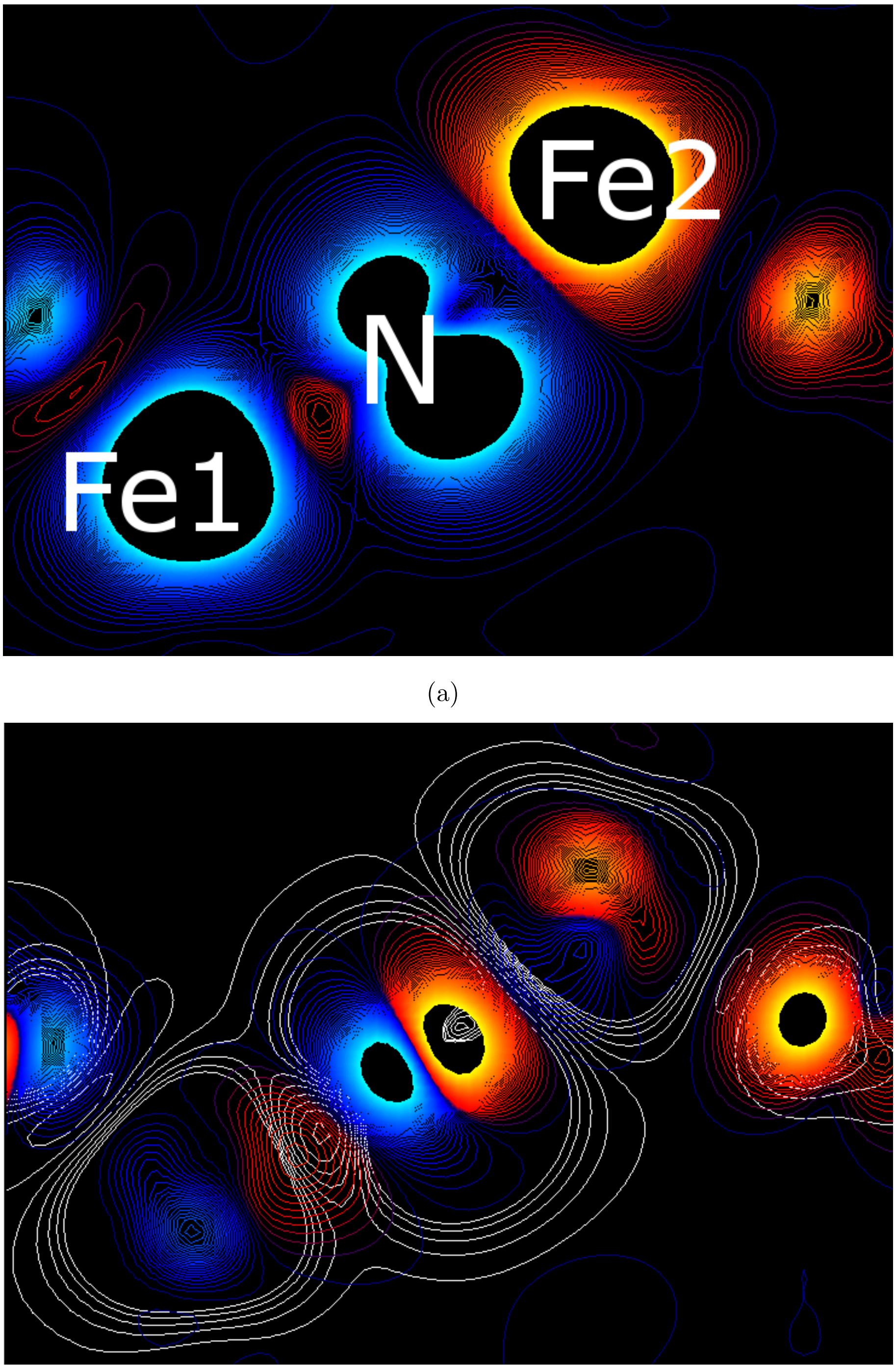

(a)

(b)

Figure 4.28: Magnetization density of the Fe1_a-N(1)-Fe2 complex in GFON(1). Given in red and blue are positive and negative spin densities, respectively. (a) shows the spin density of all occupied states. (b) gives the partial spin density in the energy range of -1 eV up to the Fermi level. This figure was created using the VisIt program [135].

less favourable in energy.

The magnetic coupling, mediated via the S atom, is similar to the one transferred by the O atom. A comparison of the AFM coupling strength of both systems is therefore reasonable. N and C on the other hand induce different magnetic coupling mechanisms such that a comparison of the AFM coupling strength with pure GFO is not meaningful (see table 4.9).

Table 4.9: Geometric, magnetic and electronic properties of single sulfur doped GFO, regarding the doping configurations (1) to (4). The simulation cell was relaxed using the GGA+U approximation, followed by an on top HSE calculation. Given are the direct band gap and the energy difference between the AFM and hypothetical FM structure.

X=	S(1)	S(2)	S(3)	S(4)
Cell volume (Å^3)	443.01(+6.4%)	443.09(+6.5%)	446.07(+7.2%)	445.19(+7.0%)
Fe1$_a$-X (Å)	2.29(+16.8%)	—	—	—
Fe1$_b$-X (Å)	2.31(+17.3%)	2.27(+17.6%)	2.31(+10.5%)	—
Fe2-X (Å)	2.24(+18.5%)	2.24(+15.5%)	2.31(+10.5%)	2.35(+10.3%)
Fe1$_a$-X-Fe2 (°)	130.17(+3.0%)	—	—	—
Fe1$_b$-X-Fe2 (°)	121.07(-1.6%)	119.35(-3.0%)	106.40(+3.7%)	—
M_{tot} (μ_B)	0	0	0	0
X(μ_B)	-0.09	+0.02	+0.03	+0.08
Fe1$_a$ (μ_B)	-4.02	-4.09	-4.13	-4.12
Fe1$_b$ (μ_B)	-4.01	-4.02	-4.01	-4.12
Fe2 (μ_B)	+4.01	+3.98	+4.01	+4.02
Band gap $\uparrow\|\downarrow$(eV)	1.81|1.87	1.77|1.85	2.07|2.16	2.03|2.58
E[AFM-FM](eV)	-1.48	-1.45	-0.44	-1.51

S(1) substitution

Substituting O(1) with a S atom increases the cell volume by 6.4%. The Fe1$_a$-S(1) and the Fe2-S(1) bond lengths are elongated by notable 16.8% and 18.5% respectively compared to stoichiometric GFO. This is in contrast to the C(1) and N(1) anion doping cases, where the Fe2-X(1) distance is decreased introducing an enhanced interaction. The enclosed angle of the Fe1$_a$-S(1)-Fe2 configuration is increased to 130.17° and the band gap becomes reduced by more than 1 eV for each spin channel. S has the smallest electronegativity of all investigated anion dopants. A large part of the electronic *p* states are therefore found in the upper part of the DOS in the energy range of -1 eV up to the Fermi level (see figure 4.29). Integrating the number of S p electrons in the energy range of -8 eV up to the Fermi level gives 2.47 occupied states. 1.35 of these states are located between -8 eV and -1 eV. The remaining 1.13 electrons, which represent 46% of the S p electrons, are found in the small energy of range of -1 eV up to the Fermi level. Both the $\mathrm{Fe1}_a$ and the Fe2 atom carry 6 d electrons and show an absolute magnetic moment of about $4\mu_B$.

Figure 4.30(a) shows the total magnetization density of the respective $\mathrm{Fe1}_a$-S(1)-Fe2 complex in GFOS(1). The inner and outer polarization show a decreased spin density compared to the $\mathrm{Fe1}_a$-O(1)-Fe2 configuration in stoichiometric GFO (see figure 4.24(a)) .

Figure 4.30(b) shows the magnetization density within the energy range of -1 eV up to the Fermi level. The outer polarization presents the covalent bonding and shows decreased intensity compared to the inner polarization. Regarding the energy range of -4 eV up to -1 eV (see figure 4.31) the inner polarization vanishes and the outer antiparallel spin density expands over the inner one. Hence, a spatially expanded positive and negative magnetization density cloud remains at the S(1) site next to the Fe1 and Fe2 atom, respectively. The covalent bond between the S and Fe atoms is therefore mainly formed in the energy range of -4 eV up to -1 eV. The accumulation of S p states near the Fermi level (see figure 4.30(b)) shows reduced interaction with the neighbouring Fe atoms and mostly forms the inner polarization.

Plotting the whole energy range shown in figure 4.30(a) gives an superimposed picture of the discussed partial energy ranges. These compensate each other adding up to a reduced total spin polarization density at the S(1) site compared to the magnetization density plots of stoichiometric, C(1) and N(1) doped GFO.

The O p electrons generating the inner and outer polarization in stoichiometric GFO (figure 4.24(a)), exhibit less energetic separation. They are almost evenly distributed along the energy range of -5 eV up to -1 eV. This is in contrast to the C(1)/C(2) and N(1)/N(2) doped case where the covalent bond between the anion and Fe atoms is formed in the energy range of -1 eV up to the Fermi level.

The calculated AFM coupling strength of stoichiometric GFO is -1.47 eV. Even though the simulation cell's geometry is altered introducing the S(1) atom the effect on the overall AFM coupling strength is small being reduced by only 60 meV (see table 4.9) .

S(2) substitution

Exchanging O(2) by a S atom has similar effects on the GFO simulation cell. The band gap reduces by more than 1 eV and the cell volume enhances by 6.5%. Both Fe-S(1) bond lengths of the $\mathrm{Fe1}_b$-S(2)-Fe2 configuration increase compared to the undoped system.

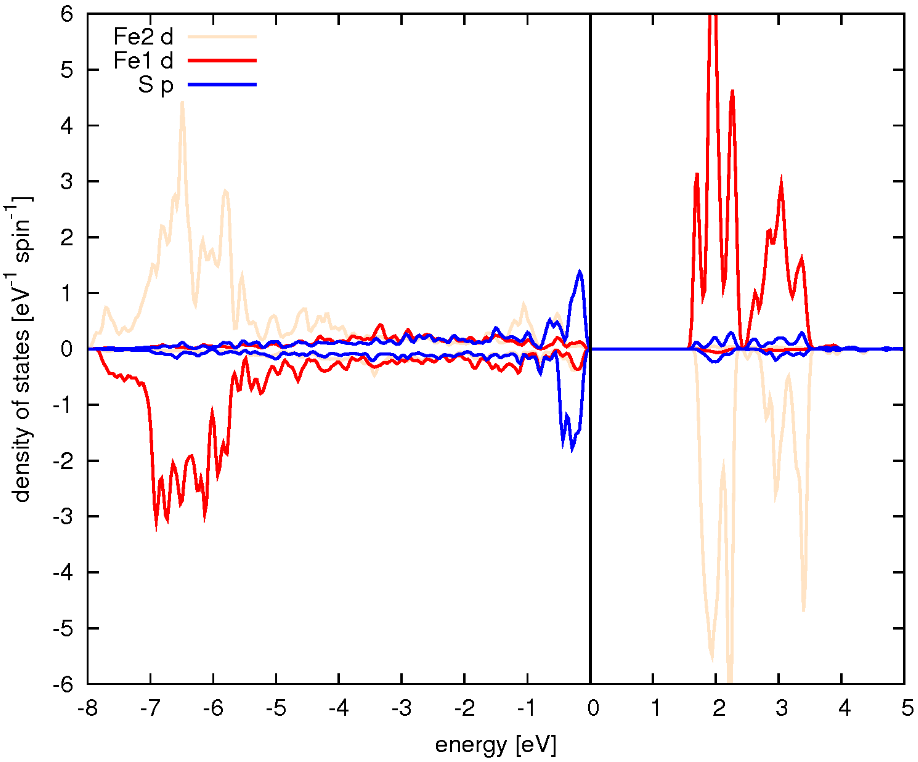

Figure 4.29: PDOS of the Fe1$_a$-S(1)-Fe2 configuration in GFOS(1). Given in red and beige are the Fe1$_a$ and Fe2 d states. Highlighted in blue are the S p states.

The Fe1$_b$-S(2)-Fe2 enclosed angle decreases to 119.35° and the AFM coupling strength is reduced to -1.45 eV.

S(3) substitution

Cell site substitution (3) shows an AFM coupling strength of only -0.44 meV. The structure of the AFM coupling strength mediating Fe1-O-Fe2 chains are distorted in a way that the respective Fe-O orbital overlap reduces. As a consequence, the respective doping configuration becomes the energetically most unfavourable one. The band gap is slightly enhanced compared to the S(1) and S(2) substitution. The Fe1$_b$-S(3)-Fe2 enclosed angle is increased to 106.40°.

S(4) substitution

In the S(4) substitution case the AFM coupling strength differs only by 30 meV compared to stoichiometric GFO. The band gap is reduced the least and the distance to the Fe2 atom is increased by +10.3%. Since the AFM coupling strength is similar to stoichiometric

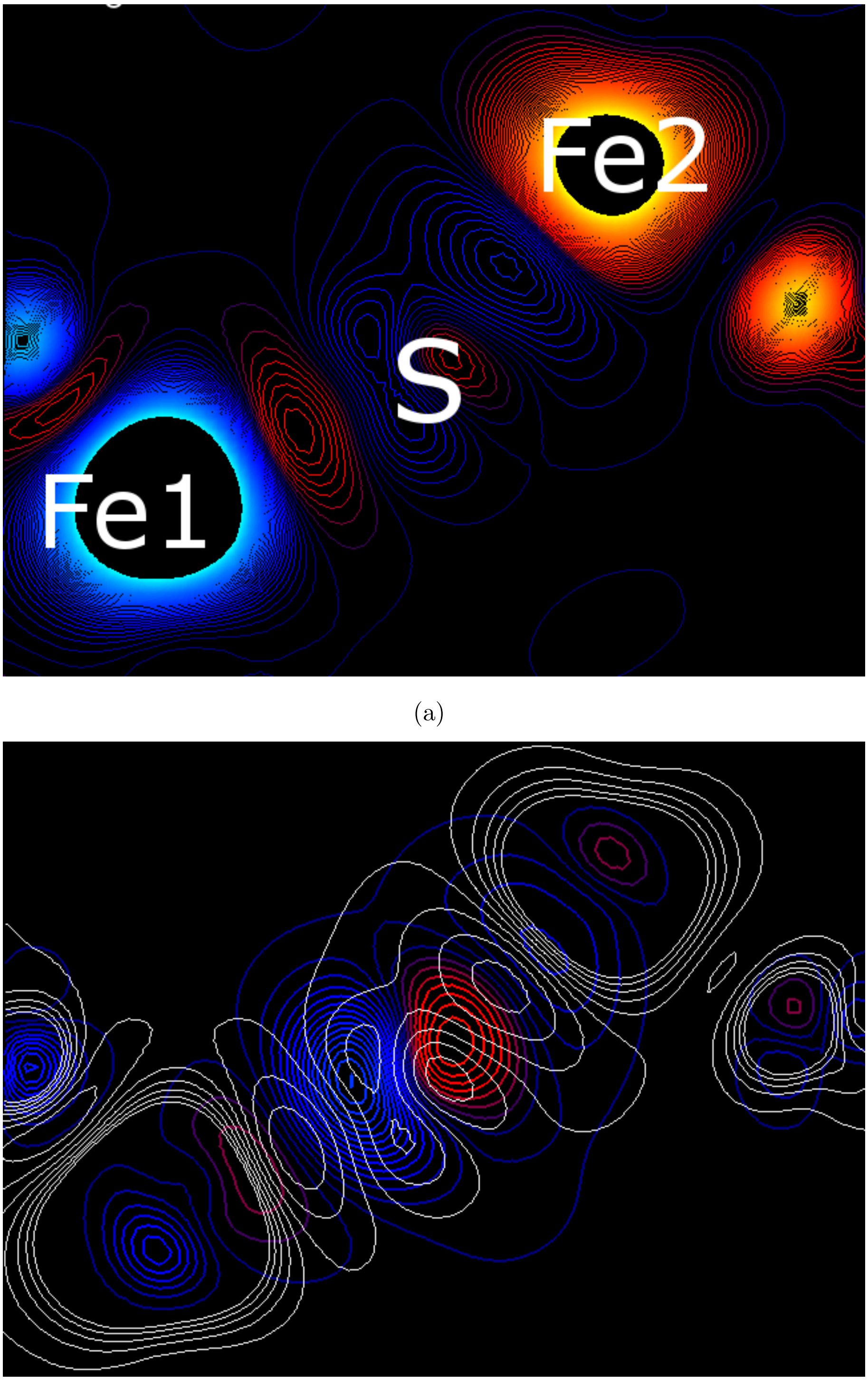

(a)

(b)

Figure 4.30: Magnetization density of the Fe1$_a$-S(1)-Fe2 complex in GFOS(1). Given in red and blue are positive and negative spin densities, respectively. (a) shows the spin density of all occupied states. (b) gives the partial spin density in the energy range of -1 eV up to the Fermi level. This figure was created using the VisIt program [135].

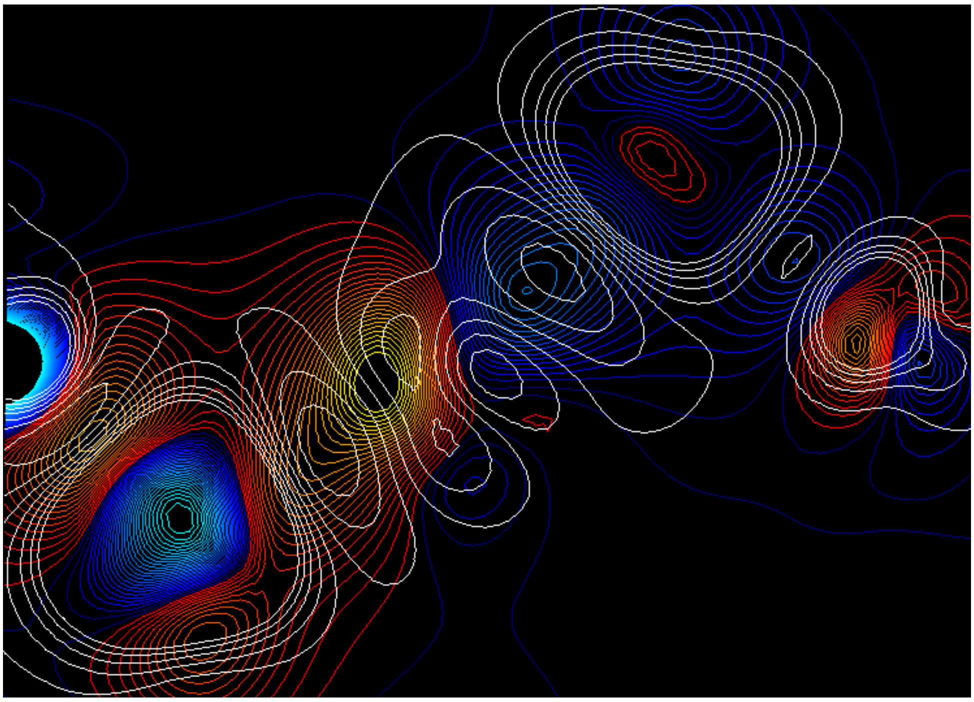

Figure 4.31: Magnetization density of the Fe1$_a$-S(1)-Fe2 complex in the energy range of -5 eV up to -1 eV. Given in red and blue are positive and negative spin densities, respectively. This figure was created using the VisIt program [135].

GFO one can assume that the Fe1-O-Fe2 chains exhibit almost no structural distortions in this doping configuration.

4.7.5 Magnetocrystalline anisotropy energy in anion doped GFO

The results presented in subsection 4.6.4 define the c and b axis as the magnetic easy and hard axis of stoichiometric GFO, respectively and agree with recent experimental and computational studies [193, 201, 203]. Substituting O with a C, N or S atom does not solely affect the total magnetic moment. It can leads to structural changes which again may alter the MAE. Calculating the MAE of the a, b and c axis of stoichiometric and anion substituted GFO the respective simulation cells were relaxed using the GGA+U approximation. Applying the HSE functional for relaxation on the anion substituted structures turned out to be computationally overly time and power consuming. We restricted ourselves to the doping configuration GFOX(1), which turned out to be the energetically most favourable doping site for all investigated doping atoms.

The first entry in table 4.10 gives the energy difference of the [001] and [100] configuration. In the [001] configuration the magnetic moments of both Fe sublattices and the respective anion dopant (if magnetic) are oriented along the ground state c direction. This energy is then subtracted from the energy of the [100] configuration where the magnetic moments of both sublattices are rotated in *a* direction. The second row in table 4.4 gives the energy difference of the [001] and the [010] configuration. Here the magnetic moments are rotated first in *c* and then in *b* direction.

Table 4.10: MAE of stoichiometric and cation doped GFO.

MAE [meV]	GFO	GFOC(1)	GFON(1)	GFOS(1)
[001]-[100]	-0.182	-0.201	-0.137	-0.287
[001]-[010]	-0.212	-0.480	-0.166	-0.343

Regarding table 4.10 the *c* and *b* axis remain for all investigated doping configurations the magnetic easy and hard axis, respectively. GFON(1) exhibits reduced MAE compared to stoichiometric GFO. Increased MAE is present in GFOC(1) and GFOS(1), whereas first has the "hardest" *b* axis of all investigated doping configurations. The relative energy difference of [001]-[100] and [001]-[010] is the biggest in GFOC(1), similar for GFOS(1) and GFON(1), and the smallest for stoichiometric GFO.

Summarizing, the overall MAE does not change introducing anion dopants, exhibiting equal magnetic easy and hard axis compared to the stoichiometric system. Their relative values, however, change which of course can be induced by structural alterations.

4.7.6 Distance and angle dependence of the magnetic interaction

In the previous section 4.6.6 the distance and angle dependence of the AFM coupling strength in stoichiometric GFO has been investigated. A single Fe1-O-Fe2 bond is therefore left inside the simulation cell, replacing six of the eight Fe atoms inside the stoichiometric GFO simulation cell with Ga atoms. Interactions with adjacent Fe1-O-Fe2 configurations could therefore be neglected revealing the unaffected angle and distance dependence of the AFM superexchange. The remaining Fe1-O-Fe2 bond was stretched and bent and the corresponding AFM coupling strength calculated. As predicted by the GK rules the AFM coupling becomes reduced increasing the bond length and decreasing the enclosed angle (see figure 4.32).

Motivated by that we are interested in the angle and distance dependence of the AFM superexchange in anion doped GFO. We therefore investigate the energetically most stable $\mathrm{Fe1}_a$-$X(1)$-Fe2 configuration for all anion doping cases, replacing all other Fe atoms inside the respective simulation cell with Ga atoms.

In a first step the anion doped simulation cell was relaxed and allowed to change in shape and volume using the GGA+U approximation. The thereby obtained structure was used for further calculations. Table 4.11 lists the respective Fe1_a-$X(1)$-Fe2 enclosed angles, bond lengths and AFM coupling strengths for each anion (X=C,O,N,S). It is obvious that the calculated angles and bond lengths differ from the previously given ones (see tables 4.6, 4.7, 4.8 and 4.9) since replacing six out of the eight Fe atoms by Ga atoms yields an altered atomic surrounding and therefore leads to a different relaxed cell geometry.

Determining the distance dependence of the AFM superexchange, the bond length of the respective Fe1_a-$X(1)$-Fe2 complex is altered stepwise and kept fix during a second relaxation. During that second relaxation all other atoms and the shape and the volume of the simulation cell were allowed to change. The corresponding Fe1_a-$X(1)$-Fe2 enclosed angle is kept constant at its equilibrium value obtained during the first relaxation. Examining the angle dependence, the enclosed angle was varied but kept fixed during a second relaxation. The respective Fe1_a-$X(1)$-Fe2 bond length was taken from the first relaxation and kept fix as well.

Table 4.11: AFM coupling strengths of the modified simulation cells containing a single Fe1-$X(1)$-Fe2 complex. The respective geometries are GGA+U relaxed and no on top HSE calculation was performed.

	enclosed angle(°)	Fe1-X (Å)	Fe2-X (Å)	E_{diff}[AFM-FM](eV)
Fe1_a-C-Fe2	129.03	2.14	1.74	-0.186
Fe1_a-O-Fe2	125.87	1.94	1.91	-0.112
Fe1_a-N-Fe2	126.39	2.04	1.90	-0.118
Fe1_a-S-Fe2	129.79	2.27	2.25	-0.156

Fe1_a-O(1)-Fe2

The Fe1_a-O(1) and Fe2-O(1) bond lengths were stretched and compressed stepwise up to 20% and the enclosed angle increased and reduced by +1.8% and -2.9%, respectively. Depending on the overall phase stability these values differ for the anion doped cases.

Figure 4.32(a) shows the AFM coupling strength designated as E_{diff}[AFM-FM][eV/cell] as a function of the varied Fe1_a-O(1)-Fe2 bond length. The upper x axis gives the total energy difference between the equilibrium ground state and the strained state. The

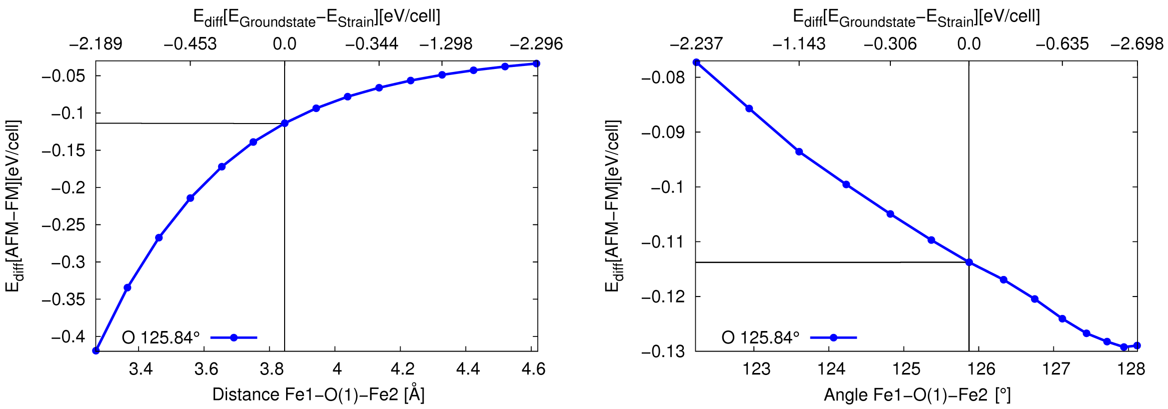

(a) (b)

Figure 4.32: (a) and (b) show the distance and the angle dependence of the AFM coupling strength for a single Fe1$_a$-O(1)-Fe2 configuration, respectively. Increasing the distance and decreasing the enclosed angle reduces the AFM coupling strength. All energies are given per 40 atom simulation cell.

AFM coupling strength increases with decreasing bond length. This can be attributed to an increased Fe-O orbital overlap, enhancing the AFM superexchange. Increasing the Fe1$_a$-O(1)-Fe2 bond length reduces the magnetic coupling and at some point leads to a paramagnetic solution where the energy difference between the AFM ground state and a hypothetic FM state vanishes.

Figure 4.32(b) shows the AFM coupling strength as a function of the enclosed angle. Increasing the Fe1$_a$-O(1)-Fe2 enclosed angle increases the AFM coupling, which again results in an enhanced Fe-O orbital overlap. Both the distance and angle dependence of the AFM superexchange inside the Fe1$_a$-O(1)-Fe2 complex coincide with the behaviour predicted by the GK rules.

Fe1$_a$-C(1)-Fe2

In the C doped case the Fe1$_a$-C(1)-Fe2 configuration's bond length was stretched and compressed by +20% and -17.5%, respectively. The Fe1$_a$-C(1) and Fe2-C(1) bond length ratio is kept constant with respect to the ground state value.

Increasing the bond length decreases the AFM coupling strength (see figure 4.33(a)) so that a paramagnetic ground state occurs stretching the Fe1$_a$-C(1)-Fe2 complex by +12.5%. In that particular case the AFM and FM states show an energy difference of only 3 meV. Stretching the Fe1$_a$-C(1)-Fe2 bond further up to +20% makes a FM coupling energetically more favourable by 67 meV. The respective configuration is by -1.09 eV less stable compared to the unstrained ground state structure. This behaviour is similar to the Fe1_a-O(1)-Fe2 undoped case.

Reducing the ground state bond length by -0.5% and more decreases the AFM coupling strength. The FM state becomes energetically more favourable compressing the bond length by -15% . This behaviour is in contrast to the undoped Fe1_a-O(1)-Fe2 configuration. Compressing the Fe1_a-C(1)-Fe2 complex further up to -17.5% favoures the FM coupling by about 79 meV. The respective strained simulation cell is 1.87 eV energetically less stable compared to the unstrained structure.

The magnetic exchange present in the Fe1_a-C(1)-Fe2 complex alters with the applied strain. To gain more insight in the varying magnetic coupling mechanism, we consider the magnetic moments and occupation numbers of the Fe1_a, C(1) and Fe2 atom. Reducing the Fe1_a-C(1)-Fe2 bond length slightly decreases the ground state magnetic moment of Fe1_a. This can be attributed to an enhanced orbital overlap and an increased interaction with the C(1) atom. The Fe1-C(1) interaction assimilates to the Fe2-C(1) interaction present inside the unstrained Fe1_a-C(1)-Fe2 complex. The magnetic moment of the C(1) and Fe2 atom reduces as well. The C(1) *p* states and both the Fe1_a and the Fe2 *d* states are slightly enhanced, especially for the Fe2 atom which is closer to the C(1) atom.

Enhancing the Fe1_a-C(1)-Fe2 bond length reduces the respective Fe-C orbital overlap. The Fe2-C(1) interaction decreases and the Fe2 magnetic moment increases from its ground state value of $+3\mu_B$ to about $+4\mu_B$. The initially between the Fe2 and C(1) atom formed additional covalent bond becomes weakened. The magnetic moment of the C(1) atom increases with decreased coupling and a FM state is favoured. The number of the occupied Fe *d* states is similar to the unstrained case whereas the C(1) *p* electrons are slightly reduced.

Figure 4.33(b) shows the angle dependence of the AFM coupling strength. The respective enclosed angle was enhanced and reduced stepwise up to +1.1% and -2.6%, respectively. The overall behaviour is similar to the undoped Fe1_a-O(1)-Fe2 complex and is in accordance with the GK rules. Increasing the enclosed angle enhances the AFM superexchange and reducing it decreases the AFM coupling strength. The occupation numbers and magnetic moments do not alter notably.

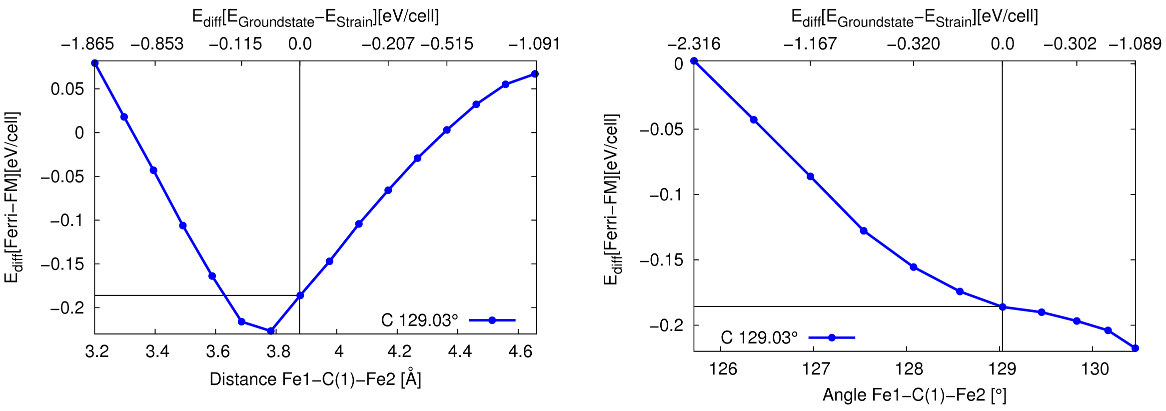

(a)

(b)

Figure 4.33: (a) and (b) show the distance and the angle dependence of the AFM coupling strength for a single Fe1$_a$-C(1)-Fe2 configuration, respectively.

Fe1$_a$-N(1)-Fe2

Figure 4.34(a) and (b) show the distance and angle dependence of the AFM superexchange in a single Fe1$_a$-N(1)-Fe2 complex. The respective Fe1$_a$-N(1)-Fe2 configuration is stretched and compressed by +20% and -20%, respectively. The corresponding enclosed angle is enhanced by +1.3% and reduced down to -2.1%.

The AFM coupling strength rises with decreasing bond length, similar to the undoped configuration. A notable jump to lower energies occurs at a bond length of 3.53 Å which corresponds to a ground state bond length reduction of 10%. Regarding the occupation numbers and the magnetic moments of the Fe1$_a$, Fe2 and N(1) atoms show that an additional covalent bond starts to be formed between the N(1) and Fe2 atom at that particular distance. The N(1) atom becomes nonmagnetic and the magnetic moment of the Fe2 atom reduces stepwise down to $+3\mu_B$ at a bond length reduction of 20%. The magnetic moment of the Fe1$_a$ atom remains about $-4\mu_B$. This is similar to the unstrained C(1) doped case. The number of Fe d and N(1) p states increases slightly especially for the Fe2 atom, which has reduced distance to the anion dopant. Stretching and compressing the Fe1$_a$-N(1)-Fe2 complex the initial Fe1$_a$-N(1) and Fe2-N(1) distance ratio is preserved. Increasing the bond length increases the AFM coupling strength, in contrast to the C(1) and undoped O(1) configuration. The magnetic moment and number of both Fe d and N(1) p states remains almost unchanged.

The angle dependence of the AFM superexchange shown in figure 4.34(b) only partly coincides with the behaviour predicted by the GK rules and differ from the O(1) and C(1) doped case. Enhancing the enclosed angle reduces the AFM coupling strength instead of increasing it and reducing the enclosed angle first increases and then decreases the AFM superexchange. The magnetic moments and occupation numbers of the Fe1_a, Fe2 and N(1) atoms do not notably change compared to the unstrained structure.

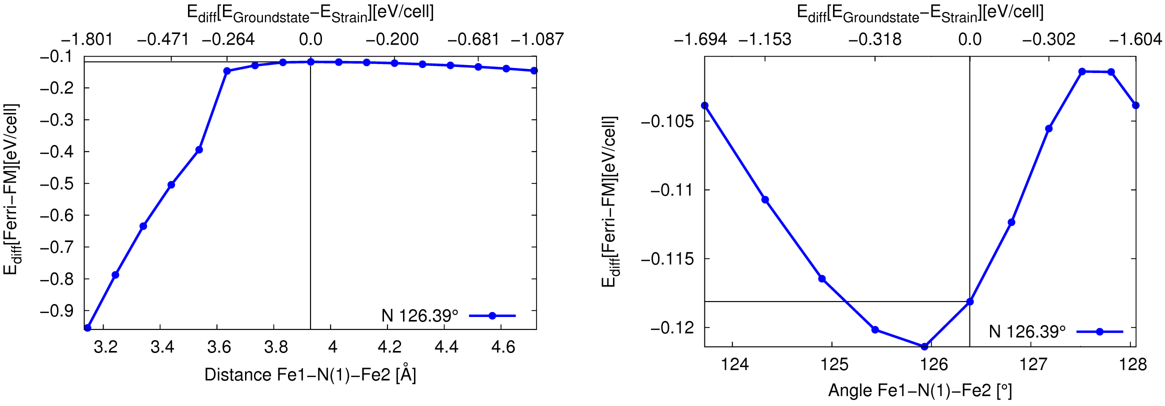

(a) (b)

Figure 4.34: (a) and (b) show the distance and the angle dependence of the AFM coupling strength for a single Fe1_a-N(1)-Fe2 configuration, respectively.

Fe1_a-S(1)-Fe2

In the S doped case the corresponding Fe1_a-S(1)-Fe2 configuration was stretched and compressed by +20% and -17.5%, respectively. The enclosed angle is enhanced and reduced by +1.7% and -2.4%, respectively. Figure 4.35(a) and (b) show the distance and angle dependence of the AFM superexchange. The overall behaviour is similar to the undoped case and follows the GK rules. This, however, is not surprising, since both the O and S atom have the same number of valence electrons.

4.7.7 Strain on anion doped GFO

After giving a detailed discussion on the magnetic exchange mechanisms mediated via the anion dopants we change into a more realistic picture. Instead of straining a single Fe1_a-X(1)-Fe2 complex inside a simulation cell with just two Fe atoms we investigate the effect of strain on the AFM coupling strength in single anion doped GFOX(1) (X = C,N,S). Cell site (1) is the most stable doping configuration for all investigated anion dopants. According to a section 4.6.6 stretching the GFO simulation cell in c direction gives the biggest changes in the AFM coupling strength. The GFOX(1) simulation cell is stretched and compressed by +3.5% and -3.5% in c direction, respectively, preserving

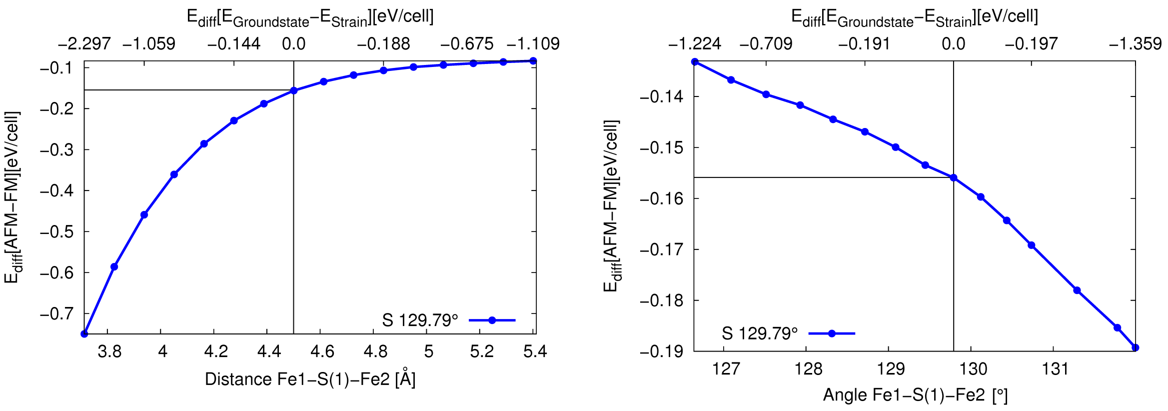

(a) (b)

Figure 4.35: (a) and (b) show the distance and the angle dependence of the AFM coupling strength for a single Fe1$_a$-S(1)-Fe2 configuration, respectively.

the cell volume. In a subsequent relaxation the atoms were allowed to relax while shape and volume of the simulation cell were kept constant.

The magnetic coupling mechanisms mediated via the anion dopants differ, hence one cannot simply compare the calculated AFM coupling strengths with each other, especially for the C and N doped case. This fact has to be kept in mind regarding figure 4.36, showing the calculated AFM coupling strength as a function of the applied strain. The shown values are calculated within the GGA+U approximation, which is a reasonable approach regarding the vast number of calculations required. Thus no on top HSE calculations were performed as done for the results given in tables 4.6, 4.7, 4.8 and 4.9. This however is an useful approach, since we are not interested in values like the band gap. The AFM coupling strengths calculated using the HSE hybrid functional are systematically higher than the ones calculated within the GGA+U approximation. As a consequence, the AFM coupling strengths for the unstrained cases shown in figure 4.36 differ from those given in the previously mentioned tables. This shift to larger coupling strengths, however is not the same for all doping cases. Regarding table 4.6 to 4.9 the N(1) doped case shows the largest AFM coupling strength with -1.58 eV followed by stoichiometric GFO with -1.47 eV. The S(1) doped case shows slightly enhanced coupling with -1.48 eV. C(1) has the lowest AFM coupling with -1.19 eV. Regarding figure 4.36, however, the S(1) doped case shows higher coupling strength than stoichiometric GFO. In the GGA+U calculated coupling strengths the S(1) doped simulation cell shows higher AFM coupling strength compared to undoped GFO. The C(1) and N(1) doped cases show an AFM coupling strength of -1.10 eV and -1.55 eV, respectively, calculated within the GGA+U approximation. Comparing the AFM coupling strengths of different doping configurations using the same anion dopant is more meaningful than comparing the AFM coupling strength for different anion types.

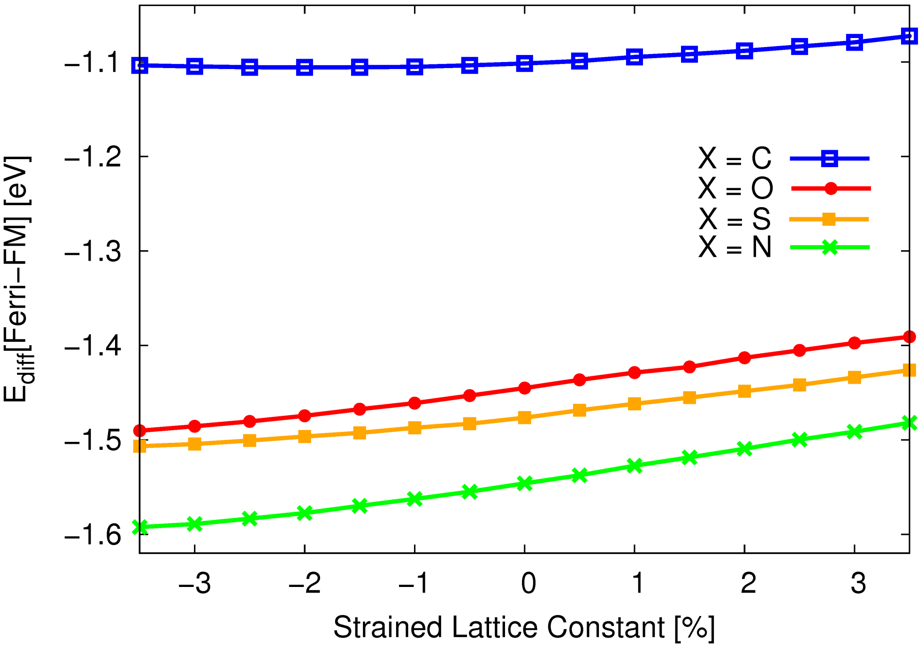

Figure 4.36: Straining stoichiometric and anion doped GaFeOX(1) (X=C,N,S) in c direction. The AFM coupling strength E_{diff} is plotted as a function of strain.

Table 4.12 lists the geometric properties of the Fe1_a-$X(1)$-Fe2 complexes inside the strained and unstrained simulation cells. The AFM coupling strength increases compressing the respective simulation cell in c direction for all investigated systems (see figure 4.36). The curves of stoichiometric and doped GFO have similar slopes. The Fe1_a-$X(1)$-Fe2 enclosed angle and bond length are both enhanced compressing the simulation cell for all investigated systems. Stretching the respective simulation cells reduces the complex' enclosed angle and bond length. The Fe1_a-X(1)-Fe2 enclosed angles show larger geometric distortions than the respective bond lengths (see 4.12). The biggest geometric alterations are induced in the S(1) doped system. Straining and compressing the simulation cell alters the enclosed angle and the complex' bond length by 6.47° and 0.05 Å, respectively. Straining GFOS(1) show the biggest changes in the AFM coupling strength.

The C(1) doped case is shifted to higher energies due to the reduced AFM coupling. The AFM coupling strength alters least in GFOC(1). Compressing and stretching the GFOC(1) simulation cell enhances the AFM coupling strength by very small 2 meV and reduces the coupling by about 30 meV, respectively. In stoichiometric GFO the AFM coupling is enhanced by about 54 meV and reduced by 45 meV compressing and stretching the simulation cell, giving a total of about 100 meV. The N(1) doped case invokes the biggest changes in the AFM coupling strength with a total of 110 meV.

The geometric changes of the respective Fe1$_a$-X(1)-Fe2 complex cannot solely predict the overall changes of the AFM coupling strength. The entire simulation cell has to be taken into account including the geometric changes of both the AFM superexchange mediating Fe1-O-Fe2 chains.

Table 4.12: Enclosed angle and bond length of the Fe1$_a$-X(1)-Fe2 bond in strained and unstrained GFOX(1). The respective geometries are GGA+U relaxed.

Strain	-3.5%	0.0%	+3.5%	Δ(-3.5% − +3.5%)
Fe1$_a$-O(1)-Fe2 - enclosed angle(°)	129.05	126.30	123.43	5.62
Fe1$_a$-O(1)-Fe2 - bond length(Å)	3.85	3.85	3.85	0.00
Fe1$_a$-C(1)-Fe2 - enclosed angle(°)	134.57	131.99	129.26	5.31
Fe1$_a$-C(1)-Fe2 - bond length(Å)	3.86	3.84	3.83	0.03
Fe1$_a$-N(1)-Fe2 - enclosed angle(°)	130.52	127.76	124.86	5.66
Fe1$_a$-N(1)-Fe2 - bond length(Å)	3.90	3.90	3.90	0.00
Fe1$_a$-S(1)-Fe2 - enclosed angle(°)	133.35	130.17	126.88	6.47
Fe1$_a$-S(1)-Fe2 - bond length(Å)	4.56	4.53	4.51	0.05

4.7.8 Conclusion

The performed calculations show that exchanging O with a C, N or S atom, changes the electronic and magnetic properties of GFO in several quite different ways. Of all investigated doping configurations (1)-(4) cell site substitution (1) is the energetically most stable substitution site for the C, N and S impurity atom.

Substituting O with C yields an either ferrimagnetic or antiferromagnetic ground state. Carbon placed on sites (1) and (2) introduces a ferrimagnetic ground state and ferrimagnetic coupling in the respective Fe1-C(1/2)-Fe2 configuration. The C(1) and the C(2) atoms form an additional covalent bond with the corresponding next nearest Fe2 atom and reduce its magnetic moment from $4\mu_B$ to $3\mu_B$ compared to the Fe1 atom. Carbon itself carries a magnetic moment of about half a μ_B on cell sites (1),(2) and (4) which is antiparallel to the magnetic moment of its next nearest Fe2 atom due to the enhanced interaction. C(3) is nonmagnetic and yields an AFM ground state in GFOC(3). The C(3) atom is part of the AFM superexchange weak mediating Fe1-C(3)-Fe2 complex.

The angle and distance dependence of the AFM superexchange inside the Fe1$_a$-O(1)-Fe2 complex follows the GK rules. This is also true for the angle dependence of the AFM coupling of the Fe1$_a$-C(1)-Fe2 configuration. The Fe1$_a$-C(1)-Fe2 distance dependence, however, shows different behaviour. Here the AFM coupling strength decreases enhancing the Fe1$_a$-C(1)-Fe2 bond length.

Regarding the calculated band gaps of the different C doping configurations with respect to the photocatalytic properties C doping shows a band gap reduction for all doping configurations. Cell site substitution (1),(2),(4) yield a magnetic ground state of -2μ_B per simulation cell yielding unequal spin up and spin down gaps. In the C(1), C(2) and C(4) doped case spin up acceptor states are introduced near the CB, leading to a reduced majority spin gap. The spin gap is reduced the most for the cell site (3) substitution for about more than 1 eV compared to stoichiometric GFO to about 1.40 eV for both spin channels. The C(3) substitution case, however, exhibits impurity states that are not attached to the CB, but located near the mid-band gap energy. Impurity states located in the middle of the band gap between the VB and CB edges are known to act as recombination centers reducing the electron-hole lifetime decreasing the photocatalytic efficiency. To create a good photocatalyst one desires a “clean” band gap with no additional states [110, 111]. This, however, is fulfilled for the C(1), C(2) and C(4) doping configurations with impurity acceptor states that are either attached or near the CB.

Substituting O with N introduces a ferrimagnetic ground state with a total magnetic moment of -1μ_B per simulation cell for all investigated doping configurations N(1-4). Nitrogen indeed mediates the AFM coupling inside the Fe1-N(1/2)-Fe2 bonds but does not induce a ferrimagnetic coupling as C(1) and C(2) in the Fe1-C(1/2)-Fe2 configurations. The N atom, however, carries a magnetic moment yielding the non zero magnetic ground state of GFON. Comparing the structural parameters of the doped Fe1-X-Fe2 bonds inside the respective GFOX simulation cell, C induces larger distortions in the atomic bonds and angles than N. This may support the fact that introducing C to the GFO host matrix enhances the MAE compared to N.

Regarding the distance dependence of the AFM superexchange shows that reducing the Fe1$_a$-N(1)-Fe2 bond length enhances the AFM coupling which is in agreement with the GK rules. Increasing the bond length reduces the AFM exchange as well, which is in contradiction to the behaviour of the Fe1$_a$-O(1)-Fe2 and Fe1$_a$-C(1)-Fe2 complex. The angle dependence of the AFM coupling strength in Fe1$_a$-N(1)-Fe2 shows different behaviour as well. Reducing the Fe1$_a$-N(1)-Fe2 enclosed angle first enhances and then reduces the AFM coupling. Increasing the enclosed angle reduces the AFM coupling strength, which again is in contrast to the GK rules.

Regarding the structure of the band gaps, N introduces acceptor states in the spin up channel near the mid-band gap. This, however, indicates an enhanced interaction with the neighbouring Fe2 atom, also represented by the reduced Fe2-N bond length. All N doping configurations show a reduction of both the spin up and spin down gap, which is more pronounced for the spin up case due to the acceptor states.

Dhanasekaran and Gupta [230], however, report increased water splitting properties incorporating N impurities to GFO. Despite the acceptor state located in the spin up channel (which may act as electron hole recombination centers reducing the photocatalytic water splitting properties) the spin down channel shows no impurity states and is reduced as well compared to stoichiometric GFO. Our results therefore support the measured enhanced photocatalytic property of N doped GFO.

Exchanging O with S yields an AFM ground state for all doping configurations (1)-(4). The magnetic exchange mechanism mediated via the S atom is similar to the O atom. S, however, introduces notably changes in the cell geometry due to its large atomic radius. Even though the Fe1-S-Fe2 bond lengths are enhanced compared to the undoped case the partial bond length ratio (Fe1-X to Fe2-X) are similar. This is in contrast to the C(1/2) and N(1/2) doping configurations where C and N show decreased and increased Fe2-X and Fe1-X bond lengths, respectively, compared to stoichiometric GFO. These geometric distortions, however, again can be used to explain the enhanced MAE in GFOS(1) compared to stoichiometric GFO. The angle and distance dependence of the $\mathrm{Fe1}_a$-S(1)-Fe2 complex follows the same behaviour as the $\mathrm{Fe1}_a$-O(1)-Fe2 configuration and therefore is in agreement with the GK rules. The S(1) and S(2) doping configurations show the highest band gap reduction and are energetically more favorable than the S(3) and S(4) substitution. The respective band gaps are free of doping states supporting the experimentally measured enhanced photocatalytic property of GFOS compared to stoichiometric GFO [230].

Regarding the AFM coupling strengths there is a highly reduced energy difference between the AFM ground state and a hypothetic FM state for doping configuration S(3). This, however, can be explained by the distinct distortion the two Fe clusters that mediate the AFM superexchange throughout the crystal. Experiments on Mn doped GFO report reduced Curie temperatures [225], which the authors try to explain either by a weakened AFM coupling of the Mn-O-Fe bonds or distorted Fe-Fe linkages and angles reducing the AFM superexchange. In the light of our results we will also expect a reduction of the Curie temperature upon doping with S.

4.8 Outlook

Based on the performed and presented calculations, there are a lot of aspects worth further investigations. Since GFO is ferroelectric it would be of interest to determine the effect of cation and anion doping on the intrinsic polarization. This may be done evaluating the distortion of the polyhedra or performing so called Berry-Phase calculations [232–236], which are implemented in the VASP code. Oxygen vacancies may also play an important role and influence the magnetic and electric properties. In addition it would be of interest to study the effect of interstitial doping as well as the interaction between dopants in systems with higher doping concentrations. Further, no simulations on the GFO surface have been performed yet. Another interesting topic, since we do not know how its magnetism behaves at the surface. This would be also needful in the sense of simulating and calculating GFO's photocatalytic properties. Investigating its surface in simulations would allow to calculate its workfunction which has not been investigated in experiments so far.

Bibliography

[1] D. Khomskii, "Multiferroics: Different ways to combine magnetism and ferroelectricity," *Journal of Magnetism and Magnetic Materials*, vol. 306, no. 1, pp. 1 – 8, 2006.

[2] N. Spaldin, S.-W. Cheong, and R. Ramesh, "Multiferroics: Past, present, and future," *Physics Today*, vol. 63, no. 10, p. 38, 2010.

[3] B. Wul and J. Goldman *C.R. Acad. Sci URSS*, vol. 51, no. 21, 1946.

[4] B. Wul and J. Goldman *C.R. Acad. Sci URSS*, vol. 64, no. 139, 1945.

[5] T. Ogawa and S. Waku *Kenkyu*, vol. 1, no. 6, 1947.

[6] L. F. Mattheiss, E. M. Gyorgy, and D. W. Johnson, "Superconductivity above 20 K in the BaKBiO system," *Phys. Rev. B*, vol. 37, pp. 3745–3746, Mar 1988.

[7] J. G. Bednorz and K. A. Müller, "Possible high T_c superconductivity in the BaLaCuO system," *Zeitschrift für Physik B Condensed Matter*, vol. 64, no. 2, pp. 189–193, 1986.

[8] M. K. Wu, J. R. Ashburn, C. J. Torng, P. H. Hor, R. L. Meng, L. Gao, Z. J. Huang, Y. Q. Wang, and C. W. Chu, "Superconductivity at 93 K in a new mixed-phase YBaCuO compound system at ambient pressure," *Phys. Rev. Lett.*, vol. 58, pp. 908–910, Mar 1987.

[9] J. B. Goodenough, "Theory of the role of covalence in the perovskite-type manganites [La,M(ii)]MnO_3," *Phys. Rev.*, vol. 100, pp. 564–573, Oct 1955.

[10] J. Kanamori, "Superexchange interaction and symmetry properties of electron orbitals," *Journal of Physics and Chemistry of Solids*, vol. 10, pp. 87–98, 7 1959.

[11] J. Goodenough, *Magnetism and the chemical bond.* Interscience monographs on chemistry: Inorganic chemistry section, Interscience Publishers, 1963.

[12] H. Schmid, “Multi-ferroic magnetoelectrics,” *Ferroelectrics*, vol. 162, no. 1, pp. 317–338, 1994.

[13] N. A. Hill, “Density functional studies of multiferroic magnetoelectrics,” *Annual Review of Materials Research*, vol. 32, no. 1, 2002.

[14] W. Eerenstein, N. D. Mathur, and J. F. Scott, “Multiferroic and magnetoelectric materials.,” *Nature*, vol. 442, pp. 759–65, Aug. 2006.

[15] G. Jonker and J. V. Santen, “Ferromagnetic compounds of manganese with perovskite structure,” *Physica*, vol. 16, no. 3, pp. 337 – 349, 1950.

[16] R. von Helmolt, J. Wecker, B. Holzapfel, L. Schultz, and K. Samwer, “Giant negative magnetoresistance in perovskitelike $La_{2/3}Ba_{1/3}MnO_x$ ferromagnetic films,” *Phys. Rev. Lett.*, vol. 71, pp. 2331–2333, Oct 1993.

[17] S. Jin, T. H. Tiefel, M. McCormack, R. A. Fastnacht, R. Ramesh, and L. H. Chen, “Thousandfold change in resistivity in magnetoresistive LaCaMnO films,” *Science*, vol. 264, no. 5157, pp. 413–415, 1994.

[18] S. Blügel, T. Brückel, R. Waser, and C. M. Schneider, eds., *Electronic Oxides - Correlation Phenomena, Exotic Phases and Novel Functionalities.* Forschungszentrum Jülich GmbH Institut für Festkörperphysik, March 2010.

[19] A. D. McNaught and A. Wilkinson, *IUPAC. Compendium of Chemical Terminology.* Blackwell Scientific Publications, Oxford, 2nd ed. (the ”gold book”) ed., 1997.

[20] T. L. Meek and L. C. Allen, “Configuration irregularities: deviations from the madelung rule and inversion of orbital energy levels,” *Chemical Physics Letters*, vol. 362, no. 5–6, pp. 362 – 364, 2002.

[21] E. Riedel, *Anorganische Chemie.* Walter de Gruyter, 1990.

[22] G. Anderson, R. Gomatam, and L. Behera, “Contradictions in the quantum mechanical explanation of the periodic table,” *Journal of Physics: Conference Series*, vol. 490, no. 1, p. 012197, 2014.

[23] N. B. Hannay and C. P. Smyth, “The dipole moment of hydrogen fluoride and the ionic character of bonds,” *Journal of the American Chemical Society*, vol. 68, no. 2, pp. 171–173, 1946.

[24] A. Allred, “Electronegativity values from thermochemical data,” *Journal of Inorganic and Nuclear Chemistry*, vol. 17, no. 3–4, pp. 215 – 221, 1961.

[25] L. O. Grondahl, “The copper-cuprous-oxide rectifier and photoelectric cell,” *Rev. Mod. Phys.*, vol. 5, pp. 141–168, Apr 1933.

[26] D. O. Scanlon, B. J. Morgan, G. W. Watson, and A. Walsh, “Acceptor levels in p-type Cu_2O: Rationalizing theory and experiment,” *Phys. Rev. Lett.*, vol. 103, p. 096405, Aug 2009.

[27] M. Ain, A. Menelle, B. M. Wanklyn, and E. F. Bertaut, “Magnetic structure of CuO by neutron diffraction with polarization analysis,” *Journal of Physics: Condensed Matter*, vol. 4, no. 23, p. 5327, 1992.

[28] A. Oral, E. Menşur, M. Aslan, and E. Başaran, “The preparation of copper(ii) oxide thin films and the study of their microstructures and optical properties,” *Materials Chemistry and Physics*, vol. 83, no. 1, pp. 140 – 144, 2004.

[29] L. Pauling, “The principles determining the structure of complex ionic crystals,” *Journal of the American Chemical Society*, vol. 51, no. 4, pp. 1010–1026, 1929.

[30] J. H. Van Vleck, “Theory of the variations in paramagnetic anisotropy among different salts of the iron group,” *Phys. Rev.*, vol. 41, pp. 208–215, Jul 1932.

[31] J. S. Griffith and L. E. Orgel, “Ligand-field theory,” *Q. Rev. Chem. Soc.*, vol. 11, pp. 381–393, 1957.

[32] W. Heisenberg, “Mehrkörperproblem und Resonanz in der Quantenmechanik,” *Zeitschrift für Physik*, vol. 38, no. 6-7, pp. 411–426, 1926.

[33] P. A. M. Dirac, “On the theory of quantum mechanics,” *Proceedings of the Royal Society of London A: Mathematical, Physical and Engineering Sciences*, vol. 112, no. 762, pp. 661–677, 1926.

[34] W. Heitler and F. London, “Wechselwirkung neutraler Atome und homöopolare Bindung nach der Quantenmechanik,” *Zeitschrift für Physik*, vol. 44, no. 6-7, pp. 455–472, 1927.

[35] M. E. McHenry, M. A. Willard, and D. E. Laughlin, “Amorphous and nanocrystalline materials for applications as soft magnets,” *Progress in Materials Science*, vol. 44, no. 4, pp. 291 – 433, 1999.

[36] C.-W. Chem, *Magnetism and metallurgy of soft magnetic materials.* New York (N.Y.): Dover publications, 1986.

[37] A. R. Wolfgang Nolting, *Quantum Theory of Magnetism.* Springer-Verlag Berlin Heidelberg, 2009.

[38] M. A. Ruderman and C. Kittel, “Indirect exchange coupling of nuclear magnetic moments by conduction electrons,” *Phys. Rev.*, vol. 96, pp. 99–102, Oct 1954.

[39] K. Yosida, “Magnetic properties of Cu-Mn alloys,” *Phys. Rev.*, vol. 106, pp. 893–898, Jun 1957.

[40] T. Kasuya, “A theory of metallic ferro- and antiferromagnetism on Zener’s model,” *Progress of Theoretical Physics*, vol. 16, no. 1, pp. 45–57, 1956.

[41] G. Jonker and J. V. Santen, “Magnetic compounds with perovskite structure iii. Ferromagnetic compounds of cobalt,” *Physica*, vol. 19, no. 1–12, pp. 120 – 130, 1953.

[42] C. Zener, “Interaction between the *d*-shells in the transition metals. ii. Ferromagnetic compounds of manganese with perovskite structure,” *Phys. Rev.*, vol. 82, pp. 403–405, May 1951.

[43] B. Bechlars, D. M. D’Alessandro, D. M. Jenkins, A. T. Iavarone, S. D. Glover, C. P. Kubiak, and J. R. Long, “High-spin ground states via electron delocalization in mixed-valence imidazolate-bridged divanadium complexes,” *Nat Chem*, vol. 2, pp. 362–368, 05 2010.

[44] J. J.W. Morris, “Materials science. Chapter 4: Defects in crystals.” University of California, Berkeley. Lecture Notes. MSE 205. Extras, 2007.

[45] J. Cao and J. Wu, “Strain effects in low-dimensional transition metal oxides,” *Materials Science and Engineering: R: Reports*, vol. 71, no. 2–4, pp. 35 – 52, 2011.

[46] D. Lee and T. W. Noh, “Giant flexoelectric effect through interfacial strain relaxation,” *Philosophical Transactions of the Royal Society of London A: Mathematical, Physical and Engineering Sciences*, vol. 370, pp. 4944–4957, sep 2012.

[47] D. Lee, A. Yoon, S. Y. Jang, J.-G. Yoon, J.-S. Chung, M. Kim, J. F. Scott, and T. W. Noh, “Giant flexoelectric effect in ferroelectric epitaxial thin films,” *Phys. Rev. Lett.*, vol. 107, p. 057602, Jul 2011.

[48] J. Cao, E. Ertekin, V. Srinivasan, W. Fan, S. Huang, H. Zheng, J. W. L. Yim, D. R. Khanal, D. F. Ogletree, J. C. Grossman, and J. Wu, “Strain engineering and one-dimensional organization of metal-insulator domains in single-crystal vanadium dioxide beams,” *Nat Nano*, vol. 4, pp. 732–737, 11 2009.

[49] I. A. Luk'yanchuk, A. Schilling, J. M. Gregg, G. Catalan, and J. F. Scott, "Origin of ferroelastic domains in free-standing single-crystal ferroelectric films," *Phys. Rev. B*, vol. 79, p. 144111, Apr 2009.

[50] N. W. Ashcroft and N. D. Mermin, *Solid State Physics.* New York: Holt, Rinehart and Winston, 1976.

[51] C. Kittel, *Introduction to solid state physics.* New York: Wiley, 1996.

[52] D. R. Hartree, "The wave mechanics of an atom with a non-coulomb central field. Part I. Theory and Methods," *Mathematical Proceedings of the Cambridge Philosophical Society*, vol. 24, pp. 89–110, 1 1928.

[53] V. Fock, "Näherungsmethode zur Lösung des quantenmechanischen Mehrkörperproblems," *Zeitschrift für Physik*, vol. 61, no. 1-2, pp. 126–148, 1930.

[54] C. D. Sherrill and H. F. S. III., "The configuration interaction method: Advances in highly correlated approaches," vol. 34 of *Advances in Quantum Chemistry*, pp. 143 – 269, Academic Press, 1999.

[55] C. J. Cramer, *Essentials of computational chemistry: Theories and models.* New York: J. Wiley, 2002.

[56] H. G. Kümmel, *A biography of the coupled cluster method.* in *Recent progress many-body theories*, (Singapore), pp. 334-348, World Scientific Publishing, 2002.

[57] I. Shavitt and R. J. Bartlett, *Many-body methods in chemistry and physics: MBPT and coupled-cluster theory.* Cambridge: Cambridge University Press, 2009.

[58] C. Möller and M. S. Plesset, "Note on an approximation treatment for many-electron systems," *Phys. Rev.*, vol. 46, pp. 618–622, Oct 1934.

[59] S. Redner, "Citation statistics from 110 years of physical review," *Physics Today*, vol. 58, pp. 49–54, 2005.

[60] P. Hohenberg and W. Kohn, "Inhomogeneous electron gas," *Phys. Rev.*, vol. 136, pp. B864–B871, Nov 1964.

[61] W. Kohn and L. J. Sham, "Self-consistent equations including exchange and correlation effects," *Phys. Rev.*, vol. 140, pp. A1133–A1138, Nov 1965.

[62] H. J. Monkhorst and J. D. Pack, "Special points for brillouin-zone integrations," *Phys. Rev. B*, vol. 13, pp. 5188–5192, Jun 1976.

[63] E. Engel and R. M. Dreizler, *Density Functioal Theory - An advanced Course.* Springer-Verlag Berlin Heidelberg, 1 ed., 2011.

[64] L. H. Thomas, "The calculation of atomic fields," *Mathematical Proceedings of the Cambridge Philosophical Society*, vol. 23, pp. 542–548, 1 1927.

[65] E. Fermi, "Eine statistische Methode zur Bestimmung einiger Eigenschaften des Atoms und ihre Anwendung auf die Theorie des periodischen Systems der Elemente," *Zeitschrift für Physik*, vol. 48, no. 1-2, pp. 73–79, 1928.

[66] W. Kohn, "Nobel lecture: Electronic structure of matter¯wave functions and density functionals," *Rev. Mod. Phys.*, vol. 71, pp. 1253–1266, Oct 1999.

[67] J. Chayes, L. Chayes, and M. Ruskai, "Density functional approach to quantum lattice systems," *Journal of Statistical Physics*, vol. 38, no. 3-4, pp. 497–518, 1985.

[68] A. K. Rajagopal and J. Callaway, "Inhomogeneous electron gas," *Phys. Rev. B*, vol. 7, pp. 1912–1919, Mar 1973.

[69] M. Marder, *Condensed Matter Physics.* Wiley-Interscience, 2000.

[70] D. M. Ceperley and B. J. Alder, "Ground state of the electron gas by a stochastic method," *Phys. Rev. Lett.*, vol. 45, pp. 566–569, Aug 1980.

[71] O. Gunnarsson, M. Jonson, and B. I. Lundqvist, "Descriptions of exchange and correlation effects in inhomogeneous electron systems," *Phys. Rev. B*, vol. 20, pp. 3136–3164, Oct 1979.

[72] A. Van de Walle and G. Ceder, "Correcting overbinding in local-density-approximation calculations," *Phys. Rev. B*, vol. 59, pp. 14992–15001, Jun 1999.

[73] J. P. Perdew, J. A. Chevary, S. H. Vosko, K. A. Jackson, M. R. Pederson, D. J. Singh, and C. Fiolhais, "Atoms, molecules, solids, and surfaces: Applications of the generalized gradient approximation for exchange and correlation," *Phys. Rev. B*, vol. 46, pp. 6671–6687, Sep 1992.

[74] V. Ozoliņš and M. Körling, "Full-potential calculations using the generalized gradient approximation: Structural properties of transition metals," *Phys. Rev. B*, vol. 48, pp. 18304–18307, Dec 1993.

[75] C. Filippi, D. J. Singh, and C. J. Umrigar, "All-electron local-density and generalized-gradient calculations of the structural properties of semiconductors," *Phys. Rev. B*, vol. 50, pp. 14947–14951, Nov 1994.

[76] J. P. Perdew, K. Burke, and M. Ernzerhof, "Generalized gradient approximation made simple," *Phys. Rev. Lett.*, vol. 78, pp. 1396–1396, Feb 1997.

[77] J. P. Perdew and A. Zunger, "Self-interaction correction to density-functional approximations for many-electron systems," *Phys. Rev. B*, vol. 23, pp. 5048–5079, May 1981.

[78] P. W. Anderson, "Localized magnetic states in metals," *Phys. Rev.*, vol. 124, pp. 41–53, Oct 1961.

[79] V. I. Anisimov, F. Aryasetiawan, and A. I. Lichtenstein, "First-principles calculations of the electronic structure and spectra of strongly correlated systems: the LDA+U method," *Journal of Physics: Condensed Matter*, vol. 9, no. 4, p. 767, 1997.

[80] A. I. Liechtenstein, V. I. Anisimov, and J. Zaanen, "Density-functional theory and strong interactions: Orbital ordering in Mott-Hubbard insulators," *Phys. Rev. B*, vol. 52, pp. R5467–R5470, Aug 1995.

[81] S. L. Dudarev, G. A. Botton, S. Y. Savrasov, C. J. Humphreys, and A. P. Sutton, "Electron-energy-loss spectra and the structural stability of nickel oxide: An LSDA+U study," *Phys. Rev. B*, vol. 57, pp. 1505–1509, Jan 1998.

[82] J. P. Perdew, S. Kurth, A. Zupan, and P. Blaha, "Accurate density functional with correct formal properties: A step beyond the generalized gradient approximation," *Phys. Rev. Lett.*, vol. 82, pp. 2544–2547, Mar 1999.

[83] J. Heyd, G. E. Scuseria, and M. Ernzerhof, "Hybrid functionals based on a screened coulomb potential," *The Journal of Chemical Physics*, vol. 118, no. 18, pp. 8207–8215, 2003.

[84] C. Lee, W. Yang, and R. G. Parr, "Development of the Colle-Salvetti correlation-energy formula into a functional of the electron density," *Phys. Rev. B*, vol. 37, pp. 785–789, Jan 1988.

[85] A. D. Becke, "A new mixing of Hartree–Fock and local density functional theories," *The Journal of Chemical Physics*, vol. 98, no. 2, pp. 1372–1377, 1993.

[86] J. P. Perdew, M. Ernzerhof, and K. Burke, "Rationale for mixing exact exchange with density functional approximations," *The Journal of Chemical Physics*, vol. 105, no. 22, pp. 9982–9985, 1996.

[87] U. of York Departement of Chemistry, "The essential chemical industry." www.essentialchemicalindustry.org, Dec. 2015.

[88] H. Ohno, "Making nonmagnetic semiconductors ferromagnetic," *Science*, vol. 281, pp. 951–956, Aug. 1998.

[89] F. Matsukura, H. Ohno, A. Shen, and Y. Sugawara, "Transport properties and origin of ferromagnetism in (Ga,Mn)As," *Phys. Rev. B*, vol. 57, pp. 2037–2040, Jan 1998.

[90] D. P. DiVincenzo, "Quantum computation," *Science*, vol. 270, no. 5234, pp. 255–261, 1995.

[91] J. B. Varley, A. Janotti, and C. G. Van de Walle, "Mechanism of visible-light photocatalysis in nitrogen-doped TiO_2," *Advanced Materials*, vol. 23, no. 20, pp. 2343–2347, 2011.

[92] P. Wang, Z. Liu, F. Lin, G. Zhou, J. Wu, W. Duan, B.-L. Gu, and S. B. Zhang, "Optimizing photoelectrochemical properties of TiO_2 by chemical codoping," *Phys. Rev. B*, vol. 82, p. 193103, Nov 2010.

[93] S. Ghosh and N. J. English, "*Ab initio* study on optoelectronic properties of interstitially versus substitutionally doped titania," *Phys. Rev. B*, vol. 86, p. 235203, Dec 2012.

[94] A. Fujishima and K. Honda, "Electrochemical photolysis of water at a semiconductor electrode," *Nature*, vol. 238, no. 1, pp. 37–38, 1972.

[95] M. A. Fox and M. T. Dulay, "Heterogeneous photocatalysis," *Chemical Reviews*, vol. 93, no. 1, pp. 341–357, 1993.

[96] M. R. Hoffmann, S. T. Martin, W. Choi, and D. W. Bahnemann, "Environmental applications of semiconductor photocatalysis," *Chemical Reviews*, vol. 95, no. 1, pp. 69–96, 1995.

[97] D. Fujishima, A. Tryk, T. Watanabe, and K. Hashimoto, "Titanium oxide-coated glass: self-cleaning and anti-fogging properties and applications.," *Int Glass Review–Flat Glass Proc*, pp. 114–116, 1998.

[98] C. Di Valentin, G. Pacchioni, and A. Selloni, "Origin of the different photoactivity of N-doped anatase and rutile TiO_2," *Phys. Rev. B*, vol. 70, p. 085116, Aug 2004.

[99] C. Di Valentin, G. Pacchioni, and A. Selloni, "Theory of carbon doping of titanium dioxide," *Chemistry of Materials*, vol. 17, no. 26, pp. 6656–6665, 2005.

[100] K. Yang, Y. Dai, B. Huang, and S. Han, "Theoretical study of N-doped TiO_2 rutile crystals," *The Journal of Physical Chemistry B*, vol. 110, no. 47, pp. 24011–24014, 2006.

[101] O. Diwald, T. L. Thompson, E. G. Goralski, S. D. Walck, and J. T. Yates, "The effect of nitrogen ion implantation on the photoactivity of TiO_2 rutile single crystals," *The Journal of Physical Chemistry B*, vol. 108, no. 1, pp. 52–57, 2004.

[102] O. Diwald, T. L. Thompson, T. Zubkov, S. D. Walck, and J. T. Yates, "Photochemical activity of nitrogen-doped rutile TiO_2(110) in visible light," *The Journal of Physical Chemistry B*, vol. 108, no. 19, pp. 6004–6008, 2004.

[103] M. Batzill, E. H. Morales, and U. Diebold, "Influence of nitrogen doping on the defect formation and surface properties of TiO_2 rutile and anatase," *Phys. Rev. Lett.*, vol. 96, p. 026103, Jan 2006.

[104] T. Dietl, H. Ohno, F. Matsukura, J. Cibert, and D. Ferrand, "Zener model description of ferromagnetism in zinc-blende magnetic semiconductors," *Science*, vol. 287, no. 5455, pp. 1019–1022, 2000.

[105] R. Memming, *Applications in Semiconductor Electrochemistry.* Wiley-VCH Verlag: Weinheim, 2000.

[106] A. Kudo and Y. Miseki, "Heterogeneous photocatalyst materials for water splitting," *Chem. Soc. Rev.*, vol. 38, pp. 253–278, 2009.

[107] S. Chen and L.-W. Wang, "Thermodynamic oxidation and reduction potentials of photocatalytic semiconductors in aqueous solution," *Chemistry of Materials*, vol. 24, no. 18, pp. 3659–3666, 2012.

[108] A. L. Linsebigler, G. Lu, and J. T. Yates, "Photocatalysis on TiO_2 surfaces: Principles, mechanisms, and selected results," *Chemical Reviews*, vol. 95, no. 3, pp. 735–758, 1995.

[109] X. Chen, S. Shen, L. Guo, and S. S. Mao, "Semiconductor-based photocatalytic hydrogen generation," *Chemical Reviews*, vol. 110, no. 11, pp. 6503–6570, 2010.

[110] W. Shockley and W. T. Read, “Statistics of the recombinations of holes and electrons,” *Phys. Rev.*, vol. 87, pp. 835–842, Sep 1952.

[111] R. N. Hall, “Electron-hole recombination in germanium,” *Phys. Rev.*, vol. 87, pp. 387–387, Jul 1952.

[112] K. F. Brennan, *The Physics of Semiconductors: With Applications to Optoelectronic Devices.* Cambridge Univerity Press, 1999.

[113] F. Grant, “Properties of rutile (titanium dioxide),” *Rev. Mod. Phys*, vol. 31, no. 3, p. 646, 1959.

[114] L. Kavan, M. Grätzel, S. E. Gilbert, C. Klemenz, and H. J. Scheel, “Electrochemical and photoelectrochemical investigation of single-crystal anatase,” *Journal of the American Chemical Society*, vol. 118, no. 28, pp. 6716–6723, 1996.

[115] K. Momma and F. Izumi, “*VESTA3* for three-dimensional visualization of crystal, volumetric and morphology data,” *Journal of Applied Crystallography*, vol. 44, pp. 1272–1276, Dec 2011.

[116] G. Kresse and J. Hafner, “*Ab initio* molecular dynamics for liquid metals,” *Phys. Rev. B*, vol. 47, pp. 558–561, Jan 1993.

[117] G. Kresse and J. Hafner, “*Ab initio* molecular-dynamics simulation of the liquid-metal amorphous-semiconductor transition in germanium,” *Phys. Rev. B*, vol. 49, pp. 14251–14269, May 1994.

[118] G. Kresse and J. Hafner, “Norm-conserving and ultrasoft pseudopotentials for first-row and transition elements,” *Journal of Physics: Condensed Matter*, vol. 6, no. 40, p. 8245, 1994.

[119] G. Kresse and J. Furthmüller, “Efficiency of ab-initio total energy calculations for metals and semiconductors using a plane-wave basis set,” *Computational Materials Science*, vol. 6, no. 1, pp. 15 – 50, 1996.

[120] G. Kresse and J. Furthmüller, “Efficient iterative schemes for *ab initio* total-energy calculations using a plane-wave basis set,” *Phys. Rev. B*, vol. 54, pp. 11169–11186, Oct 1996.

[121] G. Kresse and D. Joubert, “From ultrasoft pseudopotentials to the projector augmented-wave method,” *Phys. Rev. B*, vol. 59, pp. 1758–1775, Jan 1999.

[122] P. E. Blöchl, "Projector augmented-wave method," *Phys. Rev. B*, vol. 50, pp. 17953–17979, Dec 1994.

[123] J. P. Perdew, K. Burke, and M. Ernzerhof, "Generalized gradient approximation made simple," *Phys. Rev. Lett.*, vol. 77, pp. 3865–3868, Oct 1996.

[124] J. P. Perdew, K. Burke, and M. Ernzerhof, "Generalized gradient approximation made simple," *Phys. Rev. Lett.*, vol. 78, pp. 1396–1396, Feb 1997.

[125] J. Heyd, G. E. Scuseria, and M. Ernzerhof, "Hybrid functionals based on a screened coulomb potential'," *The Journal of Chemical Physics*, vol. 124, no. 21, p. 219906, 2006.

[126] M. E. Arroyo-de Dompablo, A. Morales-García, and M. Taravillo, "DFT+U calculations of crystal lattice, electronic structure, and phase stability under pressure of TiO_2 polymorphs," *J. Chem. Phys.*, vol. 135, no. 5, p. 054503, 2011.

[127] A. Janotti, J. B. Varley, P. Rinke, N. Umezawa, G. Kresse, and C. G. Van de Walle, "Hybrid functional studies of the oxygen vacancy in TiO_2," *Phys. Rev. B*, vol. 81, p. 085212, Feb 2010.

[128] N. N. Bao, H. M. Fan, J. Ding, and J. B. Yi, "Room temperature ferromagnetism in N-doped rutile TiO_2 films," *Journal of Applied Physics*, vol. 109, no. 7, 2011.

[129] C. G. Van de Walle and J. Neugebauer, "First-principles calculations for defects and impurities: Applications to III-nitrides," *Journal of Applied Physics*, vol. 95, no. 8, pp. 3851–3879, 2004.

[130] O. Kubaschewski, "The oxide handbook," *Berichte der Bunsengesellschaft für physikalische Chemie*, vol. 86, no. 8, pp. 761–762, 1982.

[131] K. Reuter and M. Scheffler, "Composition, structure, and stability of RuO_2(110) as a function of oxygen pressure," *Phys. Rev. B*, vol. 65, p. 035406, Dec 2001.

[132] J. K. W. Marye A. Fox, "Organische chemie," *Spektrum Akademischer Verlag*, 1994.

[133] X. Chen, Y.-B. Lou, A. Samia, C. Burda, and J. Gole, "Formation of oxynitride as the photocatalytic enhancing site in nitrogen-doped titania nanocatalysts: Comparison to a commercial nanopowder," *Advanced Functional Materials*, vol. 15, no. 1, pp. 41–49, 2005.

[134] R. Asahi and T. Morikawa, "Nitrogen complex species and its chemical nature in TiO_2 for visible-light sensitized photocatalysis," *Chemical Physics*, vol. 339, no. 1–3, pp. 57 – 63, 2007.

[135] H. Childs, E. Brugger, B. Whitlock, J. Meredith, S. Ahern, D. Pugmire, K. Biagas, M. Miller, C. Harrison, G. H. Weber, H. Krishnan, T. Fogal, A. Sanderson, C. Garth, E. W. Bethel, D. Camp, O. Rübel, M. Durant, J. M. Favre, and P. Navrátil, "VisIt: An End-User Tool For Visualizing and Analyzing Very Large Data," in *High Performance Visualization–Enabling Extreme-Scale Scientific Insight*, pp. 357–372, Oct 2012.

[136] C. R. A. Catlow, Z. X. Guo, M. Miskufova, S. A. Shevlin, A. G. H. Smith, A. A. Sokol, A. Walsh, D. J. Wilson, and S. M. Woodley, "Advances in computational studies of energy materials," *Philosophical Transactions of the Royal Society of London A: Mathematical, Physical and Engineering Sciences*, vol. 368, no. 1923, pp. 3379–3456, 2010.

[137] A. Imanishi, E. Tsuji, and Y. Nakato, "Dependence of the work function of TiO_2 (rutile) on crystal faces, studied by a scanning auger microprobe," *The Journal of Physical Chemistry C*, vol. 111, no. 5, pp. 2128–2132, 2007.

[138] L. Chun-Ming, X. Xia, Z. Yan, J. Yong, and Z. Xiao-Tao, "Magnetism of a nitrogen-implanted TiO_2 single crystal," *Chinese Physics Letters*, vol. 28, no. 12, p. 127201, 2011.

[139] Q. Xiu-Bo, L. Dong-Xiang, L. Rui-Qin, Z. Peng, L. Yu-Xiao, and W. Bao-Yi, "Defect types and room temperature ferromagnetism in N-doped rutile TiO_2 single crystals," *Chinese Physics B*, vol. 23, no. 6, p. 067502, 2014.

[140] G. Drera, M. C. Mozzati, P. Galinetto, Y. Diaz-Fernandez, L. Malavasi, F. Bondino, M. Malvestuto, and L. Sangaletti, "Enhancement of room temperature ferromagnetism in N-doped TiO_{2-X} rutile: Correlation with the local electronic properties," *Applied Physics Letters*, vol. 97, no. 1, 2010.

[141] S. Buzby, M. A. Barakat, H. Lin, C. Ni, S. A. Rykov, J. G. Chen, and S. Ismat Shah, "Visible light photocatalysis with nitrogen-doped titanium dioxide nanoparticles prepared by plasma assisted chemical vapor deposition," *Journal of Vacuum Science Technology B*, vol. 24, no. 3, pp. 1210–1214, 2006.

[142] W. Mekprasart, T. Khumtong, J. Rattanarak, W. Techitdheera, and W. Pecharapa, "Effect of nitrogen doping on optical and photocatalytic properties of TiO_2 thin film

prepared by spin coating process," *Energy Procedia*, vol. 34, pp. 746 – 750, 2013. 10th Eco-Energy and Materials Science and Engineering Symposium.

[143] Y. Jiao, A. Hellman, Y. Fang, S. Gao, and M. Käll, "Schottky barrier formation and band bending revealed by first-principles calculations," *Scientific Reports*, vol. 5, p. 11374, jun 2015.

[144] D. O. Scanlon, C. W. Dunnill, J. Buckeridge, S. A. Shevlin, A. J. Logsdail, S. M. Woodley, C. R. A. Catlow, M. J. Powell, R. G. Palgrave, I. P. Parkin, G. W. Watson, T. W. Keal, P. Sherwood, A. Walsh, and A. A. Sokol, "Band alignment of rutile and anatase TiO_2.," *Nature materials*, vol. 12, pp. 798–801, sep 2013.

[145] S. Piskunov, O. Lisovski, J. Begens, D. Bocharov, Y. F. Zhukovskii, M. Wessel, and E. Spohr, "C-, N-, S-, and Fe-doped TiO_2 and $SrTiO_3$ nanotubes for visible-light-driven photocatalytic water splitting: Prediction from first principles," *The Journal of Physical Chemistry C*, vol. 119, no. 32, pp. 18686–18696, 2015.

[146] E. Berardo and M. A. Zwijnenburg, "Modeling the water splitting activity of a TiO_2 rutile nanoparticle," *The Journal of Physical Chemistry C*, vol. 119, no. 24, pp. 13384–13393, 2015.

[147] W.-N. Zhao and Z.-P. Liu, "Mechanism and active site of photocatalytic water splitting on titania in aqueous surroundings," *Chem. Sci.*, vol. 5, pp. 2256–2264, 2014.

[148] G. Serrano, B. Bonanni, M. Di Giovannantonio, T. Kosmala, M. Schmid, U. Diebold, A. Di Carlo, J. Cheng, J. VandeVondele, K. Wandelt, and C. Goletti, "Molecular ordering at the interface between liquid water and rutile TiO_2(110)," *Advanced Materials Interfaces*, vol. 2, no. 17, p. 1500246, 2015.

[149] N. A. Spaldin and M. Fiebig, "The renaissance of magnetoelectric multiferroics," *Science*, vol. 309, no. 5733, pp. 391–392, 2005.

[150] S.-W. Cheong and M. Mostovoy, "Multiferroics: a magnetic twist for ferroelectricity," *Nat. Mater.*, vol. 6, pp. 13–20, Jan 2007.

[151] R. Ramesh and N. A. Spaldin, "Multiferroics: progress and prospects in thin films," *Nat. Mater.*, vol. 6, pp. 21–29, jan 2007.

[152] G. Catalan and J. F. Scott, "Physics and applications of bismuth ferrite," *Advanced Materials*, vol. 21, no. 24, pp. 2463–2485, 2009.

[153] L. Landau and E. Lifshitz, *Electrodynamics of Continuous Media.* Pergamon Press, 1960.

[154] W. F. Brown, R. M. Hornreich, and S. Shtrikman, "Upper bound on the magnetoelectric susceptibility," *Phys. Rev.*, vol. 168, pp. 574–577, Apr 1968.

[155] M. Fiebig, "Revival of the magnetoelectric effect," *Journal of Physics D: Applied Physics*, vol. 38, pp. R123–R152, Apr. 2005.

[156] M. Bichurin and V. Petrov, *Modelling of Magnetoelectric effects in composites.* Springer Dordrecht, 2014.

[157] S. L. Hou and N. Bloembergen, "Paramagnetoelectric effects in $NiSO_4{\cdot}6H_2O$," *Phys. Rev.*, vol. 138, pp. A1218–A1226, May 1965.

[158] J. R. Teague, R. Gerson, and W. James, "Dielectric hysteresis in single crystal $BiFeO_3$," *Solid State Communications*, vol. 8, no. 13, pp. 1073 – 1074, 1970.

[159] I. Sosnowska, T. P. Neumaier, and E. Steichele, "Spiral magnetic ordering in bismuth ferrite," *Journal of Physics C Solid State Physics*, vol. 15, pp. 4835–4846, Aug. 1982.

[160] C. Tabares Munoz, J.-P. Rivera, A. Bezinges, A. Monnier, and H. Schmid, "Measurement of the quadratic magnetoelectric effect on single crystalline $BiFeO_3$," *Japanese Journal of Applied Physics*, vol. 24, pp. 1051–1053, 1985.

[161] Y. F. Popov, A. M. Kadomtseva, G. P. Vorobev, and A. K. Zvezdin, "Discovery of the linear magnetoelectric effect in magnetic ferroelectric $BiFeO_3$ in a strong magnetic field," *Ferroelectrics*, vol. 162, no. 1, pp. 135–140, 1994.

[162] V. A. Murashov, D. N. Rakov, V. M. Ionov, I. S. Dubenko, Y. V. Titov, and V. S. Gorelik, "Magnetoelectric (Bi, Ln)FeO_3 compounds: Crystal growth, structure and properties," *Ferroelectrics*, vol. 162, no. 1, pp. 11–21, 1994.

[163] F. Bai, J. Wang, M. Wuttig, J. Li, N. Wang, A. P. Pyatakov, A. K. Zvezdin, L. E. Cross, and D. Viehland, "Destruction of spin cycloid in (111)c-oriented $BiFeO_3$ thin films by epitiaxial constraint: Enhanced polarization and release of latent magnetization," *Applied Physics Letters*, vol. 86, no. 3, 2005.

[164] I. E. Dzyaloshinskii, "On the magneto-electrical effect in antiferromagnets," *Sov. Phys.—JETP*, vol. 10, no. 3, p. 628, 1959.

[165] D. N. Astrov, “The magnetoelectric effect in antiferromagnetics,” *Sov. Phys.—JETP*, vol. 11, no. 3, p. 708, 1960.

[166] D. N. Astrov, “Magnetoelectric effect in chromium oxide,” *Sov. Phys.—JETP*, vol. 13, no. 4, p. 729, 1961.

[167] G. T. Rado and V. J. Folen, “Observation of the magnetically induced magnetoelectric effect and evidence for antiferromagnetic domains,” *Phys. Rev. Lett.*, vol. 7, pp. 310–311, Oct 1961.

[168] V. J. Folen, G. T. Rado, and E. W. Stalder, “Anisotropy of the magnetoelectric effect in Cr_2O_3,” *Phys. Rev. Lett.*, vol. 6, pp. 607–608, Jun 1961.

[169] J.-P. Rivera, “On definitions, units, measurements, tensor forms of the linear magnetoelectric effect and on a new dynamic method applied to Cr-Cl boracite,” *Ferroelectrics*, vol. 161, no. 1, pp. 165–180, 1994.

[170] N. Ortega, A. Kumar, J. F. Scott, and R. S. Katiyar, “Multifunctional magnetoelectric materials for device applications,” *Journal of Physics: Condensed Matter*, vol. 27, no. 50, p. 504002, 2015.

[171] J.-P. Rivera, “The linear magnetoelectric effect in $LiCoPO_4$ revisited,” *Ferroelectrics*, vol. 161, no. 1, pp. 147–164, 1994.

[172] R. P. BB Krichevtsov, VV Pavlov, “Giant linear magnetoelectric effect in garnet ferrite films,” *JETP Lett*, vol. 49, no. 535, 1989.

[173] G. T. Rado, J. M. Ferrari, and W. G. Maisch, “Magnetoelectric susceptibility and magnetic symmetry of magnetoelectrically annealed $TbPO_4$,” *Phys. Rev. B*, vol. 29, pp. 4041–4048, Apr 1984.

[174] R. Ramesh and N. A. Spaldin, “Multiferroics: progress and prospects in thin films,” *Nat. Mater.*, vol. 6, pp. 21–29, 01 2007.

[175] G. A. Gehring, “On the microscopic theory of the magnetoelectric effect,” *Ferroelectrics*, vol. 161, no. 1, pp. 275–285, 1994.

[176] I. Dzyaloshinsky, “A thermodynamic theory of “weak” ferromagnetism of antiferromagnetics,” *Journal of Physics and Chemistry of Solids*, vol. 4, no. 4, pp. 241 – 255, 1958.

[177] T. Moriya, “Anisotropic superexchange interaction and weak ferromagnetism,” *Phys. Rev.*, vol. 120, pp. 91–98, Oct 1960.

[178] R. Hornreich and S. Shtrikman, “Statistical mechanics and origin of the magnetoelectric effect in Cr_2O_3,” *Phys. Rev.*, vol. 161, pp. 506–512, Sep 1967.

[179] H. Schmid, “Multi-ferroic magnetoelectrics,” *Ferroelectrics*, vol. 162, no. 1, pp. 317–338, 1994.

[180] N. A. Spaldin, M. Fiebig, and M. Mostovoy, “The toroidal moment in condensed-matter physics and its relation to the magnetoelectric effect,” *Journal of Physics: Condensed Matter*, vol. 20, no. 43, p. 434203, 2008.

[181] G. A. Smolenskii and I. E. Chupis, “Ferroelectromagnets,” *Sov. Phys. Usp.*, vol. 25, pp. 475–493, 1982.

[182] G. A. Smolenskii, A. I. Agranovskaya, and V. A. Isupov *Sov. Phys. Solid State*, vol. 1, p. 149, 1959.

[183] S. M. Skinner, “Magnetically ordered ferroelectric materials,” *Parts, Materials and Packaging, IEEE Transactions on*, vol. 6, pp. 68–90, Jun 1970.

[184] F. Kubel and H. Schmid, “Structure of a ferroelectric and ferroelastic monodomain crystal of the perovskite $BiFeO_3$,” *Acta Cryst.*, vol. 46, pp. 698–702, 1990.

[185] K. Aizu, “Possible species of ferromagnetic, ferroelectric, and ferroelastic crystals,” *Phys. Rev. B*, vol. 2, pp. 754–772, Aug 1970.

[186] H. Schmid, “On a magnetoelectric classification of materials,” *International Journal of Magnetism*, vol. 4, no. 4, pp. 337–361, 1973.

[187] M. Opel, “Die Austauschwechselwirkungen,” in *Magnetism*, Lecture Notes, (Walther-Meißner-Institut, Technische Universität München), pp. 90–111, 2004/2005.

[188] J. B. Goodenough, “An interpretation of the magnetic properties of the perovskite-type mixed crystals $La_{1-x}Sr_xCoO_{3-\lambda}$,” *Journal of Physics and Chemistry of Solids*, vol. 6, no. 2–3, pp. 287 – 297, 1958.

[189] H. Kramers, “L’interaction entre les atomes magnétogènes dans un cristal paramagnétique,” *Physica*, vol. 1, no. 1–6, pp. 182 – 192, 1934.

[190] P. W. Anderson, “Antiferromagnetism. theory of superexchange interaction,” *Phys. Rev.*, vol. 79, pp. 350–356, Jul 1950.

[191] C. Timm, *Lecture notes : Theory of magnetism.* TU Dresden, 2009/10.

[192] M. Hatnean, J. Robert, M. Fernandez Diaz, E. Ressouche, A. Cousson, L. Pinsard-Gaudart, and S. Petit, "Neutron scattering study of the magnetoelectric compound $GaFeO_3$," *The European Physical Journal Special Topics*, vol. 213, pp. 69–76, Dec. 2012.

[193] F. Ibrahim and M. Alouani, "Impact of excess iron on the calculated electronic and magnetic properties of gallium ferrite," *Physical Review B*, vol. 85, p. 174411, May 2012.

[194] T. Arima, D. Higashiyama, Y. Kaneko, J. He, T. Goto, S. Miyasaka, T. Kimura, K. Oikawa, T. Kamiyama, R. Kumai, and Y. Tokura, "Structural and magnetoelectric properties of $Ga_{2-x}Fe_xO_3$ single crystals grown by a floating-zone method," *Physical Review B*, vol. 70, p. 064426, Aug. 2004.

[195] A. Thomasson, F. Ibrahim, C. Lefevre, E. Autissier, F. Roulland, C. Mény, C. Leuvrey, S. Choi, W. Jo, O. Crégut, G. Versini, S. Barre, M. Alouani, and N. Viart, "Effects of iron concentration and cationic site disorder on the optical properties of magnetoelectric gallium ferrite thin films," *RSC Advances*, vol. 3, no. 9, p. 3124, 2013.

[196] N. Wang, F. Wen, L. Li, Y. Lü, S. Liu, Y. Lu, Z. Liu, B. Xu, J. He, D. Yu, and Y. Tian, "Magnetic frustration effect in polycrystalline $Ga_{2-x}Fe_xO_3$," *Journal of Magnetism and Magnetic Materials*, vol. 322, no. 21, pp. 3595 – 3600, 2010.

[197] J. P. Remeika, "$GaFeO_3$: A ferromagnetic-piezoelectric compound," *Journal of Applied Physics*, vol. 31, no. 5, pp. 263–264, 1960.

[198] K. U. Kang, S. B. Kim, S. Y. An, S.-W. Cheong, and C. S. Kim, "Magnetic properties of $GaFeO_3$ prepared by slow cooling and quenched heat treatment method," *Journal of Magnetism and Magnetic Materials*, vol. 304, no. 2, pp. 769 – 771, 2006.

[199] C. H. Nowlin and R. V. Jones, "Magnetism of piezoelectric $Ga_{2-x}Fe_xO_3$," *Journal of Applied Physics*, vol. 34, no. 4, pp. 1262–1263, 1963.

[200] C. Lefevre, F. Roulland, A. Thomasson, C. Meny, F. Porcher, G. André, and N. Viart, "Magnetic and polar properties' optimization in the magnetoelectric $Ga_{2-x}Fe_xO_3$ compounds," *The Journal of Physical Chemistry C*, vol. 117, no. 28, pp. 14832–14839, 2013.

[201] V. Raghavendra Reddy, K. Sharma, A. Gupta, and a. Banerjee, "Magnetic anisotropy and sub-lattice magnetization study of polycrystalline magneto-electric

$Ga_{2-x}Fe_xO_3$," *Journal of Magnetism and Magnetic Materials*, vol. 362, pp. 97–103, Aug. 2014.

[202] S. Mukherjee, A. Roy, S. Auluck, R. Prasad, R. Gupta, and A. Garg, "Room Temperature Nanoscale Ferroelectricity in Magnetoelectric $GaFeO_3$ Epitaxial Thin Films," *Physical Review Letters*, vol. 111, p. 087601, Aug. 2013.

[203] J.-Y. Kim, T. Koo, and J.-H. Park, "Orbital and Bonding Anisotropy in a Half-Filled $GaFeO_3$ Magnetoelectric Ferrimagnet," *Physical Review Letters*, vol. 96, no. 4, p. 047205, 2006.

[204] D. Stoeffler, "First principles study of the electric polarization and of its switching in the multiferroic $GaFeO_3$ system," *Journal of physics. Condensed matter : an Institute of Physics journal*, vol. 24, p. 185502, May 2012.

[205] D. Stoeffler, "First principles study of the spontaneous electric polarization in $Ga_{2-x}Fe_xO_3$," *Thin Solid Films*, vol. 533, pp. 93 – 96, 2013.

[206] A. Roy, S. Mukherjee, R. Gupta, S. Auluck, R. Prasad, and A. Garg, "Electronic structure, Born effective charges and spontaneous polarization in magnetoelectric gallium ferrite.," *Journal of physics. Condensed matter : an Institute of Physics journal*, vol. 23, p. 325902, Aug. 2011.

[207] S. K. Mishra, R. Mittal, R. Singh, M. Zbiri, T. Hansen, and H. Schober, "Phase stability of multiferroic $GaFeO_3$ up to 1368K from in situ neutron diffraction," *Journal of Applied Physics*, vol. 113, no. 17, 2013.

[208] S. C. Abrahams, J. M. Reddy, and J. L. Bernstein, "Crystal structure of piezoelectric ferromagnetic gallium iron oxide," *The Journal of Chemical Physics*, vol. 42, no. 11, pp. 3957–3968, 1965.

[209] Y. F. Popov, A. M. Kadomtseva, G. P. Vorob'ev, V. A. Timofeeva, D. M. Ustinin, A. K. Zvezdin, and M. M. Tegeranchi, "Magnetoelectric effect and toroidal ordering in $Ga_{2-x}Fe_xO_3$," *Journal of Experimental and Theoretical Physics*, vol. 87, no. 1, pp. 146–151, 1998.

[210] G. T. Rado, "Observation and possible mechanisms of magnetoelectric effects in a ferromagnet," *Phys. Rev. Lett.*, vol. 13, pp. 335–337, Sep 1964.

[211] S. L. Dudarev, G. A. Botton, S. Y. Savrasov, C. J. Humphreys, and A. P. Sutton, "Electron-energy-loss spectra and the structural stability of nickel oxide: An LSDA+U study," *Phys. Rev. B*, vol. 57, pp. 1505–1509, Jan 1998.

[212] J. Heyd and G. E. Scuseria, “Efficient hybrid density functional calculations in solids: Assessment of the Heyd–Scuseria–Ernzerhof screened Coulomb hybrid functional,” *The Journal of Chemical Physics*, vol. 121, no. 3, pp. 1187–1192, 2004.

[213] A. V. Krukau, O. A. Vydrov, A. F. Izmaylov, and G. E. Scuseria, “Influence of the exchange screening parameter on the performance of screened hybrid functionals,” *The Journal of chemical physics*, vol. 125, p. 224106, December 2006.

[214] C. G. Van de Walle and A. Janotti, “Advances in electronic structure methods for defects and impurities in solids,” *physica status solidi (b)*, vol. 248, no. 1, pp. 19–27, 2011.

[215] S. J. Clark, J. Robertson, S. Lany, and A. Zunger, “Intrinsic defects in zno calculated by screened exchange and hybrid density functionals,” *Phys. Rev. B*, vol. 81, p. 115311, Mar 2010.

[216] F. Oba, A. Togo, I. Tanaka, J. Paier, and G. Kresse, “Defect energetics in ZnO: A hybrid Hartree-Fock density functional study,” *Phys. Rev. B*, vol. 77, p. 245202, Jun 2008.

[217] E. Tronc, C. Chane, and J. P. Jolivet, “Structural and Magnetic Characterization of ϵ-Fe_2O_3,” *Journal of Solid State Chemistry*, vol. 104, no. 139, pp. 93–104, 1998.

[218] R. Roy, V. G. Hill, and E. F. Osborn, “Polymorphism of Ga_2O_3 and the system Ga_2O_3-H_2O,” *Journal of the American Chemical Society*, vol. 74, no. 3, pp. 719–722, 1952.

[219] Z. Sun, S. Dai, Y. Zhou, L. Cao, and Z. Chen, “Elaboration and optical properties of $GaFeO_3$ thin films,” *Thin Solid Films*, vol. 516, no. 21, pp. 7433 – 7436, 2008.

[220] R. V. Pisarev., “The optical absorption spectrum is presented in $Pb(Fe_{0.5}Nb_{0.5})O_3$ and $GaFeO_3$,” *Soviet Physics-Solid State*, vol. 7, no. 158, 1965.

[221] J. B. Goodenough, “Goodenough-Kanamori rule,” *Scholarpedia*, vol. 3, no. 10, p. 7382, 2008. revision 91326.

[222] A. Roy, A. Garg, R. Prasad, and S. Auluck, “A First-Principles Study of Structure-Property Correlation and the Origin of Ferrimagnetism in Gallium Ferrite,” *Advances in Materials Physics and Chemistry*, vol. 02, no. 04, pp. 1–4, 2012.

[223] C.-H. Yang, D. Kan, I. Takeuchi, V. Nagarajan, and J. Seidel, “Doping $BiFeO_3$: approaches and enhanced functionality,” *Phys. Chem. Chem. Phys.*, vol. 14, pp. 15953–15962, 2012.

[224] M. Venkatesan, C. B. Fitzgerald, J. G. Lunney, and J. M. D. Coey, "Anisotropic ferromagnetism in substituted zinc oxide," *Phys. Rev. Lett.*, vol. 93, p. 177206, Oct 2004.

[225] M. B. Mohamed and H. Fuess, "Effect of mn doping on structural and magnetic properties of $GaFeO_3$," *Journal of Magnetism and Magnetic Materials*, vol. 323, no. 15, pp. 2090 – 2094, 2011.

[226] R. Saha, A. Shireen, S. N. Shirodkar, U. V. Waghmare, A. Sundaresan, and C. Rao, "Effect of Cr and Mn ions on the structure and magnetic properties of $GaFeO_3$: Role of the substitution site," *Journal of Solid State Chemistry*, vol. 184, pp. 2353–2359, Sept. 2011.

[227] T. C. Han, Y. C. Lee, and Y. T. Chu, "Effect of cobalt doping on site-disorder and magnetic behavior of magnetoelectric $GaFeO_3$ nanoparticles," *Applied Physics Letters*, vol. 105, no. 21, 2014.

[228] X. Qing-Yu, W. Zheng, G. Jin-Long, W. Di, Q. Teng, T. Shao-Long, and X. Ming-Xiang, "Multiferroic ZnO obtained by substituting oxygen with nitrogen," *Chinese Physics B*, vol. 20, no. 8, p. 087505, 2011.

[229] Y. Hu, Z. Jiang, K. Gao, G. Cheng, J. Ge, X. Lv, and X. Wu, "Fluorine doping effects on the magnetic and electric properties of $BiFeO_3$," *Chemical Physics Letters*, vol. 534, pp. 62–66, 2012.

[230] P. Dhanasekaran and N. Gupta, "Factors affecting the production of H_2 by water splitting over a novel visible-light-driven photocatalyst $GaFeO_3$," *International Journal of Hydrogen Energy*, vol. 37, pp. 4897–4907, Mar. 2012.

[231] P. Kanhere and Z. Chen, "A review on visible light active perovskite-based photocatalysts," *Molecules*, vol. 19, no. 12, p. 19995, 2014.

[232] R. D. King-Smith and D. Vanderbilt, "Theory of polarization of crystalline solids," *Phys. Rev. B*, vol. 47, pp. 1651–1654, Jan 1993.

[233] D. Vanderbilt and R. D. King-Smith, "Electric polarization as a bulk quantity and its relation to surface charge," *Phys. Rev. B*, vol. 48, pp. 4442–4455, Aug 1993.

[234] R. Resta, "Theory of the electric polarization in crystals," *Ferroelectrics*, vol. 136, no. 1, pp. 51–55, 1992.

[235] R. Resta, “Macroscopic polarization in crystalline dielectrics: the geometric phase approach,” *Rev. Mod. Phys.*, vol. 66, pp. 899–915, Jul 1994.

[236] R. Resta, “Berry phase in electronic wavefunctions,” *Troisième Cycle de la Physique en Suisse Romande*, 1995-96.

Acknowledgments

First of all I want to thank my supervisor Peter Mohn for his support during the last three and a half years. Beside the fruitful discussions concerning my scientific work, I highly appreciated all the friendly and enjoyable talks we had in between. The same applies to Josef Redinger, who never seemed frustrated, even after I had entered his room multiple times in a row asking the same question and still not getting the point. Not to forget, I want to thank Florian Mittendorfer who supported me with his wide knowledge and Maria Steiner who always helped me with all the paper work and thereby never lost her smile.

Further I want to thank my colleagues of the CMS including Andi, Christoph, Gregor, Pedro, and especially Michi and Wernfried, who accompanied me until the very end of my thesis. All of you made my working days, mostly spent in front of the computer, pleasant. Thank you for providing me with funny stories, a lot of chocolate, serious discussions, an open ear and laughter.

Special thanks deserves my family who showed me so many things and made me the person I am today. Thank you for making me feel loved unconditionally and that you still try to prepare me for life, even though I am nearly 30 now.

Furthermore I want to thank Ivo who turned out to be the best partner than I could have ever imagined. Who supports me in every way, every day and even most important no matter in which mood I am. You comfort me when everything seems to be a mess and make me laugh every time I am with you. Thank you for being you, I love you.

Last but not least there is a group of very important people in my life. These are Claudia, Conny, Hanin, Krisi, Me-lie and Zohra who I partly know since primary school and Marie, Abhi, and Alex who accompanied me during my time at university. Thank you for being there for me in so many ways. You have been amazingly supportive all the time. Hopefully we become old and weird together, never stopping to experience great moments.

Dipl.-Ing. Jacqueline Atanelov

Curriculum Vitae

Personal Data

Date of Birth	21.06.1988
Place of Birth	Vienna, Austria
Nationality	Austria
Home address	Praterstrasse 11/1/4, 1020 Vienna, Austria
E-mail	jacqueline.atanelov@hotmail.com

Education

09/2012–04/2016 **Doctoral studies in Technical Sciences**, *Vienna University of Technology*, Institut of Applied Physics, Center for Computational Materials Science, 1040 Vienna, Austria.

- Thesis: “Ab initio modelling of Transition Metal Oxides - Studies on stoichiometric and substituted TiO_2 and $GaFeO_3$”
- Supervisor: Peter Mohn

04/2010–06/2012 **Master studies in Technical Physics**, *Vienna University of Technology*, 1040 Vienna,, Austria.

- Master thesis: “Susceptibility Compensated fMRI – A Comparison of EPI Sequences Using quadratic and linear Phase RF Excitation Pulses” at the MR Centre of Excellence, Medical University Vienna
- Supervisor: Christian Windischberger

04/2010–06/2012 **Bachelor studies in Technical Physics**, *Vienna University of Technology*, 1040 Vienna,, Austria.

- Bachelor thesis: “Einführung einer neuen Charge Thermolumineszenz- detektoren für die klinische Dosimetrie und Bestrahlungsplanung ” at the Department of Radiotherapy, Hospital Hietzing
- Supervisor: Petra Schmid

09/1998–06/2006 **AHS De La Salle Schule Strebersdorf**, *Secondary School*, 1210 Vienna, Austria.

Publications

J. Atanelov, P. Mohn, “The electronic and magnetic properties of anion doped (C, N, S) $GaFeO_3$; an *ab initio* DFT study”, *Computational Materials Science*, Feb. 2016. accepted

J. Atanelov, P. Mohn, “The electronic and magnetic properties of $GaFeO_3$; ab initio calculations for varying Fe/Ga ratio, inner cationic site disorder and epitaxial strain”, *Phyiscal Review B*, vol.92, pp.104408, Sept. 2015.

J. Atanelov, C. Gruber, P. Mohn, “The electronic and magnetic structure of p-element (C,N) doped rutile-TiO_2: a hybrid DFT study”, *Computational Materials Science*, vol.98, pp.42-50, Feb. 2015.

R. Sladky, A. Höflich, J. Atanelov, C. Kraus, P. Baldinger, E. Moser, R. Lanzenberger, C. Windischberger, “Increased Neural Habituation in the Amygdala and Orbitofrontal Cortex in Social Anxiety Disorder Revealed by fMRI”, *PLoS ONE*, vol.7, pp.e50050, Nov. 2012.

A. Höflich, A. Hahn, D. Winkler, J. Atanelov, J. Losak, P. Baldinger, T. Vanicek, C. Windischberger, S. Kasper, R. Lanzenberger, “P.1.e.016 Ketamine affects brain activation during a visual integration task: a double-blind placebo-controlled pharmaco-fMRI study”, *European Neuropsychopharmacology*, vol.22, pp.201, Oct. 2012.

Conference Contributions

J. Atanelov, P. Mohn, “First-principles calculations on anion doped $GaFeO_3$”, Talk, 80th Annual Meeting of the DPG and DPG Spring Meeting (SKM), Regensburg, Germany, Mar. 2016.

J. Atanelov, P. Mohn, “First principles calculations on the effect of cation and anion doping on the magnetic properties of $GaFeO_3$”, Poster, Psi-k Conference, San Sebastian, Spain, Sept. 2015.

J. Atanelov, P. Mohn, “First principles calculations on the effect of inner cationic site disorder, single and multiple cation and anion doping on the magnetic properties of $GaFeO_3$”, Talk, 79th Annual Meeting of the DPG and DPG Spring Meeting (SKM), Berlin, Germany, Mar. 2015.

J. Atanelov, W. Mayr-Schmölzer, P. Mohn, “First principle calculations on the effect of epitaxial strain under site disorder, Cation and Anion doping on the magnetic and optical properties of $GaFeO_3$”, Talk, 59th Annual Magnetism and Magnetic Materials (MMM) Conference, Honolulu, Hawaii, Nov. 2014.

J. Atanelov, C. Gruber, P. Mohn, “Electronic and Magnetic Structure of C and N doped Rutile-TiO_2: an ab-initio DFT study”, Talk, DPG Spring Meeting (SKM), Dresden, Germany, Apr. 2014.

J. Atanelov, C. Gruber, P. Mohn, “Electronic and Magnetic Structure of C and N doped Rutile-TiO_2: an ab-initio DFT study”, Talk, APS March Meeting, Denver, USA, Mar. 2014.

J. Atanelov, M. Munk, C. Kiss, E. Moser, C. Windischberger, “High Resolution Retinotopic Mapping of the Visual Cortex at 7 Tesla”, Poster, 18th Annual Meeting of the Organization for Human Brain Mapping, Beijing, China, Jun. 2012.

J. Atanelov, J. Tröstl, R. Sladky, N. Weiskopf, C. Windischberger, “Functional Magnetic Resonance Imaging of Cerebral Blood Oxygenation Changes During Breath Holding”, Poster, 18th Annual Meeting of the Organization for Human Brain Mapping, Beijing, China, Jun. 2012.

J. Tröstl, R. Sladky, R. Boubela, J. Atanelov, E. Kacar, C. Lamm, E. Moser, C. Windischberger, “Reproducibility of Fractional Anisotropy”, Poster, 18th Annual Meeting of the Organization for Human Brain Mapping, Beijing, China, Jun. 2012.

E. Kacar, J. Atanelov, R. Sladky, J. Tröstl, R. Lanzenberger, C. Windischberger, “Optimization of White-Matter Nuisance Regressors in fMRI analysis”, Poster, 18th Annual Meeting of the Organization for Human Brain Mapping, Beijing, China, Jun. 2012.

R. Sladky, P. Baldinger, G. Kranz, J. Tröstl, A. Höflich, J. Atanelov, T. Vanicek, R. Lanzenberger, E. Moser, C. Windischberger,, “A quantitative comparison of functional MRI of the human amygdala at 3 and 7 Tesla”, Talk, 18th Annual Meeting of the Organization for Human Brain Mapping, Beijing, China, Jun. 2012.